Conceptual Design of a 1000-MW(e) Heterogeneous Oxide LMFBR
Volume 2: Appendixes

NP-1616, Volume 2
Research Project 620-32

Final Report, November 1980
Work Completed, August 1980

Prepared by

SCIENCE APPLICATIONS, INC.
1211 West 22nd Street, Suite 901
Oak Brook, Illinois 60521

Principal Investigators
W. P. Barthold
C. P. Tzanos

With Contributions by
F. Gunnison
N. Hanan
R. Jarka
P. Lam
R. May
B. Singer

Prepared for

Electric Power Research Institute
3412 Hillview Avenue
Palo Alto, California 94304

EPRI Project Manager
R. K. Winkleblack

Developing Applications and Technology Program
Nuclear Power Division

ORDERING INFORMATION

Requests for copies of this report should be directed to Research Reports Center (RRC), Box 50490, Palo Alto, CA 94303, (415) 965-4081. There is no charge for reports requested by EPRI member utilities and affiliates, contributing nonmembers, U.S. utility associations, U.S. government agencies (federal, state, and local), media, and foreign organizations with which EPRI has an information exchange agreement. On request, RRC will send a catalog of EPRI reports.

NOTICE

Prepared by
Science Applications, Inc.
Oak Brook, Illinois

EPRI PERSPECTIVE

PROJECT DESCRIPTION

The work reported herein, under RP620-32, is a follow-on to that reported in EPRI Interim Report NP-1000. Related work is reported in EPRI Final Reports NP-1615, Core Restraint and Seismic Analysis of a Large Heterogeneous Free-Flowering Core Design; and NP-1617, Hardware Concepts for a Large Low-Energetics LMFBR Core. These two reports and NP-1616 are the final reports of the project.

PROJECT OBJECTIVE

The objective of this project is to show the feasibility and practicality of large liquid metal fast breeder reactor cores that have significantly reduced sodium void coefficients of reactivity due to the placement of blanket subassemblies at strategic locations within the core assembly. Such cores will have characteristics that will reduce the energetics of a hypothetical core disruptive accident to a very low value such that the impact on the vessel head would be tolerable.

PROJECT RESULTS

The objective has been accomplished. The reference core design is shown by analysis to be a sound basis for final development of a safe, licensable, reliable, and efficient breeder core. Further improvements may be made in final engineering and experimental verification. This reference design will be an excellent "yardstick" with which to measure whether future refinements truly represent real improvements in such areas as excess plutonium production, low energetics, full-power days of power produced between shutdowns for refueling, peak clad temperatures, maximum-to-average ratio of sodium temperature at the fuel and blanket subassemblies outlets, maximum-to-average burnup ratios, and other factors of merit.

This report is directed to LMFBR core designers, neutronics and thermohydraulic analysts.

R. K. Winkleblack, Project Manager
Nuclear Power Division

ABSTRACT

A numerical core/blanket design is presented for a large--1000-MW(e)--liquid metal fast breeder reactor (LMFBR) that has a much lower sodium void coefficient of reactivity than would be the case for a core assembly made up entirely of fuel subassemblies with an appropriate number of control rods. Blanket subassemblies are placed among the fuel subassemblies to form a "heterogeneous" core/blanket assembly that would have low energetics in case of a hypothetical core disruptive accident (HCDA) but still retains good thermohydraulic performance, good breeding gain, and a reasonable fuel cycle.

APPENDICES

APPENDIX A

OPTIMIZATION OF PARKED CONTROL ROD POSITION

Control rods in their parked position are usually located at the axial blanket-core interface. While further removal of the control rods does not significantly affect reactor criticality, it has been shown that breeding performance is significantly affected by the positioning of the parked control rods. The intent of this study was to determine how breeding performance can be improved by moving the parked control rod position farther away from the upper axial blanket-core interface.

Methodology

Control rod worths were determined in hexagonal geometry. The reactor was then mocked up in RZ geometry with the discrete control rods mocked up as control rings. To assure equal reactivity worth, the poison number density had to be reduced by 30% for the RZ model. Then the assumption was made that this reduction in number density does not only apply to the poison in the core region but also to the poison located in the axial blanket region.

Results

The design parameters for this study are shown in Table A.1, and the core layout is shown in Figure A.1. The results of this investigation are summarized in Figure A.2 which shows the doubling time as a function of the position of the parked control rods and boron enrichment. Having all the control rods parked three inches above the core-blanket interface rather than at the interface itself reduces doubling time by 0.7 to 0.9 years, depending on the boron enrichment. Moving the parked positions more than 9 inches above the core-blanket interface reduces the doubling time by more than 1.5 years. Moving the parked control rods more than 15 inches above the core reduces doubling time by 2.4 years.

While these reductions are impressive, it must be remembered that it is physically

Table A.1

DESIGN PARAMETERS

Fuel Pin/Blanket Pin	
Cladding O.D., in.	0.26/0.425
Cladding Thickness, in.	0.013/0.013
Fuel Smear Density, % T.D.	88/90
Fuel Assembly/Blanket Assembly	
Pins Per Assembly	271/127
p/d	1.197/1.070
Lattice Pitch, in.	5.653/5.653
Duct Thickness, in.	0.113/0.113
Interassembly Gap, in.	0.215/0.215
Nominal Peak Linear Heat Rating, kw/ft	
Core	13.4
Internal Blanket	12.8
Radial Blanket	8.7
Number of Assemblies	
Inner Core	36
Middle Core	72
Outer Core	222
Internal Blanket 1	19
Internal Blanket 2	24
Internal Blanket 3	78
Internal Blanket 4	36
Control	24
Radial Blanket	174
Shield	198

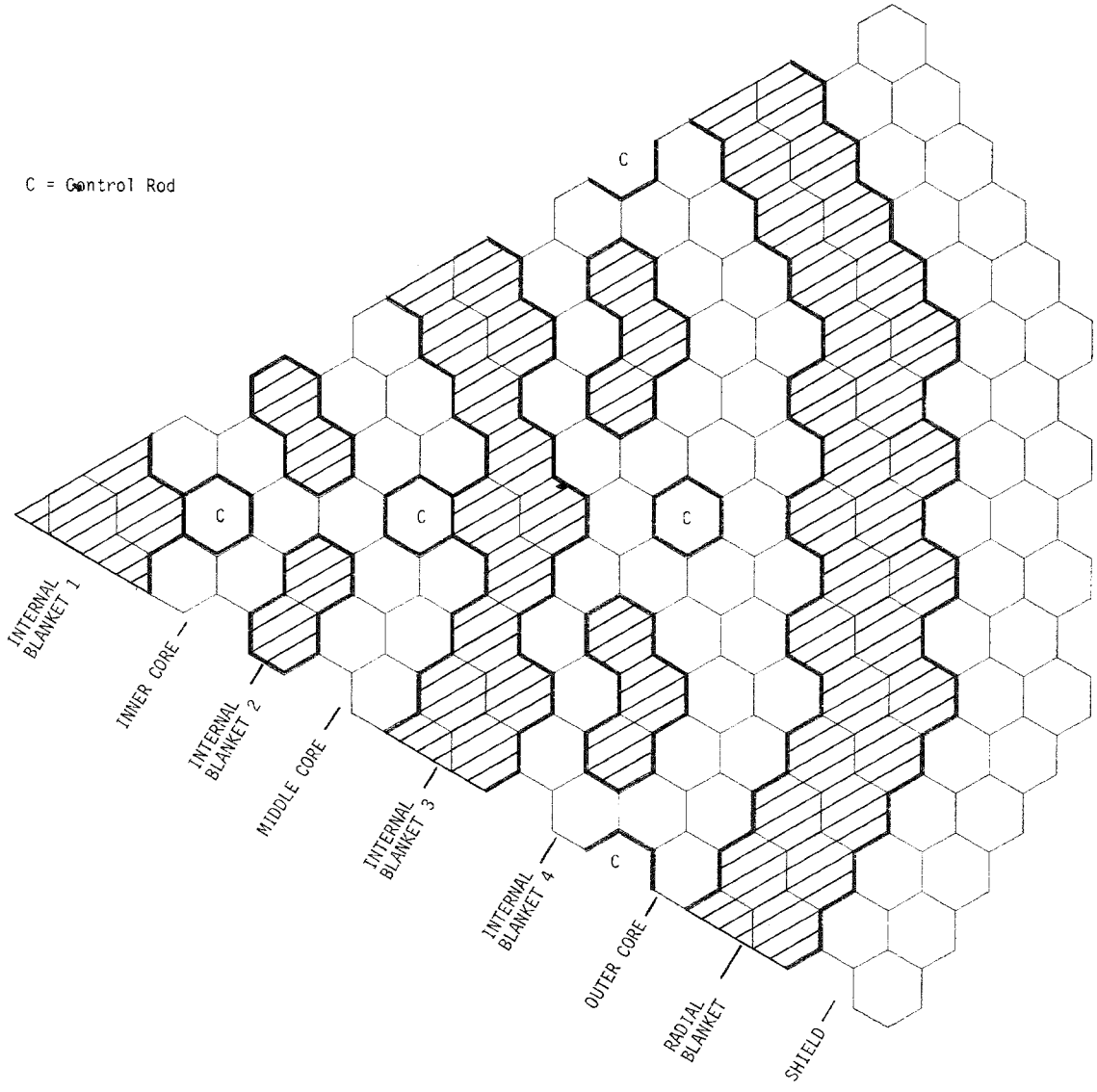

Figure A.1. Core Configuration for Reference Reactor

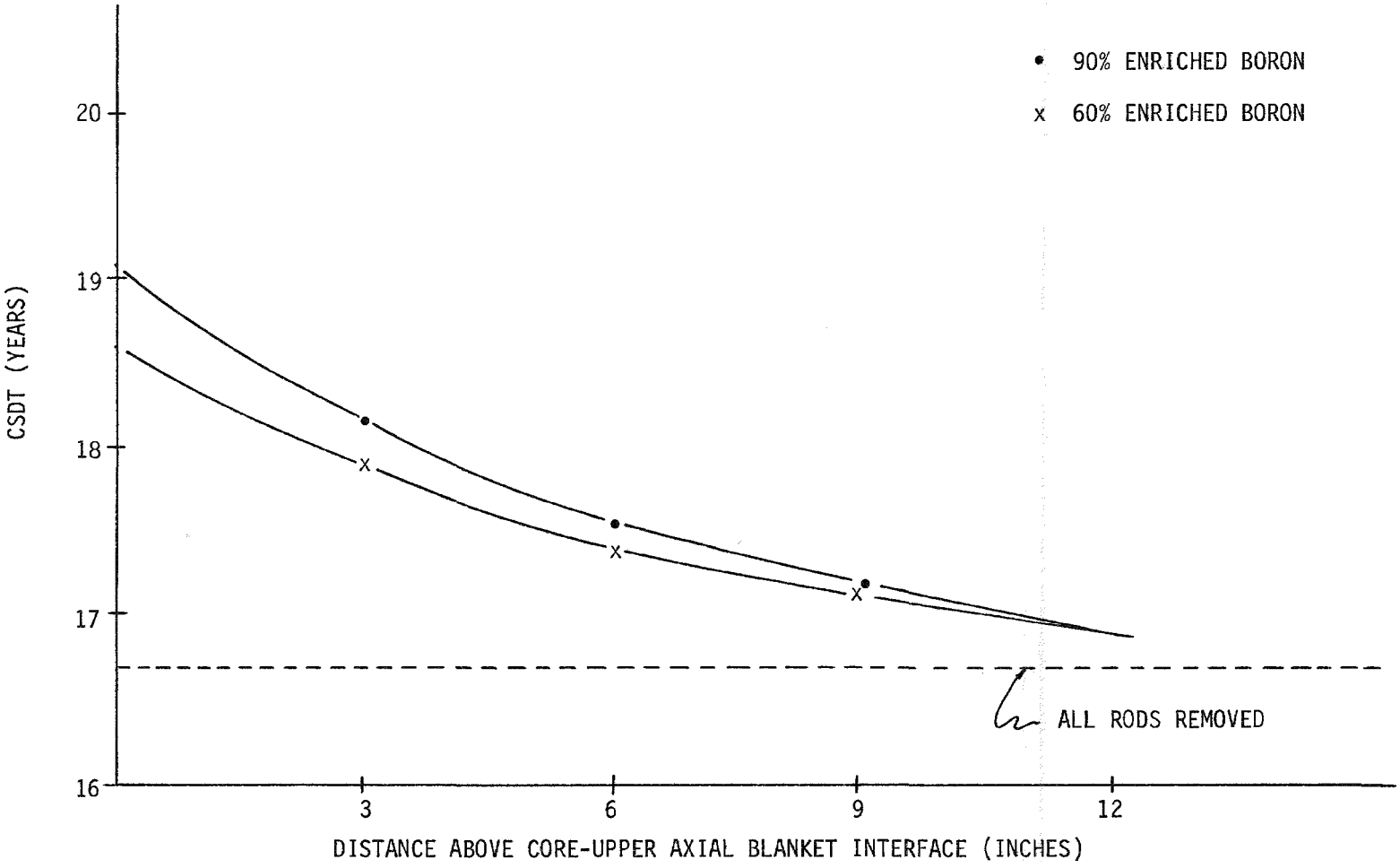

Figure A.2. Parked Position of Control Rods vs. Doubling Time (CSDT)

impossible to have the control rods parked in these locations since the control of the burnup requires the insertion of control rods. Until the end of the operating cycle these rods will extend through the upper axial blanket into the core. Therefore, in determining the impact of the location of the parked control rods on the reactor breeding performance, it is more realistic to move only the parked position of the secondary system over the core-upper axial blanket interface. Table A.2 shows the compound system doubling time for various axial blanket thicknesses and for:

a) all the control rods parked at the top of the upper axial blanket,
b) all the control rods parked at the core-upper axial blanket interface, and
c) the secondary system parked at the top of the upper axial blanket and the primary system parked at the core-upper axial blanket interface.

Moving only the parked position of the secondary system from the core-upper axial blanket interface to the top of the upper axial blanket reduces the CSDT by about one year. This is about one-half of the reduction resulting from moving all the control rods to the top of the upper axial blanket.

NOTE: Please see Appendix L which reports a brief analysis of an alternate approach using natural boron carbide control rods with fueled followers in a manner similar to the EMR-II control rods.

Table A.2

COMPOUND SYSTEM DOUBLING TIME (CSDT)
(0.260 INCH FUEL PIN DIAMETER,
255.5 FULL POWER DAYS BURN CYCLE,
2-CYCLE CORE RESIDENCE TIME)

CSDT for an Uncontrolled reactor

+LAB \ *UAB	12"	15"	18"
12"	17.66	17.16	16.87
15"	17.16	16.69	16.41
18"	16.87	16.41	16.14

CSDT for Reactor with 90% Enriched Primary
Control Rod System Parked at the
Core-Upper Axial Blanket Interface

LAB \ UAB	12"	15"	18"
12"	19.12	18.62	18.35
15"	18.53	18.07	17.81
18"	18.18	17.74	17.50

CSDT for Reactor with 90% Enriched
Primary and Secondary Control Rod Systems
Parked at the Core-Upper Axial Blanket Interface

LAB \ UAB	12"	15"	18"
12"	20.15	19.69	19.45
15"	19.50	19.06	18.84
18"	19.12	18.70	18.49

*UAB = Upper Axial Blanket Thickness (inches)
+LAB = Lower Axial Blanket Thickness (inches)

APPENDIX B

AXIAL BLANKET OPTIMIZATION

Part of the performance optimization of a heterogeneous LMFBR is the optimization of the axial blanket thickness. The performance parameters most affected by the thickness of the axial blanket are compound system doubling time (CSDT) and fuel cycle cost. The other figures of merit discussed in Section 4.2.2, will not change significantly when the axial blanket thickness is changed.

Design Basis

The optimization of the axial blanket thickness was carried out for the reference core layout using a 0.26 inch fuel pin (Appendix A). 90% enriched boron control rods are in their parked position at the core-upper axial blanket interface.

Methodology

The reactor was modeled in RZ geometry. The boron enrichment of the control rings had been adjusted so that the rings have the same worth as 90% enriched boron rods in hexagonal geometry. The control rods entering the reactor from the top introduce an axial asymmetry.

Because of this axial asymmetry rather expensive full-core calculations would be necessary unless it is possible to "synthesize" core performance from half-core calculations. Table B.1. summarizes the fissile inventories of the following types of burnup calculations for BOEC and EOEC conditions.

1. "Whole core" burnup calculations were carried out where the upper axial blanket contains the parked control rods but the lower axial blanket contains none.
2. Half-core burnup calculations were carried out for control rod-in and control rod-out configurations. The whole core fissile inventories were then "synthesized" by adding the inventories of a half-core calculation with and a

Table B.1

FISSILE INVENTORY
(15" AXIAL BLANKETS WITH CONTROL RODS PARKED
AT CORE-UPPER AXIAL BLANKET INTERFACE)

	BOEC		EOEC	
	Whole Core	Synthesized Core	Whole Core	Synthesized Core
Inner Core	404.51	404.60	369.30	369.38
Middle Core	807.55	807.71	734.70	734.82
Outer Core	2,557.26	2,557.74	2,356.35	2,356.69
Total Core	3,769.33	3,770.05	3,460.32	3,460.89
Internal Blanket 1	18.16	18.15	51.64	51.60
Internal Blanket 2	32.22	32.21	89.45	89.41
Internal Blanket 3	95.03	95.01	266.05	265.98
Internal Blanket 4	41.57	41.52	116.10	115.97
Total Internal Blanket	186.99	186.89	523.23	522.95
Axial Blanket	47.98	47.81	140.39	139.95
Radial Blanket	311.09	311.11	454.88	454.89
Total Reactor	4,315.39	4,315.86	4,578.82	4,578.68

half-core calculation without control rods

The results in Table B.1. show less than 0.01% error in the BOEC and EOEC fissile inventories. Therefore, CSDT and fuel cycle cost for the axial blanket optimization can be determined from synthesized cores.

Doubling Time vs. Axial Blanket Thickness

The relationship between doubling time and axial blanket thickness was determined for three control rod configurations:

1. Both the primary and secondary control system parked at the core-upper blanket interface (indicated by "P/S CONTROL" in Figure B.1).
2. The primary control system parked at the core-upper axial blanket interface and the secondary system parked at the top of the upper axial blanket (indicated by "P CONTROL" in Figure B.1).
3. Both control systems parked at the top of the upper axial blanket (indicated by "NO CONTROL" in Figure B.1).

Figure B.1 shows CSDT as a function of the lower axial blanket length. Increasing the upper and lower axial blanket thicknesses separately lowers doubling time at rates which depend on the position of the parked control system. In case of a control system which is parked at the top of the upper axial blanket, this decrease in doubling time is the same for the same increase in upper or lower axial blanket thickness. However, when the primary control system is parked at the core-upper axial blanket interface, and even more so when both primary and secondare control systems are parked at this location, lengthening the lower axial blanket is a slightly more effective means than lengthening the upper axial blanket. Table B.2 shows that a three inch increase in lower axial blanket thickness from 12 to 15 inches reduces doubling time from 0.5 years (no control) to 0.65 years (primary and secondary control system at interface). The same change in thickness for the upper axial blanket results in a 0.5 years and 0.46 years reduction in doubling time, respectively. These differences in axial blanket effectiveness are more pronounced when the blanket thicknesses are increased from 15 to 18 inches. For the case where primary and secondary control systems are parked at the interface, the lower axial blanket increase yields a 0.38 year reduction in doubling time whereas the lengthening of the upper axial blanket decreases doubling time by 0.24 years.

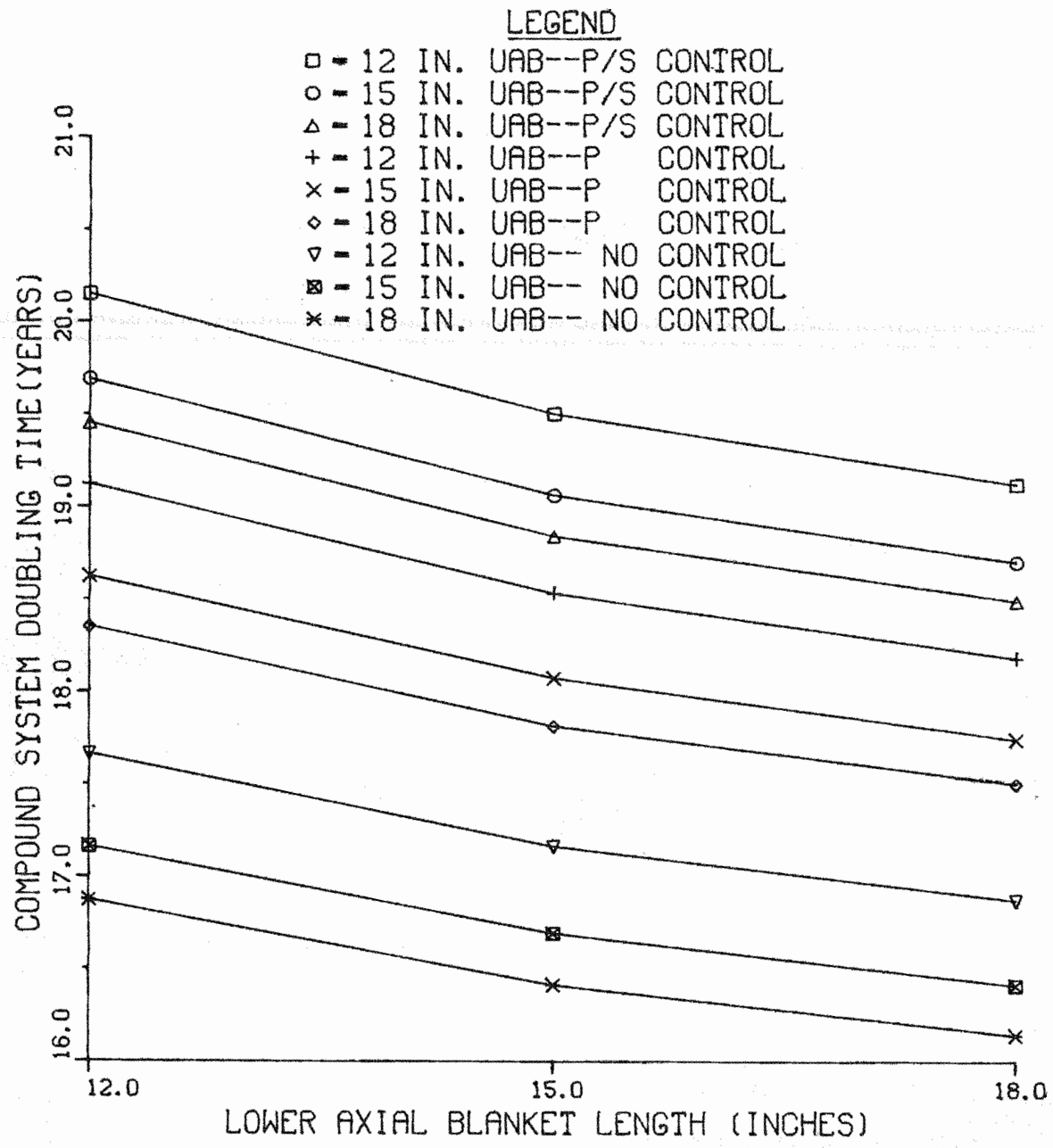

Figure B.1. Compound system doubling time vs. lower axial blanket thickness.

Table B.2

COMPOUND SYSTEM DOUBLING TIMES FOR VARIOUS AXIAL BLANKET THICKNESSES AND DIFFERENT PARKED POSITIONS OF THE 90% ENRICHED CONTROL ROD SYSTEMS

Primary and Secondary Control Systems Parked at Top of Upper Axial Blanket

+LAB \ *UAB	12	15	18
12	17.66	17.16	16.87
15	17.16	16.69	16.41
18	16.87	16.41	16.14

Primary Control System Parked at Core-Upper Axial Blanket Interface

LAB \ UAB	12	15	18
12	19.12	18.62	18.35
15	18.53	18.07	17.81
18	18.18	17.74	17.50

Primary and Secondary Control System Parked at Core-Upper Axial Blanket Interface

LAB \ UAB	12	15	18
12	20.15	19.69	19.45
15	19.50	19.06	18.84
18	19.12	18.70	18.49

*UAB = Upper Axial Blanket Thickness (inches)

+LAB = Lower Axial Blanket Thickness (inches)

While it is important to note the different effectivenesses of lower and upper axial blanket, the impact on doubling time is very small.

Fuel Cycle vs. Axial Blanket Thickness

Fuel cycle costs have been calculated for different axial blanket thicknesses and different control rod parked positions. The economic assumptions were those used by the PRLCDS (Proliferation Resistant Large Core Design Stydy[1]). The FUCOST[2] program from General Electric Company was used for the fuel cycle cost calculations. For the calculation of the fabrication cost the revised HEDL N-factor formula[3] was used. Actual commercial costs should be significantly improved.

Fuel cycle costs for different axial blanket thicknesses and different control rod parked positions, relative to the fuel cycle cost that results from a 12 inch upper and lower axial blanket without control rods, are presented in Table B.3. As the lower axial blanket thickness is increased from twelve to fifteen inches the relative fuel cycle cost increases by 0.7%. An additional three inches increases the relative cost by 1.3%. A similar trend is seen when the lower axial blanket thickness is fixed and the upper blanket thickness is increased. Finally, Table B.3 shows that if the thickness of the upper and lower axial blankets are changed uniformly, the trend is the same, i.e., as the blanket thickness increases the relative fuel cycle cost increases at an increasing rate. The impact of the control rods is similar to that observed for the CSDT, i.e., the relative costs are displaced almost uniformly upward by about 5% when both control systems are parked at the core-upper axial blanket interface.

Plutonium Recovery Costs vs. Axial Blanket Thickness

Another way to quantify the costs associated with different size axial blankets is to consider the recovery cost of the plutonium generated in the blankets. Increasing the axial blanket size increases both fissile gain and the heavy metal inventory. The total reprocessing costs are assumed to increase in proportion to heavy metal inventory. Thus, the following question arises. To what price would the plutonium value have to rise so that the value of the plutonium recovered from an increased section of the axial blanket would offset the accompanying increase in the total reprocessing costs? (The above and below assumptions maybe pessimistic.)

Assuming that the total reprocessing costs are $595/kg of heavy metal[1], the cost of the plutonium can be determined as follows:

Table B.3

RELATIVE FUEL CYCLE COSTS FOR DIFFERENT AXIAL BLANKET THICKNESSES AND DIFFERENT CONTROL ROD PARKED POSITIONS

Lower Axial Blanket Thickness, Inches	Upper Axial Blanket Thickness, Inches 12	15	18
12	1.000[a] 1.054[b]		
15	1.007[a] 1.060[b]	1.016[a]	
18	1.020[a] 1.074[b]	1.027[a] 1.085[b]	1.040[a] 1.100[b]

[a] w/o control

[b] Parked control rods at upper axial blanket interface

1. Determine the EOL heavy metal and plutonium inventories for a specified axial blanket size.
2. Increase the axial blanket thickness and determine the new EOL blanket inventories.
3. Multiply the difference of the heavy metal inventories by the total reprocessing cost per kilogram of heavy metal and then divide by the difference, in grams, of the plutonium inventories to obtain the price per gram at which the plutonium would have to sell to offset the increase in total reprocessing costs.

The CSDT changes and the plutonium value in dollars per gram for changes in axial blanket thickness,for a reactor with control rods parked at the core-upper axial blanket interface,are given in Table B.4. The upper left hand corner represents a system with a 12 inch upper and a 12 inch lower axial blanket. Across the first row, the upper axial blanket is increased in three inch increments while the lower axial blanket is held constant. Similarly, going down a column the lower axial blanket is increased by three inch increments while the upper axial blanket is held constant and diagonally both the upper and lower axial blankets are changed by three inches. The CSDT for each reactor is given immediately under the axial blanket thickness. Between the squares are the recovery costs of the plutonium in dollars per gram for the additional three inches of blanket-six inches on the diagonal. They are broken down into three cost items; the cost associated with the axial blanket above the internal blankets, the cost associated with the axial blankets above the core regions, and the cost associated with the axial blanket portion of the radial blanket region.

Table B.4 can also be used to determine the plutonium recovery costs for a reactor with the control rods removed as follows: Consider two reactors, with or without control rods parked in the upper axial blanket, which differ only in the lower axial blanket thickness.

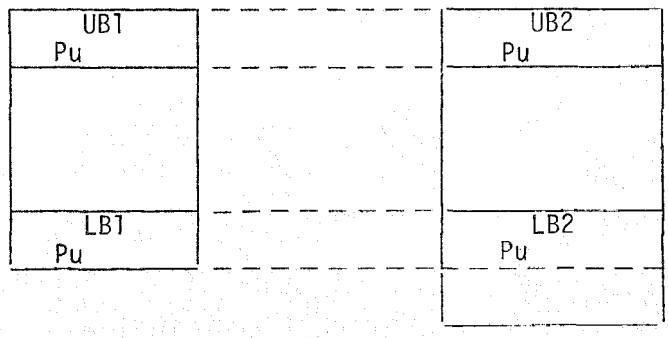

TABLE B.4

Summary of plutonium values and CSDTS
for various axial blanket thicknesses with 90%
enriched control rods parked at core-blanket interface

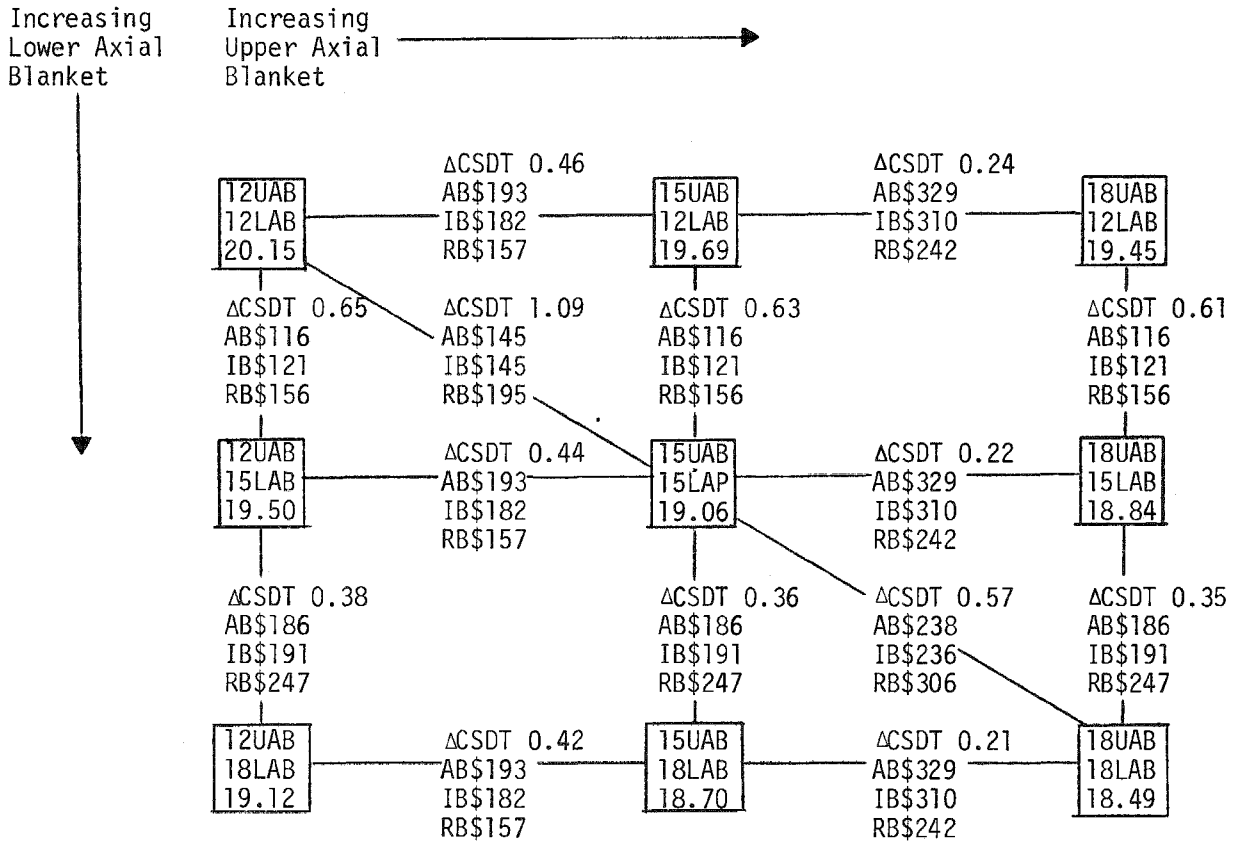

AB$: Plutonium Worth/gm in dollars for break-even.

AB : Axial blanket--blanket above core region.

IB : Internal blanket--axial blanket above internal core blanket.

RB : Radial blanket--radial blanket above core-axial blanket interface.

NOTE: $ figures are based on assumptions given on page B-6. Actual costs bases do not exist as yet for competitive commercial reprocessing and refabrications. It is conceivable that the actual costs will be much improved from those based on government R & D projects.

Since the upper and lower blankets are decoupled,

$$Pu^{UB1} = Pu^{UB2}$$

Thus, the net difference in the plutonium inventory is solely due to the differences in production in the lower axial blanket. The heavy metal loadings in the reactors, with and without parked control rods, are approximately equal. Therefore, if the upper axial blanket thickness is kept constant the plutonium recovery cost is a function of the lower axial blanket thickness and it is independent of the presence of control rods. Also when the control rods are withdrawn, the reactor is symmetrical and a three inch change in the upper axial blanket is the same as a three inch change in the lower axial blanket. Thus, for a reactor with no parked control rods the plutonium recovery costs are given by only the first column of Table B.4.

In summary the following trends have been observed as the axial blanket thickness is increased:

1. The CSDT decreases as the blanket is made thicker; but as the thickness increases the improvement in the CSDT becomes smaller.
2. The fuel cycle cost increases as the blankets become thicker. Further, the cost increases at an increasing rate as the blankets are made thicker.
3. The plutonium recovery costs substantially exceed the plutonium value for thick (18 inch and over) axial blankets.
4. The presence of control assemblies in the upper axial blanket increases the CSDT and the fuel cycle cost. The increase is weakly dependent on the axial blanket thickness and directly proportional to the number of control assemblies parked in the blanket.
5. There is no apparent advantage in using different sizes for the upper and lower axial blankets.

A 12 inch blanket has the lowest cost, but the CSDT is too large. An 18 inch blanket has the best CSDT. However, this CSDT is only 0.4 years less than the CSDT of a 15 inch blanket and the plutonium recovery cost is over a factor of two greater than the plutonium value ($100/gm) currently used.[1] Considering these trends a 15 inch upper and lower axial blanket was chosen for the final design.

Axial Blanket Thickness vs. Axial Reflector Thickness

The partial replacement of the axial blanket by reflector material is expected to improve the fuel cycle cost and penalize the reactor breeding performance. To determine the impact of an axial reflector on the reactor breeding performance, breeding ratios and fissile inventories have been determined for different axial reflector and axial blanket thicknesses at BOL conditions. The results of these calculations are shown in Table B.5.

If the axial blanket thickness is kept constant, the addition of an axial reflector does not give any significant improvement in the reactor breeding performance. The breeding ratio increases by 0.07% when a 3 inch axial reflector is placed above the 15 inch upper axial blanket. If the axial reflector is increased to 15 inches this gives a 0.13% increase in the breeding ratio.

The replacement of a part of the axial blanket (three inches) by an axial reflector decreases the breeding ratio and consequently, penalizes the reactor breeding performance. The penalty is significant when the part of the radial blanket below and above the core is replaced by reflector material. If the axial blanket thickness is equal to 15 inches this replacement increases CSDT from 16.69 years to 18.08 years, and the fuel cycle cost decreases only by 0.4%.

Other factors must be considered. Reflector/shield material is required above and below the axial blanket material, in both the fuel subassemblies and blanket subassemblies, to attenuate the neutrons escaping which would activate structural and functional components above a tolerable level. The optimum thickness for shielding will provide a thick reflector.

Table B.5

REACTOR BREEDING RATIO AND FISSILE INVENTORY
FOR VARIOUS AXIAL BLANKET AND AXIAL REFLECTOR THICKNESSES

	Fissile Mass (kg)	Breeding Ratio
15" Axial Blanket	3,844	1.487
15" Axial Blanket with 3" Reflector	3,844	1.488
15" Axial Blanket with 15" Reflector	3,844	1.489
12" Axial Blanket with 3" Reflector	3,844	1.471
12" Axial Blanket with 15" Reflector	3,844	1.472
Replace Axial Blanket Region of Radial Blanket with Reflector	3,842	1.457

REFERENCES

1. "The Proliferation Resistant Preconceptual Core Design Study," HEDL TC-1082, (1978).

2. E. V. Neil, D. P. Johnson, "COROPT, A computer Program for Finding Optimum LMFBR Mixed Oxide Fuel Cores," General Electric Company, FBRD, GEFR-00006,(1976).

3. Letter, R. P. Omberg to Distribution, "A Revised Fabrication Cost Equation for Use in FBR Core Design," HEDL,(1978).

APPENDIX C

OPTIMIZATION OF THE RADIAL BLANKET RESIDENCE TIME

The residence time of the radial blanket affects the reactor breeding performance as well as the fuel cycle cost. To determine an optimum residence time for each row of radial blanket assemblies, the impact of their residence time on the reactor breeding performance and on fuel cycle cost has been analyzed. For this analysis the 0.280 in. fuel pin diameter design presented in Appendix I has been used with a core fuel residence time of three cycles and a cycle length of 255.5 full power days. Relative fuel cycle costs have been calculated using the same assumptions as in Appendix B.

Fissile inventories, compound system doubling times and relative fuel cycle costs for different residence times for the first and second row of radial blanket assemblies are presented in Tables C.1 and C.2, respectively. As the residence time increases the fissile inventory also increases and the fissile gain decreases. Consequently, the doubling time increases as the residence time increases by $\sim$0.18 years/year for the first row and by $\sim$0.12 years/year for the second row. This increase is larger for the first row than the second row because the production of fissile material approaches saturation faster in the first row than the second row (see Figure C.1). The relative fuel cycle cost reaches a minimum at a residence time of five years for the first row and six years for the second row. There is a very small increase in fuel cycle cost when the residence time of the second row of radial blanket assemblies is reduced from six to five years. At the same time there is a small improvement in CSDT. Therefore, a five year residence time has been chosen for both rows of radial blanket assemblies.

Table C.1

FISSILE INVENTORY, CSDT, AND FUEL CYCLE COST FOR DIFFERENT RESIDENCE TIMES FOR THE FIRST ROW OF RADIAL BLANKET ASSEMBLIES

	First Row Residence Time (years)*							
	3		5		7		10	
Region	BOEC	EOEC	BOEC	EOEC	BOEC	EOEC	BOEC	EOEC
Core	4,034.7	3,773.2	4,023.8	3,765.1	4,013.1	3,757.2	3,998.2	3,746.2
Internal Blanket	366.7	690.5	362.0	682.0	357.3	673.7	350.6	661.7
Axial Blanket	115.3	225.1	114.7	224.0	114.1	222.8	113.3	221.3
Radial Blanket 1	93.4	181.7	182.1	265.7	265.5	344.4	379.0	451.0
Radial Blanket 2	105.8	156.3	111.8	165.1	117.6	173.5	125.8	185.4
Total Reactor	4,715.9	5,026.8	4,794.4	5,101.9	4,867.6	5,171.6	4,966.9	5,265.6
Gain	310.9		307.5		304.0		298.7	
CSDT (Years)	15.09		15.46		15.82		16.36	
Relative Fuel Cycle Cost	1.014		1.000		1.006		1.024	

*The residence time of the 2nd row of radial blanket assemblies is 5 cycles.

Table C.2

FISSILE INVENTORY, CSDT, AND FUEL CYCLE COST FOR DIFFERENT RESIDENCE TIMES FOR THE SECOND ROW OF RADIAL BLANKET ASSEMBLIES

Region	Second Row Residence Time (years)* 3 BOEC	3 EOEC	5 BOEC	5 EOEC	7 BOEC	7 EOEC	10 BOEC	10 EOEC
Core	4,025.6	3,766.1	4,023.8	3,765.1	4,022.1	3,764.1	4,019.7	3,762.7
Internal Blanket	363.2	684.2	362.0	682.0	360.8	680.0	359.1	577.0
Axial Blanket	114.9	224.4	114.7	224.0	114.5	223.5	114.2	223.0
Radial Blanket 1	180.8	263.9	182.1	265.7	183.4	267.6	185.3	270.2
Radial Blanket 2	57.1	112.4	111.8	165.1	164.1	215.4	238.0	286.6
Total Reactor	4,741.6	5,051.0	4,794.4	5,101.9	4,844.9	5,150.6	4,916.3	5,219.5
Gain	309.4		307.5		305.7		303.2	
CSDT (Years)	15.22		15.46		15.68		16.07	
Relative Fuel Cycle Cost	1.025		1.000		0.997		1.004	

*The residence time of the 1st row of radial blanket assemblies is 5 cycles.

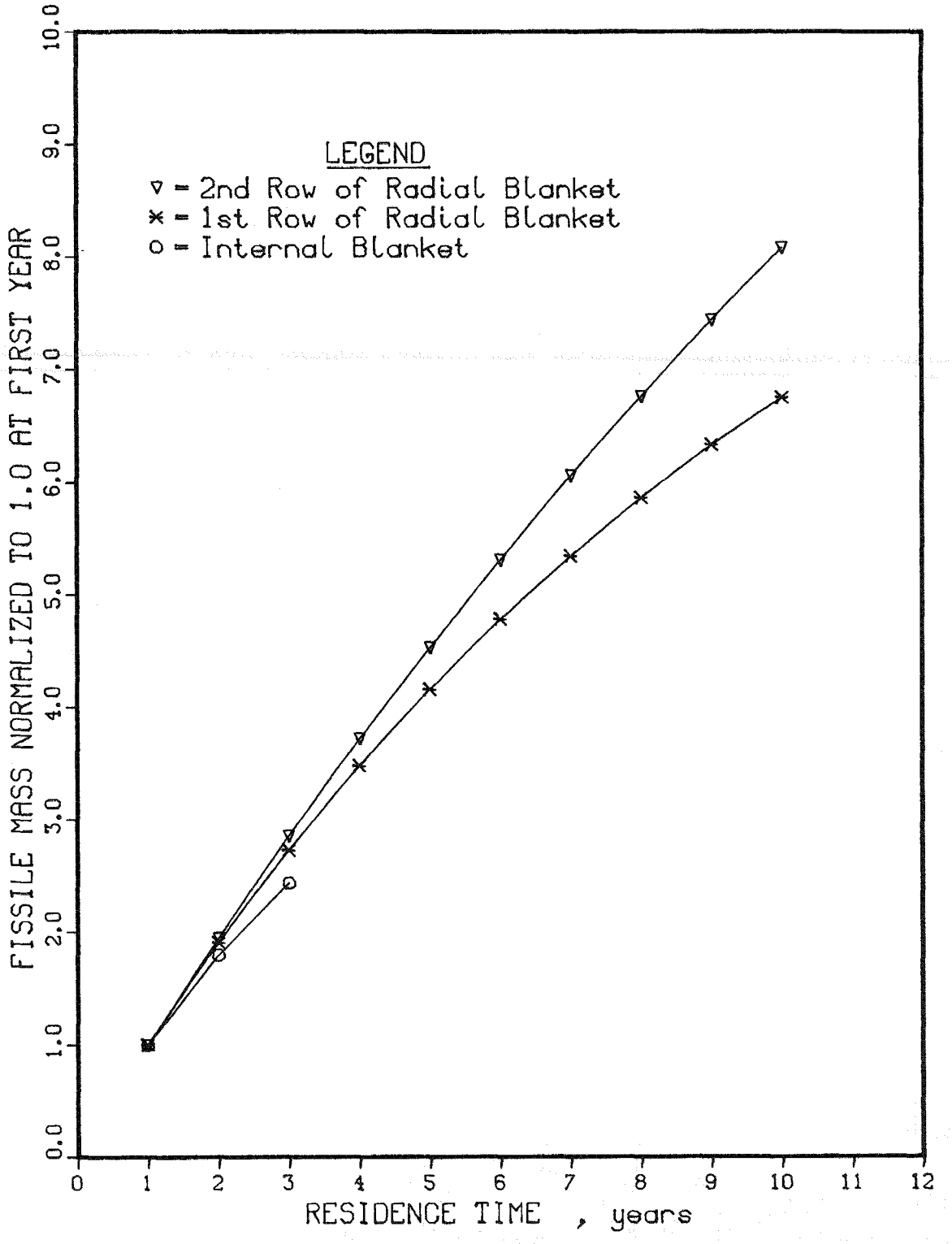

Figure C.1. Fissile material production in blanket zones vs. residence time.

APPENDIX D

CYCLE LENGTH SENSITIVITY ANALYSIS

Fuel cycle length affects the reactor breeding performance, the fuel cycle cost as well as the sodium void reactivity. To determine the impact of the cycle length on these figures of merit, CSDT, fuel cycle cost and sodium void reactivity have been determined for different cycle lengths. The 0.26 in. fuel pin diameter design described in Appendix A with an axial blanket thickness of 15 in. has been used as a reference design. The fuel residence time has been kept to two cycles for the core and internal blanket assemblies and to five cycles for the radial blanket assemblies. The fuel cycle length has been varied from 255.5 full power days (70% capacity factor) to 325 full power days. At the end of each cycle one-half of the core and internal blanket assemblies and one-fifth of the radial blanket are replaced with fresh assemblies. It was assumed that the number of fuel assemblies that are replaced at the end of each cycle does not vary with fuel cycle length and therefore, a constant downtime of 109.5 days has been used. Thus, increasing the fuel cycle length from 255.5 days to 325 days improves the capacity factor from 70% to 75%.

Fissile inventory, fissile gain, CSDT and flowing sodium void reactivity for core plus upper axial blanket voiding as functions of fuel cycle length are shown in Figures D.1 and D.2, respectively. The sodium void reactivity has been determined as described in Section 4.1.3.8 but the correction for 3-D effects has not been included. Both the fissile mass and the fissile gain increase as the cycle length increases. The reactor doubling time (i.e., the ratio of the in-core fissile mass to the product of the fissile gain times the number of cycles per year) increases from 14.6 to 14.8 years as the number of full power days is increased from 255.5 to 325 days. However, for this increase in the fuel cycle length there is a one year improvement in the CSDT. This is due to the reduction in the external fissile inventory that is included in the calculation of the CSDT.

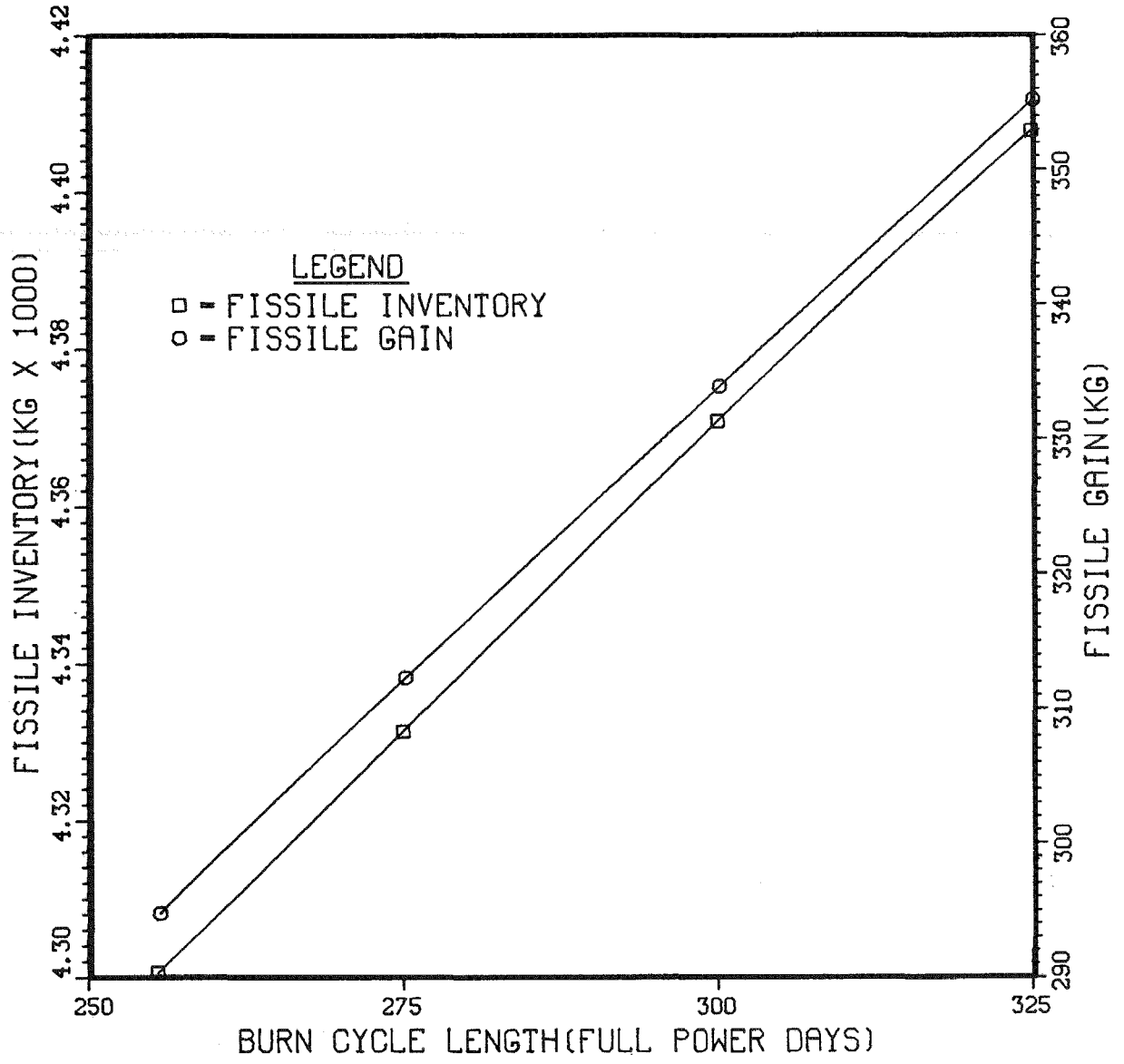

Figure D.1. Fissile inventory and gain for different burn cycle lengths.

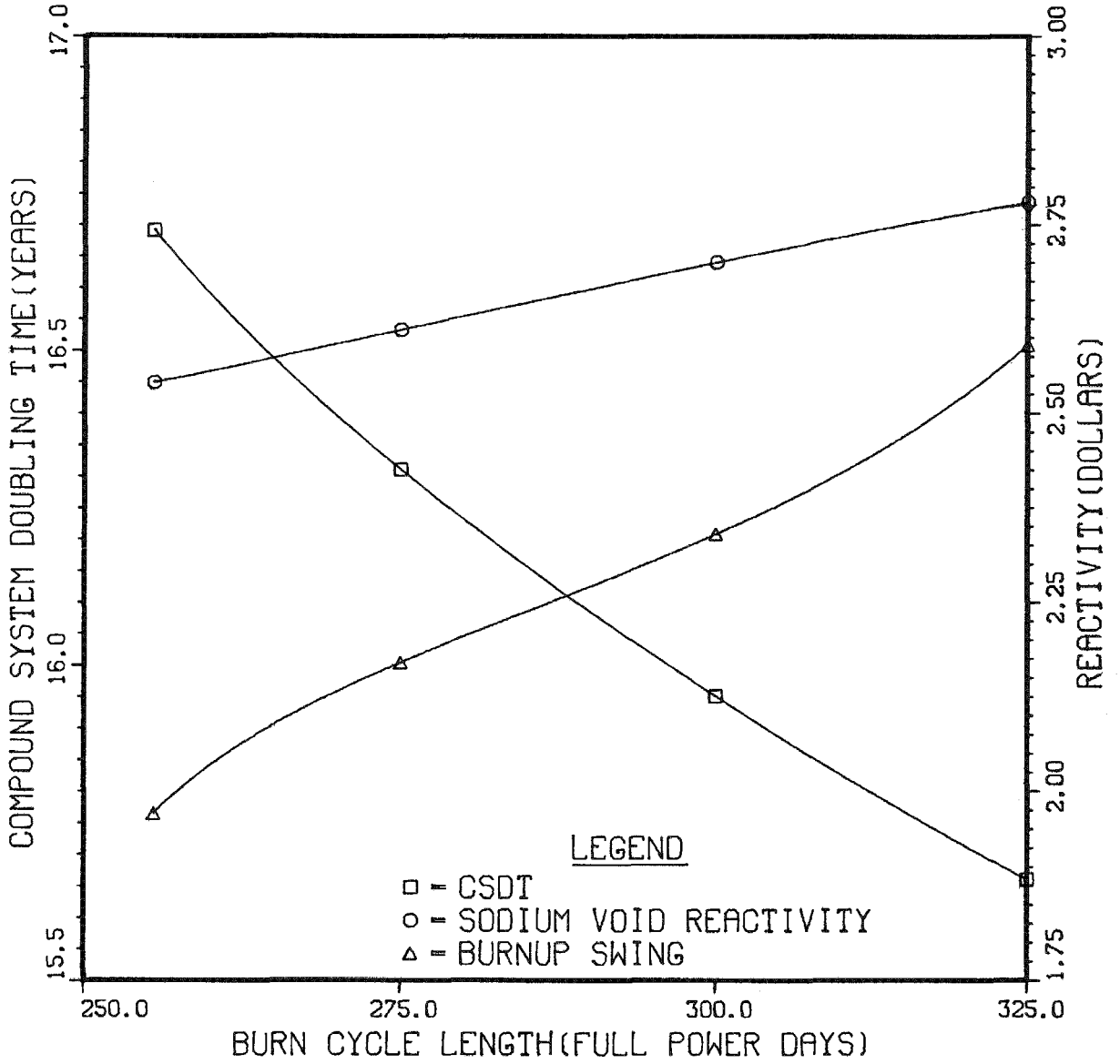

Figure D.2. Compound system doubling time, burnup swing, and flowing sodium void reactivity for different burn cycle lengths.

When the cycle length increases from 255.5 to 325 days the reactor fissile inventory increases by 107 kg; the net fissile gain* is almost constant, 264 vs. 273 kg; and the external fissile inventory is reduced by 302 kg. Thus, the CSDT, which is the ratio of the total fissile inventory (reactor plus external) to the net fissile gain, decreases.

Fuel cycle cost is reduced by about 3% for each 25 day increase in the cycle length. However, the sodium void reactivity increases as the cycle length increases. Only for a cycle length of 255.5 days is the sodium void reactivity near the design criterion of $2.50. Thus, despite the improvements in the CSDT and the fuel cycle cost, for cycle lengths greater than 255.5 days the sodium void reactivity criterion is violated for this pin diameter.

It must also be pointed out that as the cycle length increases the burn-up swing increases too. Figure D.2 shows that increasing the cycle length from 255.5 to 325 days increases the burn-up swing by 60¢. Thus, in detailed calculations of CSDT, the impact of the incremental control rod requirements, that arise from the larger burn-up swing, should be included.

*Net fissile gain = (fissile gain - processing losses - decay losses) x (number of cycles per year).

APPENDIX E

OPTIMIZATION OF ENRICHMENT ZONING

To determine the impact of the number of enrichment zones on the power peaking factor, the breeding performance,and the fuel cycle cost, the 0.26 inch fuel pin diameter design described in Appendix A has been analyzed with different enrichment zones. The number of enrichment zones were varied from one to four and they were defined as follows: 4th zone, the last ring of the outer core assemblies; 3rd zone, the rest of the outer core; 2nd zone, the middle core assemblies; 1st zone, the inner core assemblies. When the four enrichment zones were reduced to two, the 4th zone was retained and the rest of them were lumped into one zone.

The results of the analysis are presented in Table E.1. They lead to the following conclusions:

1. If the number of enrichment zones is increased from one to four:
   a. The peak/average power density ratio is reduced by 3.5%,
   b. The breeding ratio does not change,
   c. The fissile inventory increases by 0.3%, and
   d. If the allowable peak power density is fixed, the power output increases by 3.6% and the specific fissile inventory (kg/MW) is reduced by 3.2%.
2. Two enrichment zones are adequate although one enrichment zone does not give a significantly higher peak/average power density ratio.
3. Since the fissile inventory and the breeding ratio do not change significantly as the number of enrichment zones changes, the fuel cycle cost and the breeding performance do not vary significantly as the number of enrichment zones changes.
4. If the allowable peak power density is fixed, increasing the number of enrichment zones from one to two increases the power output by 2.5%.

Table E.1

POWER PEAKING FACTOR, FISSILE MASS, SPECIFIC FISSILE INVENTORY, AND BREEDING RATIO VS. NUMBER OF ENRICHMENT ZONES

Number of Enrichment Zones	Relative Enrichment				Peak/Average Power Density Ratio	Fissile Mass (kg)	Relative[a] Specific Fissile Inventory	Breeding[b] Ratio
	Zone 1	Zone 2	Zone 3	Zone 4				
1	1.0000	1.0000	1.0000	1.0000	1.596	3841.9	1.000	1.2005
2	1.0000	1.0000	1.0000	1.0138	1.557	3845.1	0.976	1.2004
4	0.9628	0.9565	0.9457	1.0000	1.540	3855.0	0.968	1.2001

[a] peak power density is kept constant

[b] 2D Hex calculation

APPENDIX F

RZ vs. HEX-Z SODIUM VOID REACTIVITY RESULTS

Since three dimensional (3D) multigroup calculations are expensive, sodium void reactivities are usually determined using an RZ multigroup model. In this model, internal blanket rings of hexagonal assemblies, even incomplete ones (broken rings), are transformed into complete cylindrical rings. To check the validity of the RZ model, sodium void reactivities have been calculated from 3D direct K_{eff} calculations. Two sets of calculations have been performed, one at BOL conditions for the 0.26 inch fuel pin diameter design (Appendix A) and another one at EOEC conditions for the 0.28 inch fuel pin diameter design (Section 3.1). In these calculations twenty-one neutron group cross sections have been used which were prepared for sodium-in and sodium-out configurations. The results show that for core and axial blanket voiding at BOL conditions the RZ model gives a 14% larger sodium void reactivity (0.00537 vs. 00471 $\Delta k/k^2$). The buildup of Pu during the burn-up in the internal blankets reduces the heterogeneity effect and, at EOEC, the RZ model gives only a 3% larger sodium void reactivity (0.01138 vs 0.01102 $\Delta k/k^2$).

APPENDIX G

THERMAL-HYDRAULIC ANALYSIS OF THE 0.26" FUEL PIN DIAMETER DESIGN

This Appendix presents the thermal-hydraulic analysis for the 0.26" fuel pin diameter design that has been used as a reference for the sensitivity and optimization analyses presented in the various Appendices. The plant conditions, the orificing strategies, and the hot channel factors are the same as for the 0.28 inch fuel pin diameter design (Sections 4.2.1, 4.2.2.1 and 4.2.3, respectively).

The assignment of assemblies to orificing zones according to assembly and peak assembly pin power are shown in Figures G.1 and G.2.

A total of nine orificing zones have been used; i.e., three for the core, four for the internal and radial blankets, one for the radial reflector and one for the control assemblies.

Assembly flow rates for the four orificing strategies discussed in Section 4.2.2.1 are given in Table G.1. The corresponding coolant velocities are given in Table G.2. The total flow rate, including the cold by-pass flow, is equal to 122,592,903 lb/hr. The flow split among the different reactor regions depends slightly on the orificing strategy. Thus, the core flow fraction varies from 69% to 75%, the flow fraction allocated to the blankets varies from 24.5% to 30.50% and the flow fraction allocated to control and shield assemblies is equal to 0.6%. The maximum assembly average coolant velocity depends on the orificing strategy too and varies from 22.4 ft/sec to 24.6 ft/sec.

Nominal peak linear power ratings for BOL and EOL conditions are given in Table G.3. The nominal peak linear power rating in the core is 13.8 kW/ft and occurs at BOL. The linear power rating of the internal and radial blankets peaks at EOL and is equal to 12.9 kW/ft and 9.5 kW/ft, respectively. Both peak linear power ratings in the core and the blankets are below the design limit values of 15 kW/ft and 16.5 kW/ft, respectively.

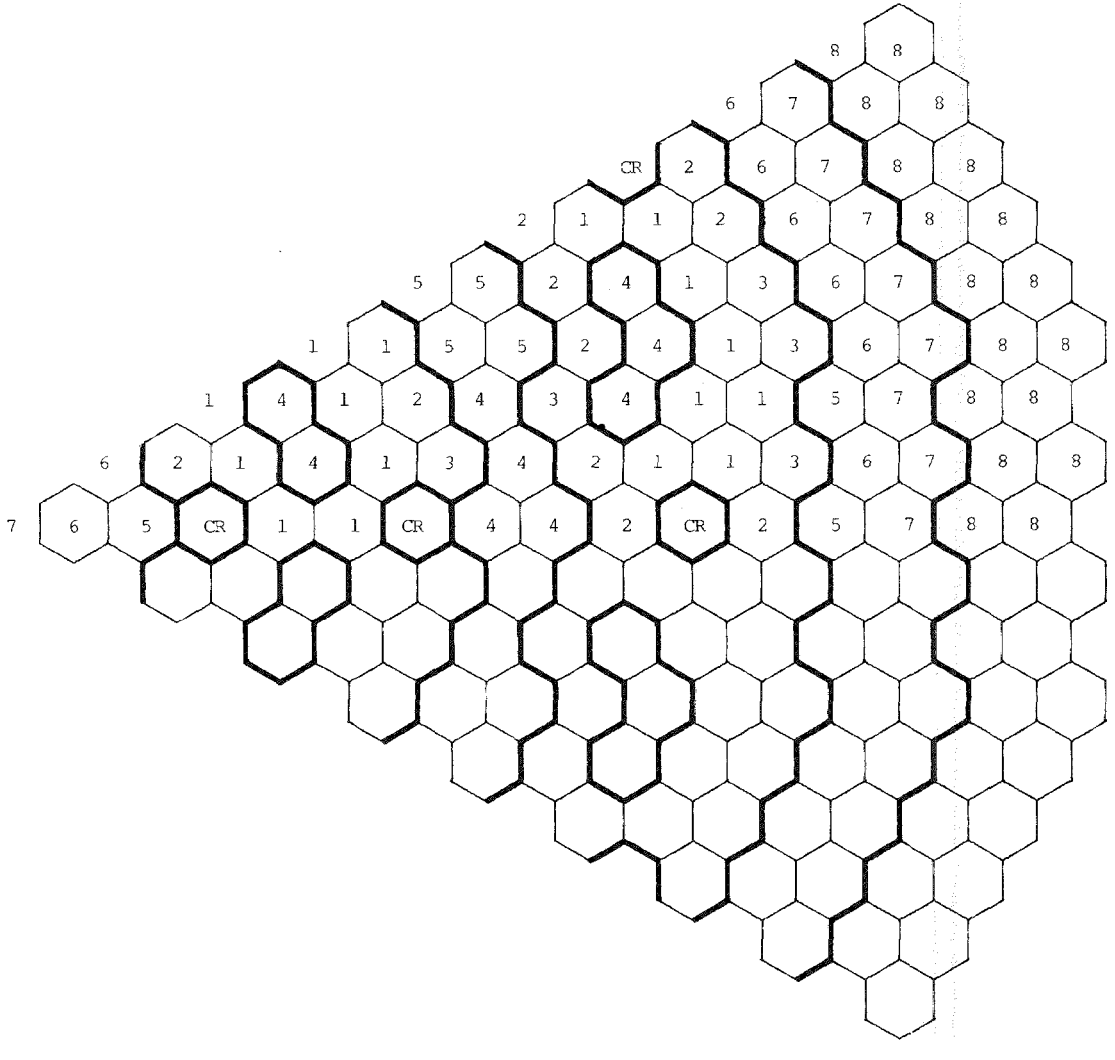

Figure G.1. Assembly Assignment to Orificing Zones According to Assembly Power

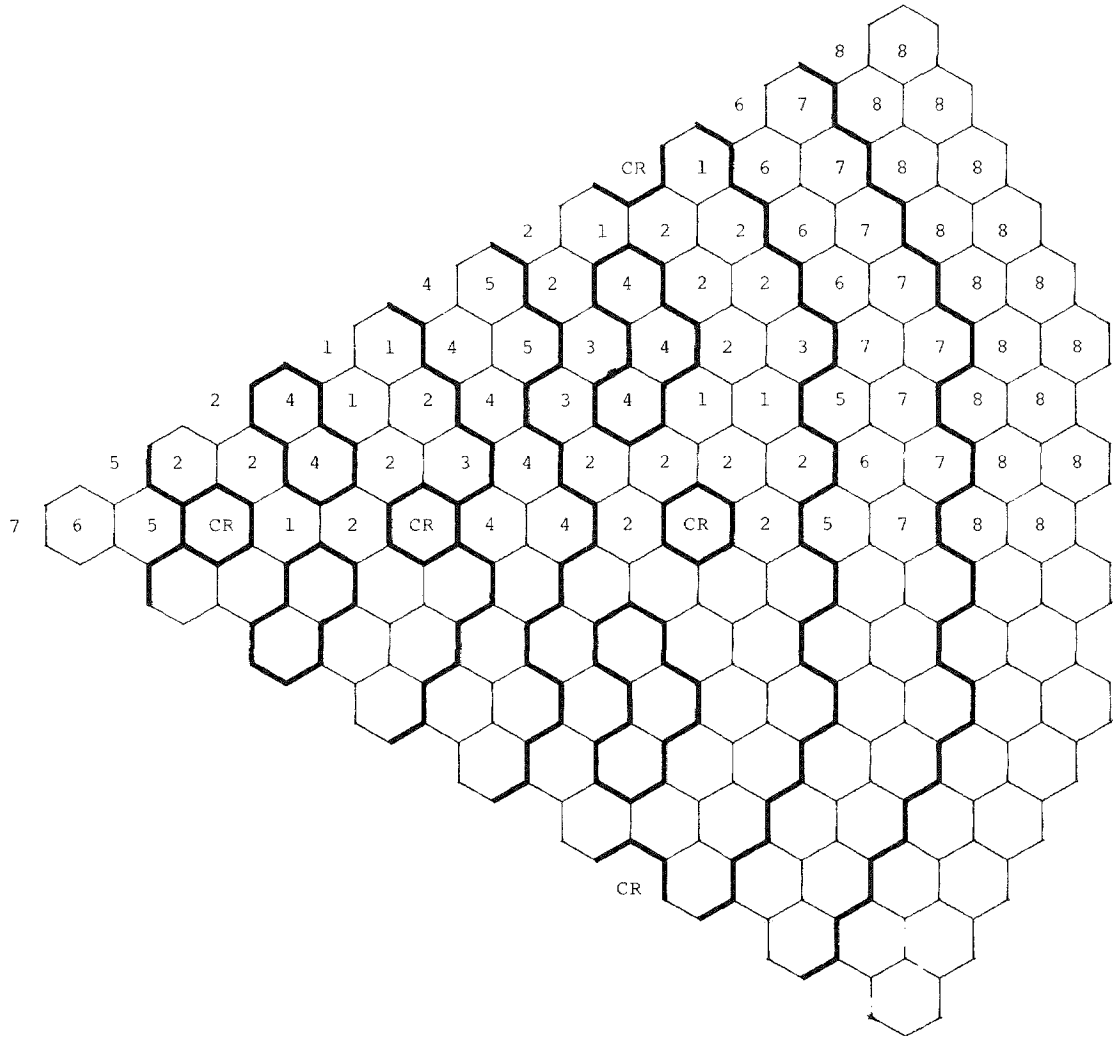

Figure G.2. Assembly Assignment to Orificing Zones According to Assembly Peak Pin Power

Table G.1

ASSEMBLY FLOW RATES (lb/hr)

Orificing Zone	Assembly Assignment to Orificing Zones Based on Assembly Power			Assembly Assignment to Orificing Zones Based on Pin Power		
	Number of Assemblies	Equal Peak Assembly Coolant Temperatures	Equal Peak Cladding Midwall Temperatures	Number of Assemblies	Equal Peak Assembly Coolant Temperatures	Equal Peak Cladding Midwall Temperatures
1	168	280106	267304	84	255024	275493
2	102	255933	258761	198	245055	256703
3	60	234030	249288	48	215172	234715
4	96	132456	131269	114	148816	127906
5	66	101808	107023	54	112788	96339
6	78	71787	74338	60	94859	82390
7	91	38976	44682	103	65742	56610
8	198	2119	2114	198	2107	2100
9	24	10734	10706	24	10682	10613
TOTAL	883	116,463,258	116,463,258	883	116,463,258	116,463,258

Table G.2

ASSEMBLY AVERAGE VELOCITIES (ft/sec)

	Assembly Assignment to Orificing Zones Based on Assembly Power		Assembly Assignment to Orificing Zones Based on Pin Power	
Orificing Zone	Equal Peak Assembly Coolant Temperatures	Equal Peak Cladding Midwall Temperatures	Equal Peak Assembly Coolant Temperatures	Equal Peak Cladding Midwall Temperatures
1	24.6	23.5	22.4	24.2
2	22.5	22.7	21.6	22.6
3	20.6	21.9	18.9	20.6
4	18.3	18.1	20.6	17.7
5	14.1	14.8	15.5	13.3
6	9.9	10.2	13.0	11.3
7	5.4	6.1	9.0	7.8

Table G.3

NOMINAL PEAK LINEAR POWER RATINGS
(kW/ft)

Reactor Region	BOL	EOL
Core	13.8	11.9
Internal Blanket	4.5	12.9
Radial Blanket	3.3	9.5

Axial distributions of the nominal and 2σ cladding midwall temperatures in the hot pin of each orificing zone are shown in Figures G.3 to G.30. In the same figures are also presented axial distributions of the average coolant, duct, and bundle temperatures for the assembly that contains the hot pin in each orificing zone. These temperatures have been calculated by the ENERGY code and therefore, interassembly heat transfer has not been taken into account. Cladding midwall temperatures in the core fuel pins peak at the top of the core and, in the blanket pins, at the top of the axial blanket.

Average assembly coolant temperatures for BOL and EOEC conditions at three axial locations, i.e., core midplane, core-upper axial blanket interface, and top of upper axial blanket, are shown in Figures G.31 to G.54. Average assembly duct wall temperatures for the same conditions and at the same locations are shown in Figures G.55 to G.78. The peak assembly coolant and duct wall temperatures as well as the nominal and 2σ peak cladding midwall temperatures that result from the four orificing strategies used in this analysis are presented in Table G.4. The orificing strategy that is based on assembly power and equal peak assembly temperatures, yields the lowest peak assembly coolant and duct wall temperatures (977^{o} F and 914^{o} F, respectively) as well as the highest cladding midwall temperatures, i.e., 1127^{o} F for nominal and 1251^{o} F for 2σ conditions. The orificing strategy that is based on pin power and equal peak cladding midwall temperatures, yields the lowest peak cladding midwall temperatures, i.e., 1061^{o} F for nominal and 1187^{o} F for 2σ conditions.

The lowest peak nominal and 2σ cladding midwall temperatures, for the 0.28 in. fuel pin diameter design (Section 4.2.4.3), are 20^{o} F and 24^{o} F, respectively, higher than the corresponding temperatures for the 0.26 in. fuel pin diameter design. This is mainly due to the larger power swing from the core zones to the blanket zones during burnup, that is present in the 0.28 fuel pin diameter design, which has a three years fuel residence time.

Rod bundle frictional pressure drops have been calculated, using Novendstern's method, for the flow rates resulting from the four orificing strategies used in this analysis. Nominal values for these pressure drops are presented in Table G.5. The limiting pressure drops occur either in the first core orificing zone or in the first blanket orificing zone (orificing zone No. 4) and they vary with the orificing strategy from 54.1 psi to 59.0 psi. To balance the pressure losses in the remaining zones with the maximum pressure loss, additional losses have to be taken in the shield/orifice region and in the core support module.

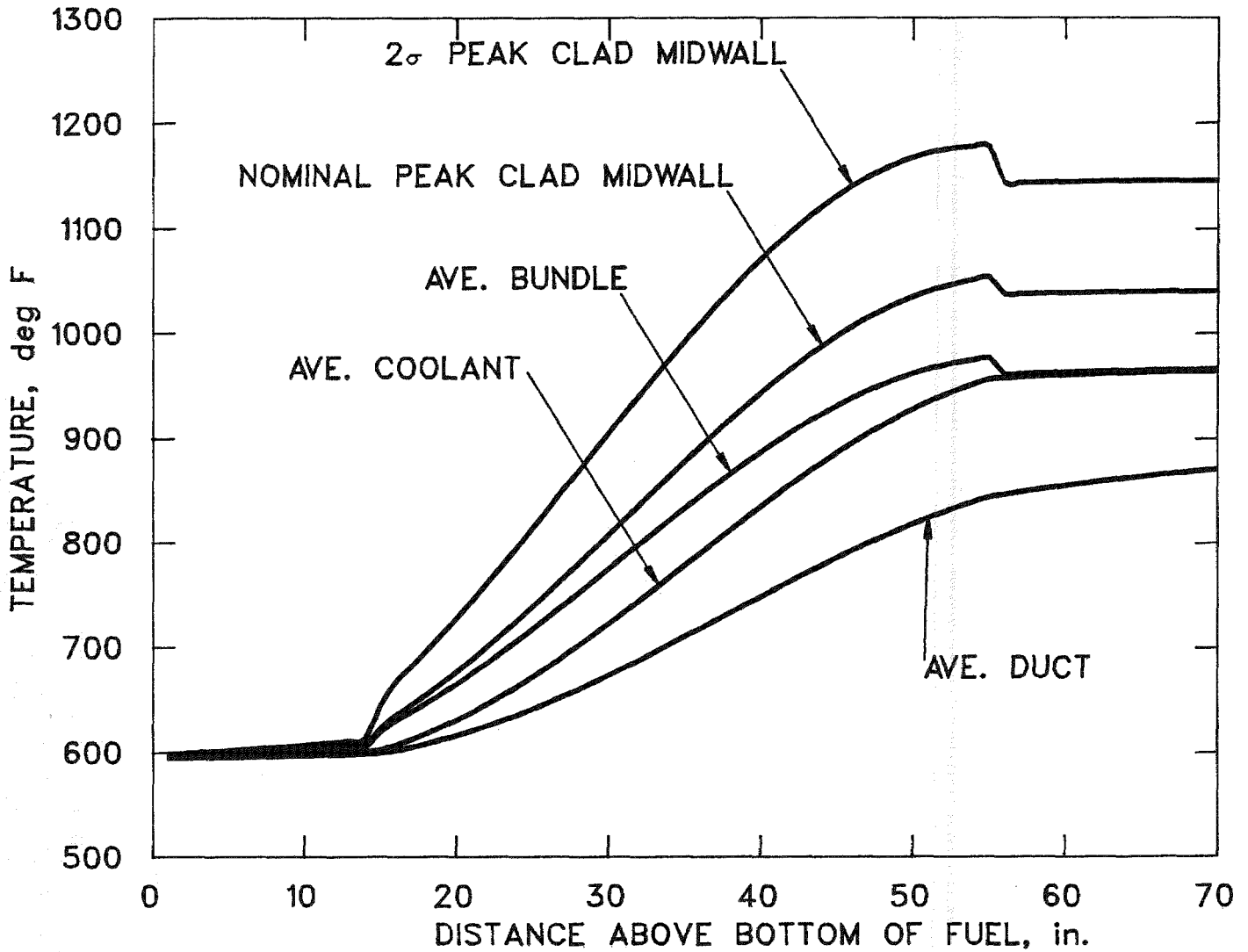

Figure G.3. Nominal and 2σ peak clad midwall temperatures and average coolant, duct and bundle temperatures. (First orificing zone, orificing based on assembly power and equal peak assembly coolant temperatures.)

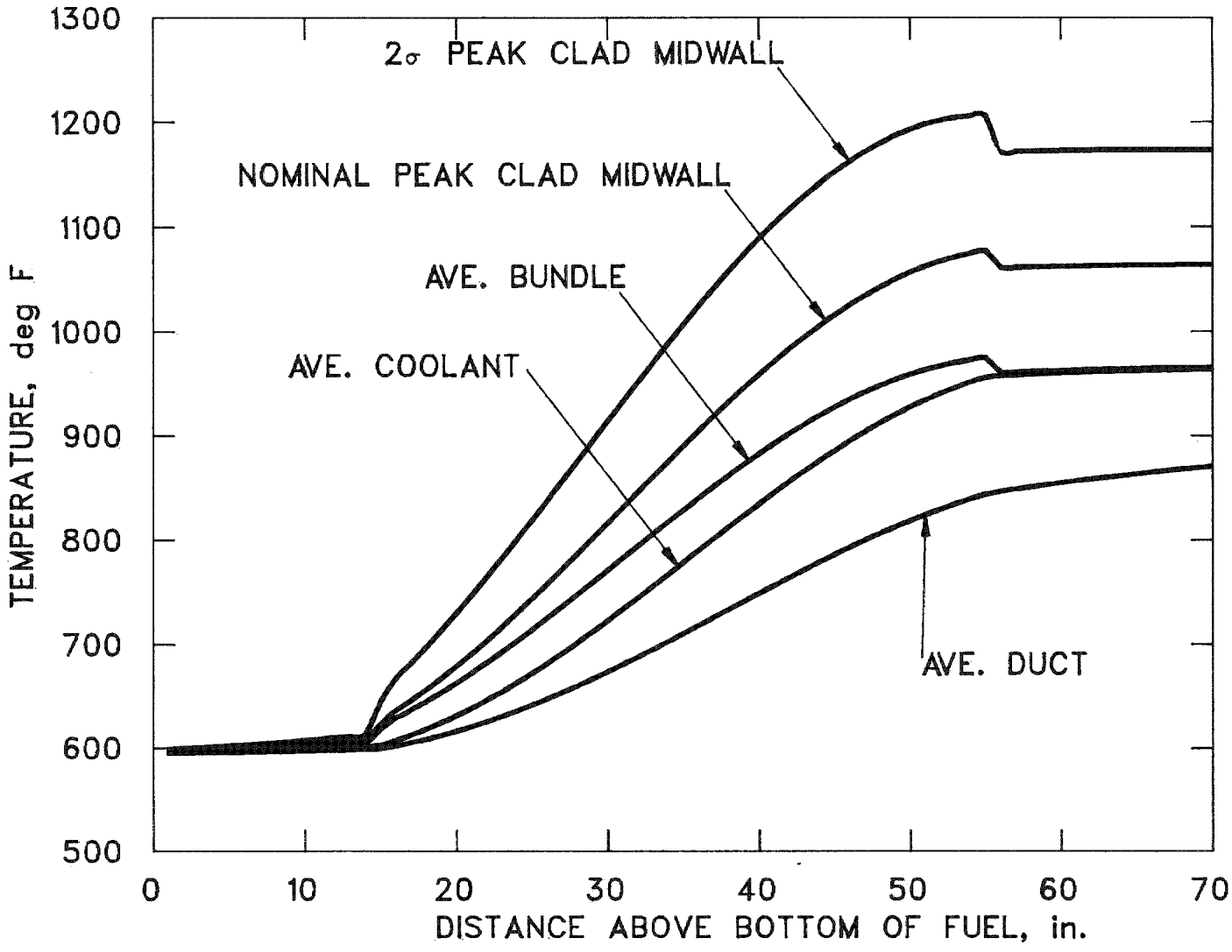

Figure G.4. Nominal and 2σ peak clad midwall temperatures and average coolant, duct and bundle temperatures. (Second orificing zone, orificing based on assembly power and equal peak assembly coolant temperatures.)

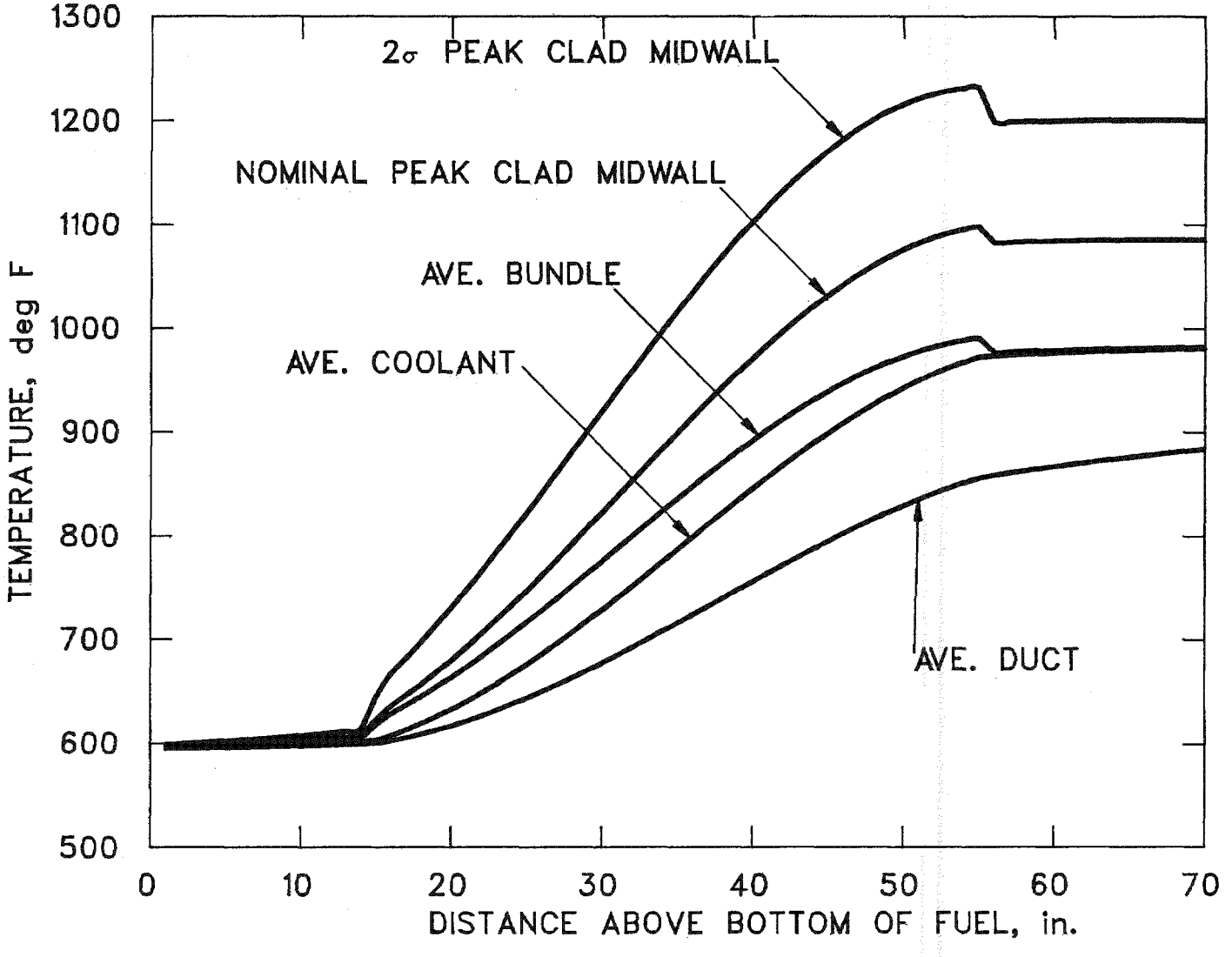

Figure G.5. Nominal and 2σ peak clad midwall temperatures and average coolant, duct and bundle temperatures. (Third orificing zone, orificing based on assembly power and equal peak assembly coolant temperatures.)

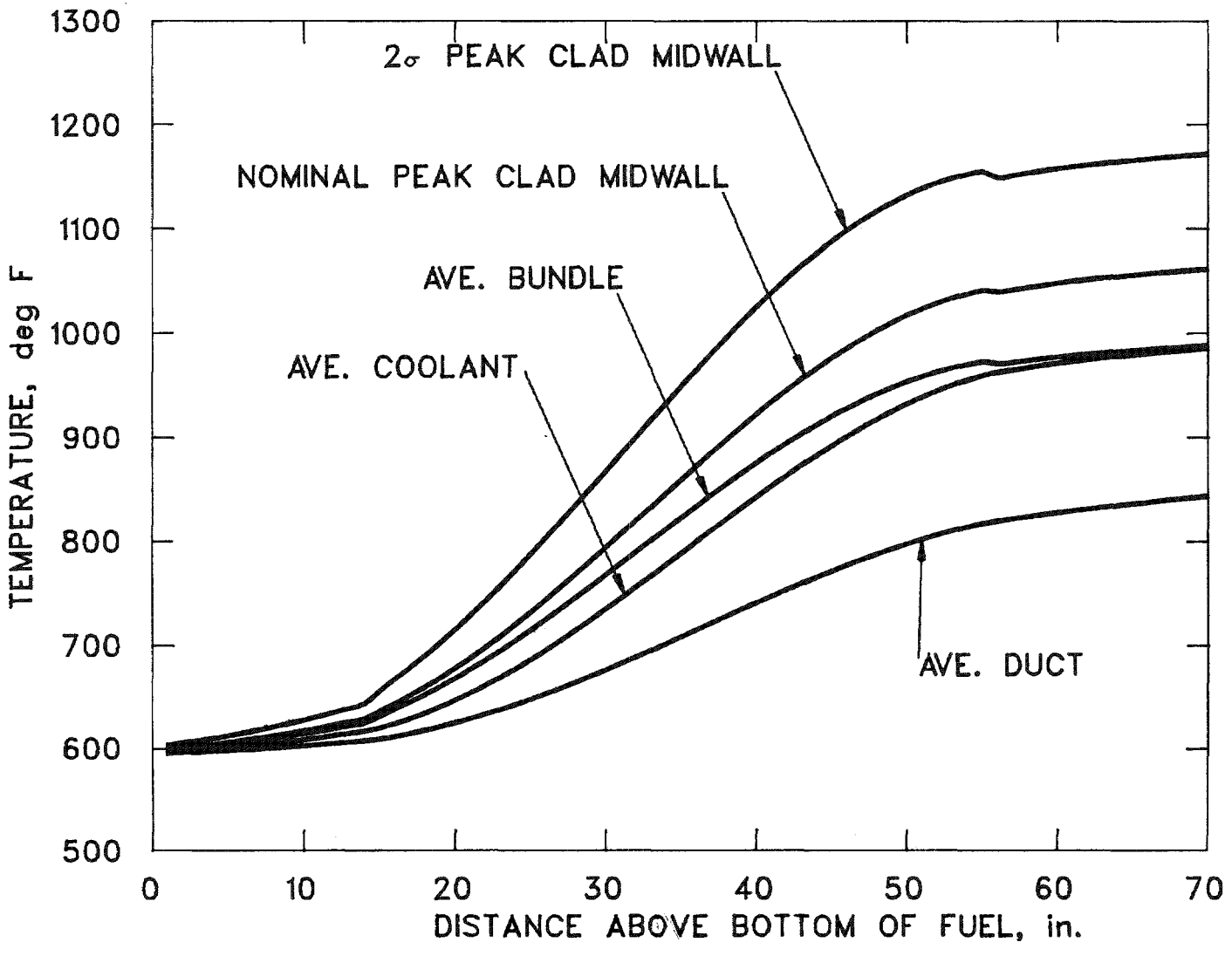

Figure G.6. Nominal and 2σ peak clad midwall temperatures and average coolant, duct and bundle temperatures. (Fourth orificing zone, orificing based on assembly power and equal peak assembly coolant temperatures.)

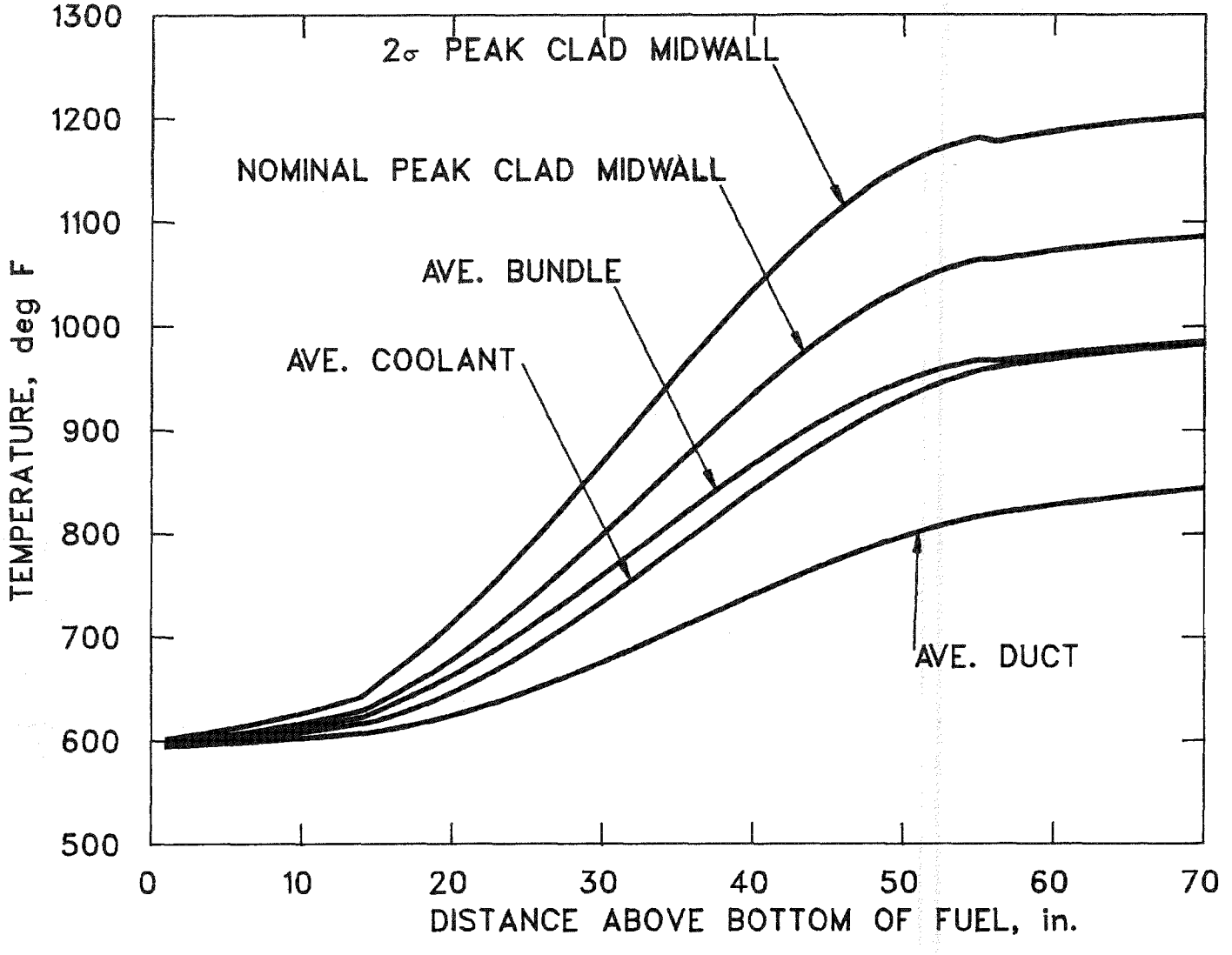

Figure G.7. Nominal and 2σ peak clad midwall temperatures and average coolant, duct and bundle temperatures. (Fifth orificing zone, orificing based on assembly power and equal peak assembly coolant temperatures.)

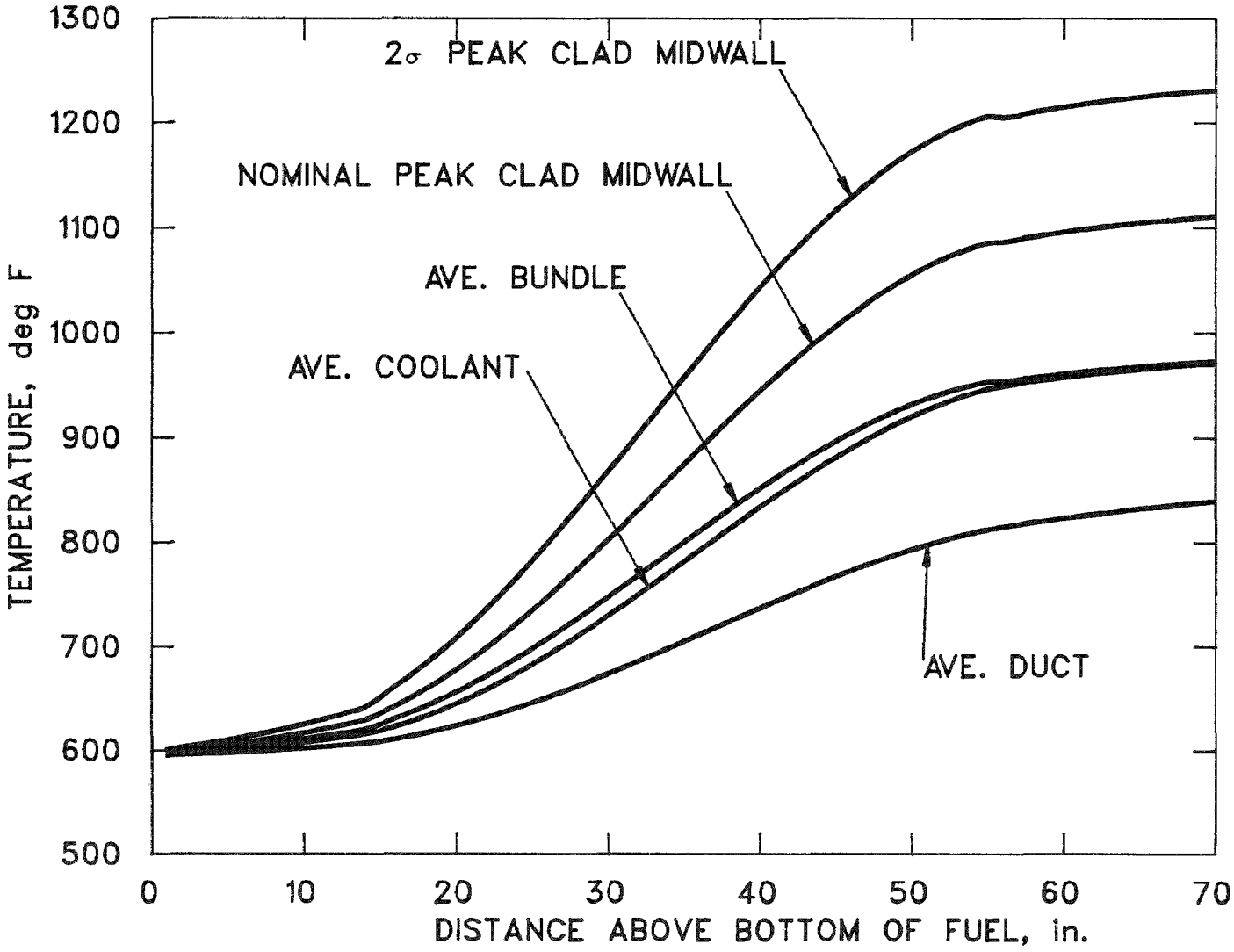

Figure G.8. Nominal and 2σ peak clad midwall temperatures and average coolant, duct and bundle temperatures. (Sixth orificing zone, orificing based on assembly power and equal peak assembly coolant temperatures.)

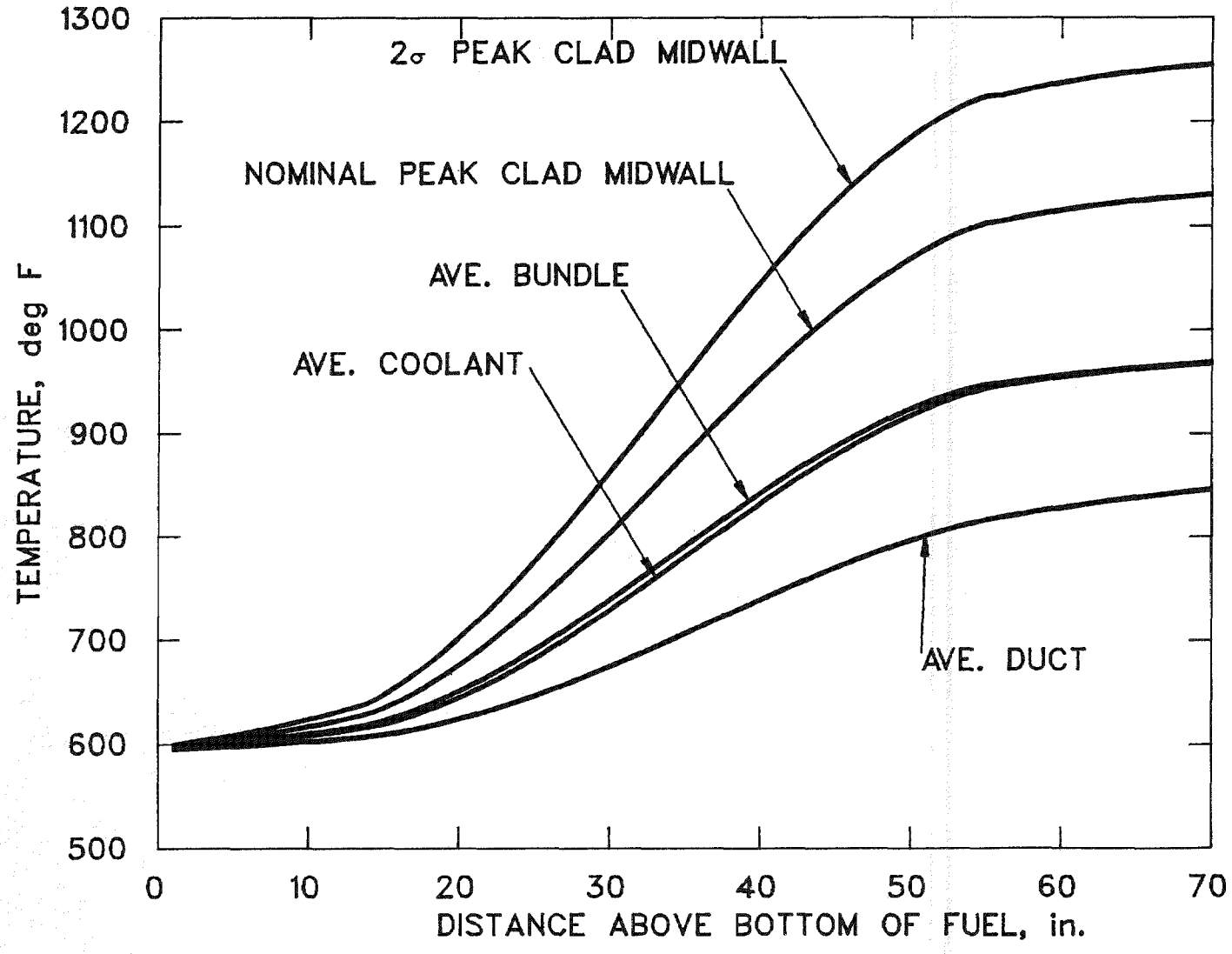

Figure G.9. Nominal and 2σ peak clad midwall temperatures and average coolant, duct and bundle temperatures. (Seventh orificing zone, orificing based on assembly power and equal peak assembly coolant temperatures.)

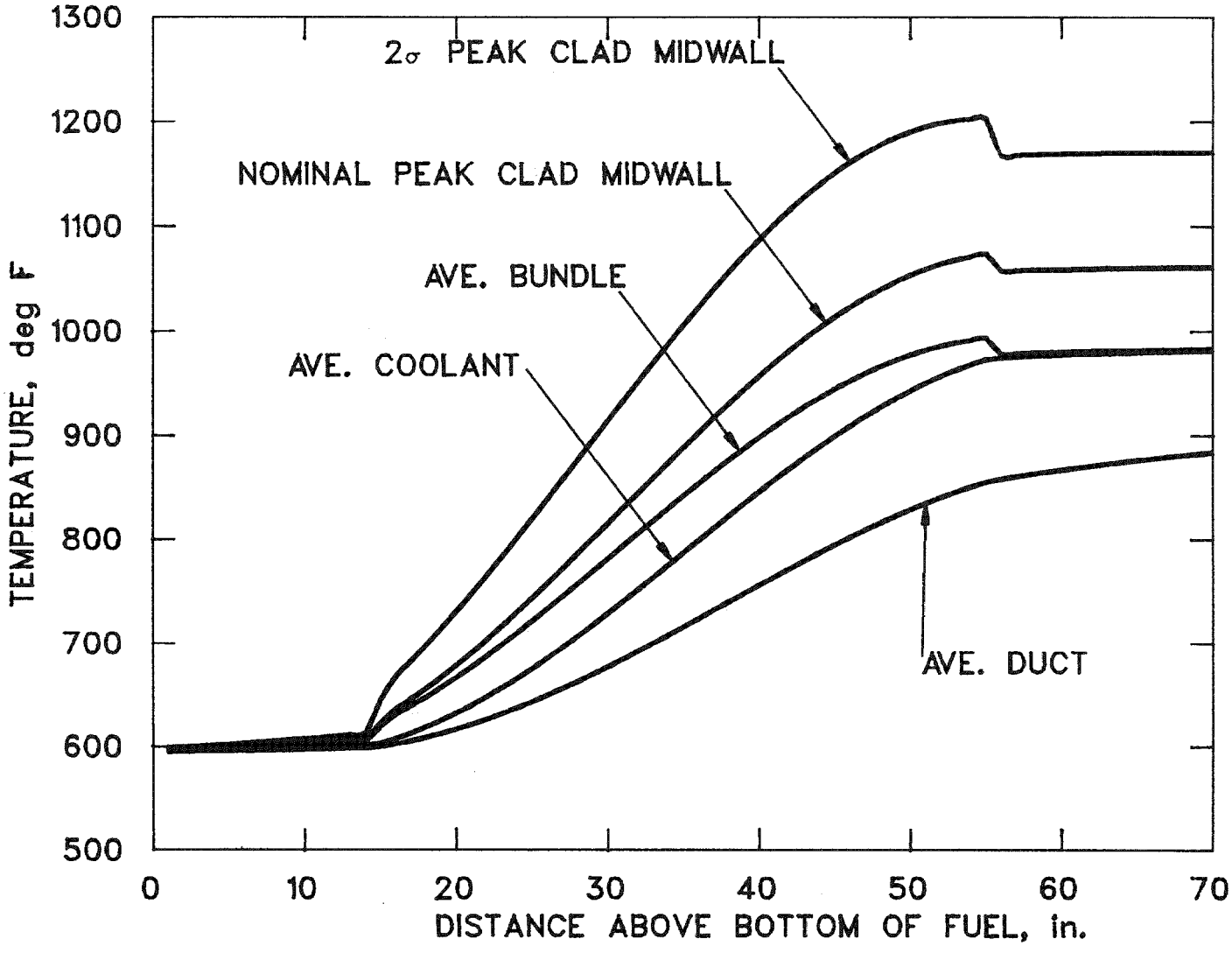

Figure G.10. Nominal and 2σ peak clad midwall temperatures and average coolant, duct and bundle temperatures. (First orificing zone, orificing based on assembly power and equal peak cladding midwall temperatures.)

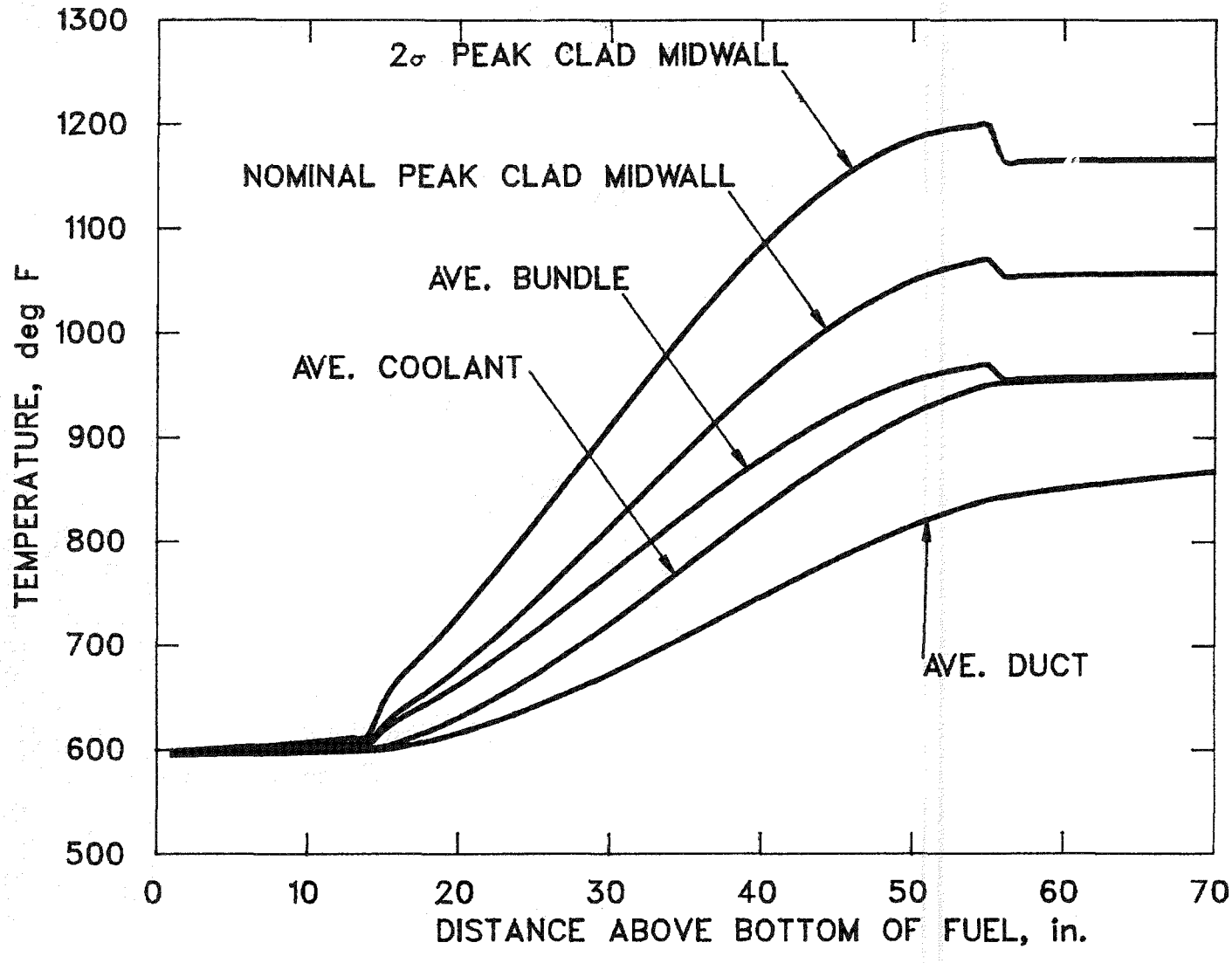

Figure G.11. Nominal and 2σ peak clad midwall temperatures and average coolant, duct and bundle temperatures. (Second orificing zone, orificing based on assembly power and equal peak cladding midwall temperatures.)

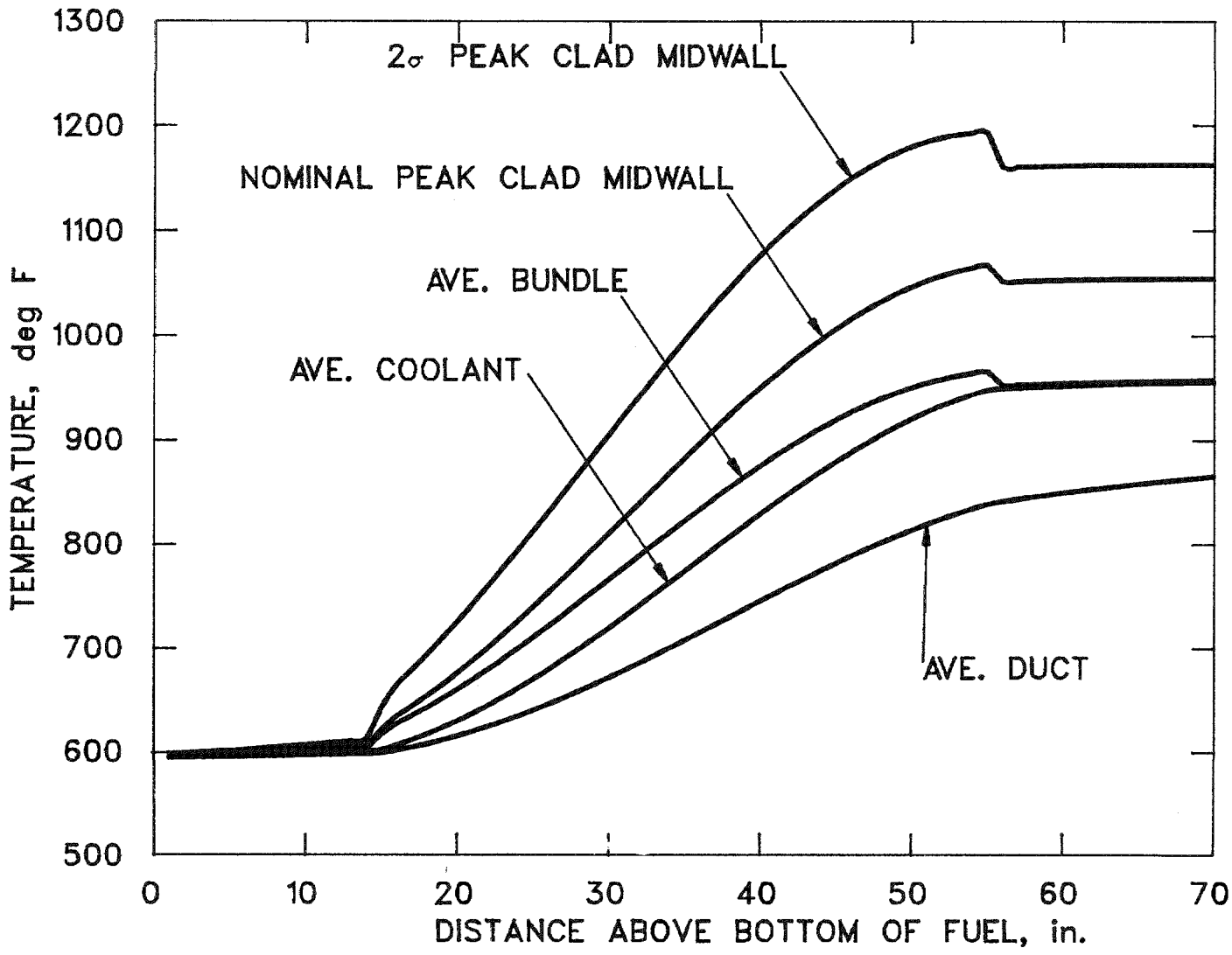

Figure G.12. Nominal and 2σ peak clad midwall temperatures and average coolant, duct and bundle temperatures. (Third orificing zone, orificing based on assembly power and equal peak cladding midwall temperatures.)

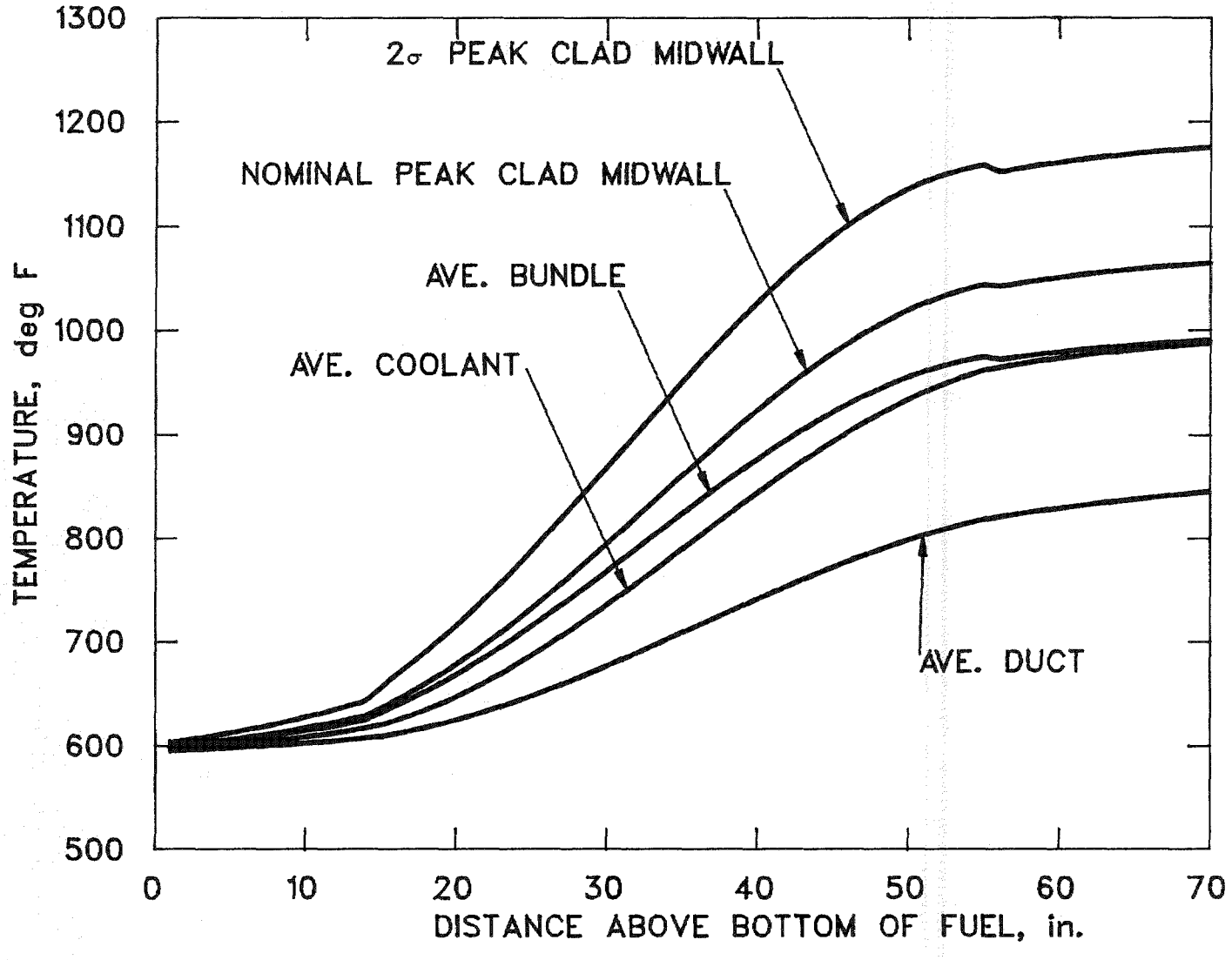

Figure G.13. Nominal and 2σ peak clad midwall temperatures and average coolant, duct and bundle temperatures. (Fourth orificing zone, orificing based on assembly power and equal peak cladding midwall temperatures.)

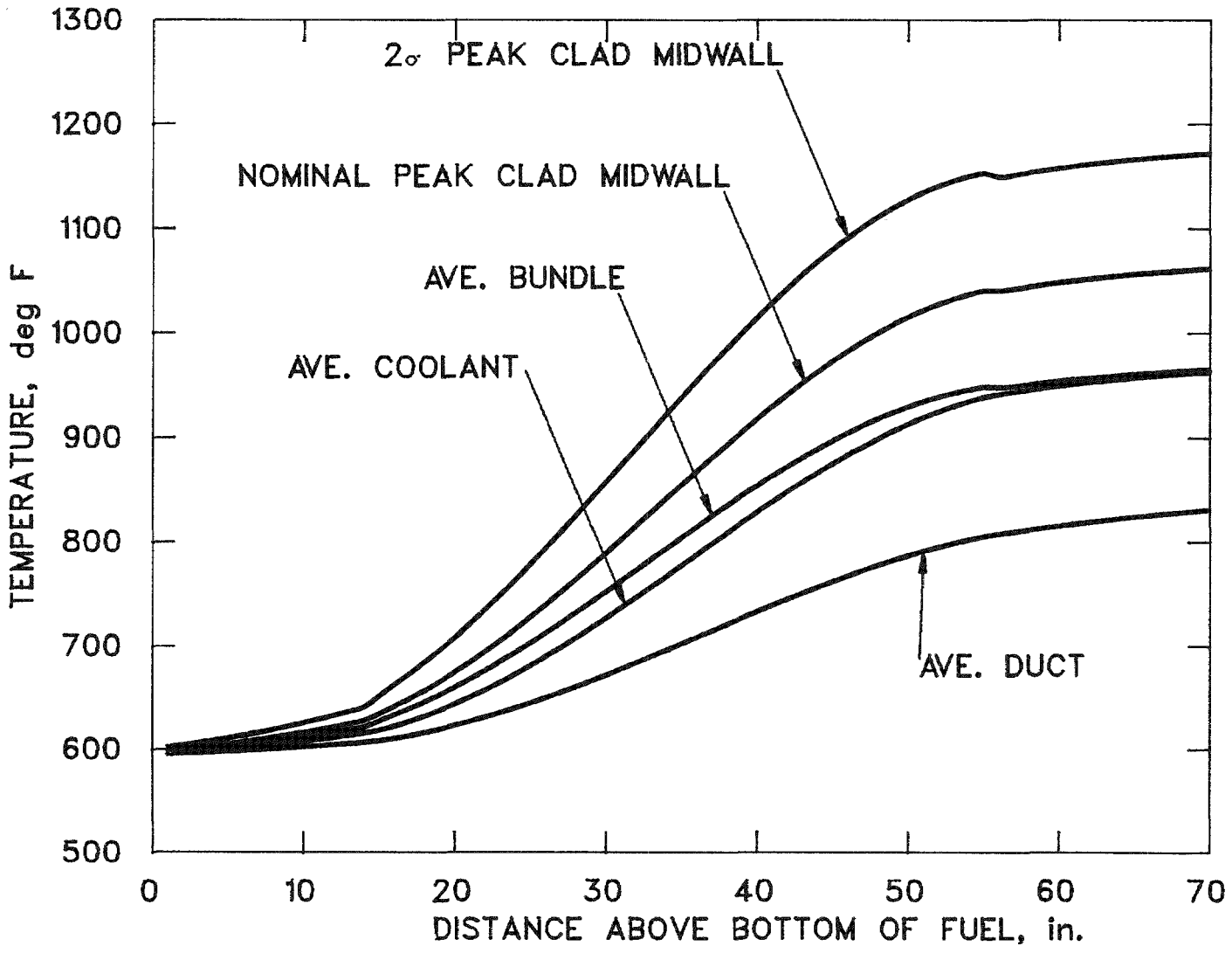

Figure G.14. Nominal and 2σ peak clad midwall temperatures and average coolant, duct and bundle temperatures. (Fifth orificing zone, orificing based on assembly power and equal peak cladding midwall temperatures.

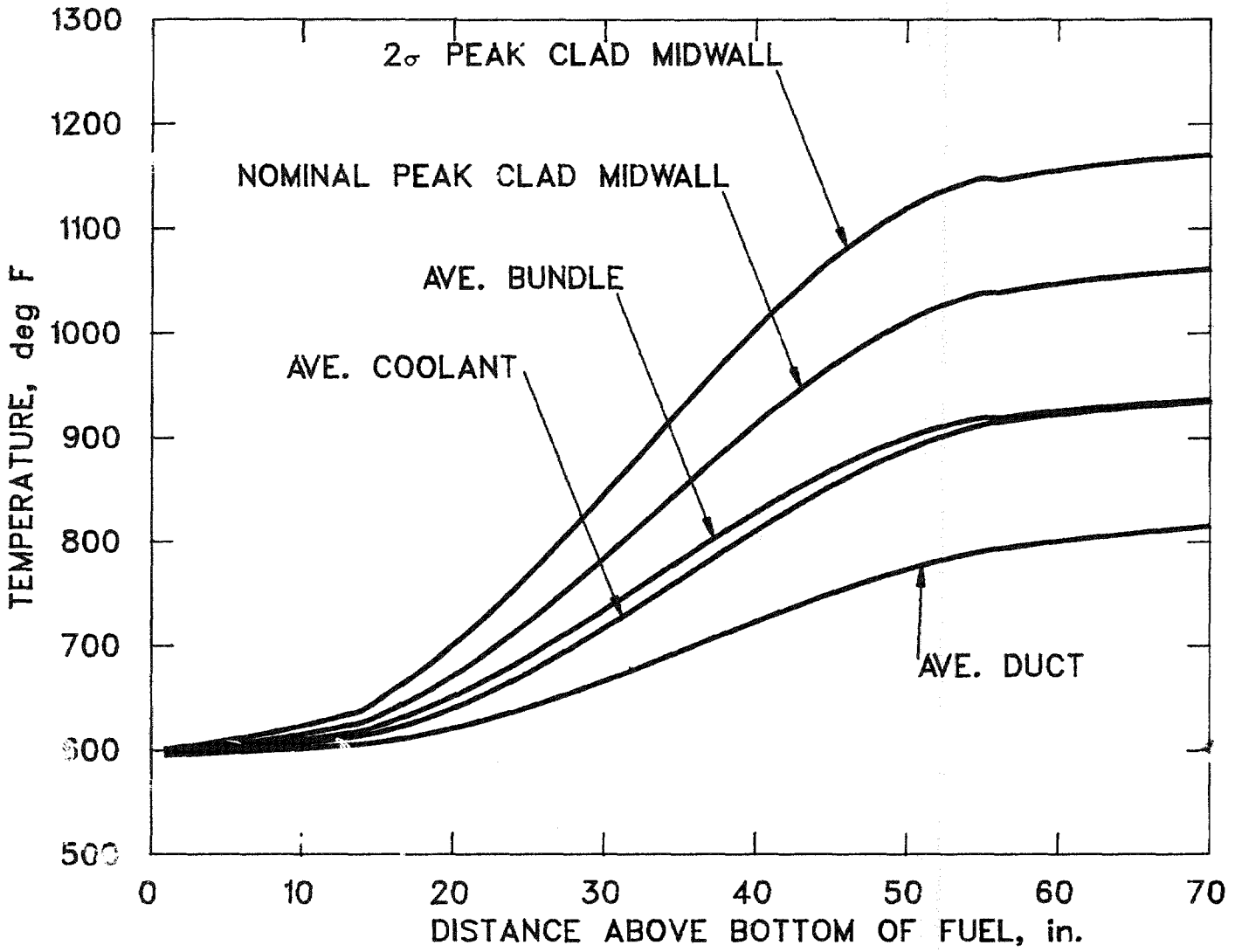

Figure G.15. Nominal and 2σ peak clad midwall temperatures and average coolant, duct and bundle temperatures. (Sixth orificing zone, orificing based on assembly power and equal peak cladding midwall temperatures.)

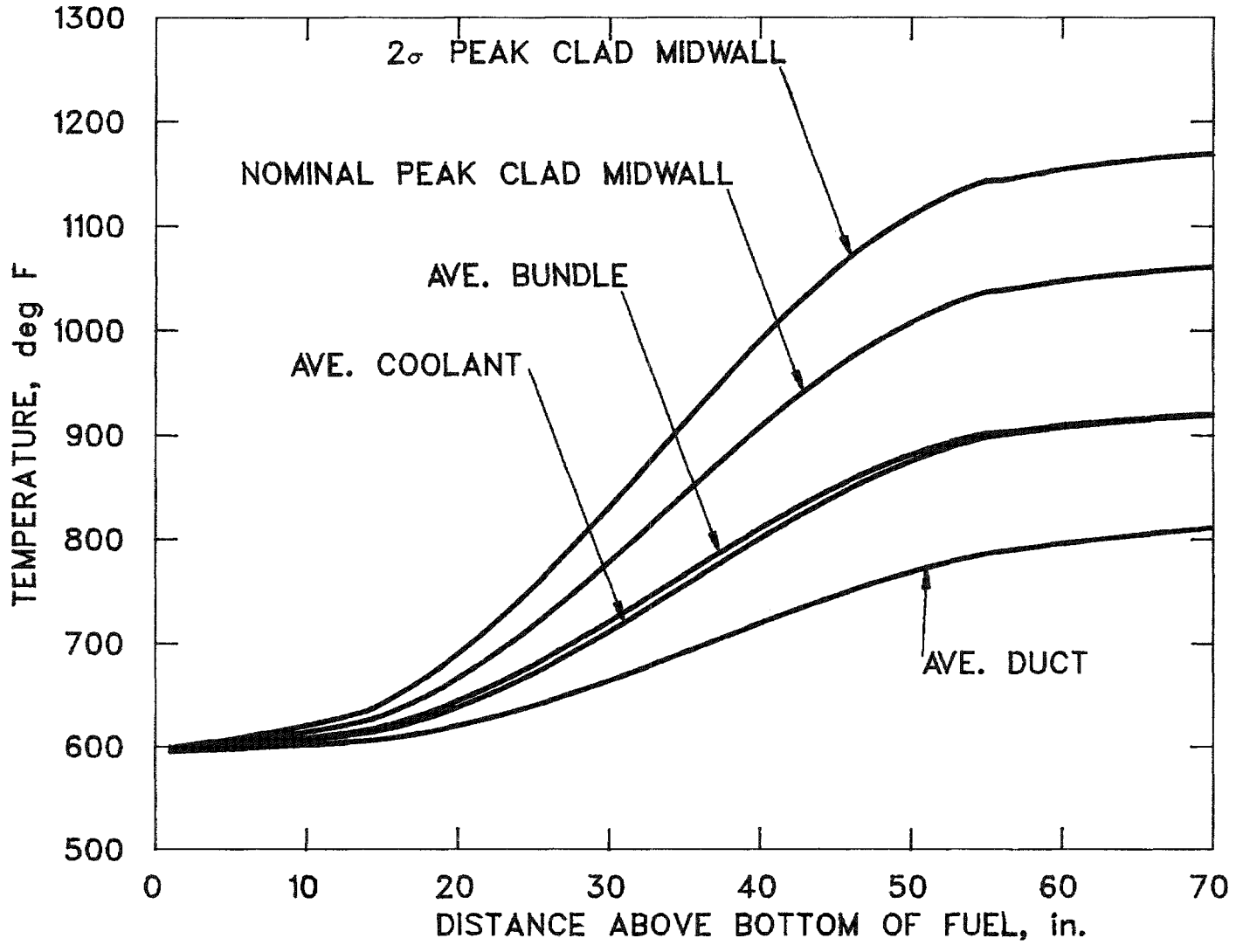

Figure G.16. Nominal and 2σ peak clad midwall temperatures and average coolant, duct and bundle temperatures. (Seventh orificing zone, orificing based on assembly power and equal peak cladding midwall temperatures.)

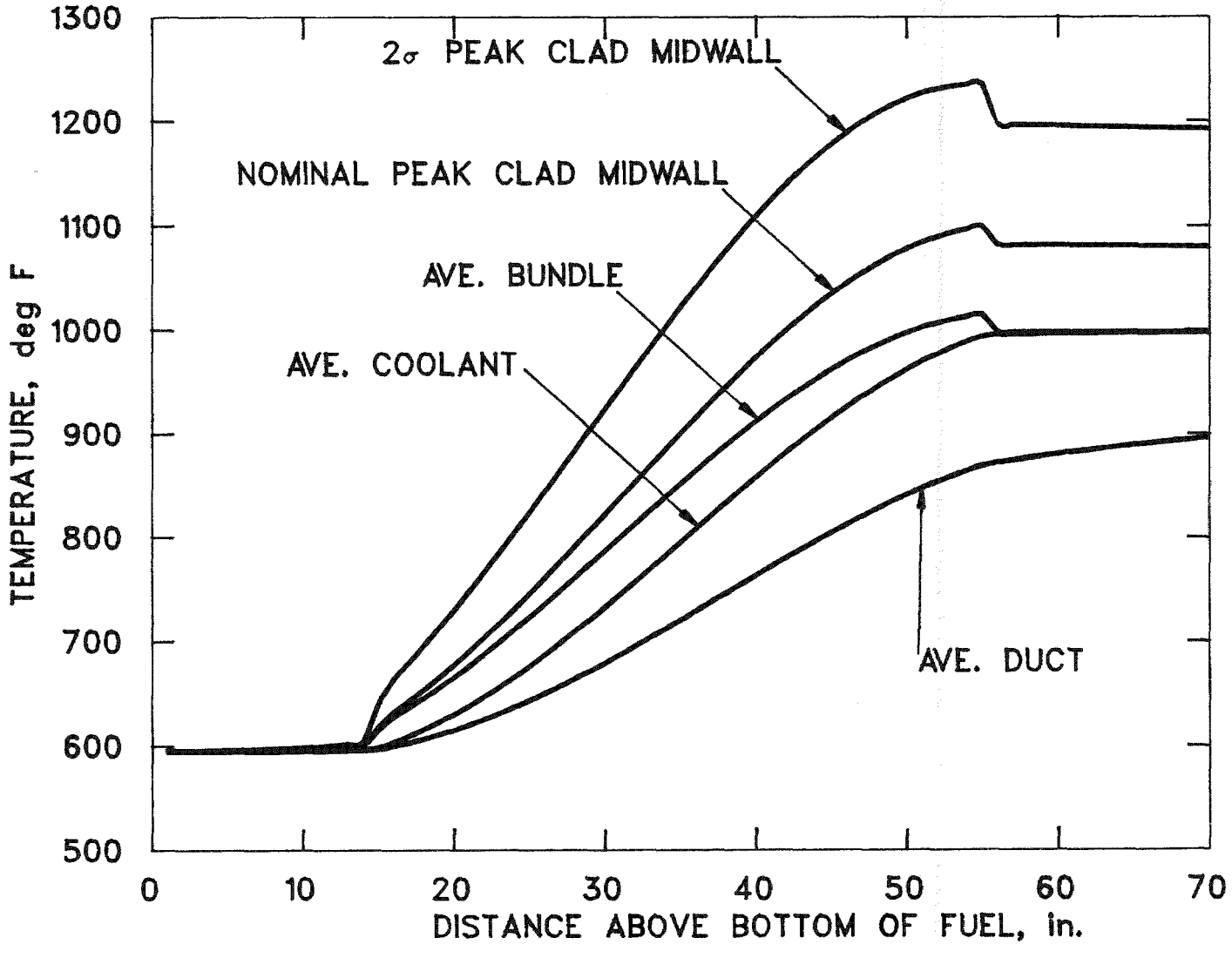

Figure G.17. Nominal and 2σ peak clad midwall temperatures and average coolant, duct and bundle temperatures. (First orificing zone, orificing based on pin power and equal peak assembly coolant temperatures.)

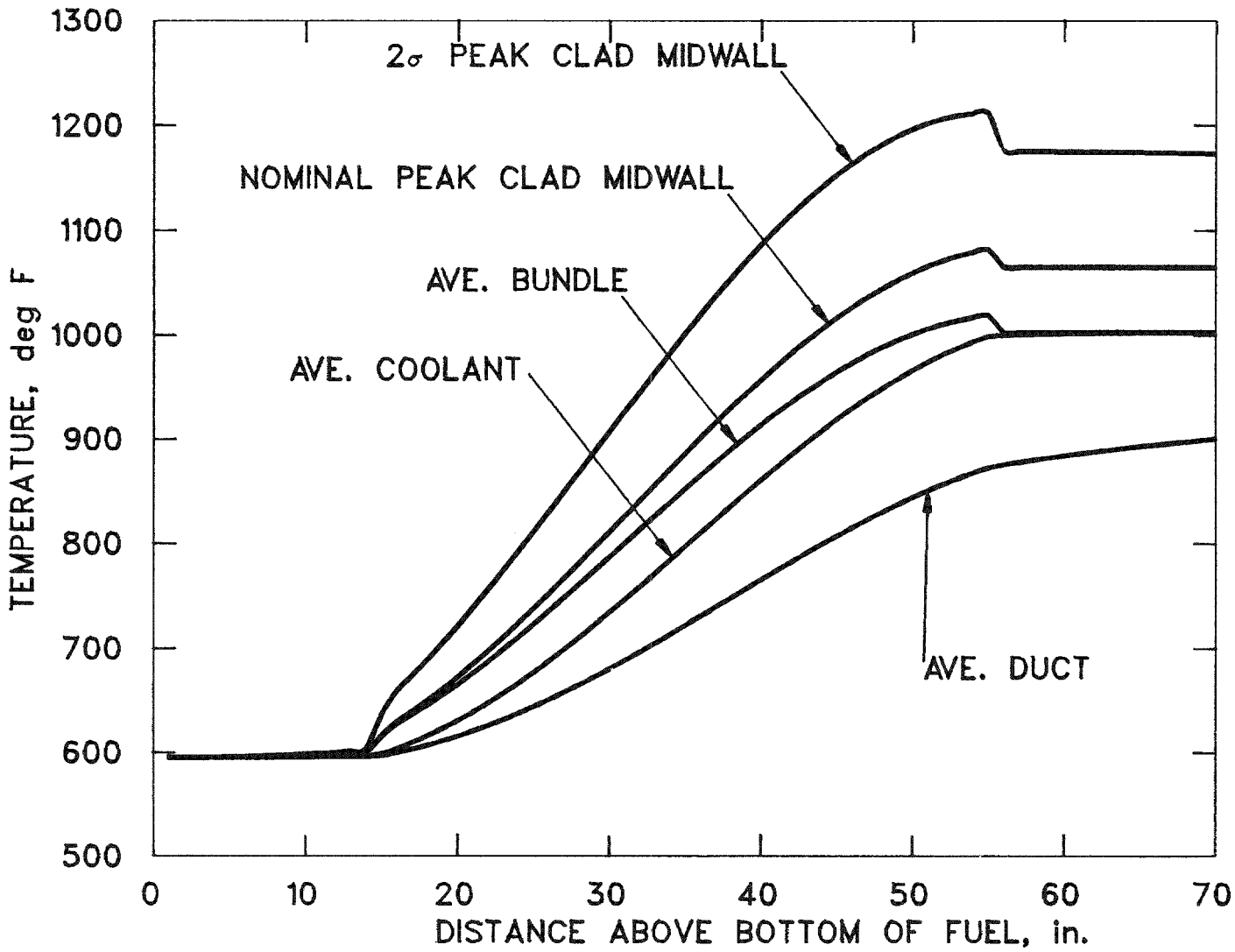

Figure G.18. Nominal and 2σ peak clad midwall temperatures and average coolant, duct and bundle temperatures. (Second orificing zone, orificing based on pin power and equal peak assembly coolant temperatures.)

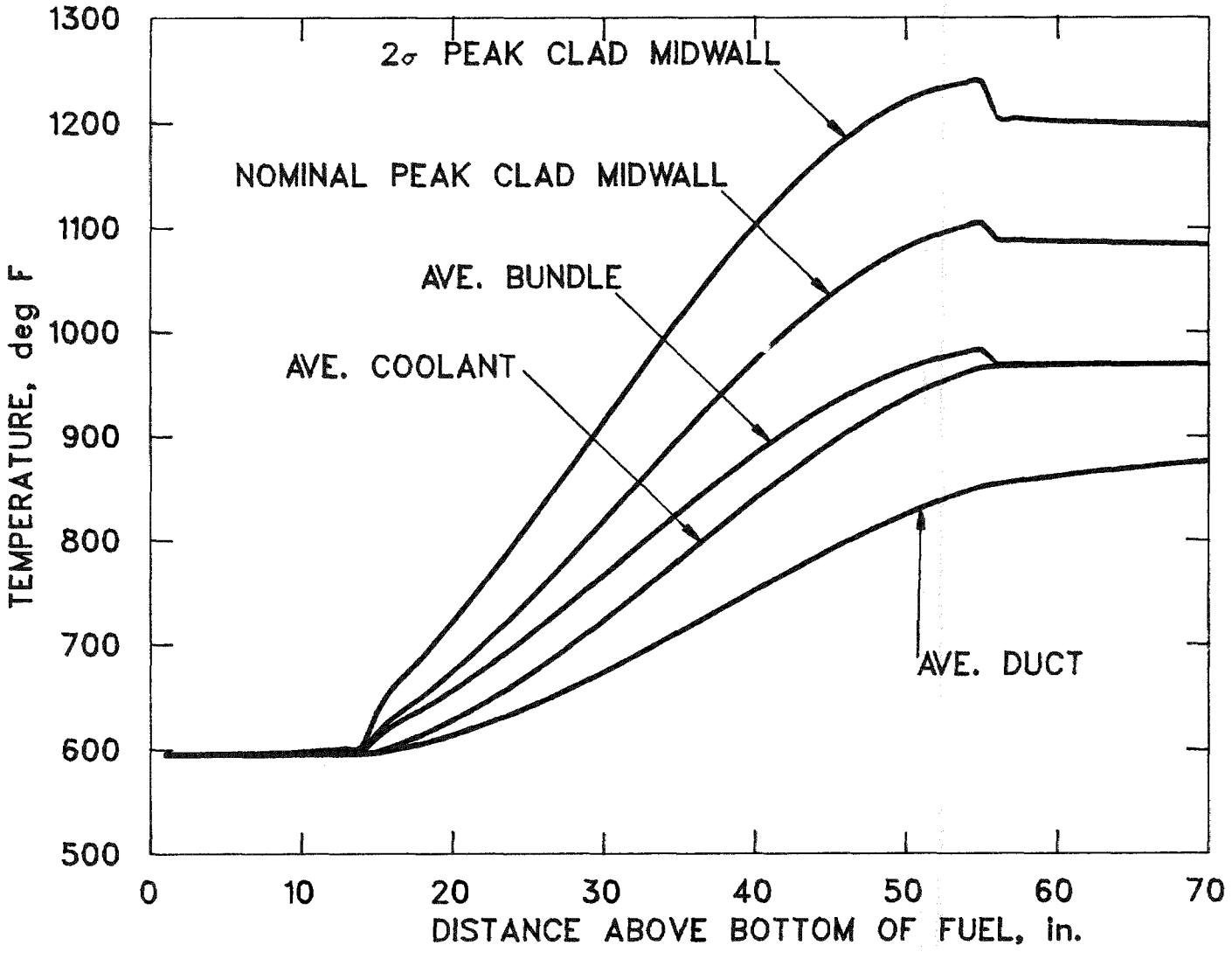

Figure G.19. Nominal and 2σ peak clad midwall temperatures and average coolant, duct and bundle temperatures. (Third orificing zone, orificing based on pin power and equal peak assembly coolant temperatures.)

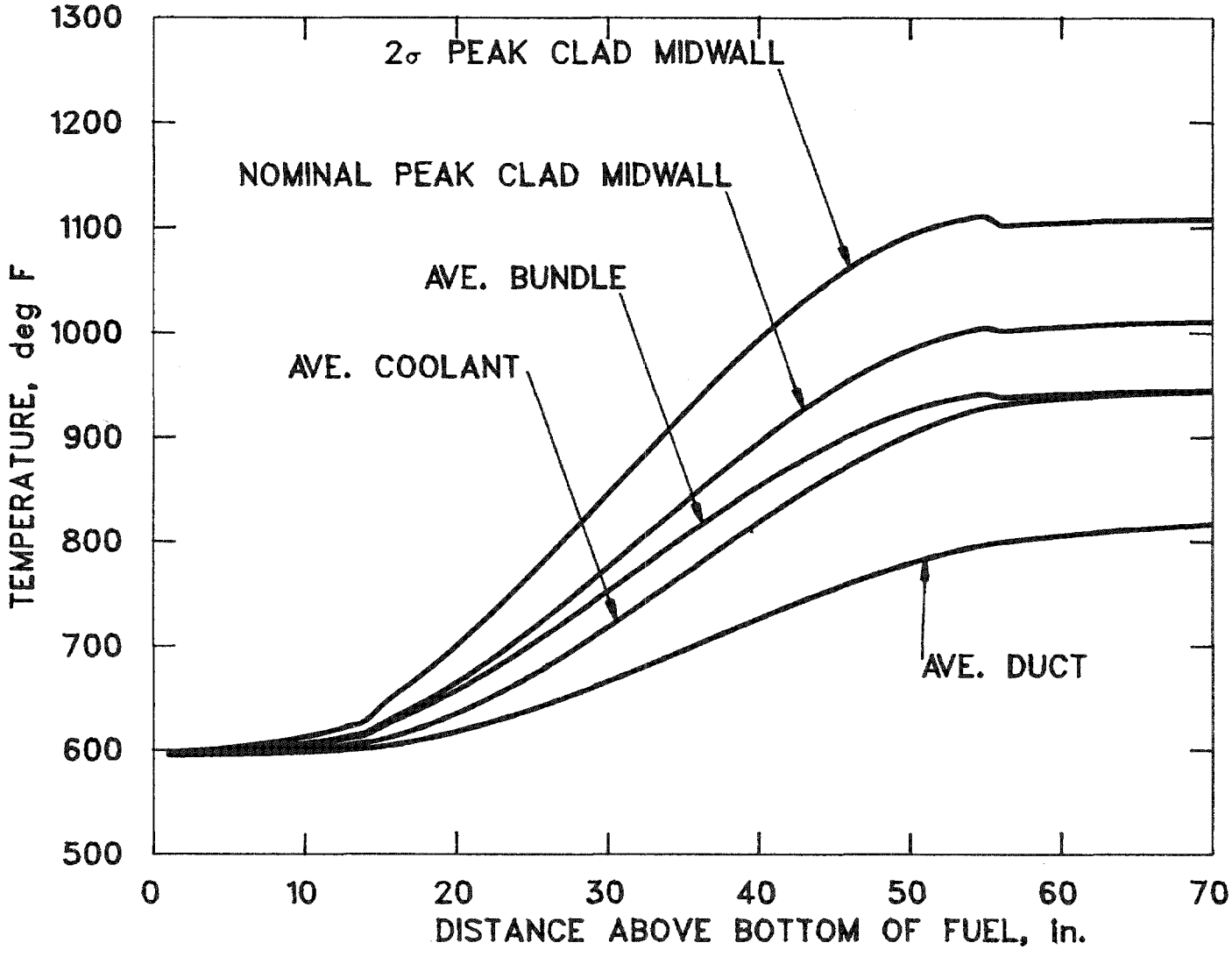

Figure G. 20 Nominal and 2σ peak clad midwall temperatures and average coolant, duct and bundle temperatures. (Fourth orificing zone, orificing based on pin power and equal peak assembly coolant temperatures.)

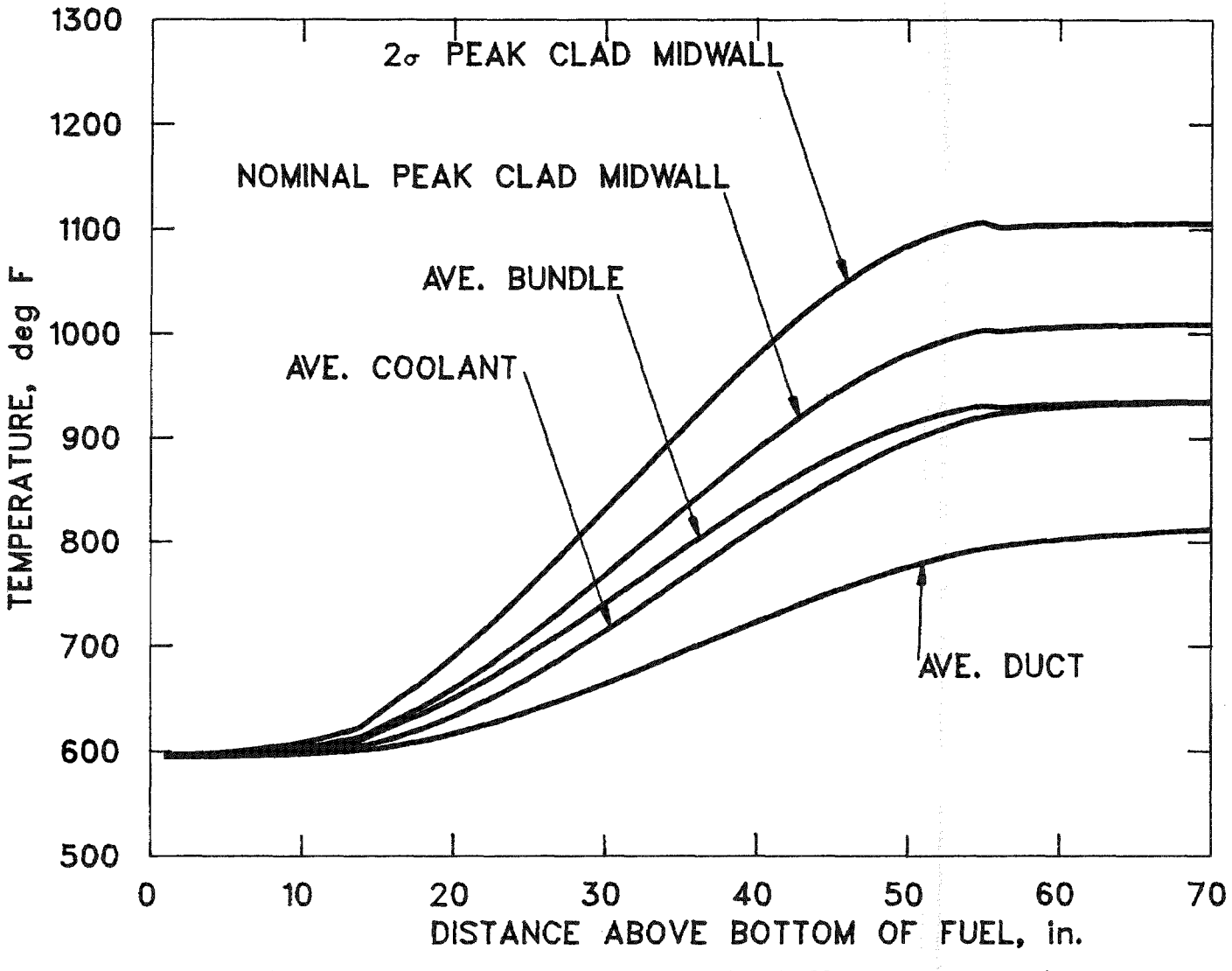

Figure G.21. Nominal and 2σ peak clad midwall temperatures and average coolant, duct and bundle temperatures. (Fifth orificing zone, orificing based on pin power and equal peak assembly coolant temperatures.)

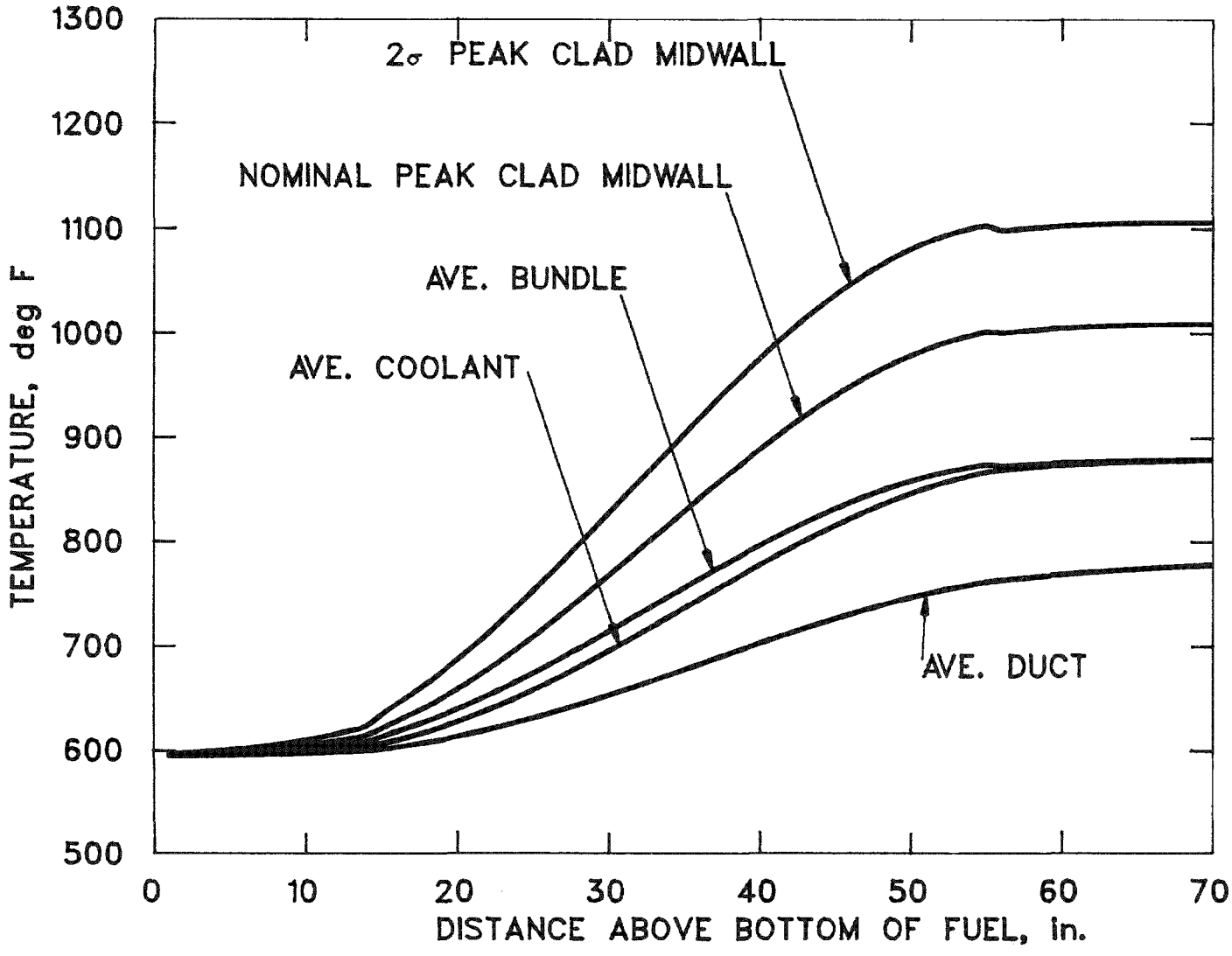

Figure G.22. Nominal and 2σ peak clad midwall temperatures and average coolant, duct and bundle temperatures. (Sixth orificing zone, orificing based on pin power and equal peak assembly coolant temperatures.)

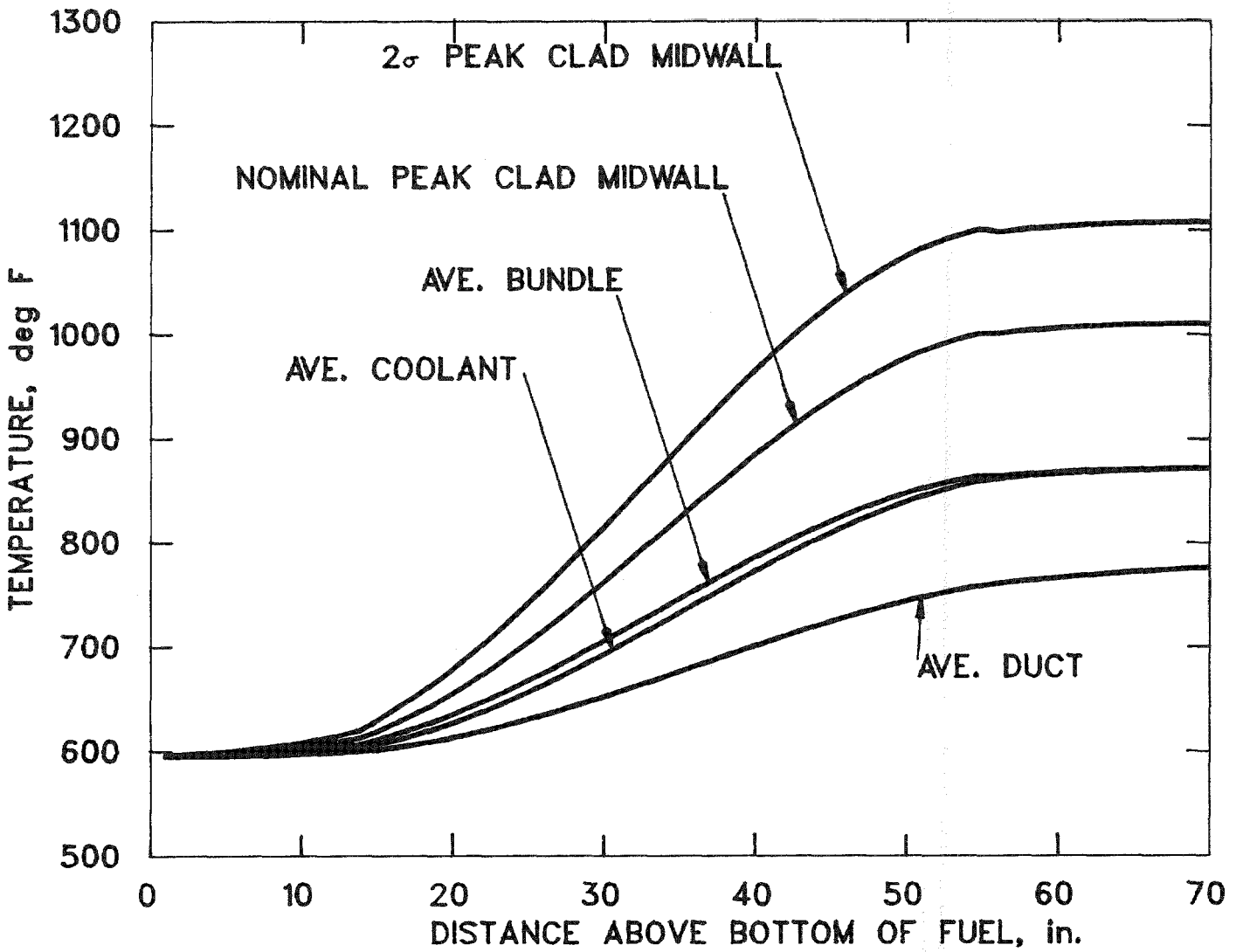

Figure G.23. Nominal and 2σ peak clad midwall temperatures and average coolant, duct and bundle temperatures. (Seventh orificing zone, orificing based on pin power and equal peak assembly coolant temperatures.)

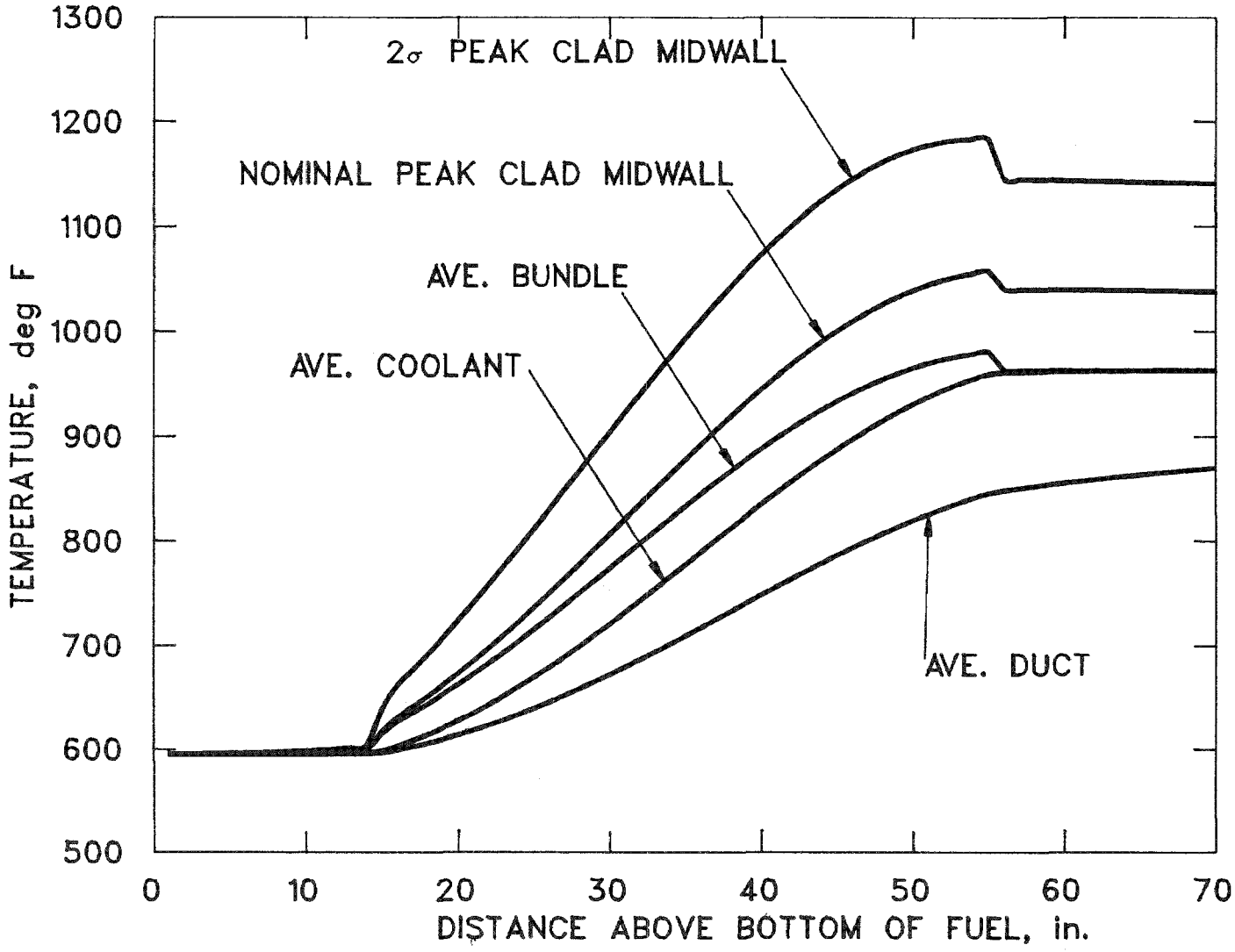

Figure G.24. Nominal and 2σ peak clad midwall temperatures and average coolant, duct and bundle temperatures. (First orificing zone, orificing based on pin power and equal peak cladding midwall temperatures.)

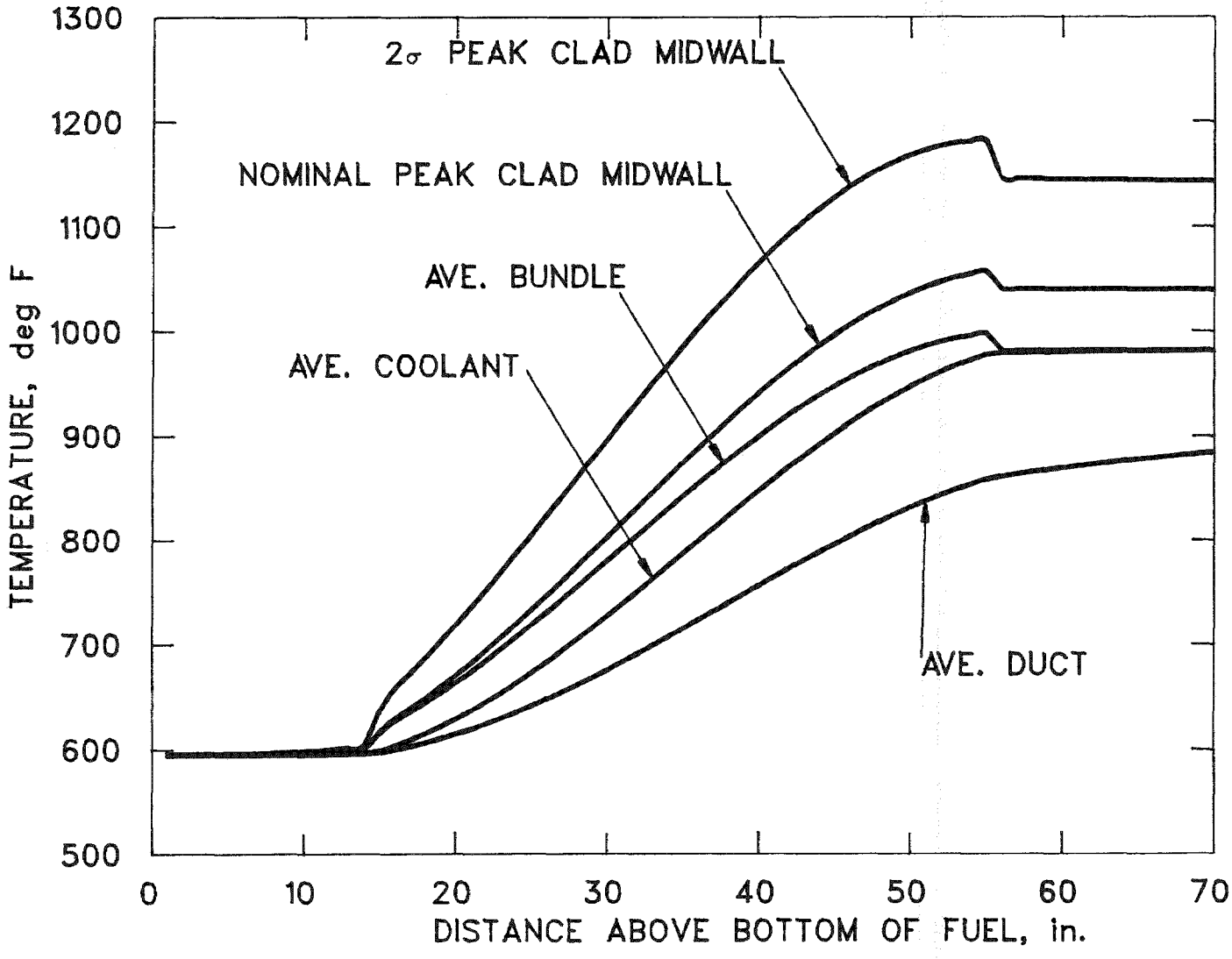

Figure G.25. Nominal and 2σ peak clad midwall temperatures and average coolant, duct and bundle temperatures. (Second orificing zone, orificing based on pin power and equal peak cladding midwall temperatures.)

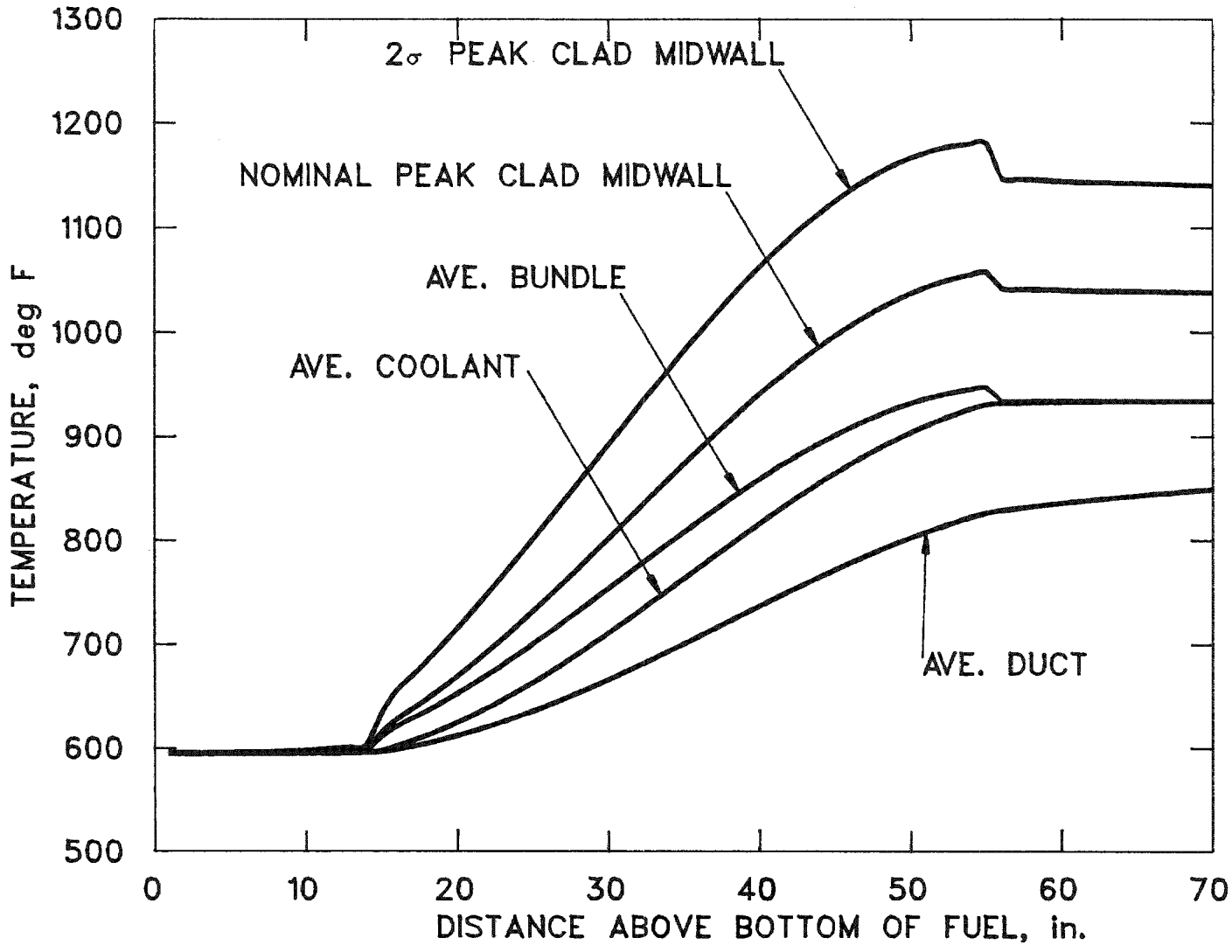

Figure G.26. Nominal and 2σ peak clad midwall temperatures and average coolant, duct and bundle temperatures. (Third orificing zone, orificing based on pin power and equal peak cladding midwall temperatures.)

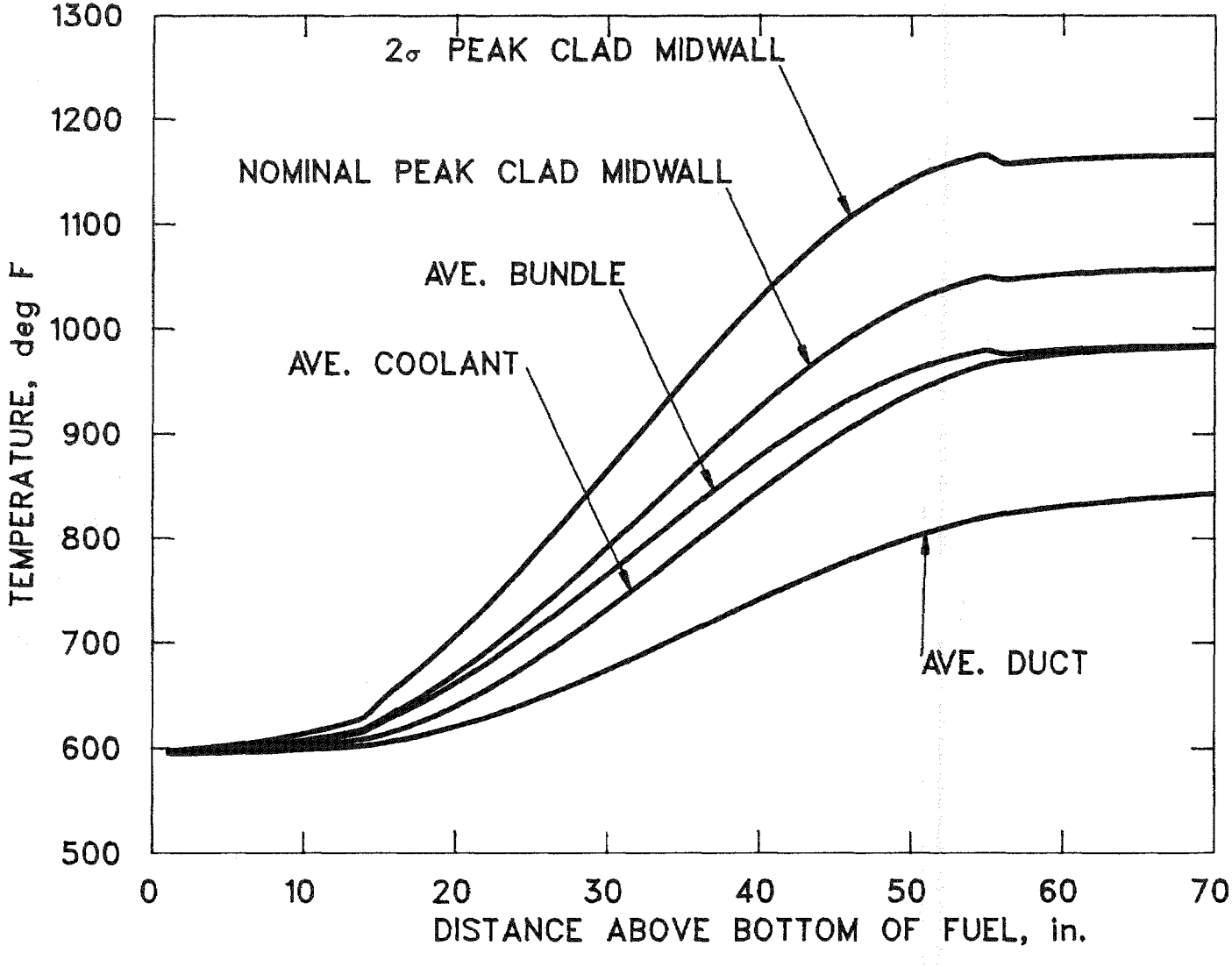

Figure G.27. Nominal and 2σ peak clad midwall temperatures and average coolant, duct and bundle temperatures. (Fourth orificing zone, orificing based on pin power and equal peak cladding midwall temperatures.)

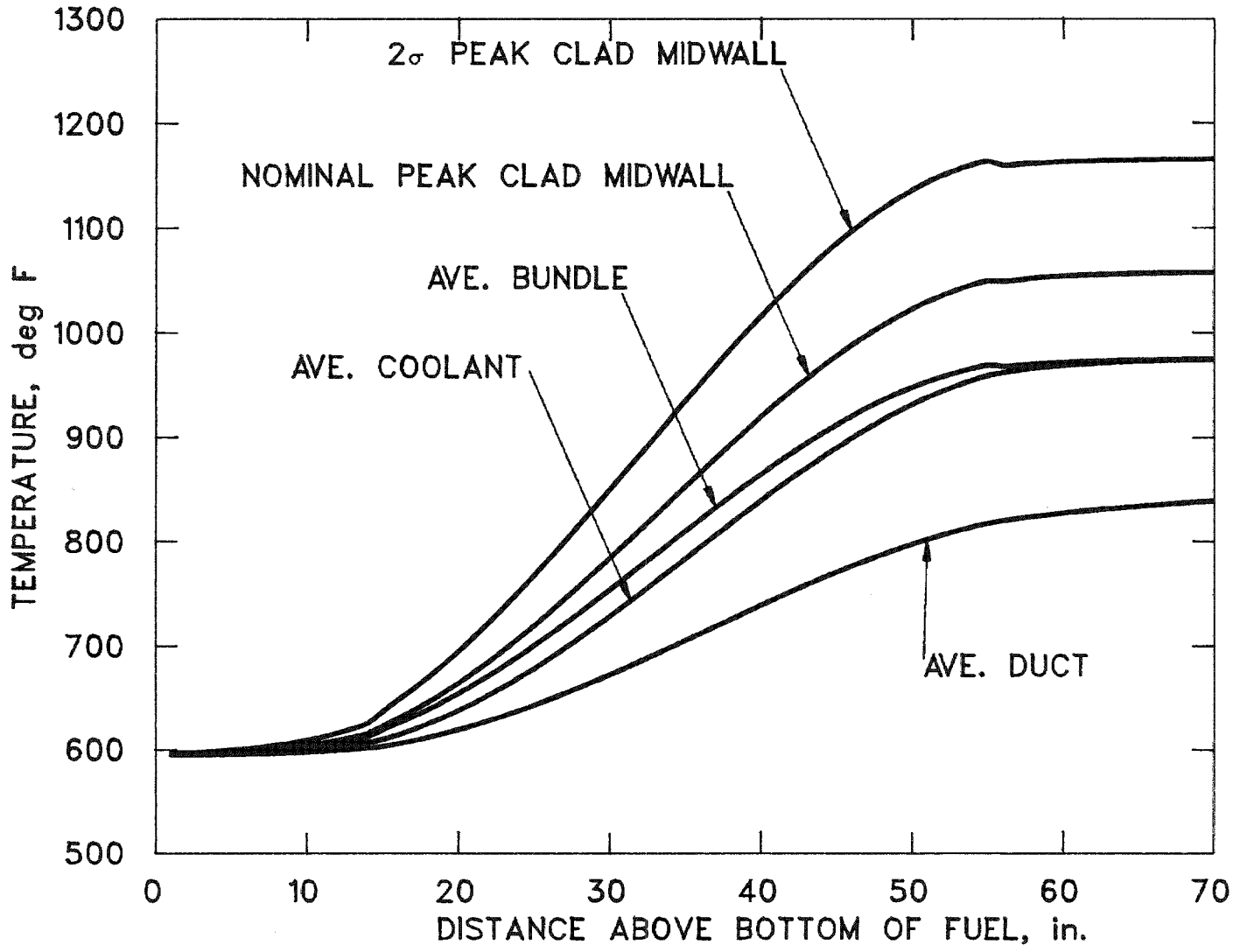

Figure G.28. Nominal and 2σ peak clad midwall temperatures and average coolant, duct and bundle temperatures. (Fifth orificing zone, orificing based on pin power and equal peak cladding midwall temperatures.)

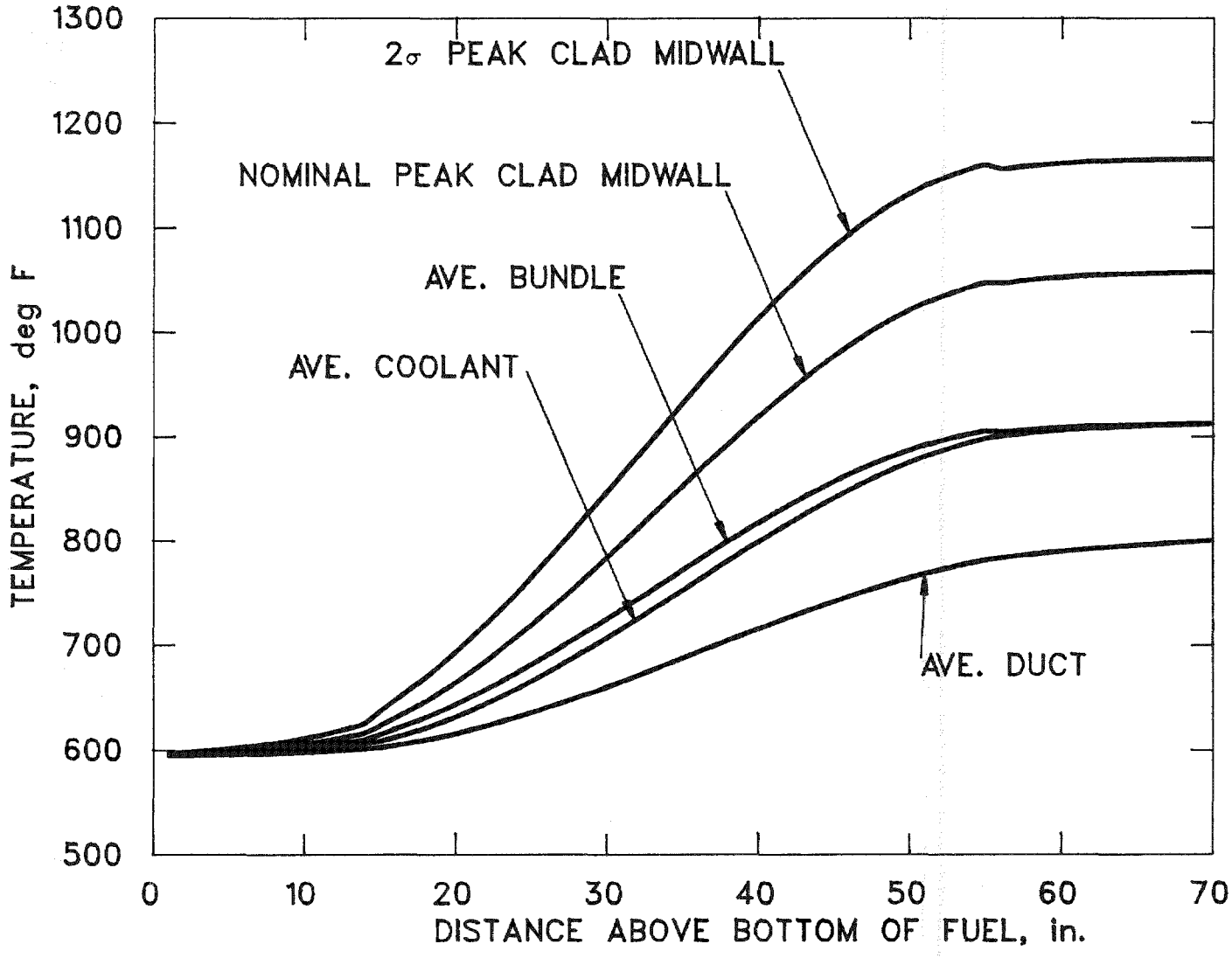

Figure G.29. Nominal and 2σ peak clad midwall temperatures and average coolant, duct and bundle temperatures. (Sixth orificing zone, orificing based on pin power and equal peak cladding midwall temperatures.)

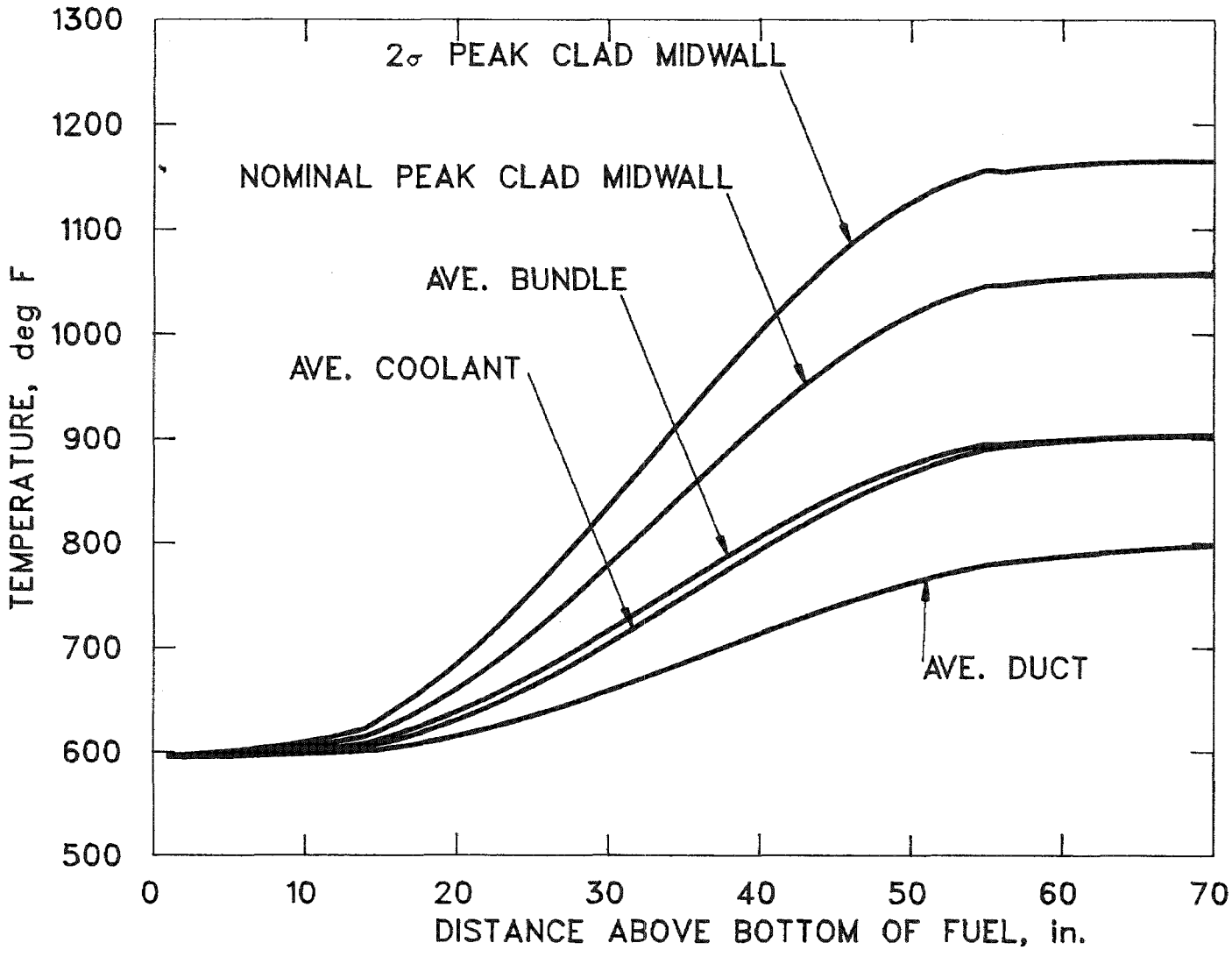

Figure G.30. Nominal and 2σ peak clad midwall temperatures and average coolant, duct and bundle temperatures. (Seventh orificing zone, orificing based on pin power and equal peak cladding midwall temperatures.)

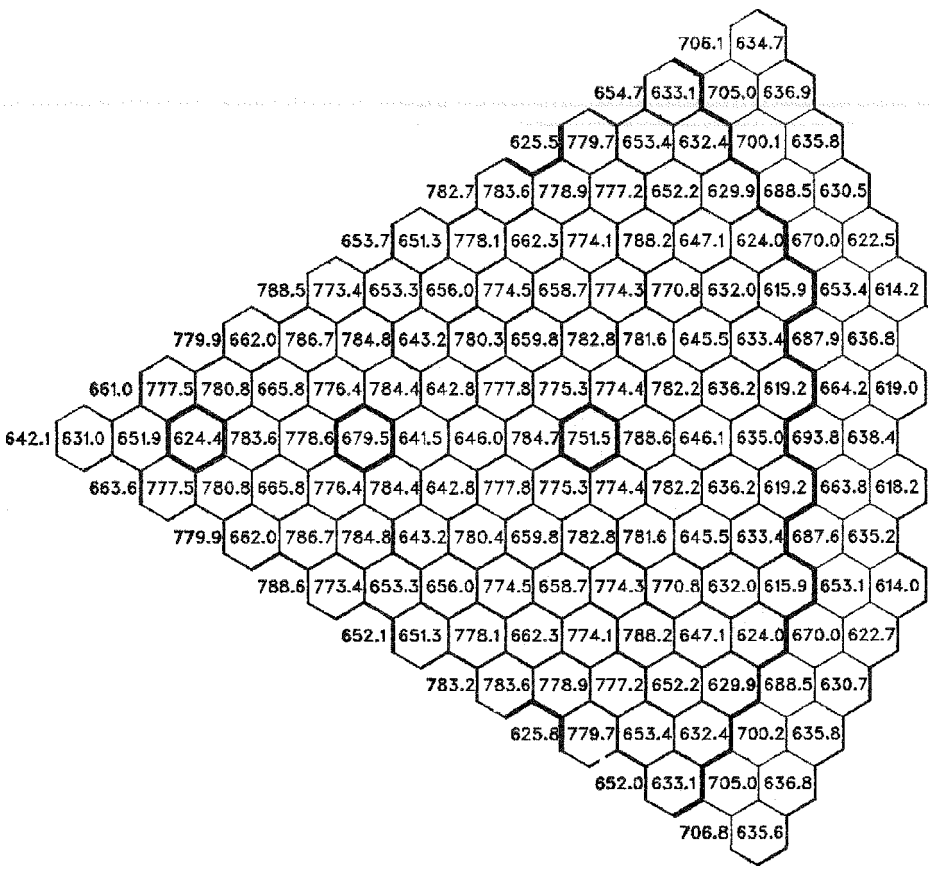

Figure G. 31. Average coolant temperatures (°F) at BOL at core midplane. (Orificing based on assembly power and equal peak assembly coolant temperatures.)

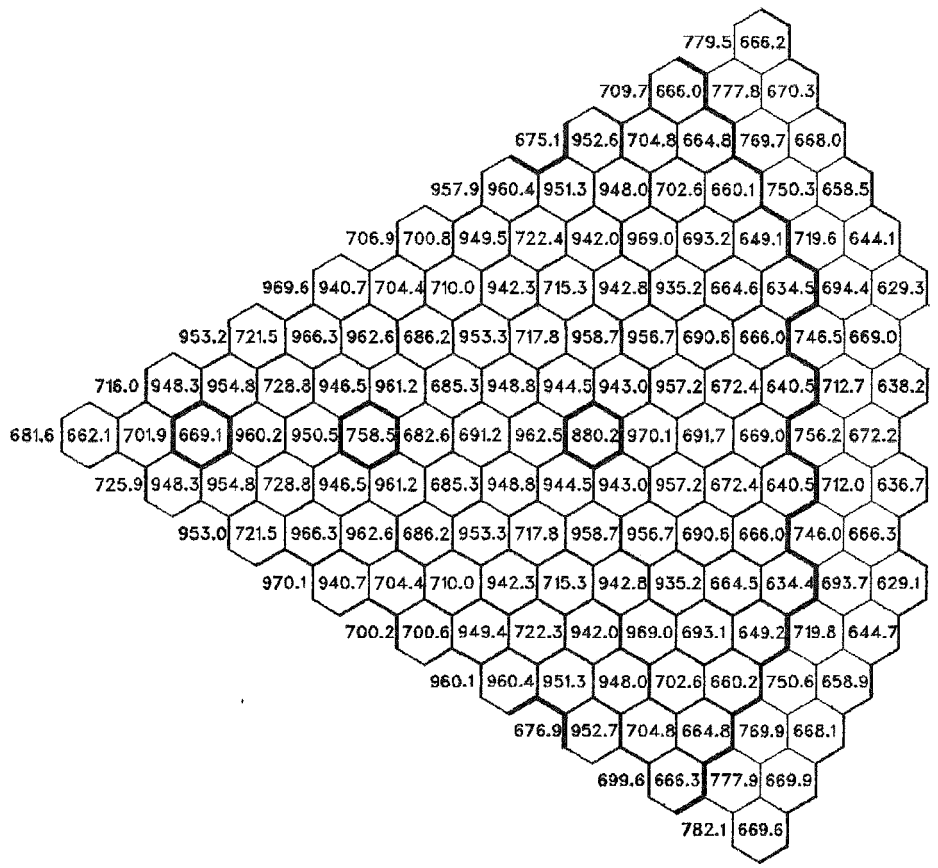

Figure G.32. Average coolant temperatures (°F) at BOL at core-upper axial blanket interface. (Orificing based on assembly power and equal peak assembly coolant temperatures.)

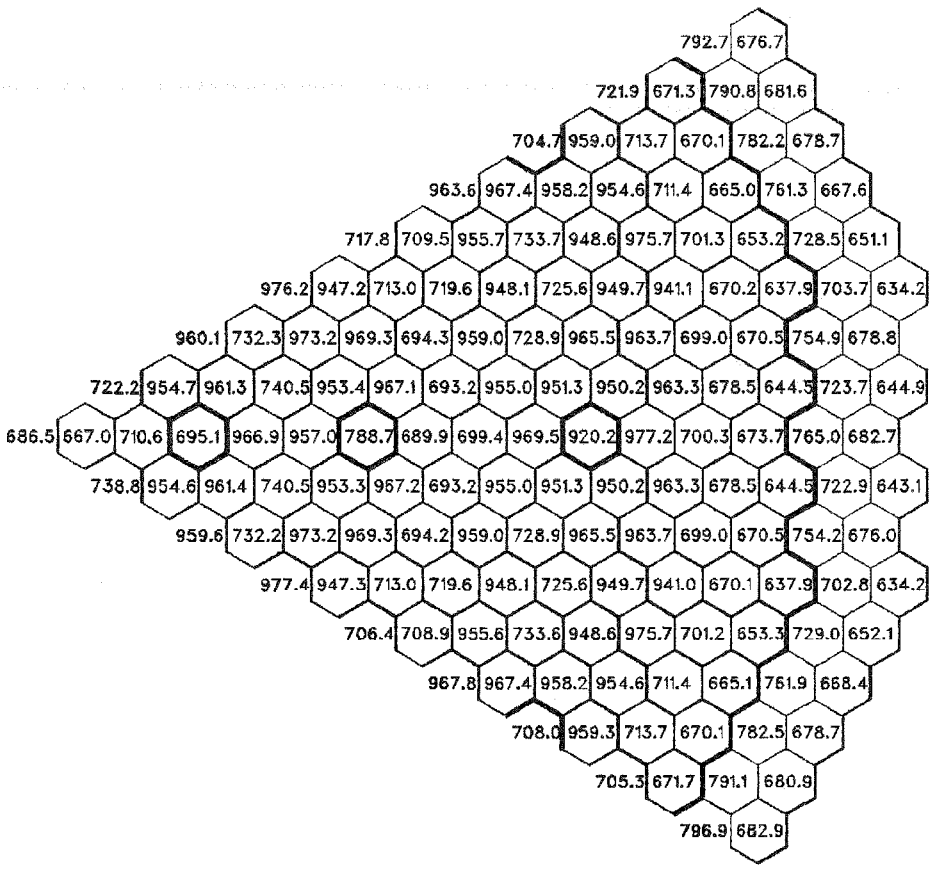

Figure G.33. Average coolant temperatures (^{o}F) at BOL at the top of the upper axial blanket. (Orificing based on assembly power and equal peak assembly coolant temperatures.)

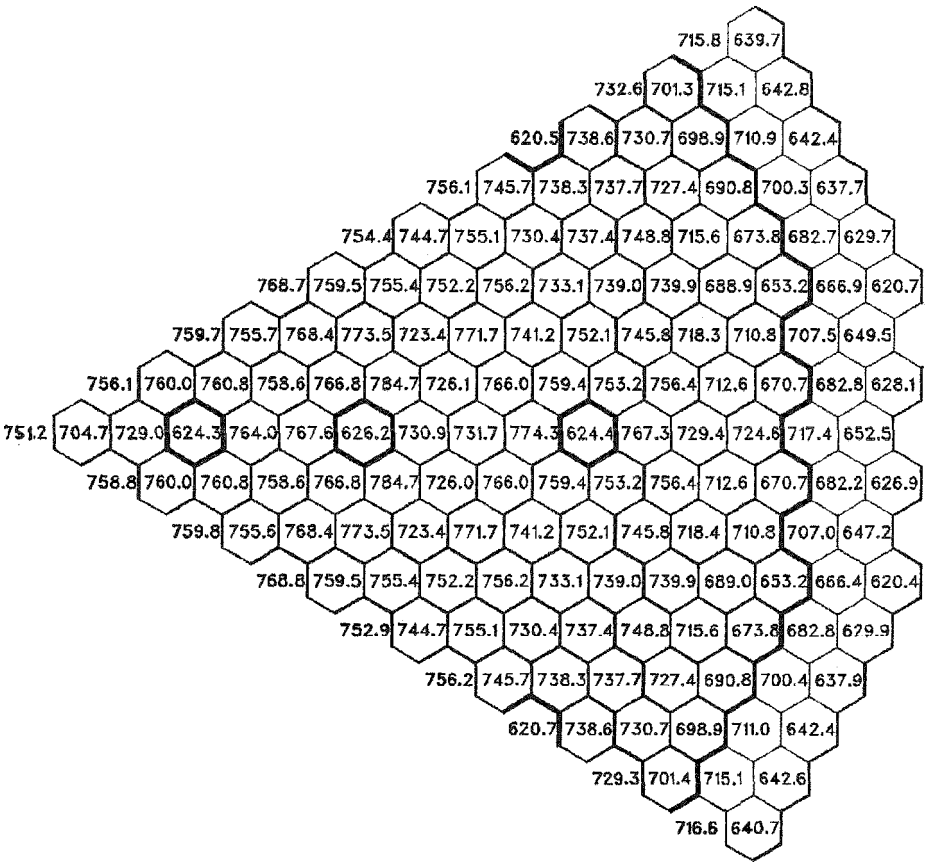

Figure G.34. Average coolant temperatures (^{o}F) at EOEC at core midplane. (Orificing based on assembly power and equal peak assembly coolant temperatures.)

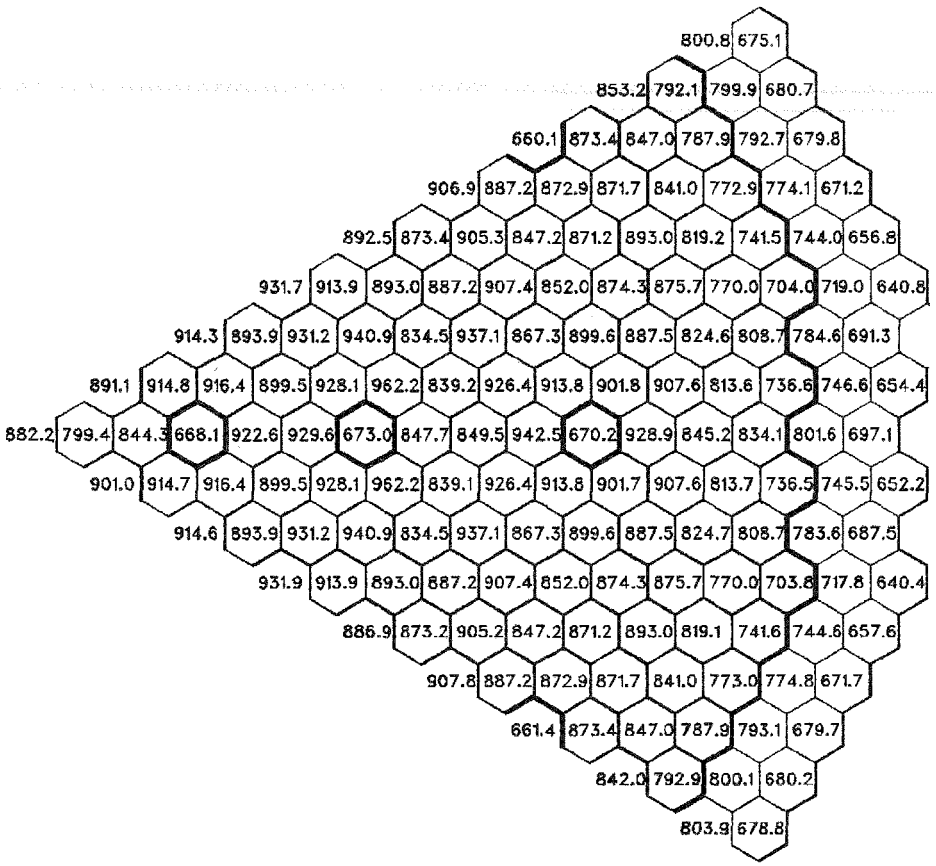

Figure G.35. Average coolant temperatures ($^{\circ}$F) at EOEC at core-upper axial blanket interface. (Orificing based on assembly power and equal peak assembly coolant temperatures.)

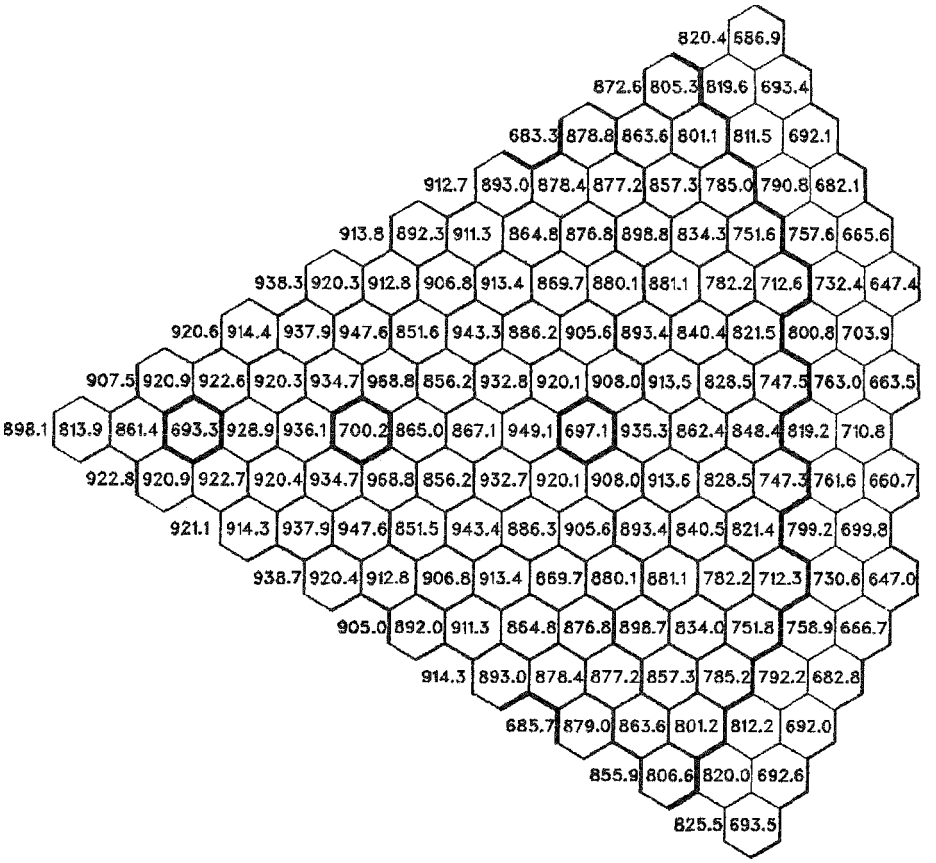

Figure G. 36. Average coolant temperatures (^{o}F) at EOEC at the top of the upper axial blanket. (Orificing based on assembly power and equal peak assembly coolant temperatures.)

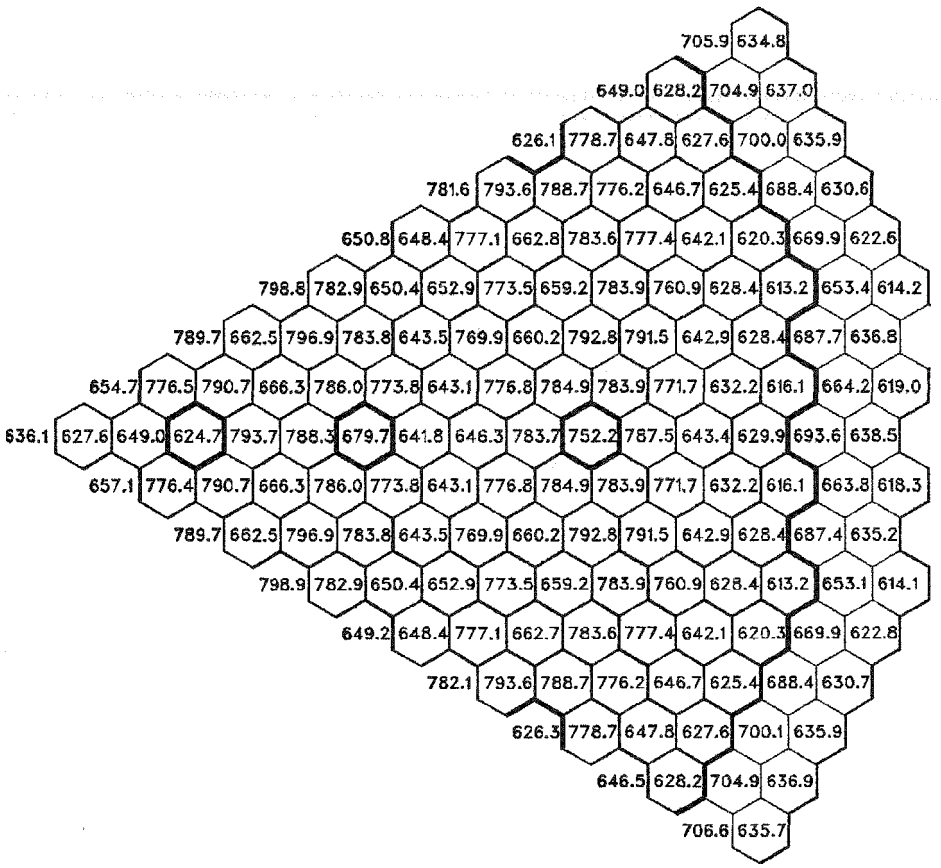

Figure G.37. Average coolant temperatures (^{o}F) at BOL at core midplane. (Orificing based on assembly power and equal peak cladding midwall temperatures.)

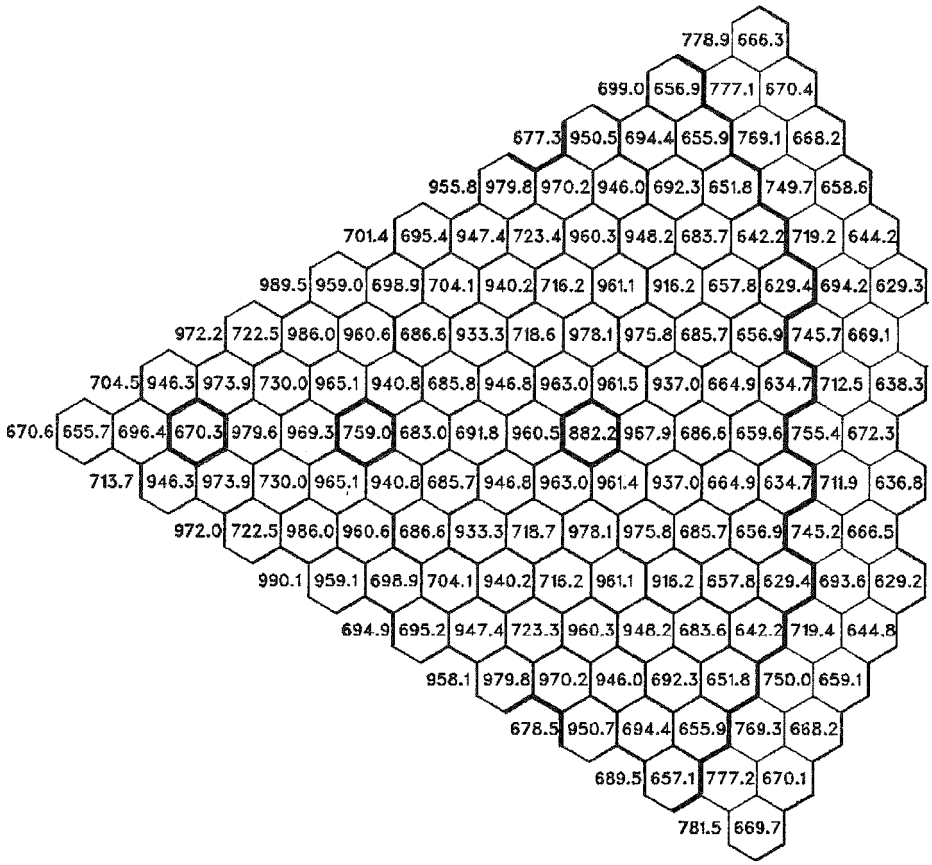

Figure G.38. Average coolant temperatures (^{o}F) at BOL at core-upper axial blanket interface. (Orificing based on assembly power and equal peak cladding midwall temperatures.)

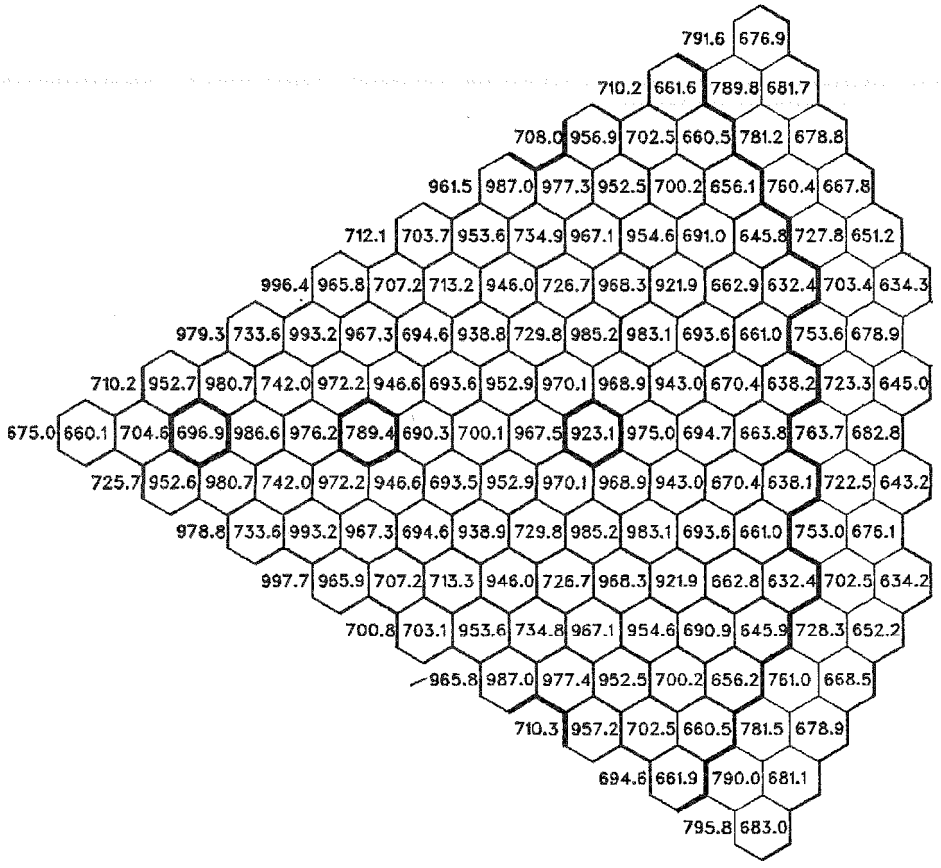

Figure G.39. Average coolant temperatures (^{o}F) at BOL at the top of the upper axial blanket. (Orificing based on assembly power and equal peak cladding midwall temperatures.)

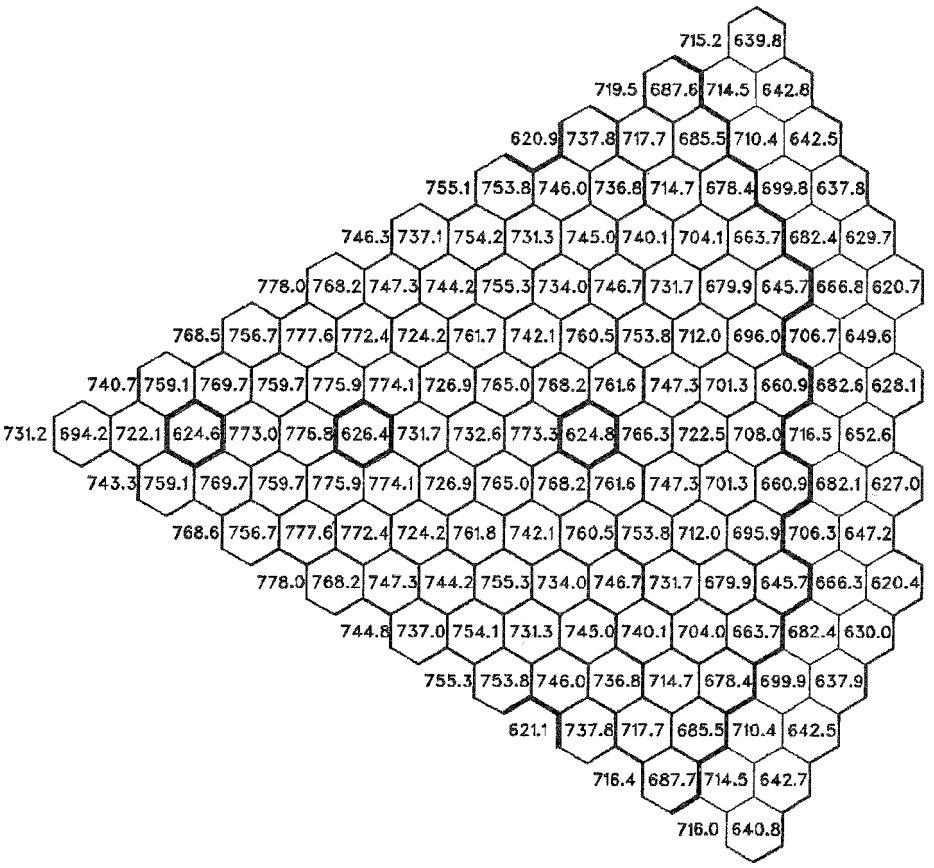

Figure G.40. Average coolant temperatures ($^{\circ}$F) at EOEC at core midplane. (Orificing based on assembly power and equal peak cladding midwall temperatures.)

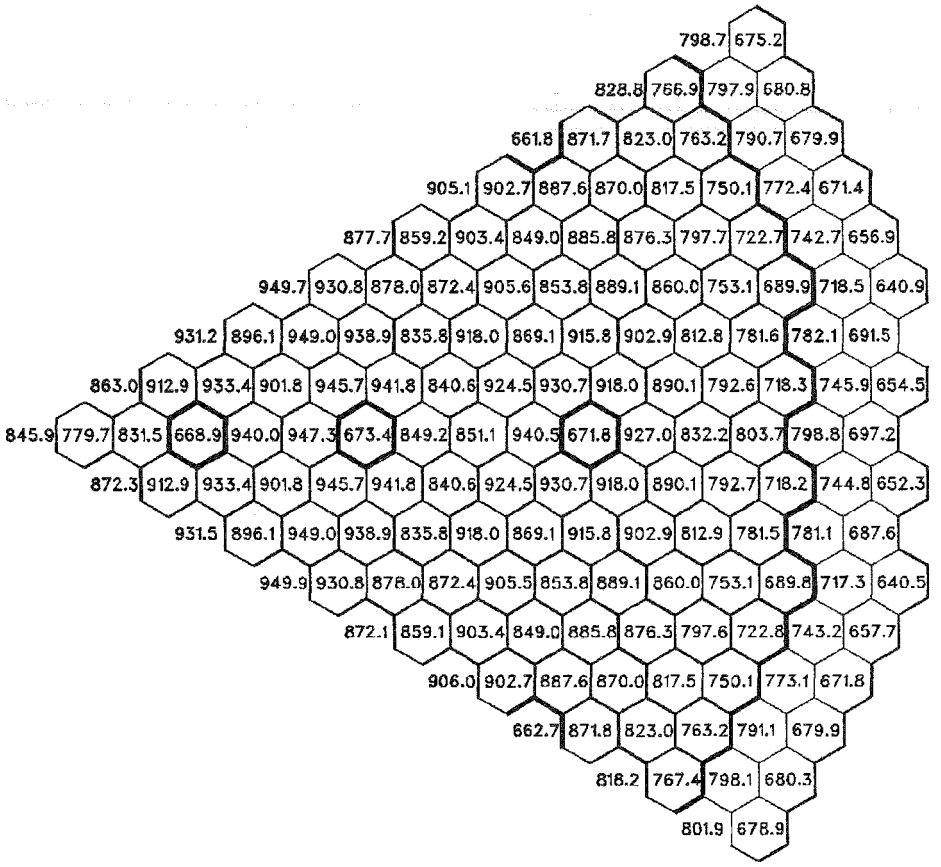

Figure G.41. Average coolant temperatures (°F) at EOEC at core-upper axial blanket interface. (Orificing based on assembly power and equal peak cladding midwall temperatures.)

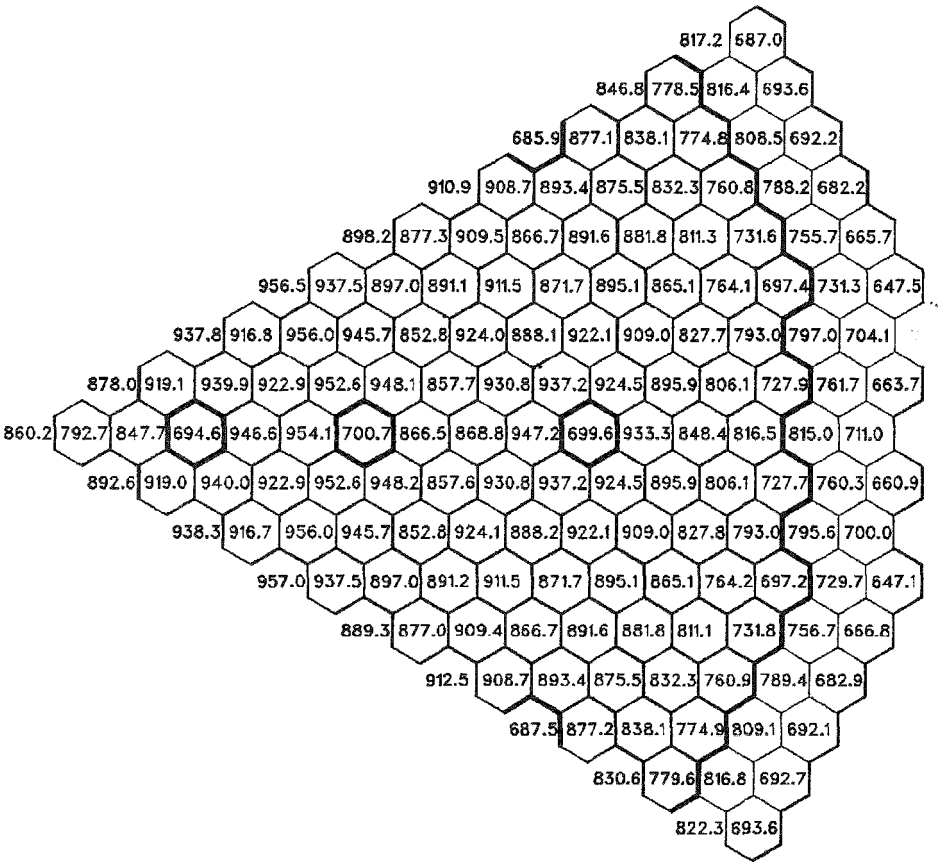

Figure G.42. Average coolant temperatures (^{o}F) at EOEC at the top of the upper axial blanket. (Orificing based on assembly power and equal peak cladding midwall temperatures.)

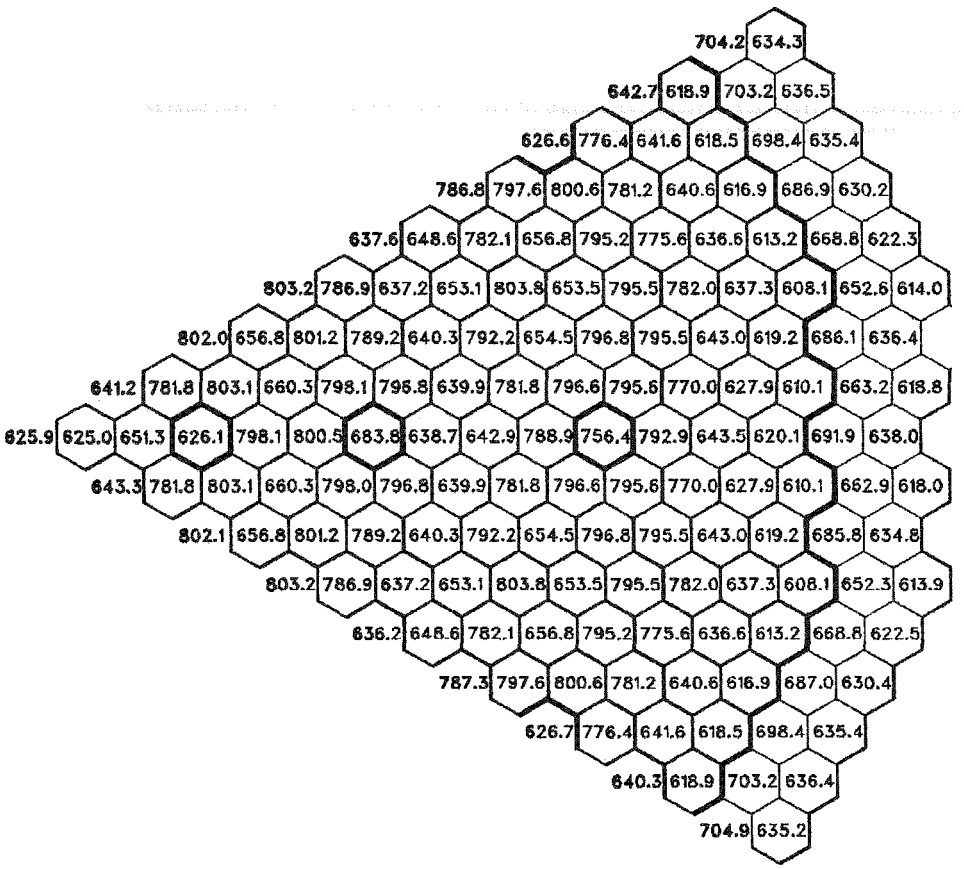

Figure G.43. Average coolant temperatures (^{o}F) at BOL at core midplane. (Orificing based on pin power and equal peak assembly coolant temperatures.)

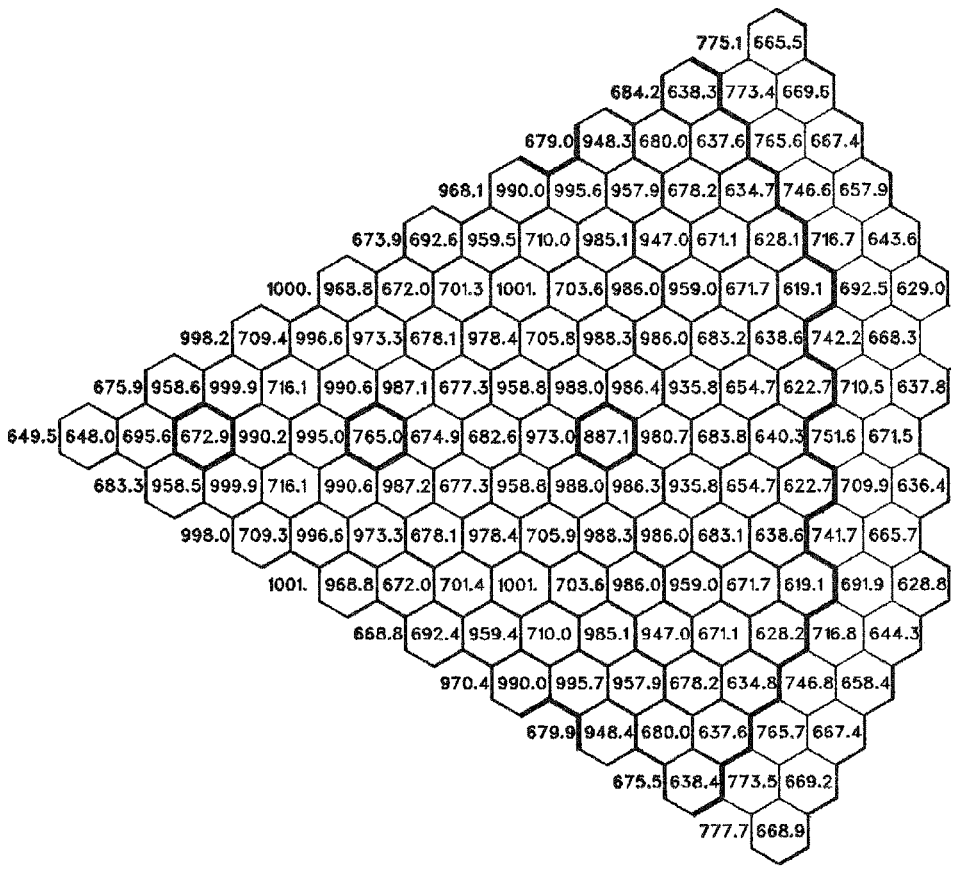

Figure G.44. Average coolant temperatures (^{o}F) at BOL at core-upper axial blanket interface. (Orificing based on pin power and equal peak assembly coolant temperatures.)

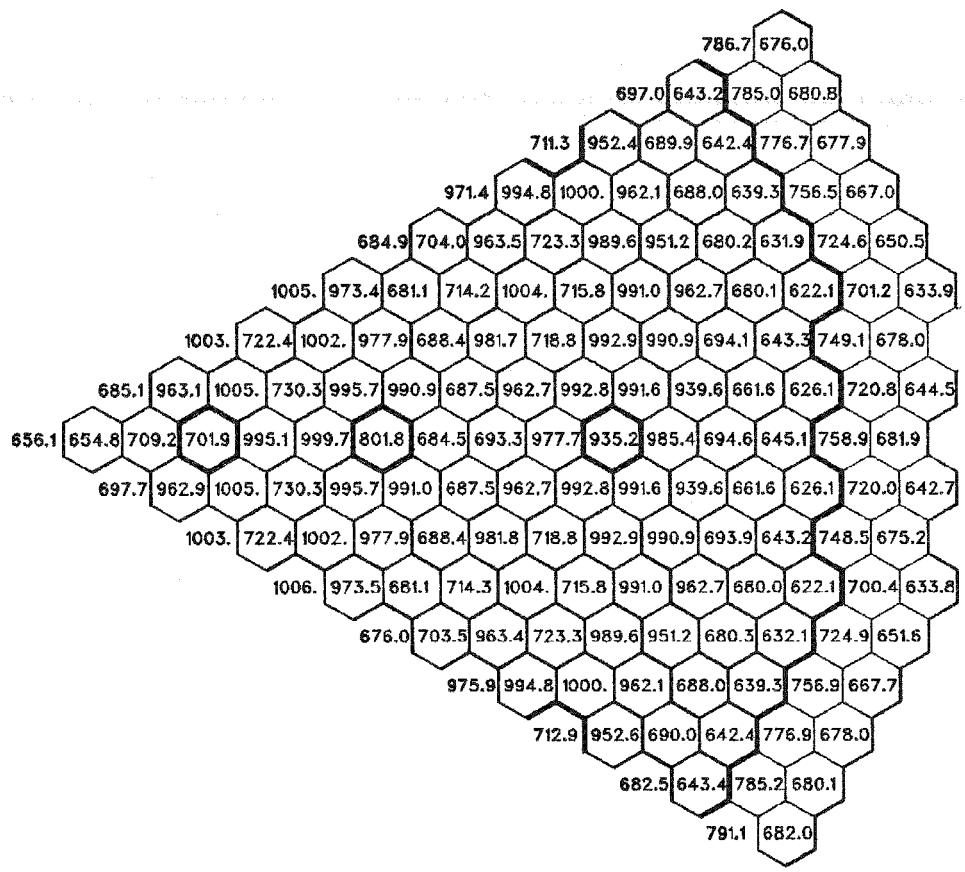

Figure G.45. Average coolant temperatures (°F) at BOL at the top of the upper axial blanket. (Orificing based on pin power and equal peak assembly coolant temperatures.)

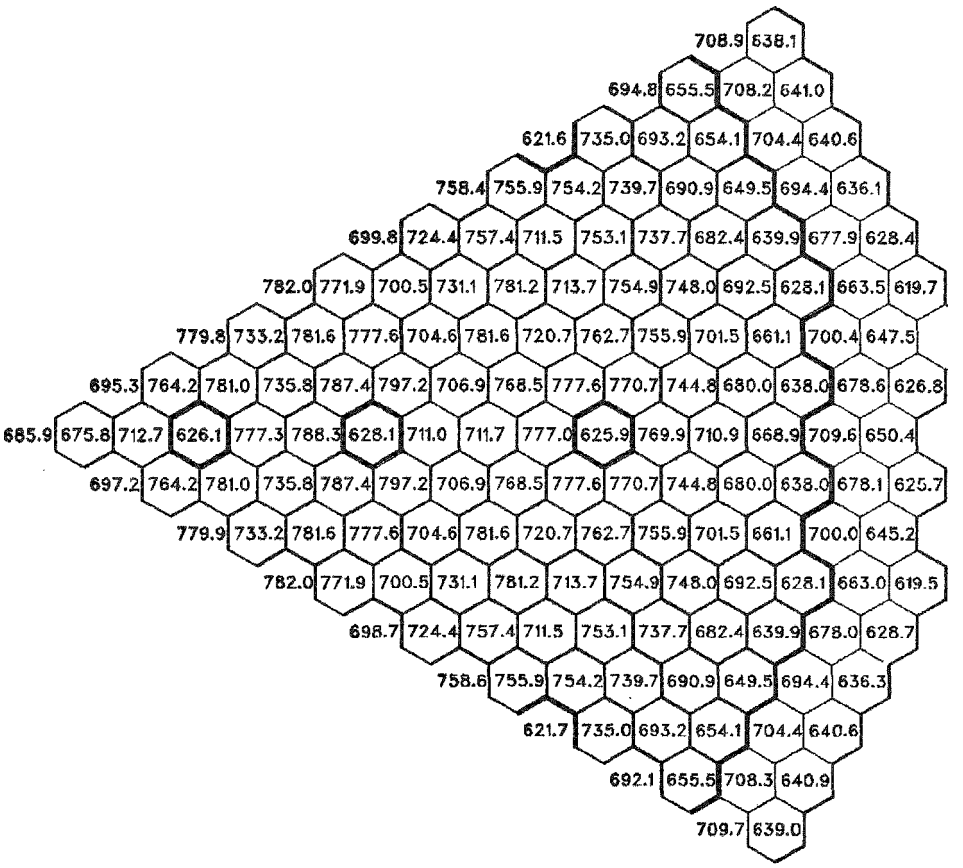

Figure G.46. Average coolant temperatures (^{o}F) at EOEC at core midplane. (Orificing based on pin power and equal peak assemby coolant temperatures.)

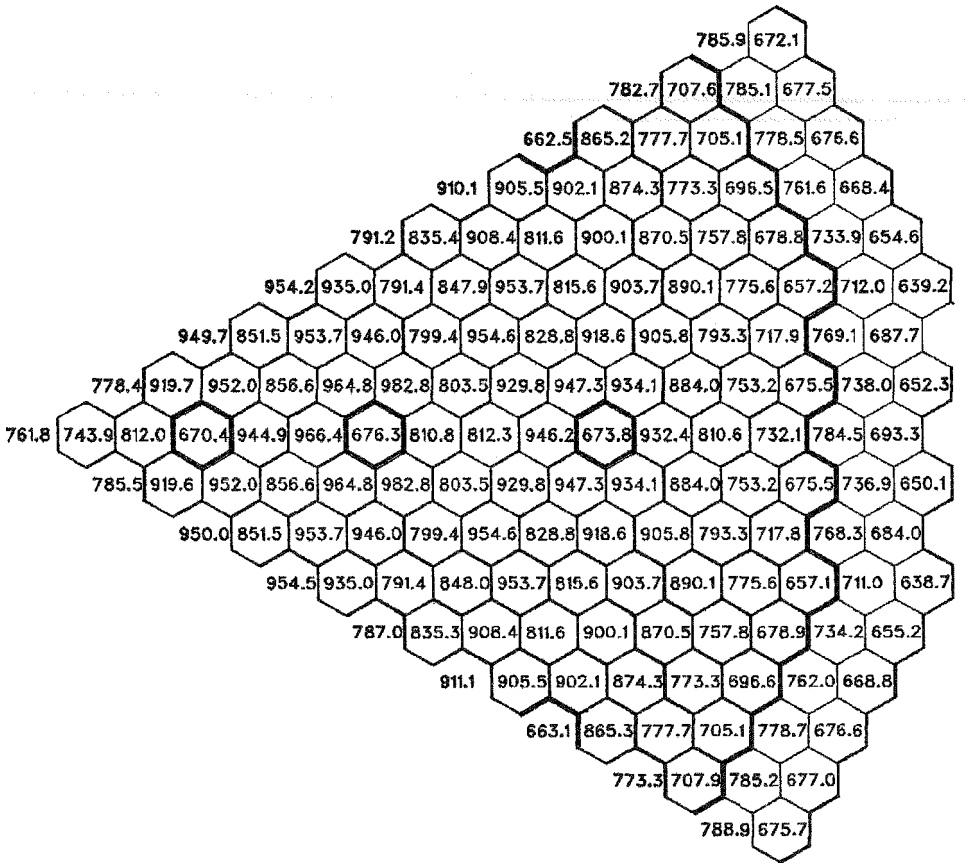

Figure G.47. Average coolant temperatures (°F) at EOEC at core-upper axial blanket interface. (Orificing based on pin power and equal peak assembly coolant temperatures.)

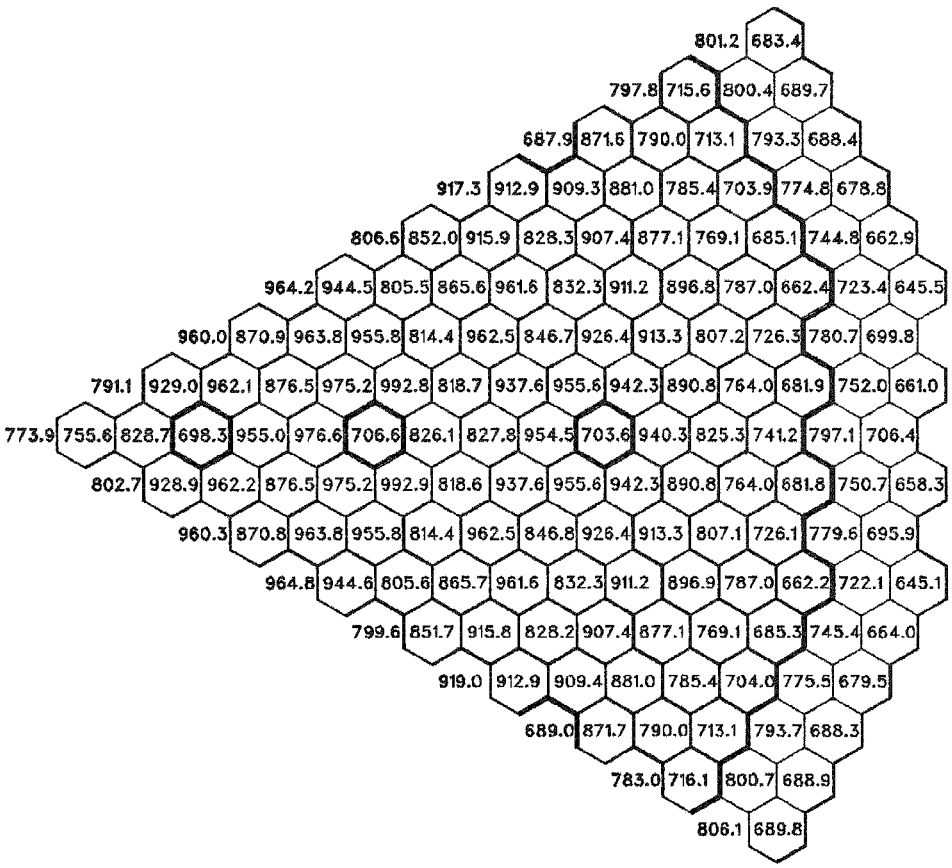

Figure G.48. Average coolant temperatures (°F) at EOEC at the top of the upper axial blanket. (Orificing based on pin power and equal peak assembly coolant temperatures.)

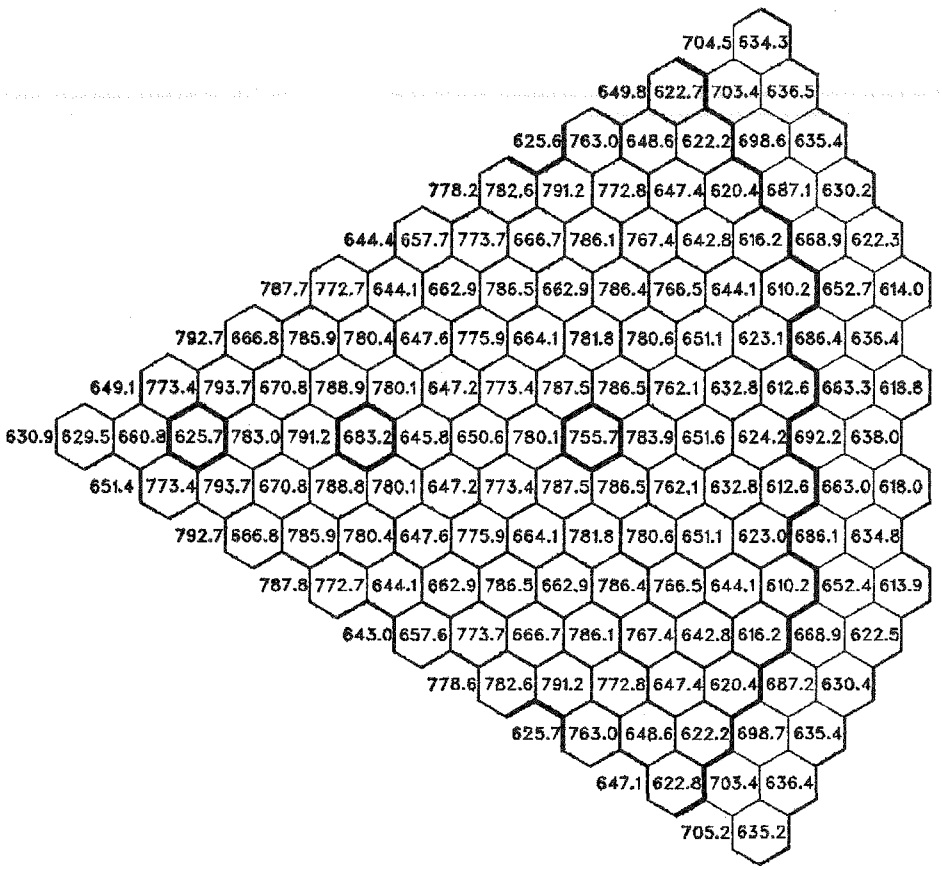

Figure G.49. Average coolant temperatures ($^{\circ}$F) at BOL at core midplane. (Orificing based on pin power and equal peak cladding midwall temperatures.)

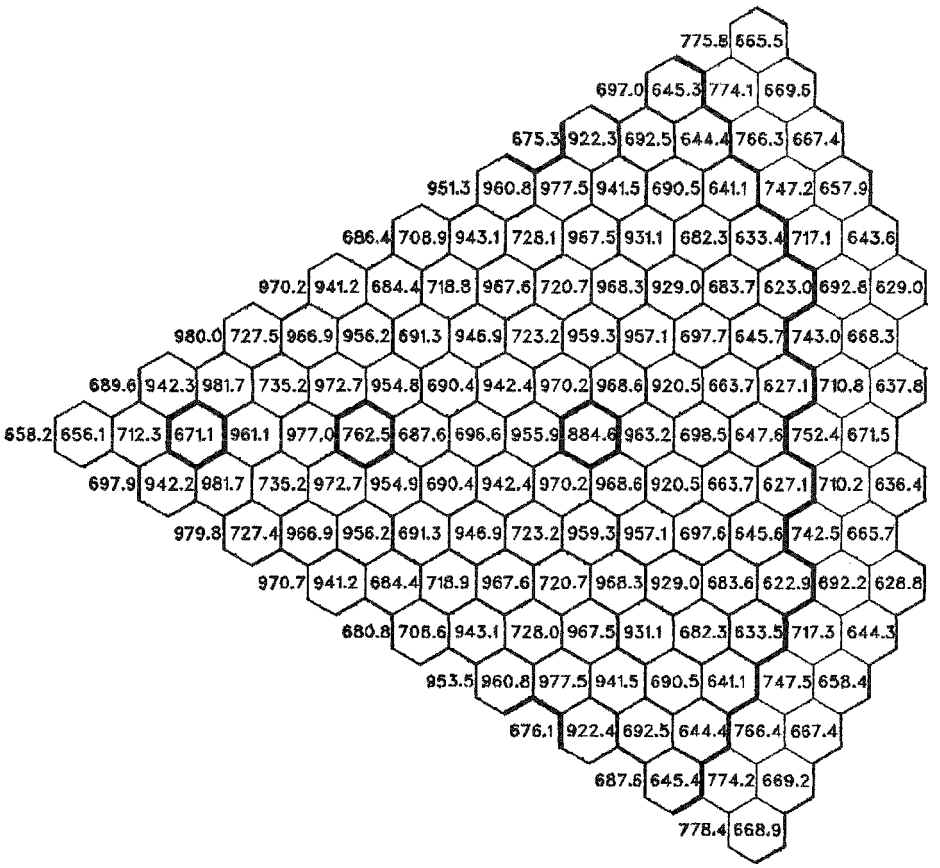

Figure G.50. Average coolant temperatures ($^{\circ}$F) at BOL at core-upper axial blanket interface. (Orificing based on pin power and equal peak cladding midwall temperatures.)

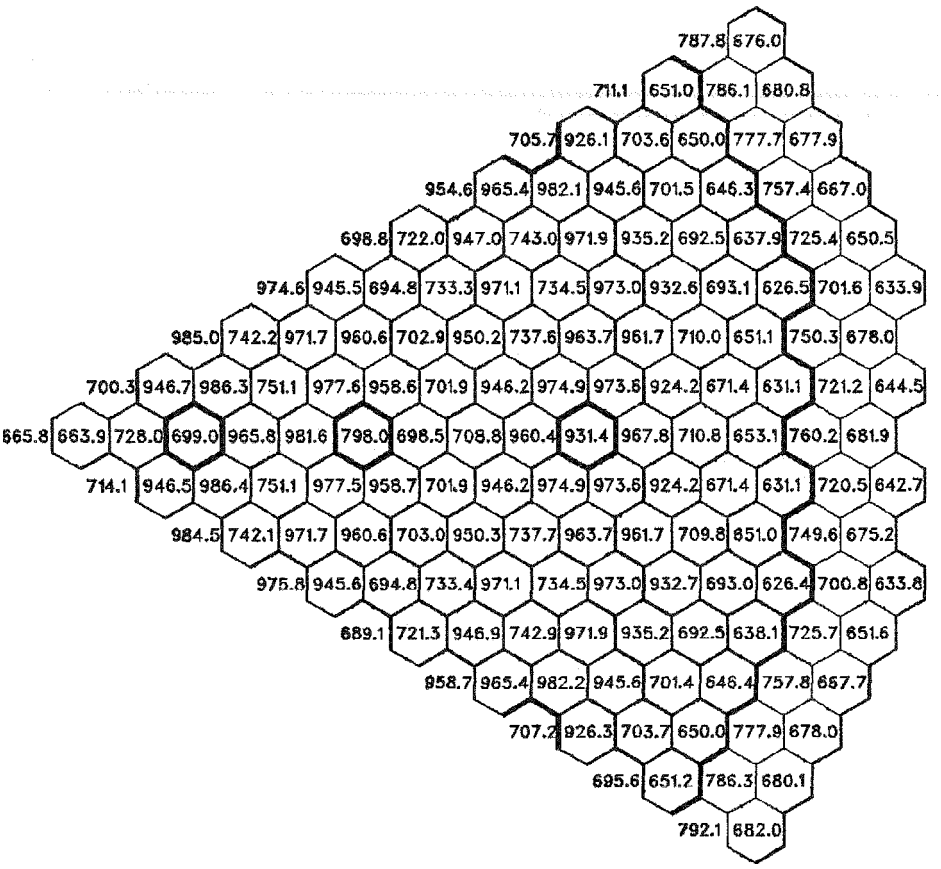

Figure G.51. Average coolant temperatures (^{o}F) at BOL at the top of the upper axial blanket. (Orificing based on pin power and equal peak cladding midwall temperatures.)

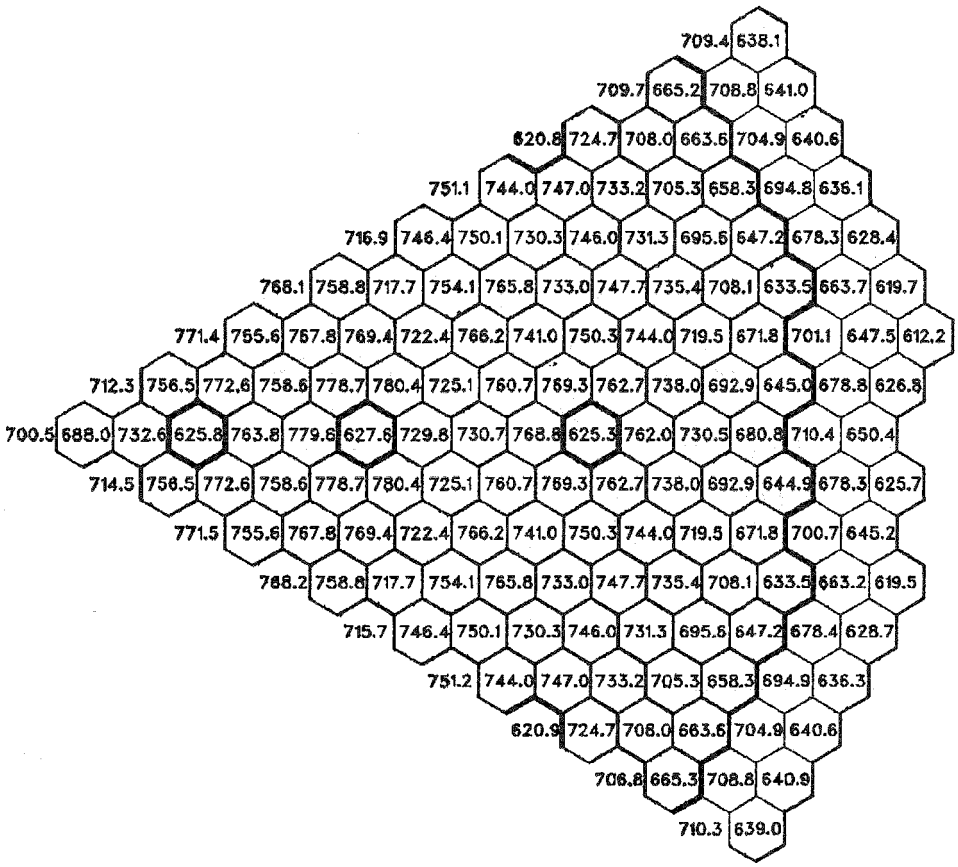

Figure G.52. Average coolant temperatures ($^{\circ}$F) at EOEC at core midplane. (Orificing based on pin power and equal peak cladding mdiwall temperatures.)

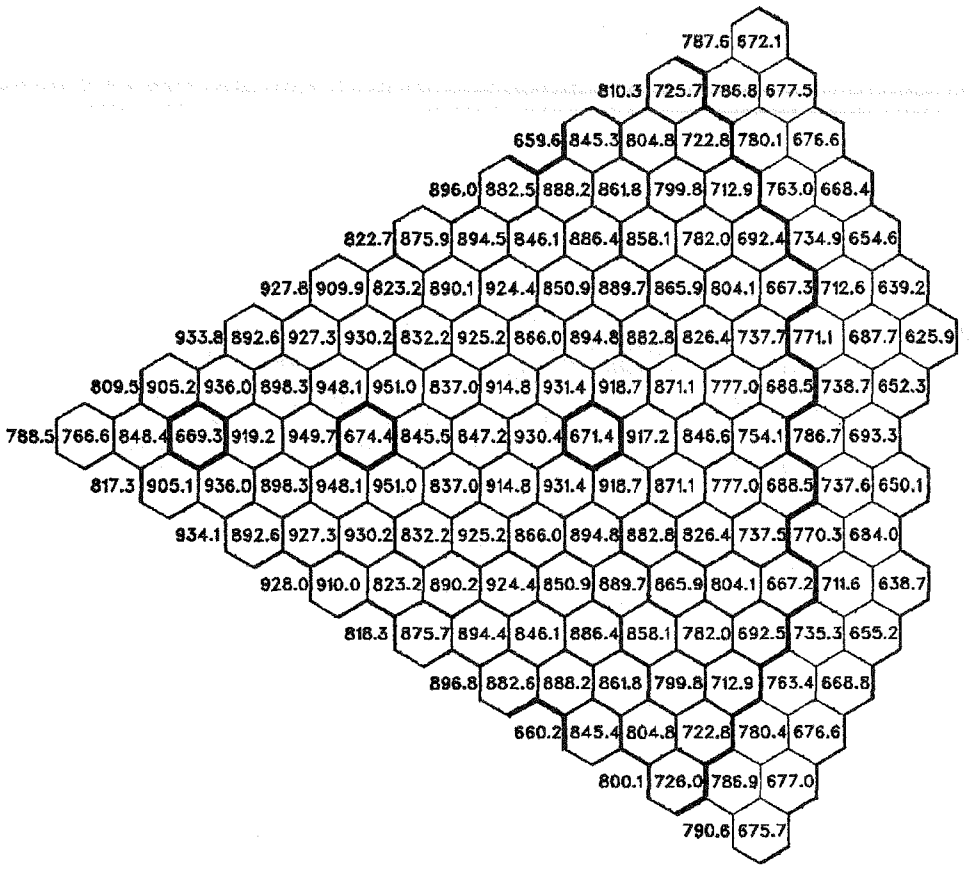

Figure G.53. Average coolant temperatures (°F) at EOEC at core-upper axial blanket interface. (Orificing based on pin power and equal peak cladding midwall temperatures.)

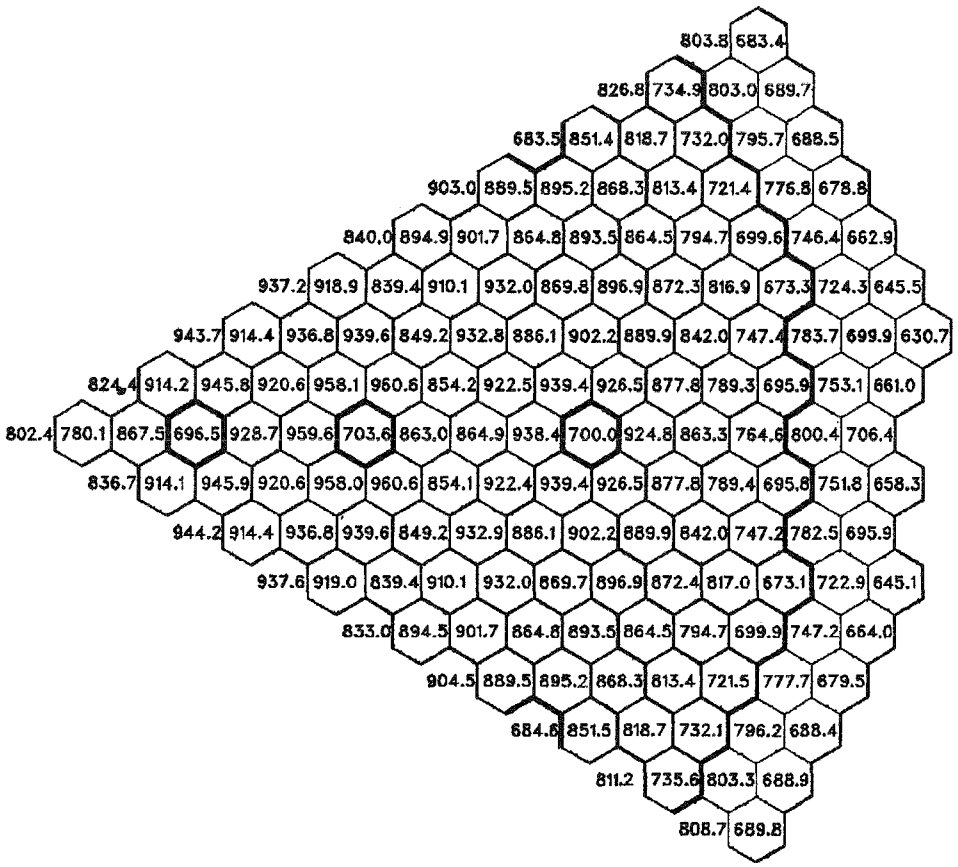

Figure G.54. Average coolant temperatures (^{o}F) at EOEC at the top of the upper axial blanket. (Orificing based on pin power and equal peak cladding midwall temperatures.)

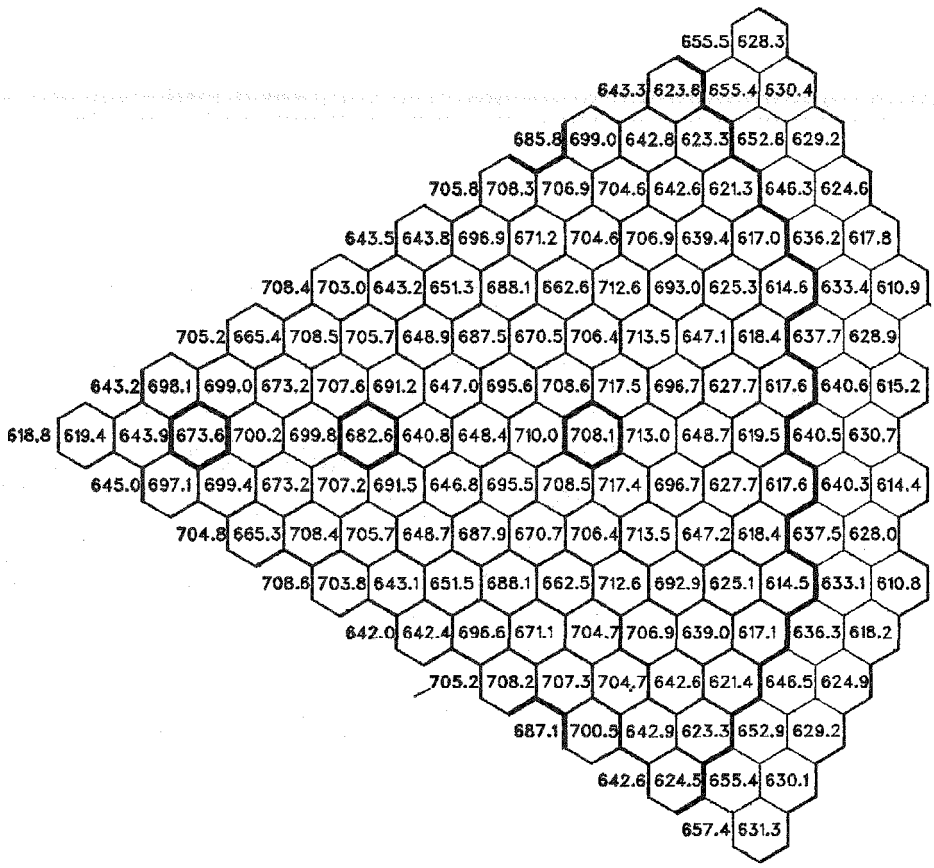

Figure G.55 Assembly average duct wall temperatures (^{o}F) at BOL at core midplane. (Orificing based on assembly power and equal peak assembly coolant temperatures.)

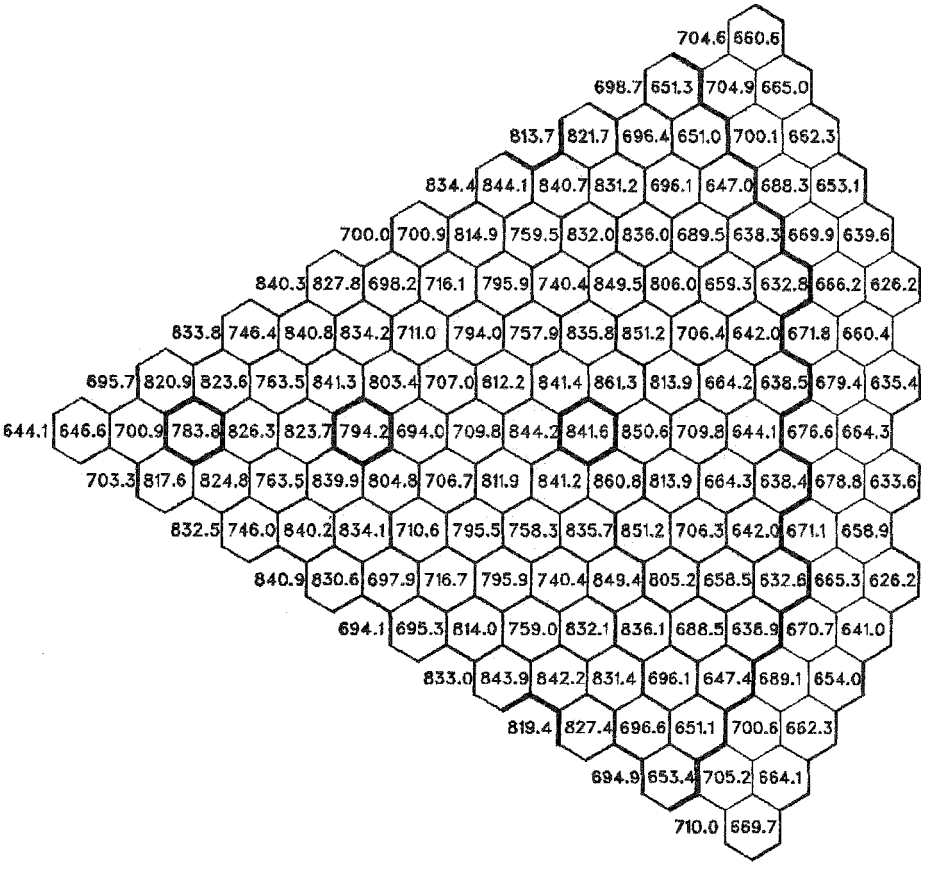

Figure G.56 Assembly average duct wall temperatures (^{o}F) at BOL at the core-upper axial blanket interface. (Orificing based on assembly power and equal peak assembly coolant temperatures.)

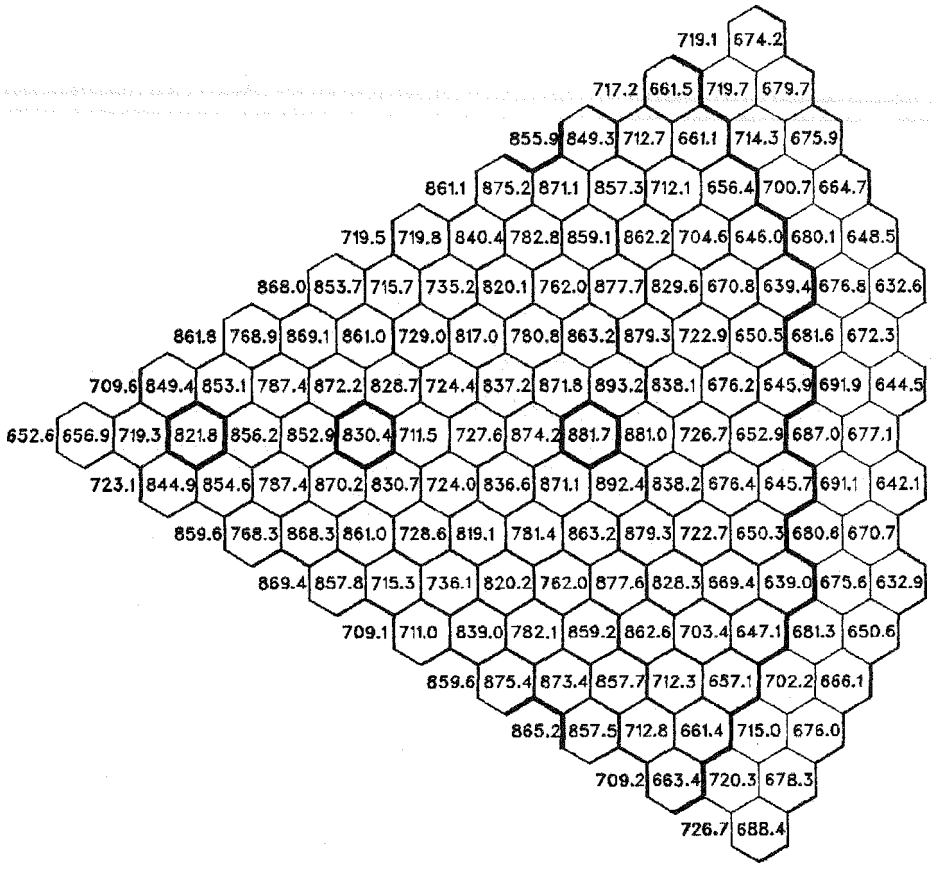

Figure G.57 Assembly average duct wall temperatures (^{o}F) at the top of the upper axial blanket. (Orificing based on assembly power and equal peak assembly coolant temperatures.)

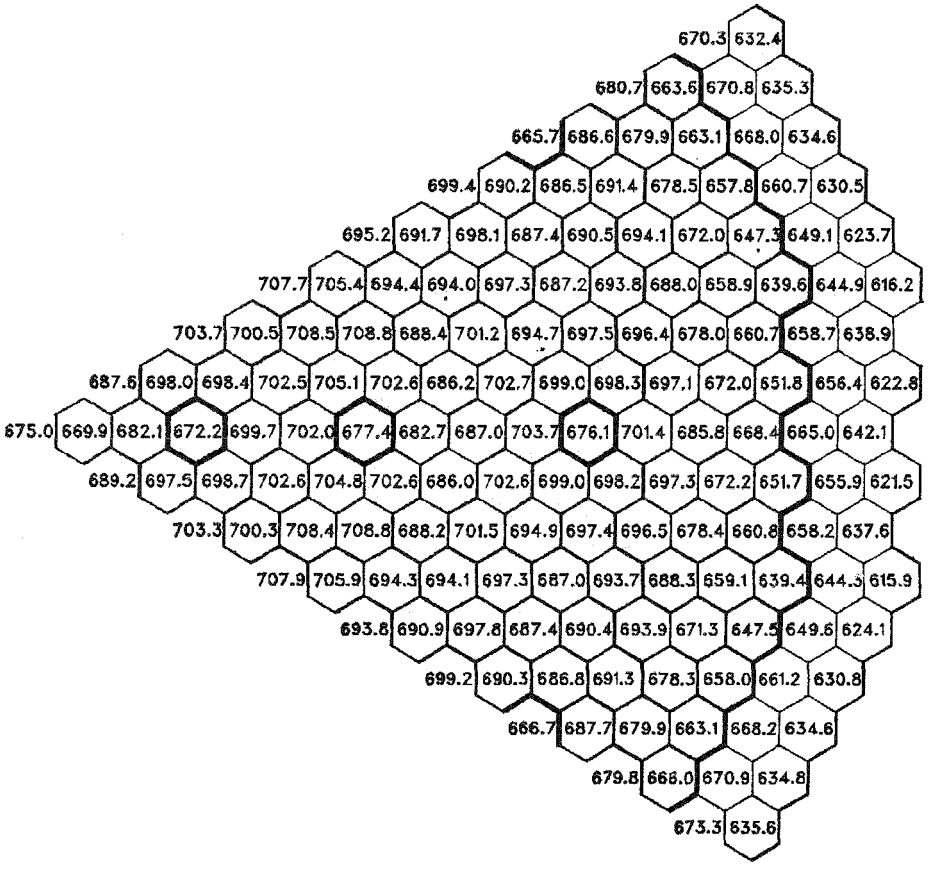

Figure G.58 Assembly average duct wall temperatures (^{o}F) at EOEC at core midplane. (Orificing based on assembly power and equal peak assembly coolant temperatures.)

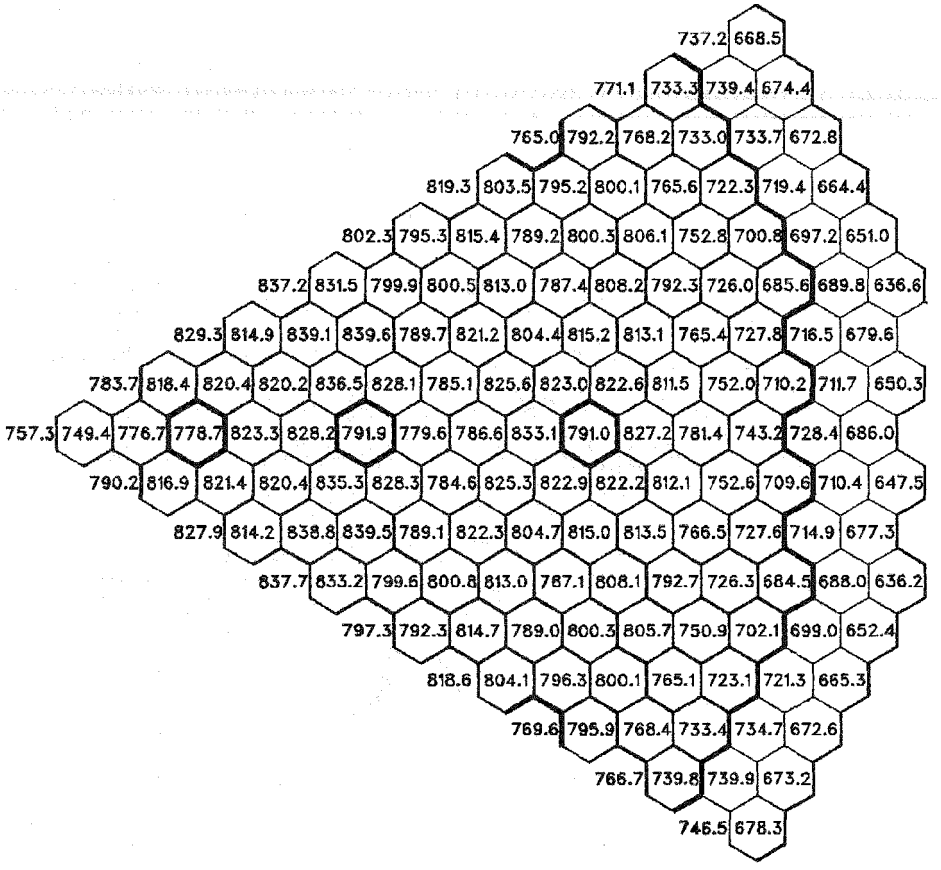

Figure G.59 Assembly average duct wall temperatures (^{o}F) at EOEC at core-upper axial blanket interface. (Orificing based on assembly power and equal peak assembly coolant temperatures.)

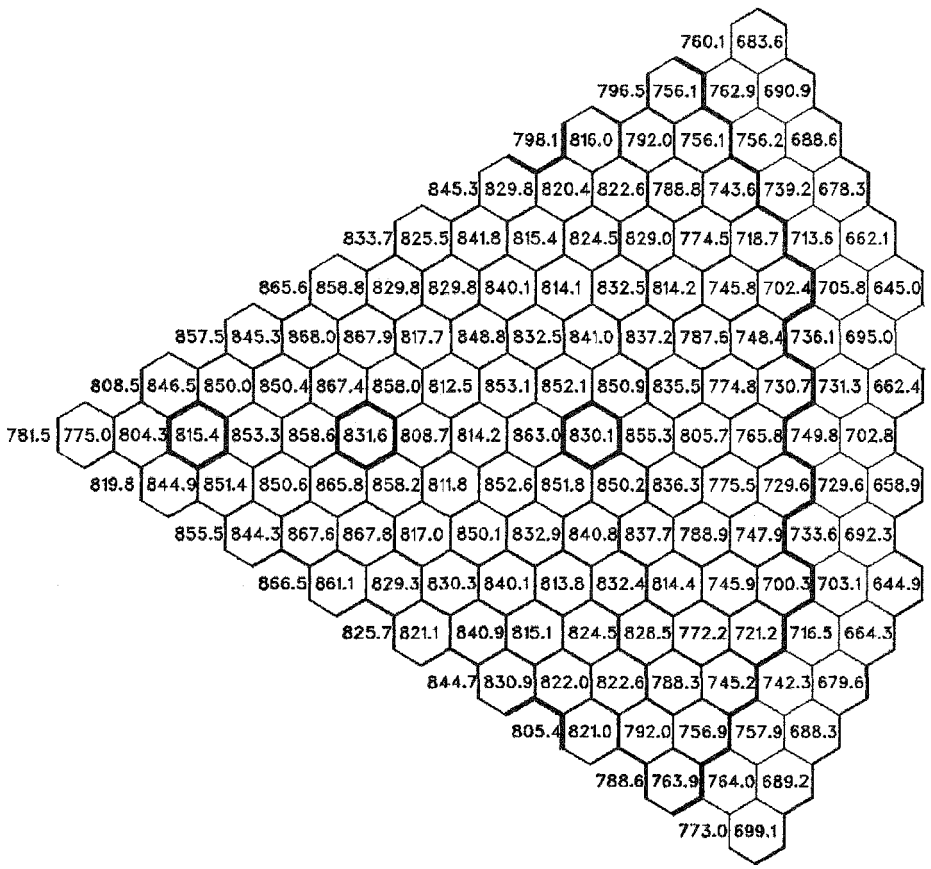

Figure G.60 Assembly average duct wall temperatures (^{o}F) at EOEC at the top of the upper axial blanket. (Orificing based on assembly power and equal peak assembly coolant temperatures.)

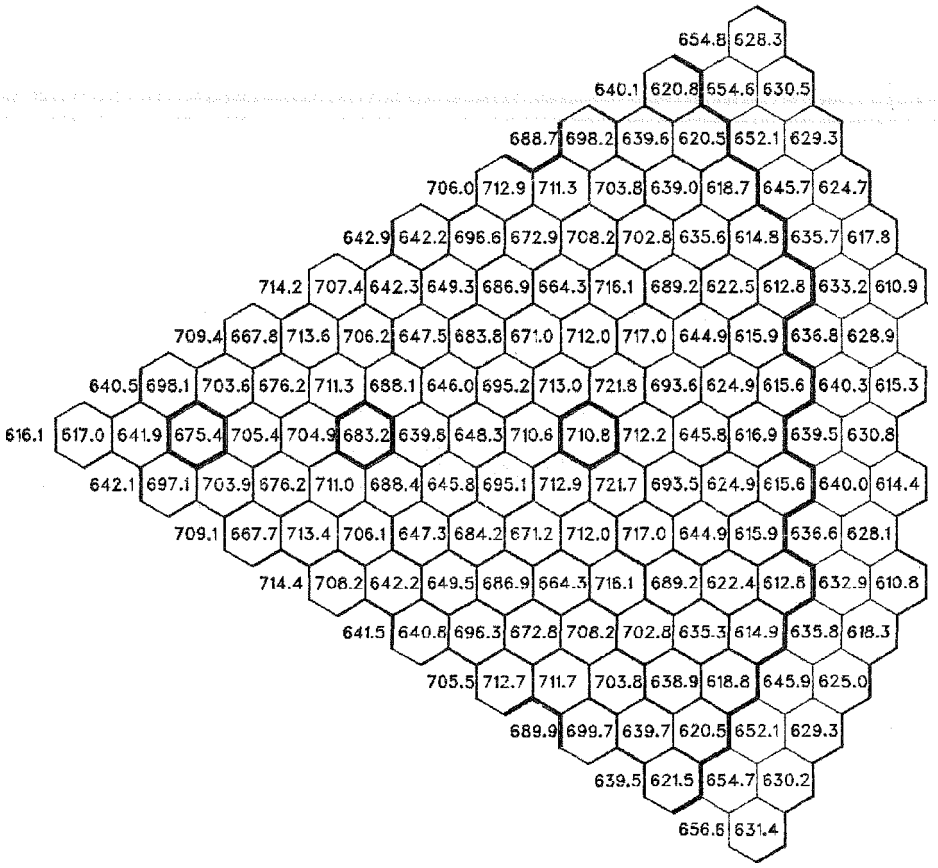

Figure G.61 Assembly average duct wall temperatures (^{o}F) at BOL at core midplane. (Orificing based on assembly power and equal peak cladding midwall temperatures.)

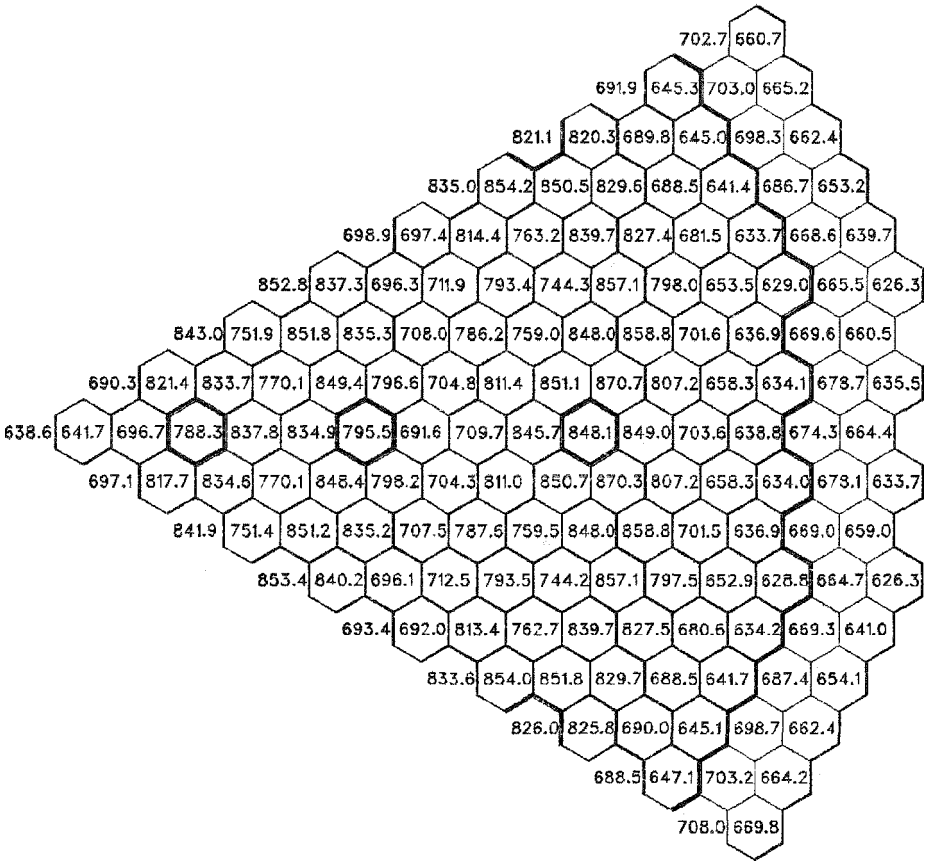

Figure G.62 Assembly average duct wall temperatures (^{o}F) at BOL at core-upper axial blanket interface. (Orificing based on assembly power and equal peak cladding midwall temperatures.)

Figure G.63 Assembly average duct wall temperatures (^{o}F) at BOL at the top of the upper axial blanket. (Orificing based on assembly power and equal peak cladding midwall temperatures.)

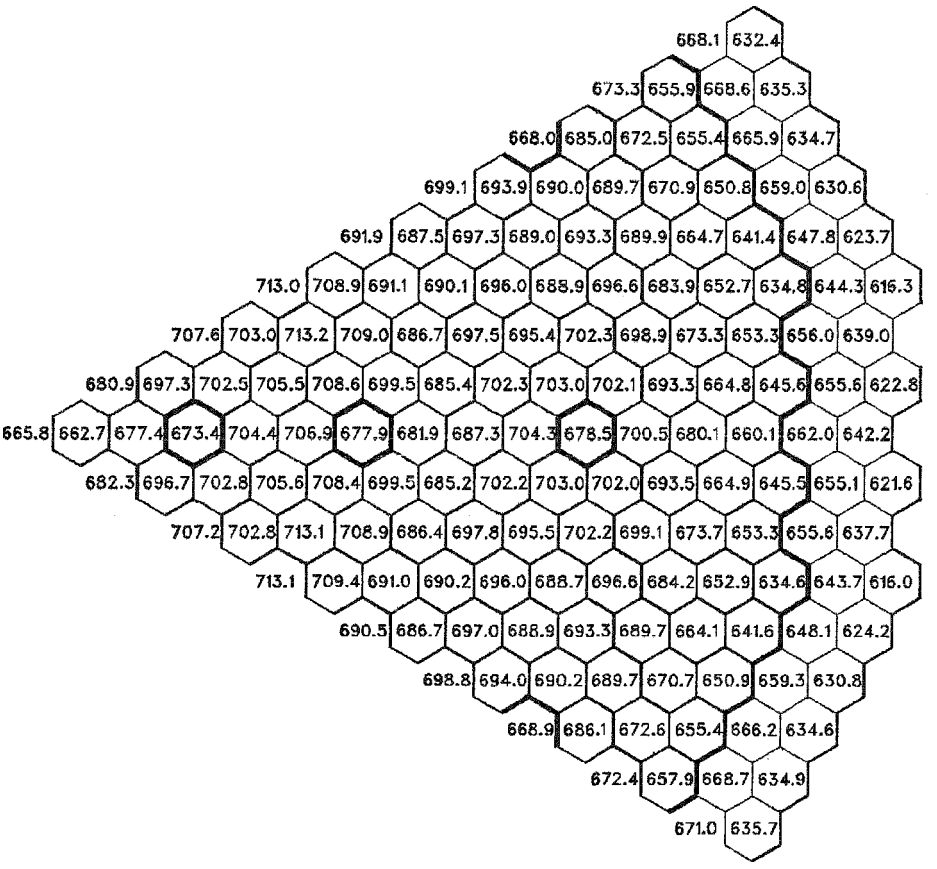

Figure G.64 Assembly average duct wall temperatures (^{o}F) at EOEC at core midplane. (Orificing based on assembly power and equal peak cladding midwall temperatures.)

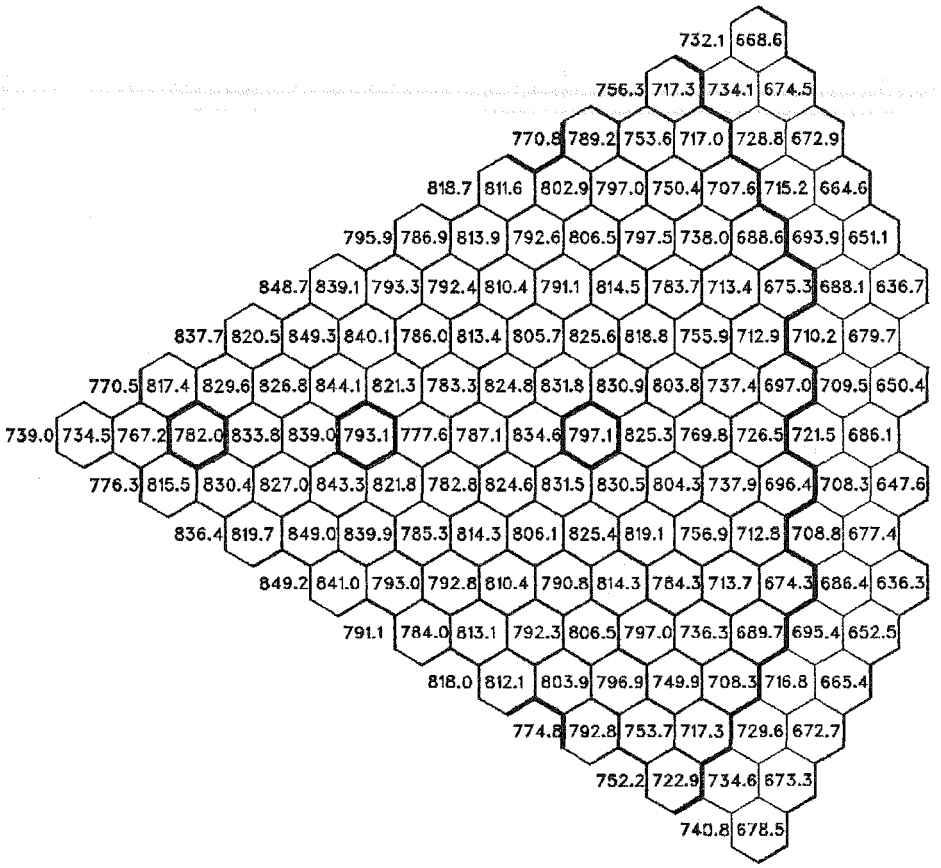

Figure G.65 Assembly average duct wall temperatures (^{O}F) at EOEC at core-upper axial blanket interface. (Orificing based on assembly power and equal peak cladding midwall temperatures.)

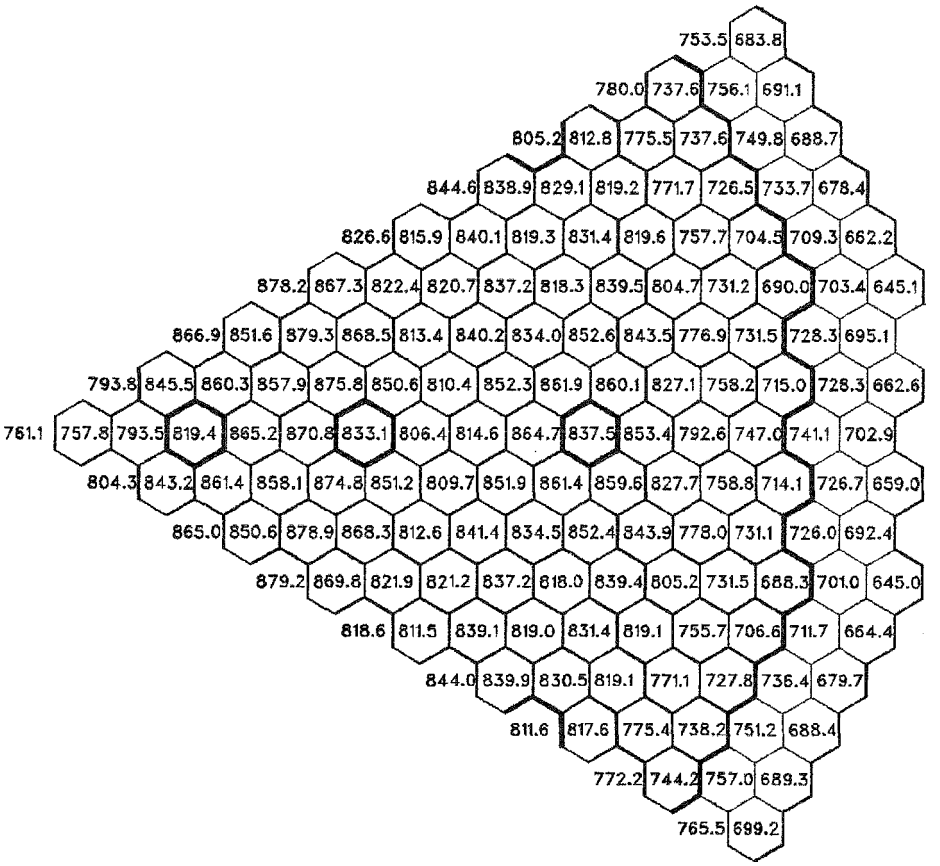

Figure G.66 Assembly average duct wall temperatures (^{o}F) at EOEC at the top of the upper axial blanket. (Orificing based on assembly power and equal peak cladding midwall temperatures.)

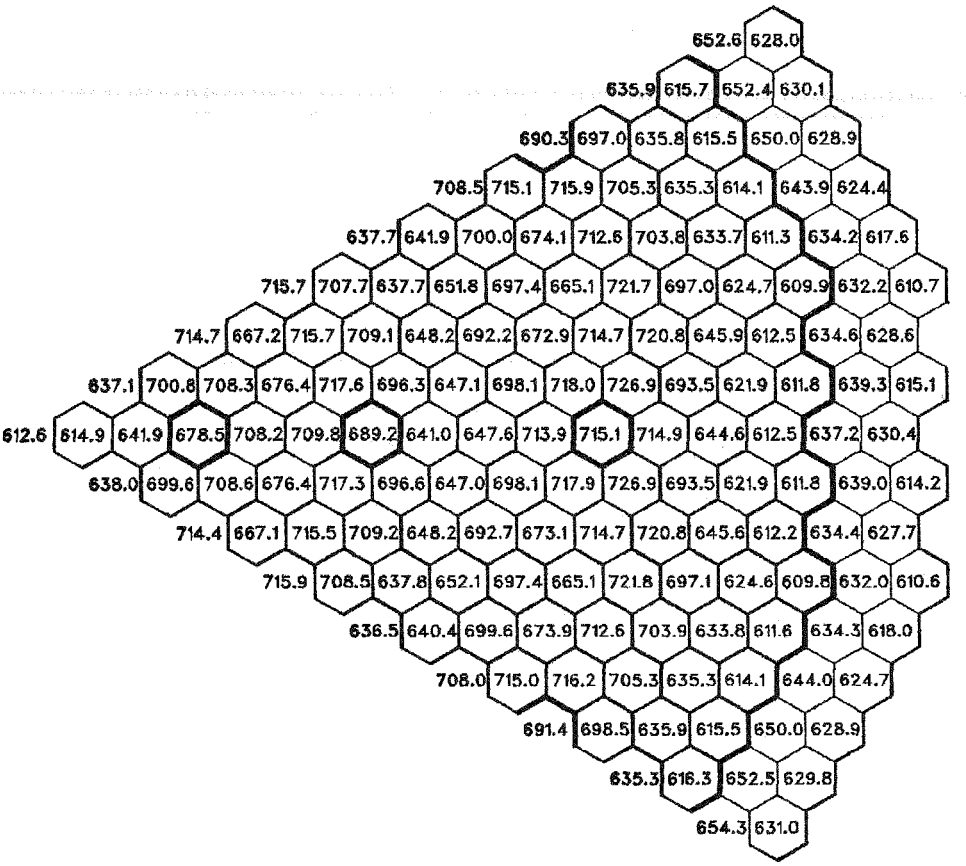

Figure G.67 Assembly average duct wall temperatures (^{o}F) at BOL at core midplane. (Orificing based on assembly power and equal peak assembly coolant temperatures.)

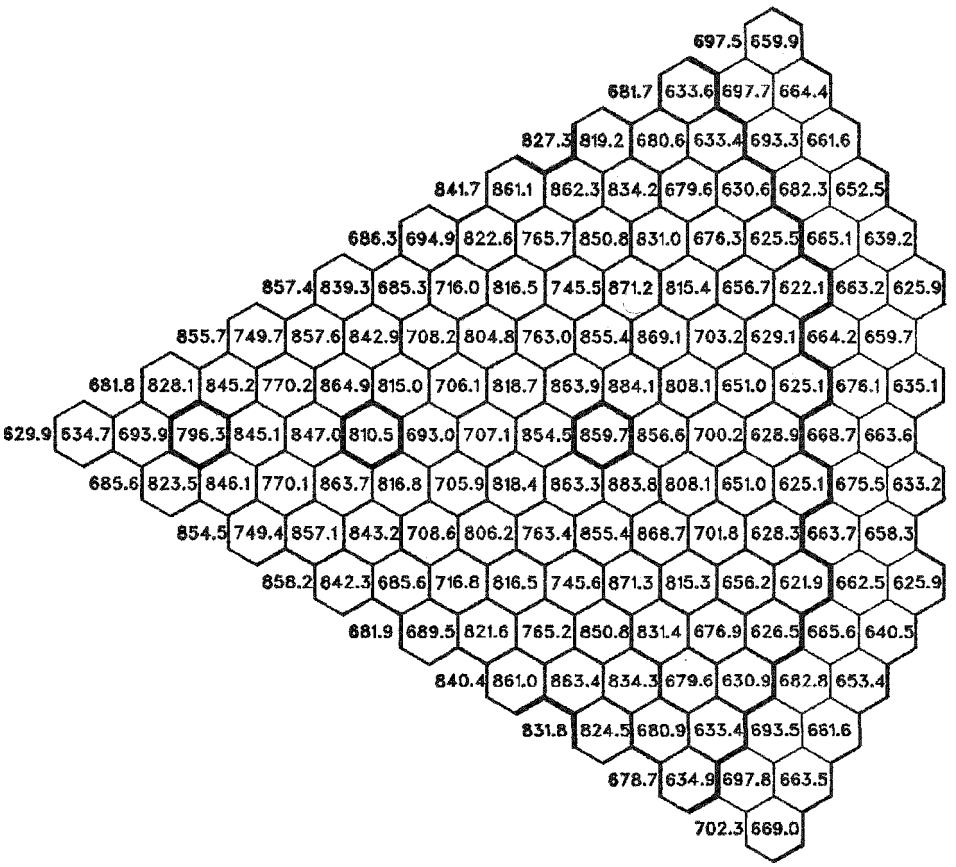

Figure G.68 Assembly average duct wall temperatures (^{o}F) at BOL at core-upper axial blanket interface. (Orificing based on assembly power and equal peak assembly coolant temperatures.)

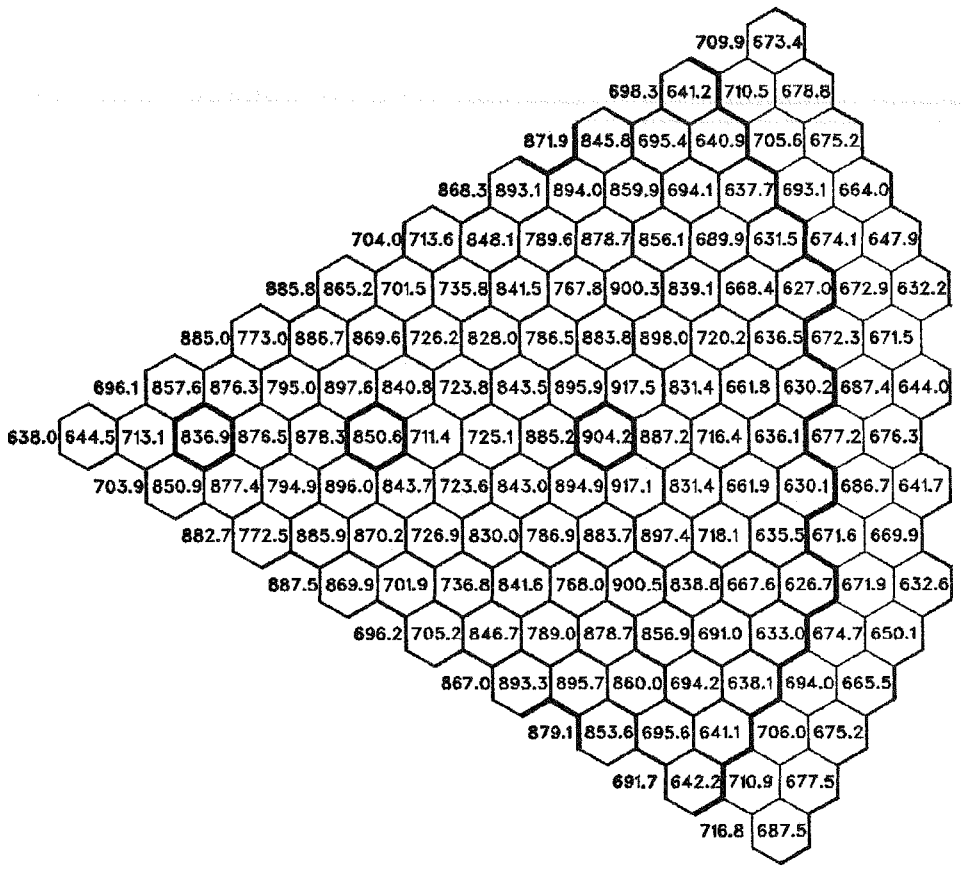

Figure G.69 Assembly average duct wall temperatures (^{o}F) at BOL at the top of the upper axial blanket. (Orificing based on assembly power and equal peak assembly coolant temperatures.)

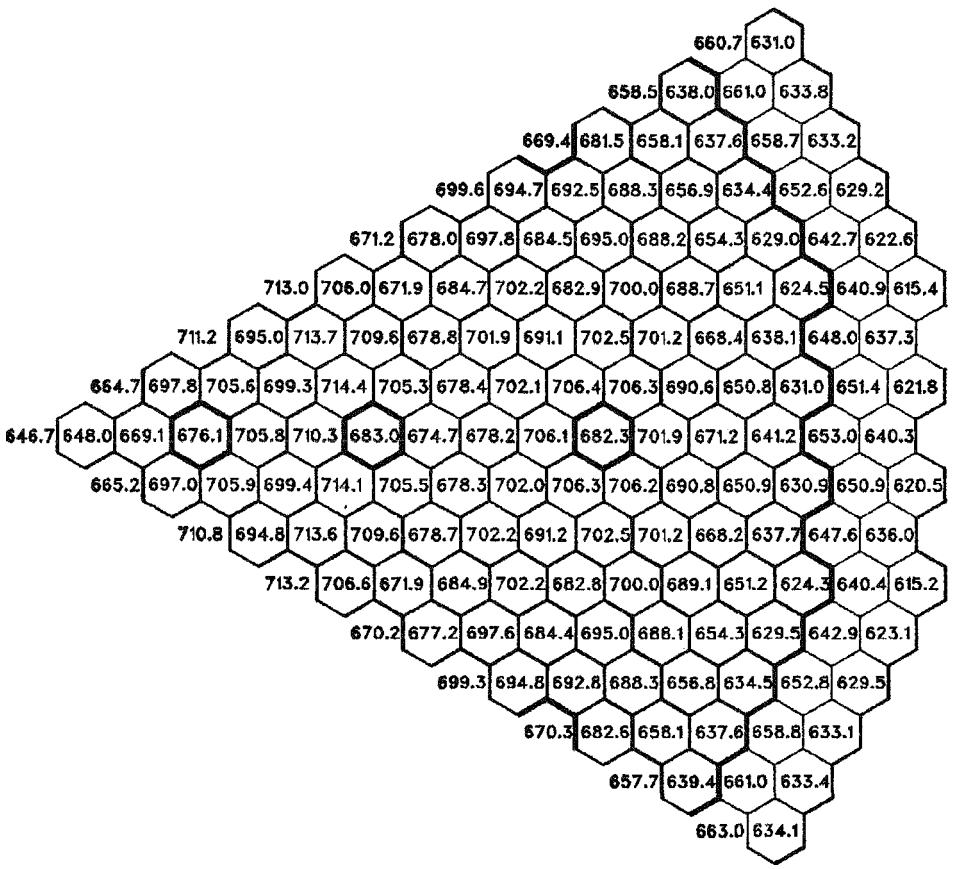

Figure G.70 Assembly average duct wall temperatures (^{o}F) at EOEC at core midplane. (Orificing based on assembly power and equal peak assembly coolant temperatures.)

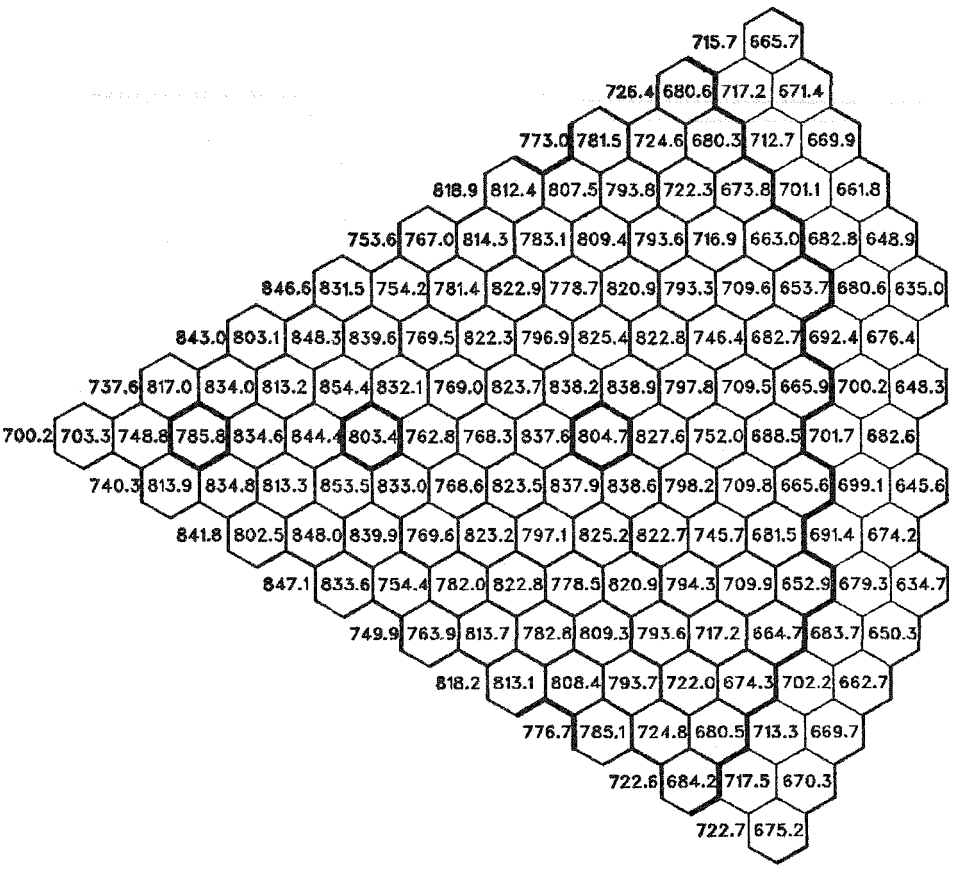

Figure G.71 Assembly average duct wall temperatures (^{o}F) at EOEC at core-upper axial blanket interface. (Orificing based on assembly power and equal peak assembly coolant temperatures.)

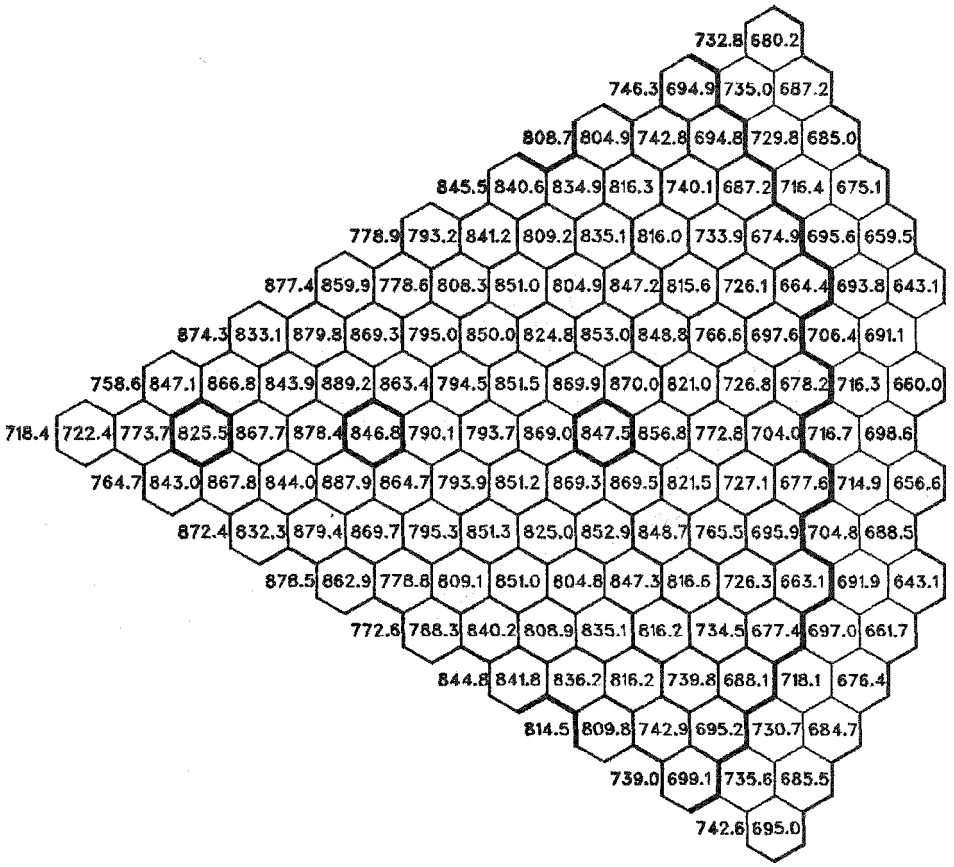

Figure G.72 Assembly average duct wall temperatures (^{o}F) at EOEC at the top of the upper axial blanket. (Orificing based on assembly power and equal peak assembly coolant temperatures.)

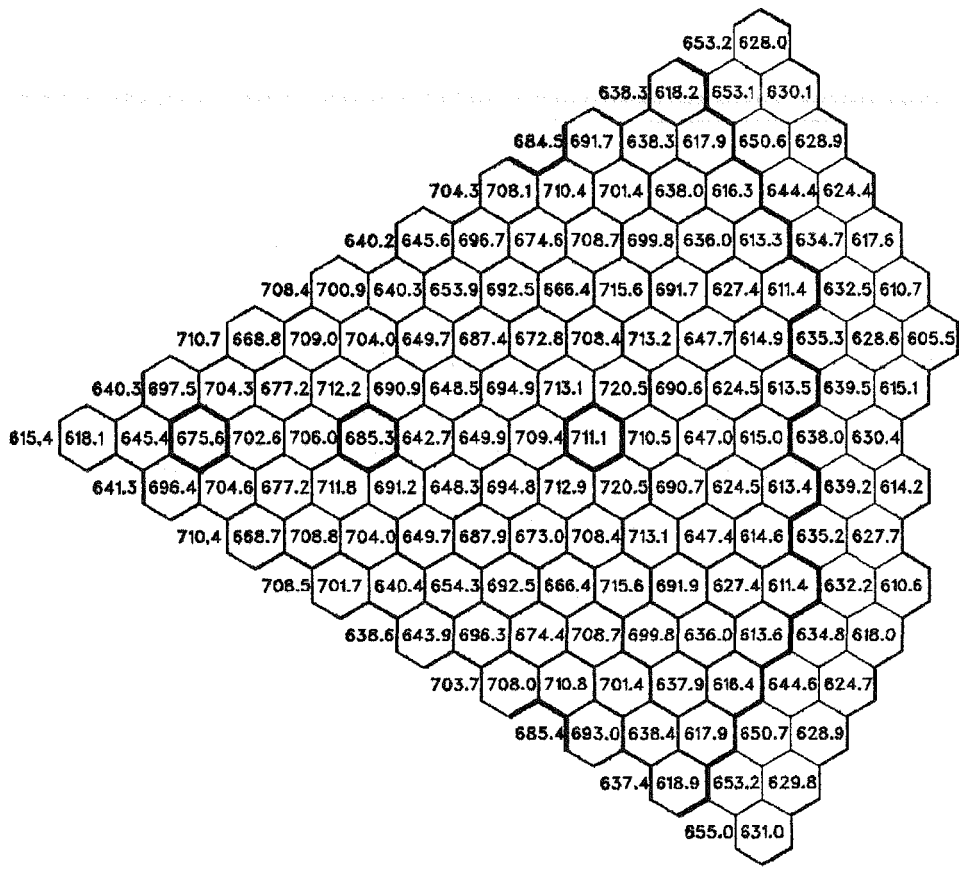

Figure G.73 Assembly average duct wall temperatures (^{O}F) at BOL at the core midplane. (Orificing based on assembly power and equal peak cladding midwall temperatures.)

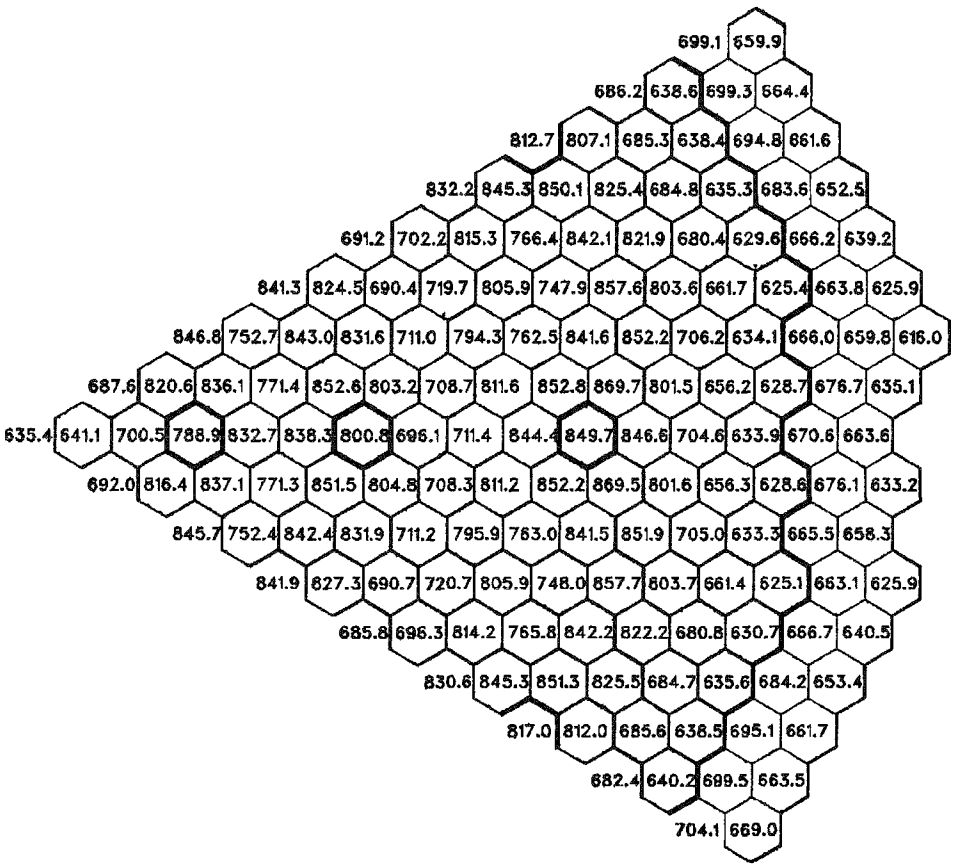

Figure G.74 Assembly average duct wall temperatures (^{O}F) at BOL at core-upper axial blanket interface. (Orificing based on assembly power and equal peak cladding midwall temperatures.)

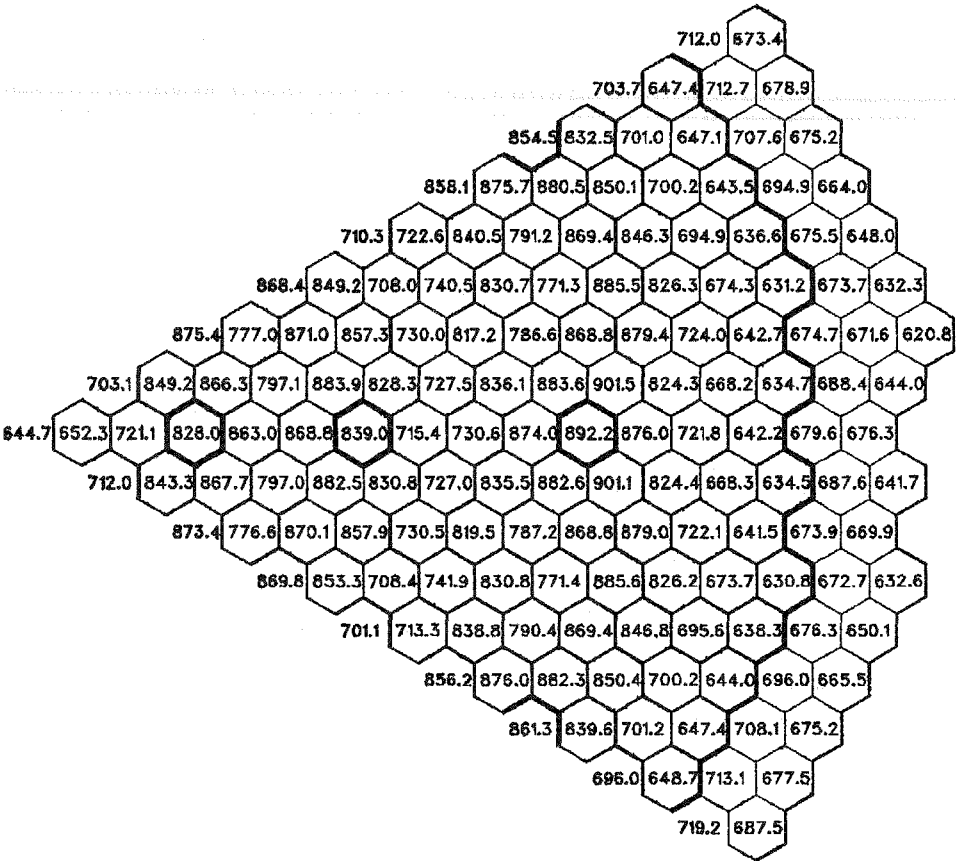

Figure G.75 Assembly average duct wall temperatures (^{o}F) at BOL at the top of the upper axial blanket. (Orificing based on assembly power and equal peak cladding midwall temperatures.)

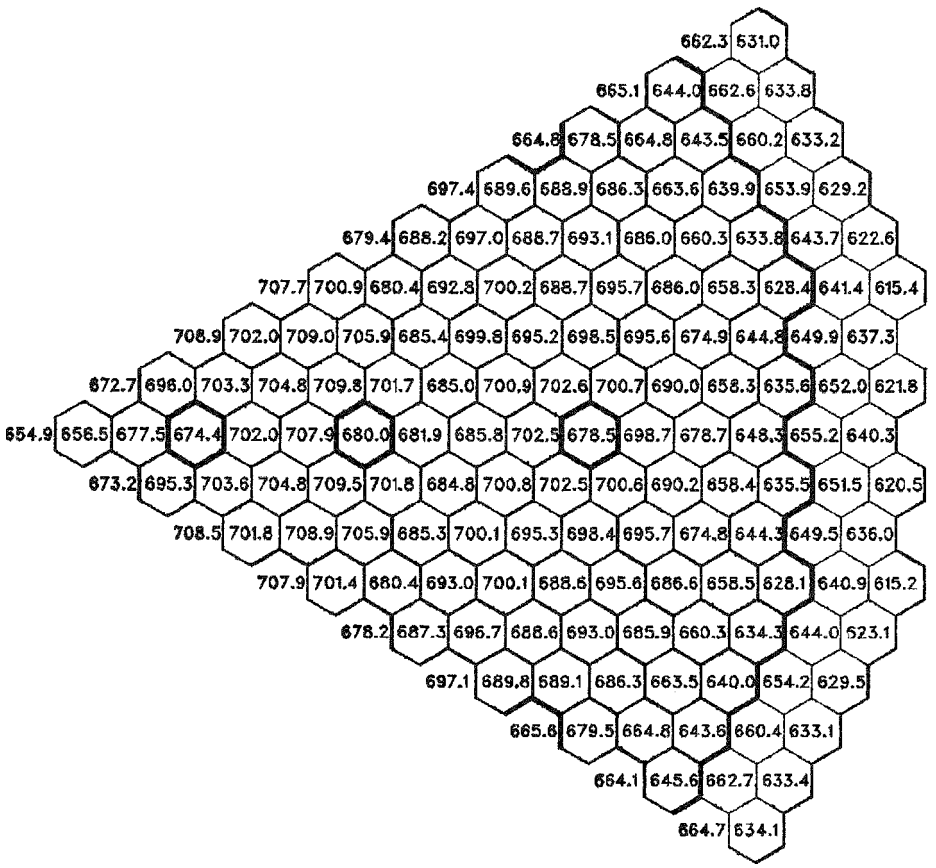

Figure G.76 Assembly average duct wall temperatures (^{o}F) at EOEC at core midplane. (Orificing based on assembly power and equal peak cladding midwall temperatures.)

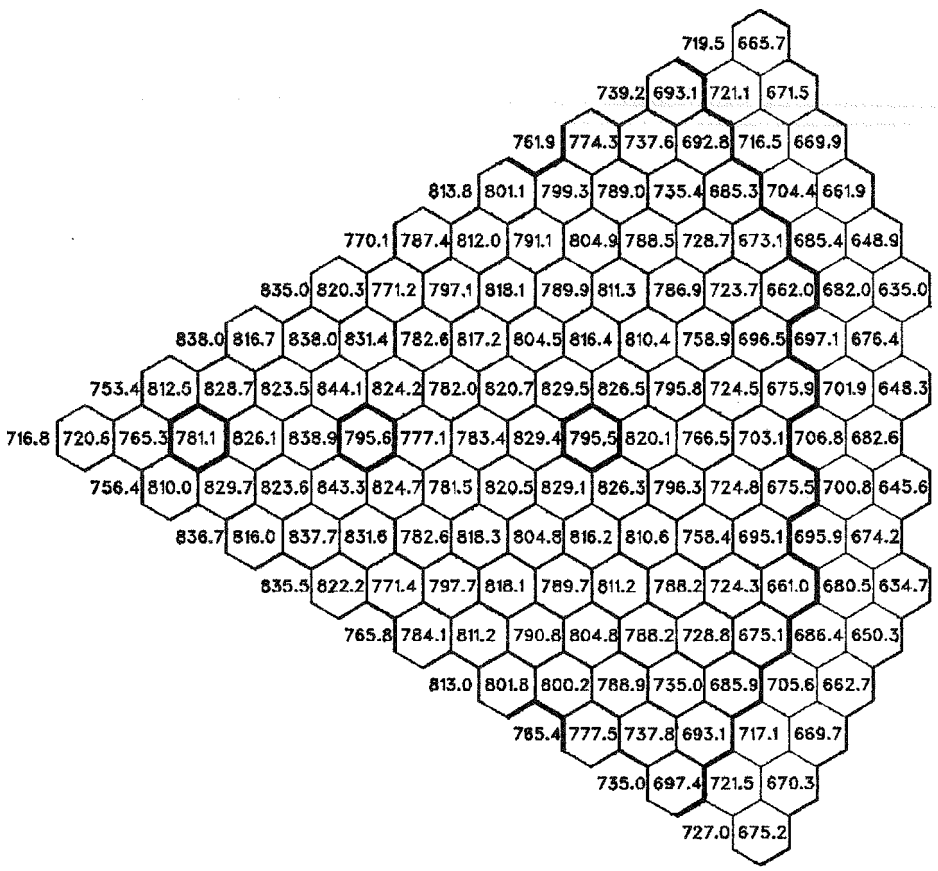

Figure G.77 Assembly average duct wall temperatures (^{O}F) at EOEC at core-upper axial blanket interface. (Orificing based on assembly power and equal peak cladding midwall temperatures.)

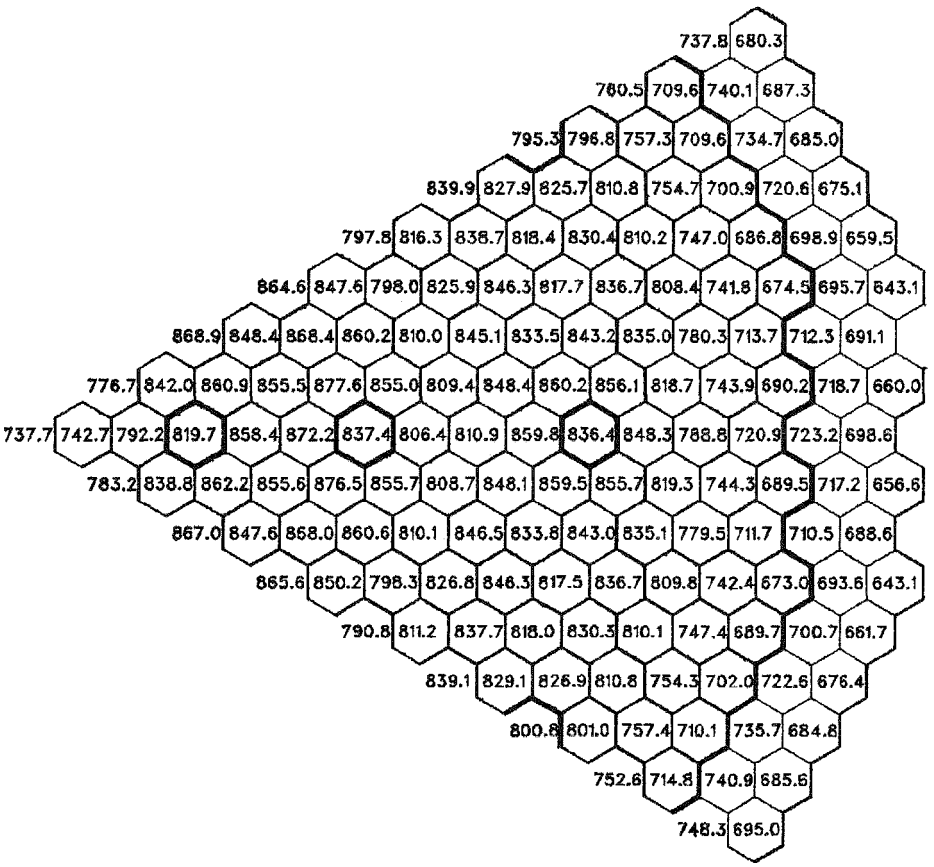

Figure G.78 Assembly average duct wall temperatures (^{o}F) at EOEC at the top of the upper axial blanket. (Orificing based on assembly power and equal peak cladding midwall temperatures.)

Table G.4

PEAK ASSEMBLY COOLANT AND DUCT WALL TEMPERATURES, AND PEAK NOMINAL, AND 2σ CLADDING MIDWALL TEMPERATURES

	Assembly Assignment to Orificing Zones Based on Assembly Power		Assembly Assignment Orificing Zones Based on Pin Power	
Temperatures(^{o}F)	Equal Peak Assembly Coolant Temperatures	Equal Peak Assembly Midwall Temperatures	Equal Peak Assembly Coolant Temperatures	Equal Peak Assembly Midwall Temperatures
Assembly Coolant	977	997	1006	986
Assembly Duct Wall	914	927	934	912
Nominal Cladding Midwall	1127	1065	1105	1061
2σ Cladding Midwall	1251	1191	1239	1187

Table G.5

ASSEMBLY PRESSURE DROPS (PSI)

Orificing Zone	Assembly Assignment to Orficing Zones Based on Assembly Power		Assembly Assignment to Orificing Zones Based on Pin Power	
	Equal Peak Assembly Coolant Temperatures	Equal Peak Cladding Midwall Temperatures	Equal Peak Assembly Coolant Temperatures	Equal Peak Cladding Midwall Temperatures
1	59.0	54.1	49.6	57.2
2	49.9	51.0	46.1	50.2
3	42.4	47.6	36.3	42.6
4	43.8	43.0	54.2	41.0
5	27.0	29.6	32.6	24.4
6	14.3	15.2	23.8	18.4
7	4.7	6.1	12.2	9.3

APPENDIX H

FUEL LIFE ANALYSIS

H.1 INTRODUCTION

A parametric study was conducted to assess the impact of various design and operating parameters on fuel element performance which is characterized collectively by complex phenomena such as plenum pressure histories, pellet-cladding gap closure, fuel-cladding mechanical interaction, and cladding stresses and strains. The design and operating parameters which are varied in the study are pin diameter, residence time, plenum volume, cladding thickness, coolant outlet temperature,and power history. The main objective of the study is to determine the sensitivity of performance parameters, e.g., plenum pressure and cladding stresses, to changes in design and operating parameters, e.g., plenum length or coolant temperature.

In view of the large number of possible combinations of design and operating parameters mentioned above, only a limited parametric study was conducted by restricting their range of values to those closely related to the current designs. The range of values of these parameters is listed below:

pin diameter, in. o.d.	0.26, 0.28
residence time, cycles	2, 3
plenum length, in.	30, 40
cladding thickness, in.	0.013, 0.014, 0.015
coolant outlet temperature, ^{o} F	890, 1000, 1050
power history	either constant flux,ϕ, or constant linear heat rate,kW/ft.

A total of 13 designs were studied and they are characterized in Table H.1.1. For the 0.26 in. o.d. pin, five different designs were investigated to determine the effect of changes in plenum length, cladding temperature,and power history on fuel pin performance. For the 0.28 in. o.d. pin, eight designs were studied and two

Table H.1.1

FUEL PIN DESIGN AND IRRADIATION PARAMETERS

Case	1	2	3	4	5	6	7	8	9	10	11	12	13
Design Parameters													
Cladding O.D., in.	0.26	0.26	0.26	0.26	0.26	0.28	0.28	0.28	0.28	0.28	0.28	0.28	0.28
Cladding Thickness, in.	0.013	0.013	0.013	0.013	0.013	0.014	0.014	0.014	0.014	0.014	0.014	0.015	0.015
Fuel Cladding Diametral Gap, mil.	6.4	6.4	6.4	6.4	6.4	7.0	7.0	7.0	7.0	7.0	7.0	7.0	7.0
Fuel Smeared Density, %	88	88	88	88	88	88	88	88	88	88	88	88	88
Plenum Length, in.	30	30	40	40	40	30	30	30	30	40	40	30	30
Irradiation Parameters													
Peak Power, kW/ft	13.4	13.4	13.4	13.4	13.4	13.4	13.4	13.4	13.4	13.4	13.4	13.4	13.4
Power Depletion with Burnup	no	yes	no	yes	yes	no	yes	yes	yes	yes	yes	no	yes
Peak Fast Fluence $n/cm^2 \times 10^{-23}$	1.48	1.48	1.48	1.48	1.48	1.97	1.97	1.97	1.97	1.97	1.97	1.97	1.97
Peak Cladding Midwall Temp., ^{o}F (^{o}C)	905 (485)	1060 (571)	905 (485)	905 (485)	1060 (571)	907 (486)	907 (486)	1016 (547)	1063 (573)	907 (486)	1063 (573)	909 (487)	1064 (573)
Coolant Outlet Temp., ^{o}F	890	1050	890	890	1050	890	890	1000	1050	890	1050	890	1050

additional variables were considered, i.e., residence time and cladding thickness. The active fuel height is 40 inches for all cases. The smeared fuel density is held at 88% of the theoretical density. In the constant flux assumption, to match as closely as possible the design analysis results, the peak linear heat rate (kW/ft) is reduced by 1.27% per atom percent burnup. The range of peak cladding midwall temperatures (905^{o} to 1064^{o} F) corresponds to three different coolant outlet temperatures: 890, 1000,and 1050^{o} F, which approximately represent the coolant outlet temperatures for an average fuel pin, a higher-than-average fuel pin, and the hottest fuel pin. The coolant inlet temperature is fixed at 595^{o} F.

H.2 METHODOLOGY

The fuel element performance in terms of fission gas release and pressure, gap closure, fuel-cladding mechanical interaction, cladding stress and strain was investigated with the LIFE-III[1] code. The variables in the study are pin diameter, residence time, plenum length, cladding thickness, coolant outlet temperature,and power history.

The fuel element is divided axially into five equal-length fueled sections and one plenum section. The axial sections are divided into seventeen cylindrical shells (twelve cylindrical shells in the fuel and five in the cladding). The thermal and mechanical conditions of the fuel element are calculated incrementally as functions of time. The reactor operating conditions are average over each time step and the behavior of the fuel element is calculated as a function of the reactor operating history.

The thermal calculations are based on the assumption of steady-state conditions for the radial heat flux in the fuel and cladding. The axial temperature distribution in the coolant is calculated from the specified coolant inlet and outlet temperatures and the axial power profile of the element. For every axial section, the radial temperature distribution is calculated from the local coolant temperature, the local linear heat rating, the cladding-coolant heat-transfer coefficient, the cladding thermal conductivity, the fuel-cladding heat-transfer coefficient, and the fuel thermal conductivity. All thermal properties vary with the operating conditions and are recalculated for every time step. The time steps are kept sufficiently short ($\sim$32 hours) so that the thermal restructuring, gas release,and mechanical analyses can be decoupled within the time step. Once the temperature distribution is calculated for a time step, the incremental fuel restructuring and

fission gas release, the thermal expansion of fuel and cladding, and the plenum pressure are calculated.

The mechanical analysis is based on the theory of generalized plane strain and the method of successive elastic solutions. The plenum pressure, the coolant pressure, and the axial loads imposed by the core restraint system provide the boundary conditions. For an open fuel-cladding gap, the radial stress boundary condition at the fuel-cladding interface is the plenum gas pressure. For a closed gap, the fuel cladding interface pressure is calculated under the assumption that the fuel and cladding displacement increments are equal at the interface. The incremental deformation is calculated for every time step. Fuel deformation mechanisms are thermal expansion, elasticity, creep, and irradiation-induced swelling. Fuel-cladding gap closure and total cladding strain are determined by a combination of all the deformation mechanisms.

Detailed descriptions of the analytical models and solutions procedures are given in Reference 1.

H.3 SUMMARY OF PERFORMANCE ANALYSIS

Key performance parameters are given in Section H.4 and are summarized in Table H.3.1. The end-of-life (EOL) fission gas release is in the range of 80 to 90% of total produced. The EOL plenum pressure varies from 530 to 1074 psia. The pellet-cladding gap closure occurs at or before 200 hours after startup for all cases considered. The gap will re-open at a time ranging from 8,000 to 13,000 hours, except for the designs with low fluences and cladding temperatures whose gaps remain closed throughout their life.

Regarding the cladding deformation, the results of this study indicate the following trends:

1. There is an incubation period for both the cladding diametral change and inelastic strain histories. For example, for the 0.26 in. o.d. pin designs with 1050^{0} F coolant outlet temperature (Case 5), the maximum diametral cladding change increases slowly from about 0.95% at 50 hours to approximately 1.25% at 6,000 hours, but then increases more rapidly to the 3.7% range at 12,000 hours. In a similar fashion, the inelastic strain increases slowly from a zero value to approximately 0.25% at 6,000 hours, and then accelarates to the range of about 1% at 12,000 hours.

Table H.3.1

SUMMARY OF FUEL PERFORMANCE

CASE	1	2	3	4	5	6	7	8	9	10	11	12	13
EOL Fission Gas Release, % of Total	84.4	87.1	83.7	79.5	85.6	89.4	83.7	89.5	90.2	83.1	90.0	89.7	90.4
EOL Plenum Pressure, Mpa (psia)	5.44 (789)	5.67 (823)	4.09 (594)	3.65 (530)	4.28 (621)	7.26 (1053)	6.28 (911)	6.96 (1010)	7.11 (1031)	4.67 (678)	5.41 (784)	7.41 (1074)	7.23 (1049)
Gap Reopening	yes	yes	no	no	yes	yes	yes	yes	yes	yes	yes	yes	yes
EOL Radial Gap Size at Peak Cladding Deformation, mm (mil)	0.001 (0.04)	0.038 (1.49	0 (0)	0 (0)	0.026 (1.02)	0.022 (0.85)	0.009 (0.36)	0.068 (2.67)	0.091 (3.58)	0.001 (0.03)	0.073 (2.86)	0.022 (0.87)	0.089 (3.50)
EOL Cladding Logitudinal Change, $\%\frac{\Delta \ell}{\ell}$	0.97	1.33	0.96	0.91	1.28	1.17	1.08	1.51	1.72	1.05	1.62	1.18	1.72
Max. Total Cladding Diametral Deformation, $\%\frac{\Delta D}{D}$	2.19	3.84	2.17	1.96	3.66	3.26	2.75	4.86	6.16	2.67	5.73	3.24	6.07
Max. Cladding Inelastic Strain, $\%\frac{\Delta D}{D}$	0.56	1.11	0.53	0.49	0.94	0.90	0.73	1.38	1.96	0.65	1.56	0.85	1.86

2. For the design and operating conditions considered, increasing the cladding thickness by 1 mil does not significantly reduce inelastic strain. For example, increasing the cladding thickness from 14 to 15 mils reduces the peak cladding inelastic strains from 1.96 to 1.86% for the 0.28 in. o.d. pins with 1050^{o} F coolant outlet temperature (Cases 9 and 13), or from 0.90 to 0.85% for the 0.28 in o.d. pin with 890^{o} F coolant outlet temperature (Cases 6 and 12).

3. Increasing the plenum length, as a means to reduce inelastic strain, is only effective for the designs with high fluences and cladding temperatures. For example, for a 890^{o} F coolant outlet temperature, increasing the plenum length from 30 to 40 inches has very little impact on the inelastic strain for both the 0.26 and 0.28 in. o.d. pins (Cases 1 and 3; Cases 7 and 10). However, when the coolant outlet temperature is raised to 1050^{o} F, increasing the plenum length from 30 to 40 inches reduces the inelastic strain by 25% from 1.96 to 1.56% (Cases 9 and 11).

4. Lowering the coolant outlet temperature has a large impact on reducing inelastic strain for the designs with high fluences and cladding temperatures. For example, decreasing the coolant outlet temperature by 50^{o} F, from 1050 to 1000^{o} F, achieves a 30% reduction in inelastic strain (from 1.96 to 1.38%) for the 0.28 in. o.d. pin (Cases 9 and 8). To achieve another 30% a further reduction in coolant temperature decrease in inelastic strain temperature change is required. This reduction is two times larger than the previous temperature change of 50^{o} F. This shows there is a regime of diminishing returns (Cases 8 and 7).

5. Using a 6% total diametral change or a 2% inelastic strain as a tentative fuel failure criterion, the designs analyzed will not fail. The 6% total diametral change is based primarily on the irradiation tests in RAPSODIE[2] Fortissimo core fuel elements. In the absence of other irradiation data, which give such a large cladding deformation (>6%), this 6% limit was used. Furthermore, extensive analytical calculations[3] for pins in the EBR-II and FFTF environment give end-of-life values for the maximum cladding diametral changes and inelastic strains in the range of 7% and 2%, respectively,

In summary, for the design and operating conditions considered, small changes in cladding thickness do not significantly reduce cladding inelastic strain. Cladding temperature and plenum volume play a key role in determining cladding

inelastic strain for the designs with high fluences. With a 6% total diametral change or a 2% inelastic strain as tentative fuel failure criteria, the designs will not fail.

H.4 TABULATION OF TIME-DEPENDENT PARAMETERS

The changes, with respect to time, of the parameters listed below, for the 13 designs analyzed are given in the following pages:

Plenum pressure
Plenum gas composition
Fission gas release
Cladding longitudinal change
Fuel center-line temperature
Cladding i.d/o.d. temperature
Gap size
Total cladding diametral change
Burnup
Linear heat rating

CASE 1

0.26" o.d. pin, 13 mil clad, constant kW/ft, 30" plenum, 890 ^{o}F coolant outlet

Time, hours	Plenum Pressure psi	Gas Comp. % Fission Gas	Fission Gas Release % of total	Clad $(1+\frac{\Delta \ell}{\ell})$
50	39.2	0.6	12.9	1.0077
1522	109.8	63.6	64.4	1.0077
2050	138.9	71.2	67.5	1.0077
2978	192.2	79.2	71.0	1.0077
4457	281.6	85.8	74.9	1.0078
5929	372.9	89.2	77.2	1.0078
8850	563.3	92.9	80.7	1.0085
12050	788.6	94.9	84.4	1.0097
12074	290.6	94.9	84.2	1.0019

CASE 1

0.26" o.d. pin, 13 mil clad, constant kW/ft, 30" plenum, 890 °F coolant outlet

Axial location, inches above bottom of active fuel

Time, hours	4	12	20	28	36	55
			Fuel center-line temp., °F			
50	3225	4305	4526	4394	3503	
1522	2444	3032	3216	3129	2706	
2050	2365	2978	3162	3077	2673	
2978	2273	2935	3123	3037	2646	
4457	2209	2884	3080	2991	2613	
5929	2163	2838	3047	2949	2578	
8850	2149	2845	3076	2961	2572	
12050	2161	2872	3101	2991	2614	
12074	70	70	70	70	70	
			Clad i.d./o.d. temp., °F			
50	682/639	763/703	838/774	897/840	925/886	886/886
1522	681/638	762/702	837/774	896/840	924/886	886/886
2050	681/638	762/702	837/774	896/839	924/885	886/886
2978	681/638	762/702	837/774	896/839	924/885	886/886
4457	681/638	762/702	837/774	896/839	924/885	886/886
5929	681/638	762/702	837/774	896/839	925/886	886/886
8850	681/638	762/702	837/774	896/840	925/886	886/886
12050	681/638	762/703	837/774	895/840	925/886	886/886
12074	70/70	70/70	70/70	70/70	70/70	70/70

CASE 1

0.26" o.d. pin, 13 mil clad, constant kW/ft, 30" plenum, 890 ^{o}F coolant outlet

Axial location, inches above bottom of active fuel

Time, hours	4	12	20	28	36	55
			Gap size, mils			
50	2.028	0.810	0.420	0.766	2.026	
1522	0.171	0	0	0	0	
2050	0.111	0	0	0	0	
2978	0.013	0	0	0	0	
4457	0	0	0	0	0	
5929	0	0	0	0	0	
8850	0	0	0	0	0	
12050	0	0	0	0.041	0.043	
12074	2.179	2.160	2.040	2.320	2.733	
			Total clad o.d. change, % $\Delta D/D$			
50	0.587	0.665	0.744	0.813	0.855	0.834
1522	0.589	0.697	0.795	0.853	0.865	0.836
2050	0.591	0.708	0.810	0.866	0.871	0.837
2978	0.595	0.732	0.839	0.891	0.884	0.839
4457	0.623	0.776	0.891	0.933	0.906	0.842
5929	0.655	0.837	0.970	0.984	0.931	0.846
8850	0.743	1.006	1.340	1.437	0.993	0.854
12050	0.862	1.208	1.786	2.196	1.313	0.865
12074	0.222	0.507	1.014	1.358	0.441	0.017

CASE 1

0.26" o.d. pin, 13 mil clad, constant kW/ft, 30" plenum, 890 ^{o}F coolant outlet

Axial location, inches above bottom of active fuel

Time, hours	4	12	20	28	36
		Burnup, atom %			
50	0.014	0.019	0.021	0.019	0.014
1522	0.792	1.136	1.247	1.136	0.792
2050	1.071	1.535	1.686	1.535	1.071
2978	1.561	2.238	2.458	2.238	1.561
4457	2.343	3.358	3.688	3.358	2.343
5929	3.120	4.472	4.911	4.472	3.120
8850	4.663	6.684	7.341	6.684	4.663
12050	6.353	9.106	10.002	9.106	6.353
12074	6.359	9.115	10.012	9.115	6.359
		kW/ft			
50	8.40	11.92	13.04	11.91	8.38
1522	8.28	11.84	12.99	11.82	8.24
2050	8.28	11.83	12.98	11.82	8.24
2978	8.28	11.83	12.98	11.82	8.24
4457	8.28	11.83	12.98	11.82	8.24
5929	8.28	11.83	12.98	11.81	8.24
8850	8.28	11.82	12.95	11.78	8.24
12050	8.27	11.81	12.92	11.72	8.22
12074	0	0	0	0	0

CASE 2

0.26" o.d. pin, 13 mil clad, constant ϕ, 30" plenum, 1050 ^{o}F coolant outlet

Time, hours	Plenum Pressure psi	Gas Comp. % Fission Gas	Fission Gas Release % of Total	Clad $(1+\frac{\Delta \ell}{\ell})$
50	40.7	0.7	14.9	1.0091
1513	125.1	64.6	68.1	1.0091
2050	159.1	72.1	71.2	1.0091
4536	322.1	86.2	78.1	1.0091
6050	421.6	89.5	79.9	1.0091
8050	549.3	92.0	81.6	1.0099
12050	822.8	94.8	87.1	1.0133
12074	277.2	94.8	86.9	1.0045

CASE 2

0.26" o.d. pin, 13 mil clad, constant ϕ, 30" plenum, 1050 ^{o}F coolant outlet

Axial location, inches above bottom of active fuel

Time, hours	4	12	20	28	36	55
			Fuel center-line temp., ^{o}F			
50	3238	4332	4558	4460	3663	
1513	2445	3034	3241	3183	2872	
2050	2360	2968	3176	3123	2830	
4536	2170	2821	3034	2985	2731	
6050	2106	2742	2965	2913	2675	
8050	2064	2693	2925	2887	2620	
12050	2023	2641	3011	3321	2996	
12074	70	70	70	70	70	
			Clad i.d./o.d. temp., ^{o}F			
50	697/654	810/751	923/861	1020/966	1079/1042	1050/1050
1513	696/654	808/750	921/861	1018/965	1077/1041	1050/1050
2050	696/654	807/750	920/860	1017/964	1076/1040	1049/1049
4536	694/653	804/748	916/857	1011/960	1071/1036	1045/1045
6050	694/653	802/747	913/855	1008/958	1068/1033	1042/1042
8050	692/651	797/743	903/847	995/945	1052/1018	1026/1026
12050	690/651	793/741	896/843	986/940	1044/1010	1018/1018
12074	70/70	70/70	70/70	70/70	70/70	70/70

CASE 2

0.26" o.d. pin, 13 mil clad, constant ϕ, 30" plenum, 1050 ^{o}F coolant outlet

Axial location, inches above bottom of active fuel

Time, hours	4	12	20	28	36	55
			Gap size, mils			
50	2.034	0.812	0.434	0.765	2.015	
1513	0.178	0	0	0	0	
2050	0.120	0	0	0	0	
4536	0	0	0	0	0	
6050	0	0	0	0	0	
8050	0	0	0	0.063	0	
12050	0	0	0.292	1.491	1.412	
12074	2.198	2.255	2.574	3.011	3.458	
			Total clad o.d. change, % ΔD/D			
50	0.604	0.717	0.840	0.954	1.032	1.020
1513	0.607	0.749	0.894	1.014	1.051	1.023
2050	0.609	0.760	0.909	1.043	1.065	1.025
4536	0.640	0.824	0.986	1.201	1.166	1.034
6050	0.671	0.888	1.055	1.320	1.238	1.043
8050	0.726	1.039	1.461	1.875	1.342	1.043
12050	0.871	1.382	2.535	3.843	2.605	1.071
12074	0.218	0.647	1.691	2.881	1.581	0.071

CASE 2

0.26" o.d. pin, 13 mil clad, constant ϕ, 30" plenum, 1050 ^{o}F coolant outlet

	Axial location, inches above bottom of active fuel				
Time, hours	4	12	20	28	36
	Burnup, atom %				
50	0.014	0.019	0.021	0.019	0.014
1513	0.784	1.122	1.231	1.122	0.784
2050	1.064	1.521	1.669	1.521	1.064
4536	2.349	3.346	3.667	3.346	2.349
6050	3.121	4.435	4.858	4.435	3.121
8050	4.129	5.851	6.402	5.851	4.129
12050	6.105	8.601	9.395	8.601	6.105
12074	6.110	8.609	9.403	8.609	6.110
	kW/ft				
50	8.40	11.92	13.03	11.89	8.37
1513	8.20	11.67	12.78	11.65	8.15
2050	8.17	11.60	12.70	11.58	8.11
4536	8.03	11.32	12.37	11.30	7.98
6050	7.95	11.16	12.17	11.13	7.89
8050	7.84	10.94	11.88	10.88	7.79
12050	7.63	10.51	11.30	10.40	7.56
12075	0	0	0	0	0

CASE 3

0.26" o.d. pin, 13 mil clad, constant ϕ, 40" plenum, 890 ^{o}F coolant outlet

Time, hours	Plenum Pressure psi	Gas Comp. % Fission Gas	Fission Gas Release % of total	Clad $(1+\Delta\ell/\ell)$
50	39.2	0.4	12.9	1.0078
1514	90.5	56.1	63.1	1.0078
2050	112.2	64.6	66.2	1.0078
2978	150.9	73.6	69.5	1.0078
4440	215.2	81.5	73.2	1.0078
6050	289.3	86.2	76.0	1.0079
8850	425.3	90.6	79.7	1.0085
12050	593.5	93.3	83.7	1.0096
12074	223.7	93.3	83.4	1.0018

CASE 3

0.26" o.d. pin, 13 mil clad, constant ϕ, 40" plenum, 890 ^{o}F coolant outlet

Axial location, inches above bottom of active fuel

Time, hours	4	12	20	28	36	60
			Fuel center line temp., ^{o}F			
50	3224	4304	4525	4393	3502	
1514	2421	3002	3186	3106	2682	
2050	2342	2949	3133	3054	2649	
2978	2239	2888	3077	2998	2610	
4440	2174	2859	3055	2972	2589	
6050	2134	2824	3031	2940	2561	
8850	2128	2844	3073	2963	2560	
12050	2144	2881	3112	2984	2592	
12074	70	70	70	70	70	
			Clad i.d./o.d. temp., ^{o}F			
50	682/639	763/703	838/774	897/840	925/886	886/886
1514	681/638	762/702	837/774	896/840	924/886	886/886
2050	681/638	762/702	837/774	896/839	924/885	886/886
2978	681/638	762/702	837/774	896/839	924/885	886/886
4440	681/638	762/702	837/774	896/839	924/885	886/886
6050	681/638	762/702	837/774	896/839	924/886	886/886
8850	681/638	762/702	837/774	896/840	924/886	886/886
12050	681/638	762/703	837/775	896/840	924/886	886/886
12074	70/70	70/70	70/70	70/70	70/70	70/70

CASE 3

0.26" o.d. pin, 13 mil clad, constant ϕ, 40" plenum, 890 ^{o}F coolant outlet

Time, hours	Axial location, inches above bottom of active fuel					
	4	12	20	28	36	60
	Gap size, mils					
50	2.029	0.812	0.422	0.768	2.027	
1514	0.230	0	0	0	0	
2050	0.153	0	0	0	0	
2978	0.055	0	0	0	0	
4440	0	0	0	0	0	
6050	0	0	0	0	0	
8850	0	0	0	0	0	
12050	0	0	0	0	0	
12074	2.125	2.224	2.104	2.360	2.179	
	Total clad o.d. change, % $\Delta D/D$					
50	0.587	0.665	0.744	0.855	0.855	0.834
1514	0.589	0.694	0.793	0.851	0.865	0.836
2050	0.590	0.706	0.808	0.864	0.871	0.836
2978	0.593	0.728	0.835	0.887	0.883	0.837
4440	0.618	0.771	0.886	0.929	0.906	0.840
6050	0.654	0.839	0.980	0.984	0.934	0.843
8850	0.744	0.999	1.334	1.424	0.996	0.849
12050	0.867	1.196	1.767	2.167	1.307	0.857
12074	0.223	0.495	0.995	1.331	0.437	0.013

CASE 3

0.26" o.d. pin, 13 mil clad, constant ϕ, 40" plenum, 890 ^{o}F coolant outlet

Axial location, inches above bottom of active fuel

Time, hours	4	12	20	28	36
			Burnup, atom %		
50	0.014	0.019	0.021	0.019	0.014
1514	0.788	1.130	1.241	1.130	0.788
2050	1.071	1.535	1.686	1.535	1.071
2978	1.561	2.238	2.458	2.238	1.561
4440	2.334	3.345	3.674	3.345	2.334
6050	3.184	4.564	5.013	4.564	3.184
8850	4.663	6.684	7.341	6.684	4.663
12050	6.353	9.106	10.002	9.106	6.353
12074	6.359	9.115	10.012	9.115	6.359
			kW/ft		
50	8.40	11.92	13.04	11.91	8.38
1514	8.29	11.84	12.99	11.82	8.24
2050	8.28	11.83	12.98	11.82	8.24
2978	8.28	11.83	12.98	11.82	8.24
4440	8.28	11.83	12.98	11.82	8.24
6050	8.28	11.83	12.98	11.81	8.24
8850	8.28	11.82	12.95	11.78	8.24
12050	8.28	11.81	12.92	11.72	8.22
12074	0	0	0	0	0

CASE 4

0.26" o.d. pin, 13 mil clad, constant ϕ, 40" plenum, 890 ^{o}F coolant outlet

Time, hours	Plenum Pressure psi	Gas Comp. % Fission Gas	Fission Gas Release % of total	Clad $(1+\Delta \ell/\ell)$
50	39.2	0.4	12.9	1.0078
1522	89.9	55.8	62.6	1.0078
2050	110.7	64.1	65.4	1.0078
3010	148.9	73.3	68.6	1.0078
4521	210.9	81.2	71.8	1.0078
6050	274.8	85.5	73.9	1.0079
9234	407.3	90.3	77.0	1.0084
12050	529.9	92.6	79.5	1.0091
12074	202.9	92.6	79.3	1.0015

CASE 4

0.26" o.d. pin, 13 mil clad, constant ϕ, 40" plenum, 890 ^{o}F coolant outlet

Axial location, inches above bottom of active fuel

Time, hours	4	12	20	28	36	60
			Fuel center-line temp., ^{o}F			
50	3224	4304	4525	4392	3501	
1522	2404	2968	3148	3074	2661	
2050	2320	2904	3083	3012	2621	
3010	2205	2821	3000	2934	2567	
4521	2114	2757	2940	2874	2522	
6050	2058	2691	2878	2812	2474	
9234	2001	2624	2819	2755	2407	
12050	1974	2595	2788	2726	2391	
12074	70	70	70	70	70	
			Clad i.d./o.d. temp., ^{o}F			
50	682/639	763/703	838/774	897/840	925/886	886/886
1522	680/638	760/702	836/773	895/839	923/885	886/886
2050	680/638	760/702	835/773	894/839	923/885	886/886
3010	680/638	760/702	834/772	893/838	922/884	885/885
4521	680/638	758/701	832/771	890/836	920/882	883/883
6050	679/638	765/700	829/770	887/834	918/880	881/881
9234	677/637	751/697	820/763	876/824	905/869	870/870
12050	676/636	748/696	816/760	871/822	901/865	866/866
12074	70/70	70/70	70/70	70/70	70/70	70/70

CASE 4

0.26" o.d. pin, 13 mil clad, constant ϕ, 40" plenum, 890 ^{o}F coolant outlet

Time, hours	Axial location, inches above bottom of active fuel					
	4	12	20	28	36	60
	Gap size, mils					
50	2.030	0.813	0.423	0.769	2.028	
1522	0.239	0	0	0	0	
2050	0.166	0	0	0	0	
3010	0.068	0	0	0	0	
4521	0	0	0	0	0	
6050	0	0	0	0	0	
9234	0	0	0	0	0	
12050	0	0	0	0	0	
12074	1.991	2.324	2.288	2.517	2.681	
	Total clad o.d. change, % $\Delta D/D$					
50	0.587	0.665	0.774	0.813	0.855	0.834
1522	0.589	0.693	0.791	0.849	0.864	0.835
2050	0.590	0.704	0.805	0.862	0.869	0.836
3010	0.593	0.725	0.831	0.883	0.881	0.836
4521	0.615	0.768	0.879	0.922	0.903	0.836
6050	0.648	0.830	0.971	0.971	0.927	0.837
9234	0.748	0.996	1.328	1.425	0.988	0.829
12050	0.862	1.155	1.638	1.960	1.257	0.832
12074	0.219	0.464	0.885	1.147	0.409	0.012

CASE 4

0.26" o.d. pin, 13 mil clad, constant ϕ, 40" plenum, 890 ^{o}F coolant outlet

Time, hours	Axial location, inches above bottom of active fuel				
	4	12	20	28	36
	Burnup, atom %				
50	0.014	0.019	0.021	0.019	0.014
1522	0.789	1.128	1.238	1.128	0.789
2050	1.064	1.521	1.669	1.521	1.064
3010	1.563	2.231	2.447	2.231	1.563
4521	2.341	3.334	3.655	3.334	2.341
6050	3.121	4.435	4.857	4.435	3.121
9234	4.719	6.675	7.300	6.675	4.719
12050	6.104	8.600	9.394	8.600	6.104
12074	6.110	8.608	9.402	8.608	6.110
	kW/ft				
50	8.40	11.92	13.04	11.90	8.38
1522	8.21	11.67	12.79	11.66	8.16
2050	8.17	11.60	12.71	11.59	8.13
3010	8.12	11.50	12.58	11.48	8.08
4521	8.04	11.33	12.38	11.32	8.00
6050	7.95	11.16	12.18	11.15	7.91
9234	7.78	10.82	11.75	10.78	7.74
12050	7.64	10.52	11.39	10.46	7.59
12074	0	0	0	0	0

CASE 5

0.26" o.d. pin, 13 mil clad, constant ϕ, 40" plenum, 1050 ^{o}F coolant outlet

Time, hours	Plenum Pressure psi	Gas Comp. % Fission Gas	Fission Gas Release % of Total	Clad $(1+\frac{\Delta \ell}{\ell})$
50	43.7	0.5	14.9	1.0092
1519	103.7	57.4	66.9	1.0092
4521	246.8	82.1	76.5	1.0092
6082	323.4	86.4	78.8	1.0093
8050	417.0	89.5	80.7	1.0099
10829	557.1	92.3	83.9	1.0119
12050	620.7	93.1	85.6	1.0128
12074	212.9	93.1	85.3	1.0039

CASE 5

0.26" o.d. pin, 13 mil clad, constant ϕ, 40" plenum, 1050 ^{o}F coolant outlet

Time, hours	Axial location, inches above bottom of active fuel					
	4	12	20	28	36	60
	Fuel center-line temp., ^{o}F					
50	3237	4331	4557	4459	3662	
1519	2418	3003	3211	3160	2853	
4521	2138	2800	3013	2971	2717	
6082	2081	2732	2953	2908	2668	
8050	2043	2689	2920	2867	2616	
10829	2018	2664	2892	3064	2707	
12050	2007	2649	2896	3186	2838	
12074	70	70	70	70	70	
	Clad i.d./o.d. temp., ^{o}F					
50	697/654	810/751	923/861	1020/966	1079/1042	1050/1050
1519	696/654	808/750	921/861	1018/965	1077/1041	1049/1049
4521	695/653	804/748	916/857	1011/960	1071/1036	1045/1045
6082	694/653	802/747	913/855	1008/957	1068/1033	1042/1042
8050	692/651	797/743	903/847	995/945	1052/1018	1026/1026
10829	691/651	794/742	898/844	989/941	1046/1012	1021/1021
12050	690/651	793/741	896/843	986/940	1044/1010	1018/1018
12074	70/70	70/70	70/70	70/70	70/70	70/70

CASE 5

0.26" o.d. pin, 13 mil clad, constant ϕ, 40" plenum, 1050 ^{o}F coolant outlet

Axial location, inches above bottom of active fuel

Time, hours	4	12	20	28	36	60
			Gap size, mils			
50	2.035	0.815	0.436	0.767	2.016	
1519	0.235	0	0	0	0	
4521	0	0	0	0	0	
6082	0	0	0	0	0	
8050	0	0	0	0.003	0	
10829	0	0	0	0.569	0.348	
12050	0	0	0.055	1.023	0.808	
12074	2.071	2.342	2.634	3.207	3.578	
			Total clad O.D. change, % $\Delta D/D$			
50	0.604	0.716	0.840	0.953	1.031	1.020
1519	0.606	0.747	0.892	2.012	1.050	1.022
4521	0.634	0.820	0.987	1.192	1.165	1.028
6082	0.668	0.885	1.055	1.311	1.240	1.033
8050	0.724	1.033	1.453	1.846	1.343	1.027
10829	0.826	1.267	2.157	3.087	1.996	1.039
12050	0.876	1.370	2.466	3.661	2.472	1.045
12074	0.219	0.634	1.627	2.705	1.453	0.049

CASE 5

0.26" o.d. pin, 13 mil clad, constant ϕ, 40" plenum, 1050 ^{o}F coolant outlet

Axial locations, inches above bottom of active fuel

Time, hours	4	12	20	28	36	60
			Burnup, atom %			
50	0.014	0.019	0.021	0.019	0.014	
1519	0.787	1.126	1.236	1.126	0.787	
4521	2.342	3.335	3.655	3.335	2.342	
6082	3.137	4.458	4.883	4.458	3.137	
8050	4.129	5.850	6.402	5.850	4.129	
10829	5.507	7.772	8.494	7.772	5.507	
12050	6.104	8.601	9.394	8.601	6.104	
12074	6.110	8.609	9.403	8.609	6.110	
			kW/ft			
50	8.40	11.92	13.03	11.89	8.37	
1519	8.21	11.67	12.78	11.65	8.15	
4521	8.03	11.33	12.37	11.30	7.98	
6082	7.95	11.15	12.16	11.13	7.89	
8050	7.84	10.93	11.88	10.88	7.79	
10829	7.70	10.64	11.48	10.51	7.62	
12050	7.63	10.51	11.30	10.37	7.54	
12074	0	0	0	0	0	

CASE 6

0.28" o.d. pin, 14 mil clad, constant kW/ft, 30" plenum, 890 ^{o}F coolant outlet

Time, hours	Plenum Pressure psi	Gas Comp. % Fission Gas	Fission Gas Release % of Total	Clad $(1+\Delta\ell/\ell)$
50	38.9	0.4	10.8	1.0077
5147	280.3	85.7	74.8	1.0078
8050	436.0	90.8	78.3	1.0080
13050	731.8	94.5	83.8	1.0095
15354	876.8	95.4	86.2	1.0105
17052	987.7	95.9	88.2	1.0113
18050	1052.8	96.2	89.4	1.0117
18074	388.5	96.2	89.3	1.0039

CASE 6

0.28" o.d. pin, 14 mil clad, constant kW/ft, 30" plenum, 890 °F coolant outlet

Time, hours	Axial location, inches above bottom of active fuel					
	4	12	20	28	36	55
	Fuel center-line temp., °F					
50	3185	4284	4533	4383	3467	
5147	2186	2866	3057	2974	2598	
8050	2133	2820	3029	2932	2562	
13050	2149	2860	3079	2972	2597	
15354	2156	2868	3079	3105	2763	
17052	2162	2870	3071	3243	2974	
18050	2165	2869	3085	3320	3115	
18074	70	70	70	70	70	
	Clad i.d./o.d. temp., °F					
50	684/640	765/705	840/777	899/842	927/888	886/886
5147	682/639	764/705	840/776	898/842	926/887	886/886
8050	682/640	764/705	840/777	898/842	926/887	886/886
13050	682/640	764/705	840/778	898/843	926/887	886/886
15354	682/640	764/705	840/778	899/844	926/888	886/886
17052	682/640	764/706	840/778	899/844	926/888	886/886
18050	682/640	764/706	840/778	899/845	926/888	886/886
18074	70/70	70/70	70/70	70/70	70/70	70/70

CASE 6

0.28" o.d. pin, 14 mil clad, constant kW/ft, 30" plenum, 890 ^{o}F coolant outlet

Time, hours	Axial location, inches above bottom of active fuel					
	4	12	20	28	36	55
	Gap size, mils					
50	2.299	1.109	0.699	1.043	2.322	
5147	0	0	0	0	0	
8050	0	0	0	0	0	
13050	0	0	0	0.032	0.027	
15354	0	0	0	0.297	0.390	
17052	0	0	0.004	0.626	0.970	
18050	0	0	0.037	0.853	1.500	
18074	2.439	2.240	2.206	2.736	3.721	
	Total clad o.d. change, % $\Delta D/D$					
50	0.589	0.667	0.747	0.816	0.857	0.834
5147	0.615	0.769	0.886	0.927	0.903	0.842
8050	0.671	0.888	1.101	1.064	0.946	0.849
13050	0.817	1.155	1.719	2.075	1.207	0.862
15354	0.894	1.286	2.013	2.597	1.659	0.869
17052	0.952	1.386	2.235	3.007	2.035	0.875
18050	0.987	1.445	2.372	3.258	2.265	0.878
18074	0.343	0.742	1.591	2.400	1.376	0.025

CASE 6

0.28" o.d. pin, 14 mil clad, constant kW/ft, 30" plenum, 890 ^{o}F coolant outlet

	Axial location, inches above bottom of active fuel				
Time, hours	4	12	20	28	36
	Burnup, atom %				
50	0.012	0.017	0.018	0.017	0.012
5147	2.337	3.350	3.679	3.350	2.337
8050	3.660	5.246	5.762	5.246	3.660
13050	5.939	8.513	9.351	8.513	5.939
15354	6.989	10.019	11.004	10.019	6.989
17052	7.764	11.128	12.223	11.128	7.764
18050	8.218	11.780	12.939	11.780	8.218
18074	8.224	11.788	12.947	11.788	8.224
	kW/ft				
50	8.40	11.94	13.07	11.92	8.38
5147	8.28	11.83	12.98	11.81	8.23
8050	8.28	11.83	12.97	11.80	8.23
13050	8.27	11.81	12.92	11.72	8.22
15354	8.27	11.81	12.90	11.68	8.19
17052	8.27	11.81	12.88	11.66	8.18
18050	8.27	11.80	12.87	11.67	8.19
18074	0	0	0	0	0

CASE 7

0.28" o.d. pin, 14 mil clad, constant ϕ, 30" plenum, 890 ^{o}F coolant outlet

Time, hours	Plenum Pressure psi	Gas Comp. % Fission Gas	Fission Gas Release % of Total	Clad $(1+\Delta\ell/\ell)$
50	38.9	0.4	10.7	1.0077
5250	275.5	85.5	73.5	1.0078
8050	410.3	90.3	76.0	1.0079
12530	634.1	93.7	79.8	1.0090
14435	729.2	94.6	81.1	1.0096
16355	825.3	95.2	82.4	1.0103
18050	911.2	95.7	83.7	1.0108
18074	341.7	95.7	83.5	1.0033

CASE 7

0.28" o.d. pin, 14 mil clad, constant ϕ, 30" plenum, 890 ^{o}F coolant outlet

Time, hours	Axial location, inches above bottom of active fuel					
	4	12	20	28	36	55
	Fuel center-line temp., ^{o}F					
50	3185	4283	4533	4383	3467	
5250	2126	2765	2942	2876	2531	
8050	2038	2656	2841	2777	2454	
12530	1996	2606	2789	2732	2409	
14435	1979	2581	2759	2704	2412	
16355	1962	2552	2722	2733	2462	
18050	1946	2525	2686	2809	2540	
18074	70	70	70	70	70	
	Clad i.d./o.d. temp., ^{o}F					
50	684/640	765/705	840/777	899/842	927/888	886/886
5250	681/639	760/703	834/774	892/838	921/884	883/883
8050	680/639	757/702	830/771	887/835	917/880	879/879
12530	678/638	752/699	822/766	878/827	906/871	869/869
14435	677/638	750/697	818/763	873/824	902/866	866/866
16355	676/637	748/696	815/761	869/821	898/863	862/862
18050	675/636	746/695	812/759	865/818	894/860	858/858
18074	70/70	70/70	70/70	70/70	70/70	70/70

CASE 7

0.28" o.d. pin, 14 mil clad, constant ϕ, 30" plenum, 890 ^{o}F coolant outlet

Time, hours	Axial location, inches above bottom of active fuel					
	4	12	20	28	36	55
	Gap size, mils					
50	2.300	1.109	0.700	1.044	2.322	
5250	0	0	0	0	0	
8050	0	0	0	0	0	
12530	0	0	0	0	0	
14435	0	0	0	0.009	0.036	
16355	0	0	0	0.132	0.195	
18050	0	0	0	0.357	0.438	
18074	2.394	2.455	2.470	3.086	3.516	
	Total clad o.d. change, % $\Delta D/D$					
50	0.589	0.667	0.747	0.816	0.857	0.834
5250	0.612	0.766	0.879	0.919	0.899	0.839
8050	0.663	0.874	1.085	1.044	0.936	0.841
12530	0.793	1.089	1.558	1.806	1.103	0.840
14435	0.858	1.184	1.748	2.128	1.368	0.840
16355	0.928	1.280	1.933	2.456	1.683	0.840
18050	0.993	1.365	2.093	2.747	1.964	0.842
18074	0.348	0.677	1.343	1.932	1.116	0.022

CASE 7

0.28" o.d. pin, 14 mil clad, constant ϕ, 30" plenum, 890 ^{o}F coolant outlet

	Axial location, inches above bottom of active fuel				
Time, hours	4	12	20	28	36
	Burnup, atom %				
50	0.012	0.017	0.018	0.017	0.012
5250	2.349	3.345	3.666	3.345	2.349
8050	3.577	5.077	5.558	5.077	3.577
12530	5.501	7.764	8.486	7.764	5.501
14435	6.304	8.878	9.695	8.878	6.304
16355	7.105	9.982	10.893	9.982	7.105
18050	7.805	10.942	11.933	10.942	7.805
18074	7.810	10.949	11.940	10.949	7.810
	kW/ft				
50	8.40	11.94	13.07	11.92	8.38
5250	8.03	11.33	12.38	11.81	7.99
8050	7.90	11.06	12.05	11.04	7.86
12530	7.70	10.65	11.54	10.58	7.65
14435	7.62	10.49	11.34	10.40	7.55
16355	7.53	10.32	11.12	10.20	7.45
18050	7.45	10.17	10.94	10.04	7.36
18074	0	0	0	0	0

CASE 8

0.28" o.d. pin, 14 mil clad, constant ϕ, 30" plenum, 1000 ^{o}F coolant outlet

Time, hours	Plenum Pressure psi	Gas Comp. % Fission Gas	Fission Gas Release % of Total	Clad $(1+\frac{\Delta \ell}{\ell})$
50	42.0	0.5	11.9	1.0086
1763	120.9	64.4	67.1	1.0086
5238	306.9	86.0	76.7	1.0086
8050	459.1	90.6	79.5	1.0089
13050	739.5	94.3	84.5	1.0117
16346	924.0	95.5	88.4	1.0139
18050	1009.6	96.0	89.5	1.0151
18074	355.2	96.0	89.6	1.0067

CASE 8

0.28" o.d. pin, 14 mil clad, constant ϕ, 30" plenum, 1000 ^{o}F coolant outlet

Time, hours	Axial location, inches above bottom of active fuel					
	4	12	20	28	36	55
	Fuel center-line temp., ^{o}F					
50	3195	4305	4560	4435	3580	
1763	2446	3003	3199	3141	2805	
5238	2142	2793	2991	2943	2673	
8050	2061	2694	2903	2851	2601	
13050	2014	2634	2871	3097	2732	
16346	1985	2584	3033	3363	3145	
18050	1969	2554	3142	3426	3266	
18074	70	70	70	70	70	
	Clad i.d./o.d. temp., ^{o}F					
50	695/651	798/739	900/838	985/930	1034/997	1000/1000
1763	693/651	796/738	898/837	983/830	1032/996	1000/1000
5238	692/650	793/737	893/834	977/925	1027/991	995/995
8050	691/650	790/735	889/831	972/921	1022/986	991/991
13050	688/648	783/731	878/823	958/910	1006/972	976/976
16346	686/648	779/728	870/818	950/903	997/963	966/966
18050	685/647	776/726	867/815	946/900	992/959	961/961
18074	70/70	70/70	70/70	70/70	70/70	70/70

CASE 8

0.28" o.d. pin, 14 mil clad, constant ϕ, 30" plenum, 1000 ^{o}F coolant outlet

Time, hours	Axial location, inches above bottom of active fuel					
	4	12	20	28	36	55
	Gap size, mils					
50	2.303	1.108	0.703	1.033	2.334	
1763	0.269	0	0	0	0	
5238	0	0	0	0	0	
8050	0	0	0	0	0	
13050	0	0	0.069	0.773	0.564	
16346	0	0	0.535	2.065	2.517	
18050	0	0	0.915	2.671	3.663	
18074	2.403	2.411	2.810	3.844	4.727	
	Total clad o.d. change, % $\Delta D/D$					
50	0.601	0.704	0.814	0.913	0.979	0.963
1763	0.604	0.731	0.862	0.958	0.992	0.965
5238	0.626	0.802	0.951	1.073	1.068	0.969
8050	0.678	0.930	1.182	1.270	1.154	0.972
13050	0.822	1.257	2.143	2.953	1.847	0.976
16346	0.936	1.471	2.789	4.198	2.968	0.980
18050	0.999	1.580	3.126	4.860	3.575	0.982
18074	0.345	0.862	2.305	3.930	2.596	0.043

CASE 8

0.28" o.d. pin, 14 mil clad, constant ϕ, 30" plenum, 1000 ^{o}F coolant outlet

Time, hours	Axial location, inches above bottom of active fuel				
	4	12	20	28	36	55
	Burnup, atom %				
50	0.012	0.017	0.018	0.017	0.012
1763	0.791	1.131	1.241	1.131	0.791
5238	2.343	3.337	3.658	3.337	2.343
8050	3.577	5.076	5.558	5.076	3.577
13050	5.722	8.070	8.818	8.070	5.722
16346	7.101	9.977	10.887	9.977	7.101
18050	7.804	10.942	11.932	10.942	7.804
18074	7.809	10.948	11.940	10.948	7.809
	kW/ft				
50	8.40	11.94	13.06	11.91	8.37
1736	8.21	11.68	12.79	11.65	8.15
5238	8.03	11.33	12.38	11.31	7.98
8050	7.90	11.06	12.05	11.03	7.85
13050	7.67	10.59	11.42	10.48	7.60
16346	7.53	10.30	11.04	10.20	7.47
18050	7.45	10.15	10.87	10.07	7.42
18074	0	0	0	0	0

CASE 9

0.28" o.d. pin, 14 mil clad, constant ϕ, 30" plenum, 1050 ^{o}F coolant outlet

Time, hours	Plenum Pressure psi	Gas Comp. % Fission Gas	Fission Gas Release % of Total	Clad $(1+\frac{\Delta \ell}{\ell})$
50	43.4	0.5	12.5	1.0091
5256	321.8	86.2	78.1	1.0091
8050	479.7	90.8	80.7	1.0095
13050	773.0	94.4	86.9	1.0131
16346	949.3	95.6	89.7	1.0158
18050	1030.9	96.0	90.2	1.0172
10874	350.0	96.0	90.4	1.0084

CASE 9

0.28 " o.d. pin, 14 mil clad, constant ϕ, 30" plenum, 1050 ^{o}F coolant outlet

Axial location, inches above bottom of active fuel

Time, hours	4	12	20	28	36	55
			Fuel center-line temp., ^{o}F			
50	3200	4314	4571	4456	3629	
5256	2148	2804	3011	2970	2723	
8050	2070	2709	2930	2884	2652	
13050	2024	2649	3030	3312	2997	
16346	1994	2595	3248	3490	3292	
18050	1978	2565	3316	3522	3333	
18074	70	70	70	70	70	
			Clad i.d./o.d. temp., ^{o}F			
50	699/656	813/754	926/865	1023/969	1081/1044	1050/1050
5256	696/655	807/751	919/861	1015/963	1074/1038	1045/1045
8050	695/654	804/749	914/857	1009/959	1067/1033	1039/1039
10350	692/653	797/745	902/849	994/947	1050/1017	1023/1023
16346	691/652	792/741	895/843	986/941	1041/1008	1012/1012
18050	690/651	789/740	891/841	983/938	1036/1003	1006/1006
18074	70/70	70/70	70/70	70/70	70/70	70/70

CASE 9

0.28" o.d. pin, 14 mil clad, constant ϕ, 30" plenum, 1050 ^{o}F coolant outlet

Time, hours	Axial location, inches above bottom of active fuel					
	4	12	20	28	36	55
	Gap size, mils					
50	2.304	1.108	0.705	1.035	2.335	
5256	0	0	0	0	0	
8050	0	0	0	0	0	
13050	0	0	0.342	1.511	1.467	
16346	0	0	1.123	2.922	3.791	
18050	0	0	1.533	3.576	4.709	
18074	2.438	2.493	3.004	4.654	5.578	
	Total clad o.d. change, % ΔD/D					
50	0.606	0.720	0.843	0.957	1.034	1.020
5256	0.632	0.819	0.988	1.201	1.159	1.036
8050	0.684	0.952	1.234	1.540	2.273	1.052
13050	0.826	1.332	2.471	3.702	2.468	1.079
16346	0.938	1.577	3.325	5.297	3.813	1.097
18050	1.001	1.700	3.773	6.155	4.547	1.105
18074	0.343	0.968	2.917	5.168	3.506	0.112

CASE 9

0.28" o.d. pin, 14 mil clad, constant ϕ, 30" plenum, 1050 ^{o}F coolant outlet

Axial location, inches above bottom of active fuel

Time, hours	4	12	20	28	36	55
			Burnup, atom %			
50	0.012	0.017	0.018	0.017	0.012	
5256	2.351	3.349	3.670	3.349	2.351	
8050	3.577	5.076	5.558	5.076	3.577	
13050	5.722	8.071	8.818	8.071	5.722	
16346	7.102	9.977	10.887	9.977	7.102	
18050	7.805	10.942	11.933	10.942	7.805	
18074	7.809	10.949	11.940	10.949	7.809	
			kW/ft			
50	8.40	11.94	13.05	11.90	8.37	
5256	8.03	11.32	12.37	11.30	7.98	
8050	7.90	11.06	12.04	11.02	7.84	
13050	7.67	10.59	11.39	10.48	7.60	
16346	7.53	10.29	11.04	10.20	7.49	
18050	7.45	10.14	10.88	10.06	7.43	
18074	0	0	0	0	0	

CASE 10

Time, hours	Plenum Pressure psi	Gas Comp. % Fission Gas	Fission Gas Release % of Total	Clad (1+ $\Delta\ell/\ell$)
50	29.3	0.4	11.3	1.0078
5240	205.2	85.5	73.5	1.0078
8050	306.5	90.3	76.1	1.0079
12530	474.0	93.7	79.8	1.0089
14424	544.8	94.6	81.1	1.0095
16361	616.3	95.2	82.2	1.0100
18050	677.9	95.6	83.1	1.0105
18074	259.8	95.6	82.8	1.0029

CASE 10

0.28" o.d. pin, 14 mil clad, constant ϕ, 40" plenum, 890 ^{o}F coolant outlet

Time, hours	Axial location, inches above bottom of active fuel					
	4	12	20	28	36	60
	Fuel center-line temp., ^{o}F					
50	3202	4304	4551	4402	3484	
5240	2125	2750	2932	2864	2529	
8050	2037	2646	2836	2769	2451	
12530	1995	2602	2795	2733	2406	
14424	1978	2579	2768	2706	2397	
16361	1960	2554	2737	2676	2389	
18050	1945	2529	2705	2659	2405	
18074	70	70	70	70	70	
	Clad i.d./o.d. temp., ^{o}F					
50	683/640	765/705	840/777	899/842	924/888	886/886
5240	681/639	760/703	834/773	892/838	921/884	883/883
8050	680/639	757/702	830/771	887/835	917/880	879/879
12530	677/638	752/699	822/765	877/827	906/870	869/869
14424	677/637	750/697	818/763	873/824	902/866	866/866
16361	676/637	748/696	815/761	869/820	898/863	861/861
18050	675/636	746/695	812/759	865/818	894/859	858/858
18074	70/70	70/70	70/70	70/70	70/70	70/70

CASE 10

0.28" o.d. pin, 14 mil clad, constant ϕ, 40" plenum, 890 ^{o}F coolant outlet

Axial location, inches above bottom of active fuel

Time, hours	4	12	20	28	36	60
			Gap size, mils			
50	2.281	1.065	0.645	0.998	2.301	
5240	0	0	0	0	0	
8050	0	0	0	0	0	
12530	0	0	0	0	0	
14424	0	0	0	0	0	
16361	0	0	0	0	0.010	
18050	0	0	0	0.034	0.081	
18074	2.375	2.468	2.550	3.006	3.434	
			Total clad o.d. change, % $\Delta D/D$			
50	0.589	0.667	0.745	0.815	0.857	0.834
5240	0.612	0.767	0.878	0.920	0.899	0.836
8050	0.663	0.874	1.081	1.042	0.936	0.836
12530	0.794	1.086	1.537	1.795	1.103	0.833
14424	0.858	1.178	1.718	2.107	1.356	0.835
16361	0.929	1.272	1.896	2.411	1.642	0.831
18050	0.994	1.354	2.047	2.671	1.897	0.831
18074	0.347	0.665	1.298	1.861	1.054	0.017

CASE 10

0.28" o.d. pin, 14 mil clad, constant ϕ, 40" plenum, 890 ^{o}F coolant outlet

	Axial location, inches above bottom of active fuel				
Time, hours	4	12	20	28	36
	Burnup, atom %				
50	0.012	0.017	0.018	0.017	0.012
5240	2.344	3.338	3.659	3.338	2.334
8050	3.577	5.076	5.558	5.076	3.577
12530	5.501	7.764	8.485	7.764	5.501
14424	6.300	8.871	9.687	8.871	6.300
16361	7.107	9.985	10.896	9.985	7.107
18050	7.804	10.941	11.932	10.941	7.804
18074	7.809	10.948	11.939	10.948	7.809
	kW/ft				
50	8.40	11.94	13.06	11.91	8.38
5240	8.03	11.33	12.38	11.31	7.99
8050	7.90	11.06	12.05	11.04	7.86
12530	7.70	10.65	11.54	10.58	7.65
14424	7.61	10.48	11.33	10.40	7.55
16361	7.53	10.31	11.12	10.21	7.45
18050	7.45	10.16	10.94	10.04	7.36
18074	0	0	0	0	0

CASE 11

0.28" o.d. pin, 14 mil clad, constant ϕ, 40" plenum, 1050 ^{o}F coolant outlet

Time, hours	Plenum Pressure psi	Gas Comp. % Fission Gas	Fission Gas Release % of Total	Clad $(1+\frac{\Delta \ell}{\ell})$
50	32.6	0.5	13.1	1.0092
5257	240.9	86.2	78.1	1.0092
8050	359.0	90.8	80.7	1.0096
13050	578.4	94.4	86.1	1.0127
16344	718.2	95.6	89.1	1.0151
18050	784.9	96.0	90.0	1.0162
18074	272.2	96.0	90.1	1.0074

CASE 11

0.28" o.d. pin, 14 mil clad, constant ϕ, 40" plenum, 1050 ^{o}F coolant outlet

	Axial location, inches above bottom of active fuel					
Time, hours	4	12	20	28	36	60
	Fuel center-line temp., ^{o}F					
50	3216	4335	4536	4473	3645	
5257	2147	2790	3004	2962	2715	
8050	2069	2701	2931	2881	2645	
13050	2023	2649	2919	3205	2849	
16344	1992	2602	3088	3394	3180	
18050	1976	2574	3184	3435	3259	
18074	70	70	70	70	70	
	Clad i.d./o.d. temp., ^{o}F					
50	699/656	813/754	926/865	1023/969	1081/1044	1050/1050
5257	696/655	807/751	919/860	1015/963	1074/1038	1045/1045
8050	695/654	804/749	914/857	1009/959	1067/1033	1039/1039
13050	692/653	797/745	902/849	994/947	1050/1017	1023/1023
16344	691/652	792/742	895/843	986/940	1040/1007	1012/1012
18050	690/652	790/740	891/840	982/937	1035/1003	1006/1006
18074	70/70	70/70	70/70	70/70	70/70	70/70

CASE 11

0.28" o.d. pin, 14 mil clad, constant ϕ, 40" plenum, 1050 ^{o}F coolant outlet

Axial location, inches above bottom of active fuel

Time, hours	4	12	20	28	36	60
			Gap size, mils			
50	2.286	1.034	0.626	0.989	2.312	
5257	0	0	0	0	0	
8050	0	0	0	0	0	
13050	0	0	0.092	1.076	0.835	
16344	0	0	0.605	2.286	2.767	
18050	0	0	0.992	2.860	3.749	
18074	2.424	2.532	3.068	4.102	4.902	
			Total clad, o.d. change, % $\Delta D/D$			
50	0.606	0.719	0.843	0.957	1.034	1.020
5257	0.632	0.819	0.982	1.199	1.160	1.028
8050	0.684	9.951	1.220	1.530	1.275	1.037
13050	0.827	1.324	2.386	3.527	2.338	1.051
16344	0.940	1.561	3.162	4.966	3.534	1.061
18050	1.002	1.681	3.564	5.734	4.186	1.066
18074	0.342	0.949	2.717	4.759	3.156	0.080

CASE 11

0.28" o.d. pin, 14 mil clad, constant ϕ, 40" plenum, 1050 ^{o}F coolant outlet

	Axial location, inches above bottom of active fuel				
Time, hours	4	12	20	28	36	60
	Burnup, atom %				
50	0.012	0.017	0.018	0.017	0.012
5257	2.352	3.349	3.671	3.349	2.352
8050	3.577	5.077	5.558	5.077	3.577
13050	5.722	8.071	8.819	8.071	5.722
16344	7.101	9.976	10.866	9.976	7.101
18050	7.805	10.942	11.933	10.942	7.805
18074	7.810	10.949	11.940	10.949	7.810
	kW/ft				
50	8.40	11.93	13.04	11.90	8.37
5257	8.03	11.32	12.36	11.30	7.97
8050	7.90	11.05	12.03	11.02	7.84
13050	7.67	10.58	11.39	10.46	7.58
16344	7.53	10.28	11.00	10.16	7.45
18050	7.45	10.13	10.83	10.02	7.39
18074	0	0	0	0	0

CASE 12

0.28" o.d. pin, 15 mil clad, constant kW/ft, 30" plenum, 890 ^{o}F coolant outlet

Time, hours	Plenum Pressure psi	Gas Comp. % Fission Gas	Fission Gas Release % of Total	Clad $(1+\Delta\ell/\ell)$
50	39.6	0.4	11.2	1.0077
5969	281.9	85.6	75.0	1.0078
8050	445.3	90.8	78.7	1.0080
13050	747.4	94.5	84.2	1.0096
15122	880.2	95.4	86.3	1.0105
16786	990.5	95.9	88.3	1.0112
18050	1074.3	96.2	89.7	1.0118
18074	396.9	96.2	89.7	1.0040

CASE 12

0.28" o.d. pin, 15 mil clad, constant kW/ft, 30" plenum, 890 ^{o}F coolant outlet

	Axial location, inches above bottom of active fuel					
Time, hours	4	12	20	28	36	55
	Fuel center-line temp., ^{o}F					
50	3197	4293	4538	4391	3477	
5096	2194	2869	3060	2976	2603	
8050	2141	2823	3035	2935	2567	
13050	2156	2864	3084	2978	2603	
15122	2163	2870	3083	3098	2751	
16786	2168	2872	3075	3230	2951	
18050	2172	2872	3089	3325	3130	
18074	70	70	70	70	70	
	Clad i.d./o.d. temp., ^{o}F					
50	687/640	769/705	845/776	903/842	930/888	886/886
5069	685/639	768/705	844/776	902/842	929/887	886/886
8050	686/640	768/705	844/777	902/842	929/887	886/886
13050	686/640	768/705	845/778	903/843	929/887	886/886
15122	686/640	769/705	845/778	903/844	929/888	886/886
16786	686/640	769/705	845/778	903/844	929/888	886/886
18050	686/640	769/706	845/778	903/845	929/888	886/886
18074	70/70	70/70	70/70	70/70	70/70	70/70

CASE 12

0.28" o.d. pin, 15 mil clad, constant kW/ft, 30" plenum, 890 ^{o}F coolant outlet

Axial location, inches above bottom of active fuel

Time, hours	4	12	20	28	36	55
			Gap size, mils			
50	2.305	1.101	0.694	1.038	2.319	
5069	0	0	0	0	0	
8050	0	0	0	0	0	
13050	0	0	0	0.039	0.030	
15122	0	0	0	0.276	0.353	
16786	0	0	0	0.588	0.895	
18050	0	0	0.040	0.867	1.557	
18074	2.468	2.183	2.140	2.647	3.566	
			Total clad o.d. change, % $\Delta D/D$			
50	0.590	0.669	0.749	0.818	0.858	0.834
5069	0.613	0.763	0.876	0.920	0.900	0.841
8050	0.667	0.880	1.087	1.053	0.941	0.848
13050	0.801	1.140	1.704	2.061	1.198	0.860
15122	0.864	1.255	1.967	2.527	1.597	0.866
16786	0.916	1.350	2.183	2.924	1.959	0.872
18050	0.957	1.423	2.355	3.239	2.246	0.876
18074	0.317	0.720	1.574	2.381	1.356	0.024

CASE 12

0.28" o.d. pin, 15 mil clad, constant kw/ft, 30" plenum, 890 ^{o}F coolant outlet

	Axial location, inches above bottom of active fuel				
Time, hours	4	12	20	28	36
	Burnup, atom %				
50	0.012	0.017	0.019	0.017	0.012
5069	2.340	3.353	3.683	3.353	2.340
8050	3.721	5.333	5.858	5.333	3.721
13050	6.037	8.654	9.505	8.654	6.037
15122	6.998	10.031	11.017	10.031	6.998
16786	7.769	11.136	12.231	11.136	7.769
18050	8.354	11.975	13.153	11.975	8.354
18074	8.360	11.983	13.162	11.983	8.360
	kW/ft				
50	8.40	11.94	13.07	11.92	8.38
5069	8.27	11.83	12.98	11.80	8.23
8050	8.27	11.82	12.96	11.80	8.23
13050	8.27	11.81	12.92	11.71	8.22
15122	8.27	11.81	12.90	11.68	8.19
16786	8.27	11.80	12.88	11.66	8.18
18050	8.27	11.80	12.86	11.67	8.19
18074	0	0	0	0	0

CASE 13

0.28" o.d. pin, 15 mil clad, constant ϕ, 30" plenum, 1050 ^{o}F coolant outlet

Time, hours	Plenum Pressure psi	Gas Comp. % Fission Gas	Fission Gas Release % of Total	Clad $(1+\frac{\Delta \ell}{\ell})$
50	44.1	0.5	13.1	1.0091
5117	323.8	86.1	78.2	1.0091
8050	489.2	90.8	81.0	1.0095
13050	787.5	94.5	87.1	1.0131
16090	953.4	95.6	89.7	1.0157
18050	1049.2	96.1	90.4	1.0172
18074	355.8	96.1	90.5	1.0085

CASE 13

0.28" o.d. pin, 15 mil clad, constant ϕ, 30" plenum, 1050 ^{o}F coolant outlet

	Axial location, inches above bottom of active fuel					
Time, hours	4	12	20	28	36	55
	Fuel center-line temp., ^{o}F					
50	3211	4325	4574	4462	3639	
5117	2156	2805	3012	2792	2724	
8050	2076	2708	2930	2883	2651	
13050	2028	2646	3030	3309	2990	
16090	1999	2596	3233	3473	3274	
18050	1980	2560	3310	3511	3325	
18074	70	70	70	70	70	
	Clad i.d./o.d. temp., ^{o}F					
50	703/656	817/754	931/865	1027/969	1084/1044	1050/1050
5117	699/655	811/751	923/860	1019/963	1076/1038	1045/1045
8050	698/654	808/749	918/857	1012/958	1070/1032	1039/1039
13050	695/653	800/745	906/848	997/947	1053/1016	1022/1022
16090	693/652	796/741	899/843	989/940	1043/1008	1012/1012
18050	692/651	793/739	895/840	985/937	1037/1002	1005/1005
18074	70/70	70/70	70/70	70/70	70/70	70/70

CASE 13

0.28" o.d. pin, 15 mil clad, constant ϕ, 30" plenum, 1050 ^{o}F coolant outlet

Axial location, inches above bottom of active fuel

Time, hours	4	12	20	28	36	55
			Gap size, mils			
50	2.039	1.070	0.676	1.030	2.320	
5117	0	0	0	0	0	
8050	0	0	0	0	0	
13050	0	0	0.348	1.506	1.446	
16090	0	0	1.065	2.771	3.573	
18050	0	0	1.528	3.501	4.613	
18074	2.392	2.508	3.804	4.629	5.557	
			Total clad o.d. change, % $\Delta D/D$			
50	0.608	0.722	0.846	0.959	1.035	1.020
5117	0.630	0.812	0.978	1.186	1.150	1.034
8050	0.679	0.942	1.220	1.527	1.262	1.049
13050	0.810	1.317	2.453	3.665	2.435	1.073
16090	0.905	1.538	3.233	5.106	3.640	1.086
18050	0.971	1.678	3.740	6.070	4.460	1.094
18074	0.317	0.947	2.885	5.085	3.421	0.104

CASE 13

0.28" o.d. pin, 15 mil clad, constant ϕ, 30" plenum, 1050 ^{o}F coolant outlet

Axial location, inches above bottom of active fuel

Time, hours	4	12	20	28	36	55
			Burnup, atom %			
50	0.012	0.017	0.019	0.017	0.012	
5117	2.354	3.353	3.675	3.353	2.354	
8050	3.635	5.158	5.646	5.158	3.635	
13050	5.813	8.197	8.956	8.197	5.813	
16090	7.106	9.983	10.894	9.983	7.106	
18050	7.927	11.110	12.114	11.110	7.927	
18074	7.932	11.117	12.121	11.117	7.932	
			kW/ft			
50	8.40	11.93	13.04	11.90	8.37	
5117	8.02	11.32	12.36	11.30	7.98	
8050	7.89	11.04	12.02	11.01	7.84	
13050	7.66	10.56	11.36	10.46	7.59	
16090	7.52	10.28	11.03	10.20	7.49	
18050	7.43	10.11	10.85	20.03	7.42	
18074	0	0	0	0	0	

Reference

1. M. C. Billone, B. L. Harbourne, et al., "The LIFE-III Fuel Element Performance Code User's Manual," Argonne National Laboratory Draft Report, (1977).

2. D. Marbach, P. Millet, and R. Peray, "Cladding Deformations in RAPSODIE and Consequences," International Conference on Fast Breeder Reactor Fuel Performance, ISBN089448-105-3, 123, (1979).

3. U. P. Nayjak, A. Boltax, F. J. Shalka, and A. Biancheria, "An Analytical Comparison of the Irradiation Behavior of Fast Reactor Carbide and Oxide Fuel Pins," Advanced LMFBR Fuels Proc., ERDA 4455, 537, (1977).

APPENDIX I

PIN DIAMETER SELECTION

The selection of the fuel pin diameter is subjected to design and performance criteria. The design criteria are:

- the outside flat-to-flat distance of the assembly should be less than 6 inches
- The fuel pin pitch-to-diameter ratio should be not less than 1.17.

The performance criteria consist of two groups: a) performance constraints, and b) performance measures. The performance constraints are:

- sodium void reactivity of $\leq$ \$2.50
- doubling time of 15-16 year or less.

The performance measures used in addition to the above listed criteria in selecting the optimum pin diamter are:

- fissile material gain per cycle
- fissile inventory
- burnup swing per cycle
- peak discharge burnup
- fuel cycle cost

This approach to optimize a fuel pin is somewhat more complex than the standard optimizations which seek to minimize an objective function. The increased complexity is a reflection of the complex problem of optimizing a quantity which is constrained by data which are uncertain to some degree.

Ducts that are somewhat larger than 6 inches are not unfeasible.

The p/d criterion is more substantive. For p/d ratios of less than 1.18, part of the coolant flow will "stream" through the fuel bundle and not follow the wire wrapping, thus reducing the cross flow. The mathematical modeling of the flow conditions becomes more difficult and the difference between duct wall and average cladding temperatures increases. This in turn increases bundle-duct interaction, and reduces pin life.

A doubling time constraint, 15-16 years, is not violated by a doubling time of 16.1 years. The sodium void reactivity constraint of $2.50 is not violated by a system which has a sodium void reactivity of $2.55. Both constraints are targets which have to be approached as closely as possible.

The selection process is then carried further by comparing fuel cycle costs for different systems. Here again, one has to realize that the parameters which effect fuel cycle cost are very uncertain, too. Fabrication cost, reprocessing cost, cost of waste disposal, and plutonium price are not much more than educated guesses. Therefore, advantages in fuel cycle cost performance have to be substantial to be significant.

The fissile material gain per cycle is an important parameter whenever large supplies of plutonium exist, i.e., when the installation of LMFBRs is not plutonium-limited.

The fissile inventory requirements relate to the growth in a plutonium-limited economy as well as the fuel cycle cost. The higher the fissile inventory, the higher the fuel cycle cost. The burnup swing per cycle is related to the number of control rods needed in the primary and secondary system.

The peak discharge burnup finally relates to maximim achievable burnup based on current irradiation experience.

Following is a discussion of the fuel pin optimization.

1. Duct Size

   Varying the fuel pin diameter from 0.25 inches to 0.28 inches changed the duct dimensions from 5.3 inches to 5.8 inches.

2. Fuel Pin Pitch-to-Diameter Ratio

The variation in fuel pin diameter from 0.25 inches to 0.28 inches changes the p/d ratio from 1.21 to 1.17 when the fuel bundle pressure drop is kept constant at 72 psi. This means that the p/d ratio does not limit the fuel pin diameter selection.

3. Sodium Void Reactivity

The sodium void reactivity calculations were carried out in RZ geometry. They were obtained from perturbation calculations which were corrected for the difference between direct eigenvalue and perturbation calculations.

End-of-equilibrium cycle sodium void reactivities were determined for 2 and 3 year residence times for cores with 0.26, 0.27 and 0.28 inch fuel pins. The following results were obtained.

Fuel O.D., In.	0.26	0.27	0.28	
	$2.54	$2.48	$2.43	2 cycles
	$2.80	$2.73	$2.65	3 cycles

The larger the fuel pin o.d., the lower is the sodium void reactivity. The longer the residence time, the higher is the sodium void reactivity.

With approximately a $2.50 limit on sodium void reactivity, all 2 cycle cores and the 3 cycle core with 0.28 inch fuel pins are feasibile. Three dimensional hexagonal-Z geometry calculations showed nearly 30¢ lower sodium void reactivities than the RZ results for BOL conditions. For EOEC conditions, this difference is expected to be smaller but still large enough to reduce the $2.65 void reacitivity to the $2.50 range for the 0.28 inch fuel pins.

4. Doubling Time

The compound system doubling times for the three pin sizes are listed below:

Fuel O.D., In.	0.26	0.27	0.28	
	16.7	16.6	16.6	2 cycles
	15.7	15.5	15.5	3 cycles

It is known that heterogeneous cores show a broad minimum in doubling time vs. fuel pin diameter plots. The above listed results bear out this earlier finding. A one year reduction in doubling time is obtained when the fuel residence time is increased from 2 cycles to 3 cycles.

5. Fissile Material Gain per Cycle

The gains in fissile material (kg) produced per cycle are listed below:

Fuel Pin O.D., In.	0.26	0.27	0.28	
	295	310	324	2 cycles
	277	293	308	3 cycles

As the pin diameter increases, the fissile gain per cycle increases, too. Because of the higher fission product inventory, 3 cycle cores have lower fissile gains than 2 cycle cores.

6. Fissile Inventory

The fissile inventories (kg) for the 6 different cores at BOEC conditions ar listed below:

Fuel O.D., In.	0.26	0.27	0.28	
	4300	4497	4700	2 cycles
	4398	4595	4800	3 cycles

As the fuel pin diameter increases, the fissile inventory increases. The relative increase is less than the realtive increase in fuel volume since the enrichment decreases. Extending the residence time from 2 to 3 cycles typically increases the fissile inventory by 100 kg.

7. Burnup Swing per Cycle

The changes in fuel pin diameter also affect the burnup swing per cycle:

Fuel pin O.D., In.	0.26	0.27	0.28	
Burnup Swing, $\Delta k/k$	0.007	0.006	0.005	2 cycles
	0.007	0.005	0.004	3 cycles

The larger the fuel pin diameter, the smaller the burnup swing. An increase in residence time from 2 to 3 cycles reduces the burnup swing because of the build-up of fissile material in the internal blanket assemblies which offsets the increased fission product level.

8. Peak Discharge Burnup

The peak pellet discharge burnups for the different cores are:

Fuel Pin O.D., In.	0.26	0.27	0.28	
MWD/kg	85	78	72	2 cycles
	124	115	107	3 cycles

As the fuel pin diameter increases the peak burnup decreases. Going from a 2 cycle to a 3 cycle operation increases burnup by approximately 50%.

9. Fuel Cycle Cost

Fuel cycle costs were calculated for the various cores with different residence times and fuel pin diameters. Fabrication costs were calculated for each assembly using the HEDL-N factor formula. The costs were then normalized setting the cost for the reactor with 0.28 inch pins and a 3 year residence time to 1.00. The relative costs are shown below:

Fuel Pin O.D. In.	0.26	0.27	0.28	
	1.28	1.33	1.39	2 cycles
	0.93		1.00	3 cycles

As the fuel pin diameter increases, fuel cycle costs increase slightly. These differences, however, could be reduced by optimizing each design. The major differences in fuel cycle costs occur when the fuel residence time is increased from 2 to 3 cycles. This reduction is nearly 30% and is far greater than any savings coming from fuel pin or duct optimization.

In regard to fuel pin optimization, the following summary relates the performance criteria to fuel pin size.

PERFORMANCE CRITERION	FAVORS SMALL PINS	INDIFFERENT	FAVORS LARGE PINS
Sodium Reactivity			X
Doubling Time			X
Fissile Material Gain/Cycle			X
Fissile Inventory	X		
Burnup Swing/Cycle			X
Peak Discharge Burnup			X
Fuel Cycle Cost		X	

Clearly, large fuel pins have more advantages than disadvantages.

In regard to residence time both sodium void reactivity and peak discharge burnup are adversely affected by an increase in residence time. But, for 0.28 inch fuel pins both data are within accepted limits. The major advantage in going from a 2

year to a 3 year cycle is the reduction in fuel cycle cost. While fuel inventory costs go slightly up and plutonium credit goes down somewhat, there are drastic reductions in fabrication and reprocessing costs.

Therefore, a 0.28 inch fuel pin with a 3 year residence time is selected as the reference design/condition. Going to smaller pins would lead to a substantial increase in sodium void reactivity. On the other hand, going to larger pins would not improve the breeding performance significantly. The sodium void reactivity could be further decreased. But, there are no obvious benefits to be derived.

Fissile inventory would increase and the p/d ratio would drop well below 1.18. Both are unfavorable design characteristics.

APPENDIX J
DISCRETE FUEL MANAGEMENT

J.1 Nuclear Analysis

As discussed in Section 4.1.3.1 the nuclear and the thermal-hydraulic performances of the reactor analyzed in this report are based on the first cycle and an equilibrium cycle where fresh and irradiated fuel are homogenized for the neutronic calculations. To obtain a measure for the differences between this approach and a discrete fuel management, a limited discrete fuel management analysis has been performed for the first four cycles. This discrete fuel management has not been optimized.

At the end of each cycle one third of the core fuel and internal blanket assemblies and one fifth of the radial blanket assemblies are replaced with fresh assemblies. The replacement is done in a scattered scheme and a 30^{o} symmetry is conserved to reduce computational cost. The core layout and the fuel management patterns analyzed are shown in Figures J.1 to J.4. Two fresh fuel enrichment zones have been used. The second enrichment zone consists of the last row of core fuel assemblies and the enrichment split has been determined such that, at the end-of-cycle, the power peaks in the two enrichment zones are equal. No control rods are present in the reactor during burnup and the end-of-cycle k_{eff} is always equal to 1.0000. Hexagonal-2D geometry has been used with an axial buckling to account for axial leakage.

At the end of the third cycle, the core and internal blanket assemblies that are discharged, one third of the total, have been irradiated for three cycles. This is the first batch of assemblies that have reached EOL conditions. The core and internal blanket assemblies discharged at the end of the fourth cycle are the second batch of assemblies that have reached EOL conditions.

Average fuel enrichment, fissile inventories and fissile gain as well as breeding ratios for the first four cycles and the equilibrium cycle are presented in Tables

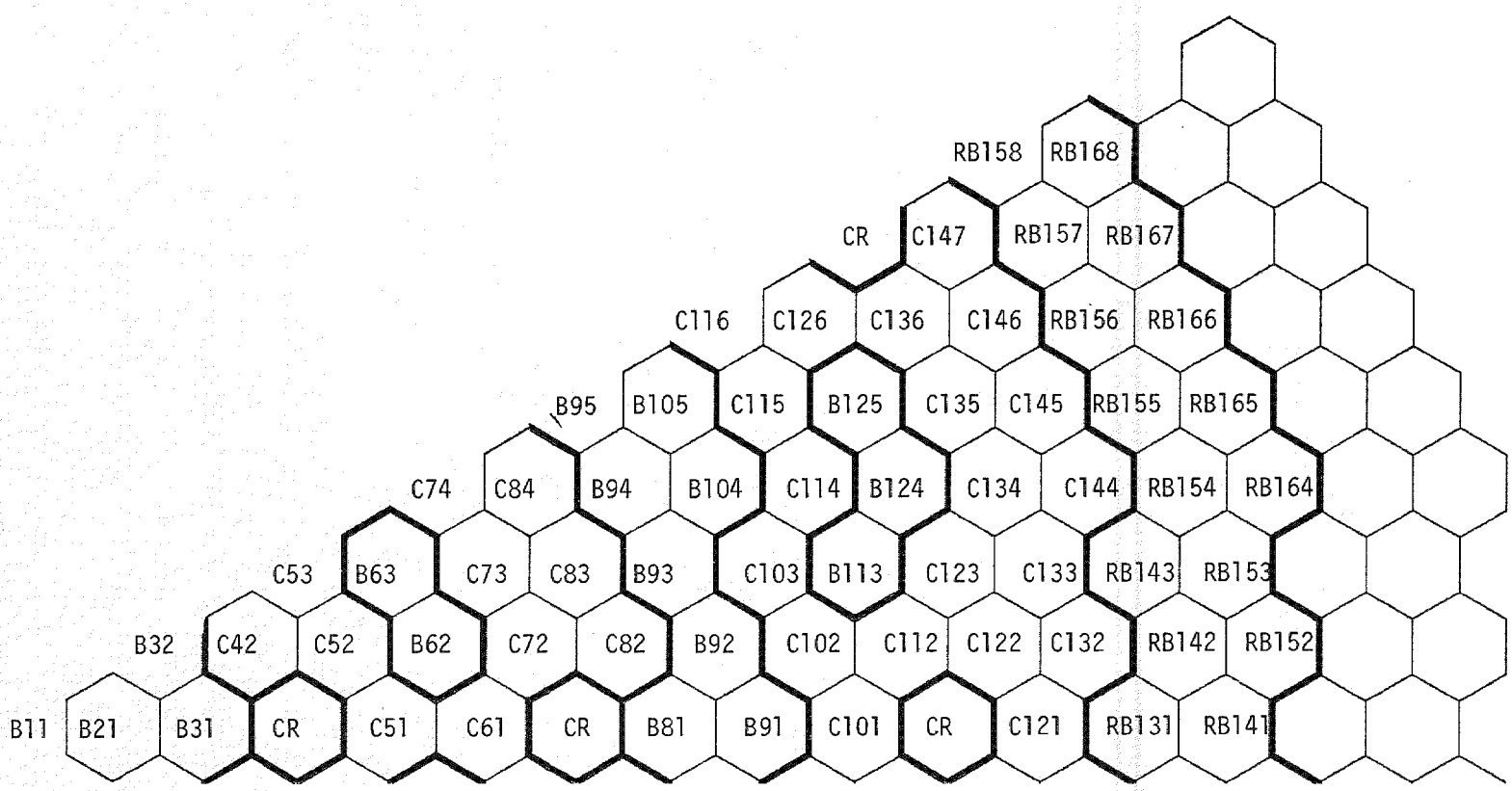

Figure J.1. Core layout (One twelfth of core)

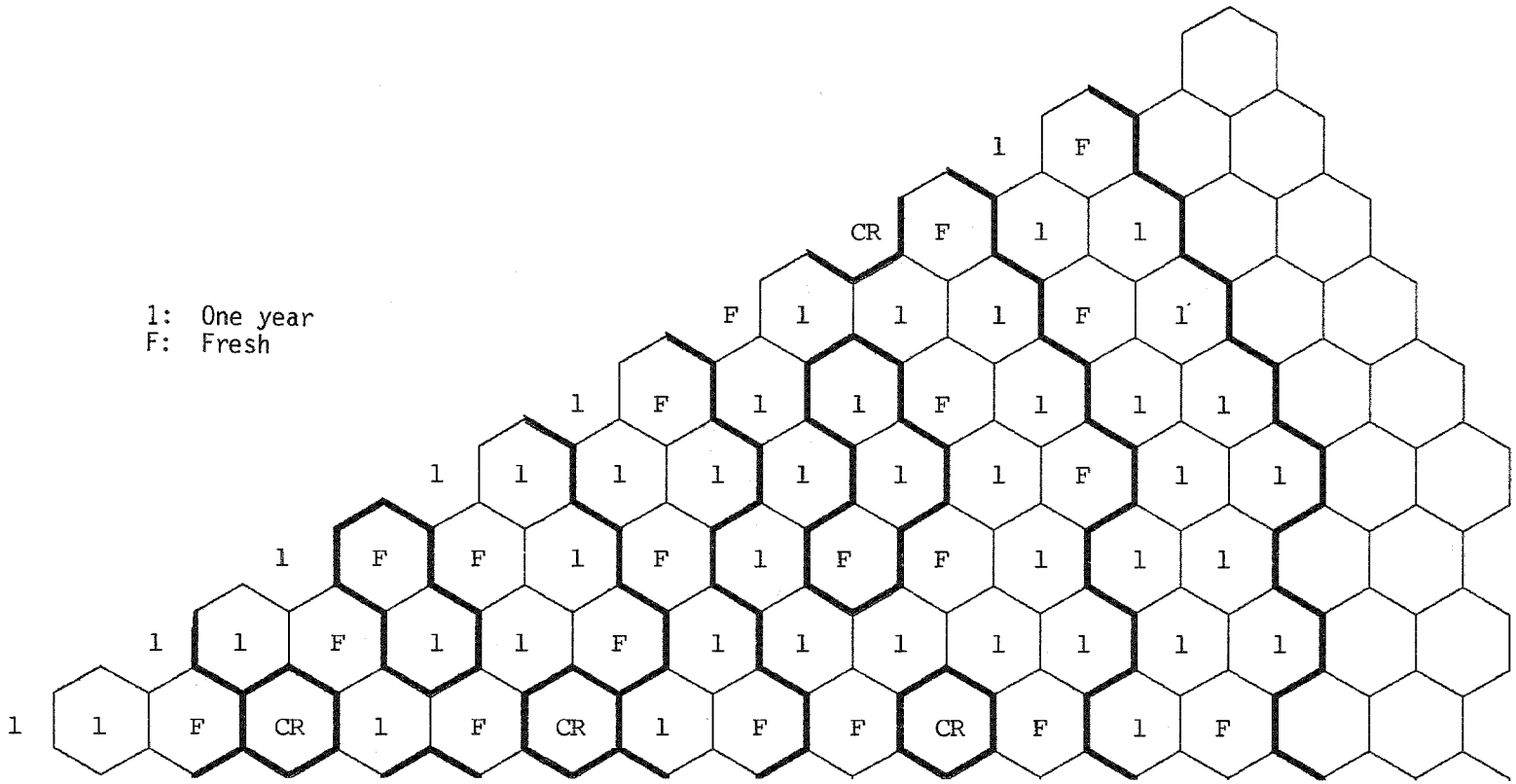

Figure J.2. Beginning of the second cycle

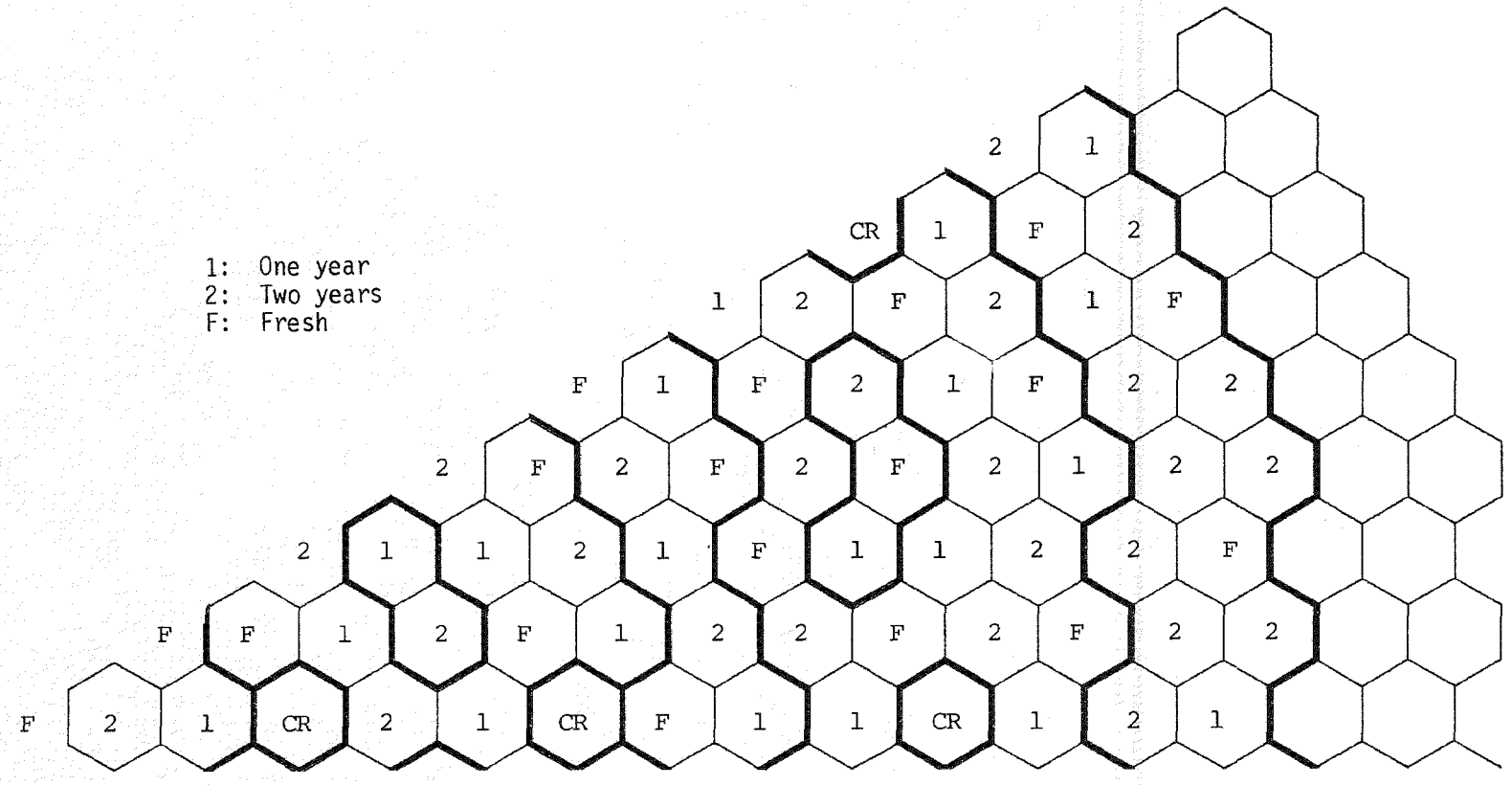

Figure J.3 Beginning of the third cycle

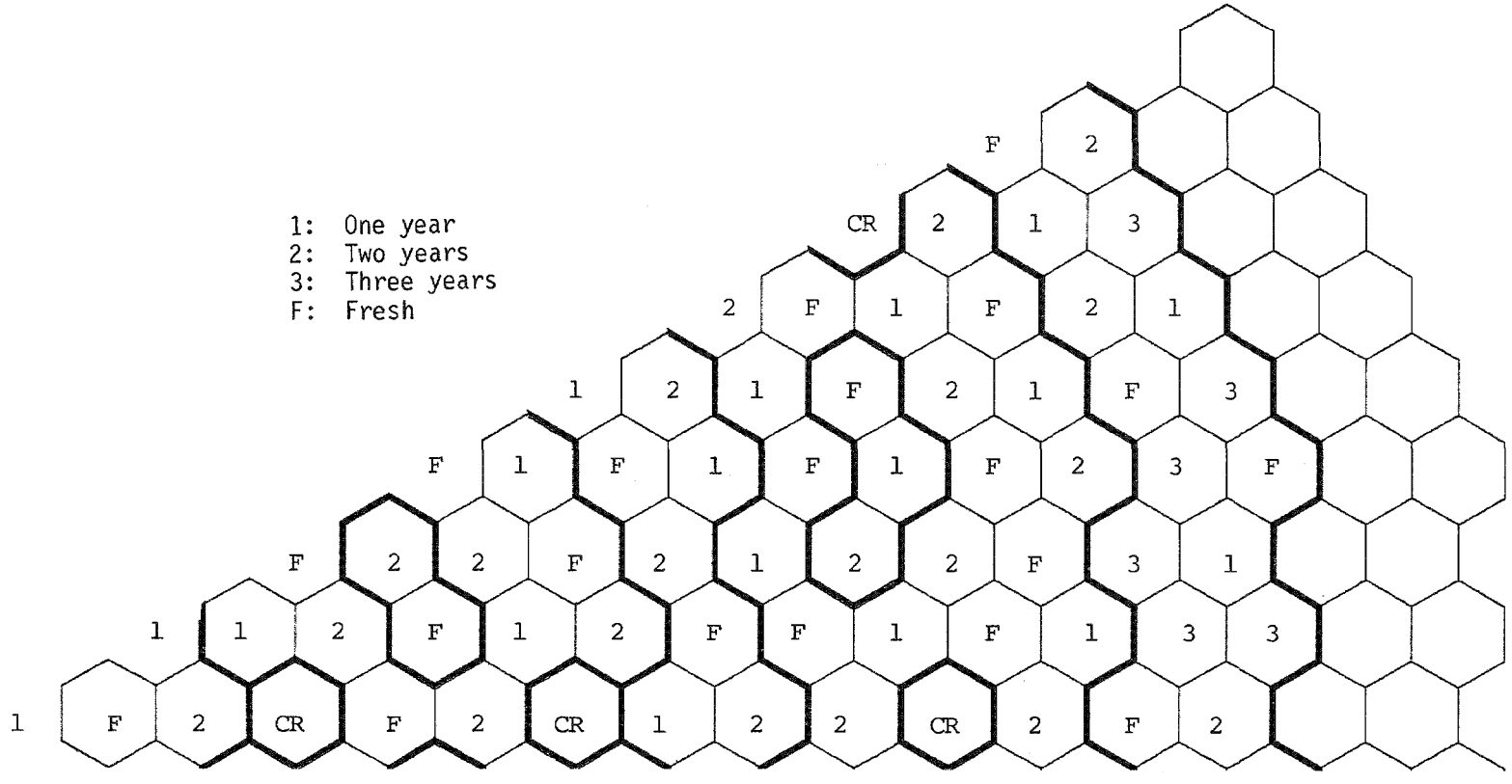

Figure J.4. Beginning of the fourth cycle

J.1, J.2, and J.3, respectively. The results show that the core, internal blanket, and radial blanket values of these quantities converge to their equilibrium values as we proceed from the first to the fourth cycle. The rate of convergence increases as we move from the radial blanket to the internal blanket, to the core and the whole reactor (in 2D hexagonal geometry).

Fresh feed-fuel enrichments and enrichment splits, the BOC control rod insertion patterns that minimize the BOC peak to average power density ratios, as well as the BOC and EOC peak to average power density ratios are presented in Table J.4 The fresh feed-fuel enrichment splits (first enrichment zone/second enrichment zone) vary from 1.000/0.931 to 1.000/1.336. The fresh feed-fuel enrichments vary from 16.14% to 22.06%. Finally, the peak to average power density ratios vary from 1.48 to 1.67.

Nominal peak linear power ratings for BOC and EOC conditions are given in Table J.5. The maximum nominal peak linear power rating in the core is 14.2 kW/ft and occurs at BOL. As has already been mentioned, only internal blanket assemblies have reached EOL conditions. The maximum nominal value of the peak linear power rating in the internal blanket is 16.4 kW/ft and occurs at the end of the third cycle. Both maximum values of peak linear power ratings in the core and the internal blanket are below the design limiting values of 15 kW/ft and 16.5 kW/ft, respectively (Section 2.1).

Average and peak assembly discharge burnups are presented in Table J.6. The maximum peak discharge burnups for the core and internal blanket assemblies that reached EOL conditions are 127,803 MWD/T and 29,463 MWD/T, respectively. The maximum peak discharge burnup in the core is ~19% higher than the value determined from the equilibrium cycle analysis (Section 4.1.3.5). The maximum peak discharge burnup in the internal blanket is ~12% lower than the value determined from the equilibrium cycle analysis.

J.2 Thermal-Hydraulic Analysis

As discussed in Section 4.2.4.3, the orificing strategy that is based on assigning assemblies to orificing zones according to assembly peak pin power and on equalizing the peak cladding midwall temperatures, yields the lowest 2σ peak cladding midwall temperature. This orificing strategy has been used in the thermal-hydraulic analysis of the reactor for a discrete fuel management scheme. Since only four cycles were analyzed, only two-thirds of the core and internal blanket assemblies

Table J.1

FISSILE ENRICHMENTS (%)

Reactor Region	Cycle 1		Cycle 2		Cycle 3		Cycle 4		Equilibrium	
	BOC	EOC	BOC	EOC	BOC	EOC	BOC	EOC	BOC	EOC
Inner Core	17.02	16.26	16.69	15.96	16.24	15.59	16.37	15.77	16.45	15.80
Middle Core	17.02	16.23	16.76	15.99	16.32	15.63	16.22	15.61	16.42	15.74
Outer Core 1	17.02	16.22	16.55	15.86	16.16	15.54	16.51	15.80	16.43	15.75
Outer Core 2	18.47	17.59	18.80	17.96	19.57	18.63	18.55	17.70	18.40	17.58
Total Core	17.36	16.55	17.15	16.40	17.01	16.30	16.91	16.20	16.89	16.19
Internal Blanket 1	0.0	1.42	0.90	2.18	1.23	2.57	1.54	2.65	1.36	2.60
Internal Blanket 2	0.0	2.15	1.07	3.02	3.02	4.59	1.99	3.58	1.94	3.66
Internal Blanket 3	0.0	1.91	1.18	2.78	1.76	3.36	1.92	3.48	1.78	3.38
Internal Blanket 4	0.0	2.09	1.37	3.02	1.83	3.46	1.89	3.59	1.88	3.54
Total Internal Blanket	0.0	1.93	1.17	2.80	1.90	3.47	1.88	3.42	1.78	3.36
Radial Blanket	0.0	0.88	0.72	1.42	1.11	1.88	1.38	2.16	1.60	2.33

Table J.2

FISSILE INVENTORIES AND FISSILE GAIN* (kg)

Reactor Region	Cycle 1		Cycle 2		Cycle 3		Cycle 4		Equilibrium	
	BOC	EOC	BOC	EOC	BOC	EOC	BOC	EOC	BOC	EOC
					Fissile Inventories					
Inner Core	462.2	428.7	444.3	412.4	427.2	398.3	431.2	404.7	434.3	405.6
Middle Core	924.4	854.4	893.7	825.7	860.3	799.2	848.2	794.3	865.5	805.6
Outer Core 1	1848.8	1707.9	1756.1	1633.8	1698.4	1588.4	1749.2	1624.4	1732.6	1614.1
Outer Core 2	1087.6	1007.3	1087.9	1012.0	1119.7	1036.5	1058.4	981.6	1054.2	980.3
Total Core	4323.0	3998.3	4182.0	3883.9	4105.6	3822.4	4087.0	3805.0	4086.6	3805.6
Internal Blanket 1	0.0	26.9	17.2	41.2	23.3	48.6	29.1	50.1	25.8	49.2
Internal Blanket 2	0.0	51.3	25.6	71.9	71.9	108.2	47.4	84.9	46.4	86.6
Internal Blanket 3	0.0	148.6	91.6	215.6	136.8	259.5	149.2	268.5	138.7	260.7
Internal Blanket 4	0.0	74.8	49.2	107.6	65.4	123.1	67.7	127.6	67.3	126.0
Total Internal Blanket	0.0	301.6	183.6	436.3	297.4	539.4	293.4	531.1	278.2	522.5
Radial Blanket	0.0	152.1	125.8	246.4	192.7	325.2	239.2	373.4	277.4	403.8
Total	4323.0	4452.0	4491.4	4566.6	4595.7	4687.0	4619.6	4709.5	4642.2	4731.9

Table J.2

FISSILLE INVENTORIES AND FISSILE GAIN* (kg) (continued)

Reactor Region	Cycle 1		Cycle 2		Cycle 3		Cycle 4		Equilibrium	
	BOC	EOC	BOC	EOC	BOC	EOC	BOC	EOC	BOC	EOC
				Fissile Gain						
	129		75.2		97.3		89.9		89.7	

*From 2D hexagonal calculations

Table J.3

BREEDING RATIOS

Reactor Region	Cycle 1		Cycle 2		Cycle 3		Cycle 4		Equilibrium	
	BOC	EOC	BOC	EOC	BOC	EOC	BOC	EOC	BOC	EOC
Inner Core	0.056	0.067	0.062	0.070	0.060	0.066	0.050	0.060	0.055	0.063
Middle Core	0.120	0.139	0.132	0.144	0.125	0.136	0.110	0.126	0.119	0.131
Outer Core 1	0.272	0.248	0.258	0.243	0.246	0.231	0.262	0.243	0.253	0.236
Outer Core 2	0.122	0.104	0.110	0.099	0.108	0.096	0.116	0.101	0.112	0.099
Total Core	0.570	0.558	0.562	0.556	0.539	0.529	0.538	0.530	0.539	0.529
Internal Blanket 1	0.033	0.040	0.032	0.370	0.035	0.041	0.029	0.036	0.033	0.039
Internal Blanket 2	0.067	0.077	0.068	0.074	0.067	0.073	0.058	0.067	0.064	0.071
Internal Blanket 3	0.202	0.212	0.186	0.194	0.197	0.205	0.195	0.203	0.196	0.204
Internal Blanket 4	0.112	0.100	0.095	0.089	0.100	0.092	0.106	0.098	0.103	0.095
Total Internal Blanket	0.414	0.429	0.381	0.394	0.399	0.411	0.388	0.404	0.396	0.408
Radial Blanket	0.219	0.189	0.180	0.162	0.209	0.187	0.218	0.193	0.210	0.187
Total	1.203	1.176	1.123	1.112	1.147	1.127	1.144	1.127	1.145	1.125

Table J.4

FRESH FEED-FUEL ENRICHMENTS, ENRICHMENT SPLITS, CONTROL ROD INSERTION PATTERNS, AND PEAK TO AVERAGE POWER DENSITY RATIOS

	Cycle 1	Cycle 2	Cycle 3	Cycle 4	Equilibrium
Fresh Fuel Enrichment Split (Inner Zone/Outer Zone)	1.000/1.085	1.000/1.1777	1.000/1.336	1.000/0.931	1.000/1.124
Fresh Fuel Fissile Enrichment (Inner Zone/Outer Zone)	17.02/18.47	17.59/20.70	16.51/22.06	17.34/16.14	17.16/19.27
Control Rod Insertion Pattern Row 11/Row 13	1.0/9.873	1.000/9.873	1.000/5.500	1.000/13.854	
Peak/Average Power Density Ratio (BOC/EOC)	1.484/1.511	1.598/1.670	1.587/1.584	1.562/1.594	1.482*

*EOEC

Table J.5

NOMINAL PEAK LINEAR POWER RATINGS (kW/ft)

	Cycle 1		Cycle 2		Cycle 3		Cycle 4	
Reactor Region	BOC	EOC	BOC	EOC	BOC	EOC	BOC	EOC
Core	14.2	13.6	14.1	13.9	13.9	12.8	13.7	12.8
Internal Blanket	4.8	9.6	10.2	13.8	13.2	16.4*	12.7	15.6*
Radial Blanket	3.4	5.0	4.4	5.9	5.4	7.4	6.0	7.4

*EOL

Table J.6

ASSEMBLY DISCHARGE BURNUPS
(MWD/T)

	Cycle 1		Cycle 2		Cycle 3*		Cycle 4*	
Subassembly	Average	Peak	Average	Peak	Average	Peak	Average	Peak
				CORE				
C42			47534	66738				
C51					80650	105974		
C52	27230	35454					78672	102273
C53					77722	100920		
C61	28903	37529					82848	108738
C72			57189	74460				
C73	29014	37737					83582	109576
C74					82859	107634		
C82	25817	35346					75755	101284
C83					77200	105185		
C84			52756	73331				
C101	31348	42141					86513	116966
C102					76617	104008		
C103			47548	63714				
C112			59967	79995				
C114					69965	91479		
C115			48646	65940				
C116	25233	33997					73884	99646
C121	31437	44684					91288	127803
C122					84482	112825		
C123	30684	40894					83878	112313
C126					75583	98711		
C132			46515	71214				
C133					78071	108010		
C134					74688	100156		
C135	26539	34787					74167	98567

Table J.6

ASSEMBLY DISCHARGE BURNUPS (continued)
(MWD/T)

	Cycle 1		Cycle 2		Cycle 3*		Cycle 4*	
Subassembly	Average	Peak	Average	Peak	Average	Peak	Average	Peak
			CORE (continued)					
C136			51146	67820				
C144	22185	33459					67041	99925
C145			44303	65302				
C146					64774	92756		
C147	23534	34285					70576	102476
			INTERNAL BLANKET					
B11			2418	3120				
B21					6244	9076		
B31	2557	4026					12993	19914
B32			5575	8502				
B62					22312	29463		
B63	4386	5816					21192	28217
B81			9352	13467				
B91	3795	5475					18283	26136
B92					16480	22545		
B93	3256	4546					16331	21785
B94					14951	21454		
B95			7956	11341				
B104			8193	11393				
B105	2786	3905					14560	20323
B113	4576	6296					20695	28228
B124			10756	14494				
B125					18491	24538		

Table J.6

ASSEMBLY DISCHARGE BURNUPS (continued)
(MWD/T)

	Cycle 1		Cycle 2		Cycle 3*		Cycle 4*	
Subassembly	Average	Peak	Average	Peak	Average	Peak	Average	Peak
			RADIAL BLANKET					
RB131					10480	17270		
RB141	1286	2439						
RB142							9148	16462
RB153			1451	2465				
RB154							6944	12315
RB155					6042	10506		
RB156	1575	3097						
RB157			3827	6380				
RB158					6722	11220		
RB164					1288	2108		
RB166			1122	1846				
RB167							3383	5446
RB168	457	769						

* All core and internal blanket assemblies discharged at the end of cycles 3 and 4 have reached end of life.

and none of the radial blanket assemblies reached EOL. For the assemblies that did not reach EOL conditions, EOL powers were obtained by extrapolating their power history during the four cycles to EOL.

For each core assembly position, the peak pin power was determined during the four cycles and the assembly position was assigned to an orificing zone according to this peak pin power. For each blanket assembly position, the peak pin power at EOL was determined and the assembly position was assigned to an orificing zone according to this peak pin power. A total of nine orificing zones were used, i.e., three for the core, four for the internal and radial blankets, one for the radial reflector, and one for the control assemblies. The assignment of assemblies to orificing zones is shown in Figure J.5.

Assembly coolant flow rates, coolant velocities, and assembly bundle pressure drops are given in Table J.7. The flow fractions allocated to the core and blanket assemblies are 72.4% and 27%, respectively. The flow fraction allocated to control and shield assemblies is equal to 0.6%. The maximum average coolant velocity is 22.8 ft/sec and occurs in the first core orificing zone. The maximum assembly bundle average pressure drop is 54 psi and occurs in the first blanket orificing zone.

Average assembly coolant temperatures, at the beginning and end of the four cycles analyzed, at the top of the upper axial blanket are shown in Figures J.6 to J.13. The peak average assembly coolant temperature at the top of the upper axial blanket as well as the peak nominal and 2σ cladding midwall temperatures are given in Table J.8. The peak average assembly coolant temperature at the top of the upper axial blanket is 1006^{o} F and the peak nominal and 2σ cladding midwall temperatures are 1078^{o} F and 1207^{o} F, respectively.

Assembly duct wall temperatures and duct wall temperature differences at the beginning and end of each cycle are shown in Figures J.14 to J.21. Maximum duct wall temperature differences in the different reactor regions, at the beginning and end of each cycle, are given in Table J.9. The maximum duct wall temperature decreases in the core assemblies and increases in the blanket assemblies as we proceed from the beginning of a cycle to the end of this cycle. The maximum duct wall difference decreases in all reactor regions as we proceed from the beginning of a cycle to the end of this cycle. The highest duct wall temperature and duct wall temperature difference, for the core assemblies, occur at the beginning of the first

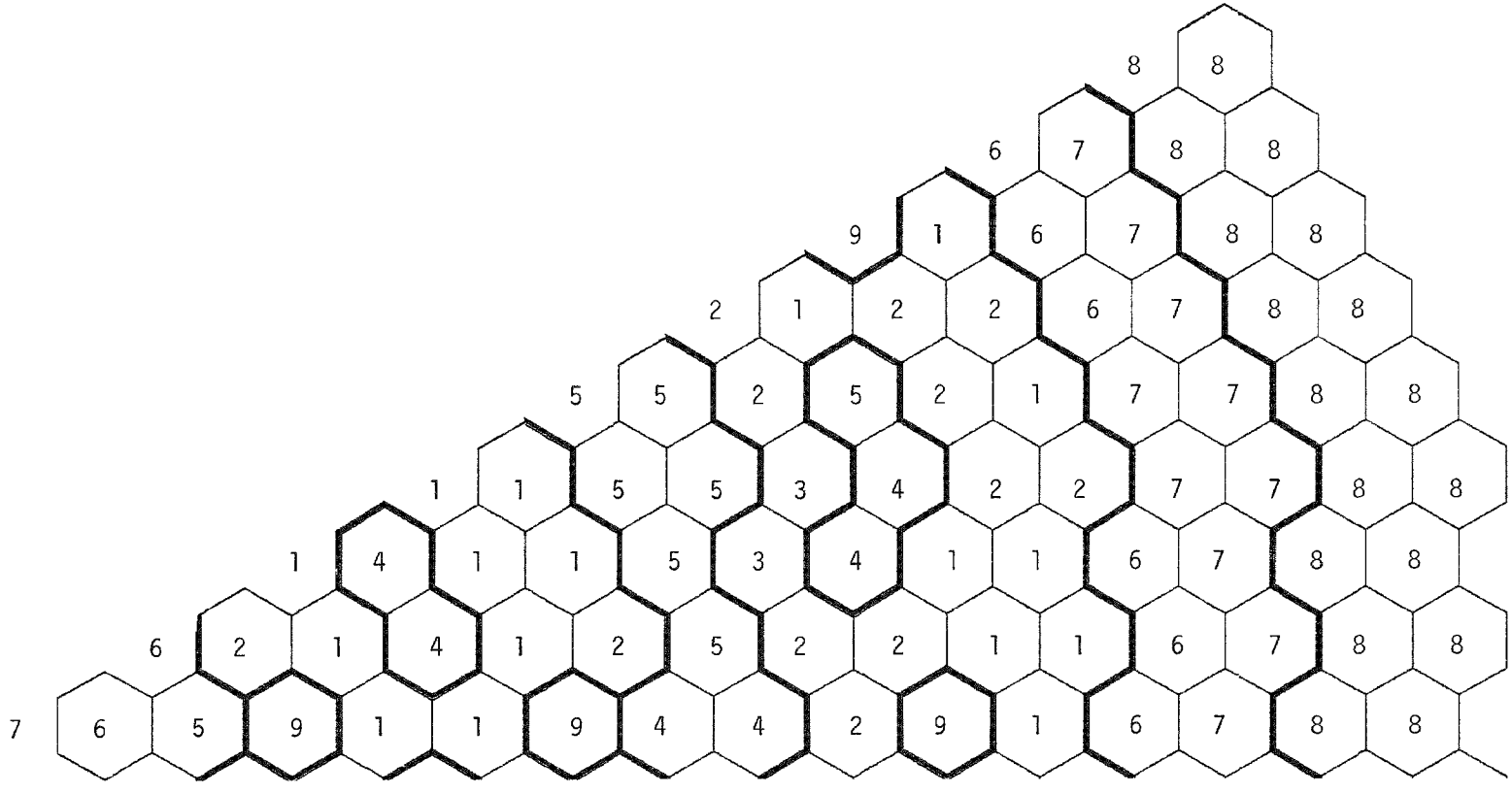

Figure J.5. Assignment of assemblies to orificing zones

Table J.7

ASSEMBLY ASSIGNMENT TO ORIFICING ZONES BASED
ON PIN POWER, AND EQUAL PEAK CLADDING MIDWALL TEMPERATURES

Orificing Zone	Assembly Coolant Flow Rate (lbm/hr)	Assembly Average Coolant Velocity (ft/sec)	Assembly Bundle Average Pressure Drop (psi)
1	268,016	22.8	52.2
2	245,217	20.9	44.3
3	221,826	18.9	36.9
4	164,812	20.9	54.0
5	123,890	15.6	32.0
6	77,636	9.8	13.6
7	48,498	6.1	5.8
8	2,108	---	---
9	10,670	---	---

TOTAL FLOW 116,463,258

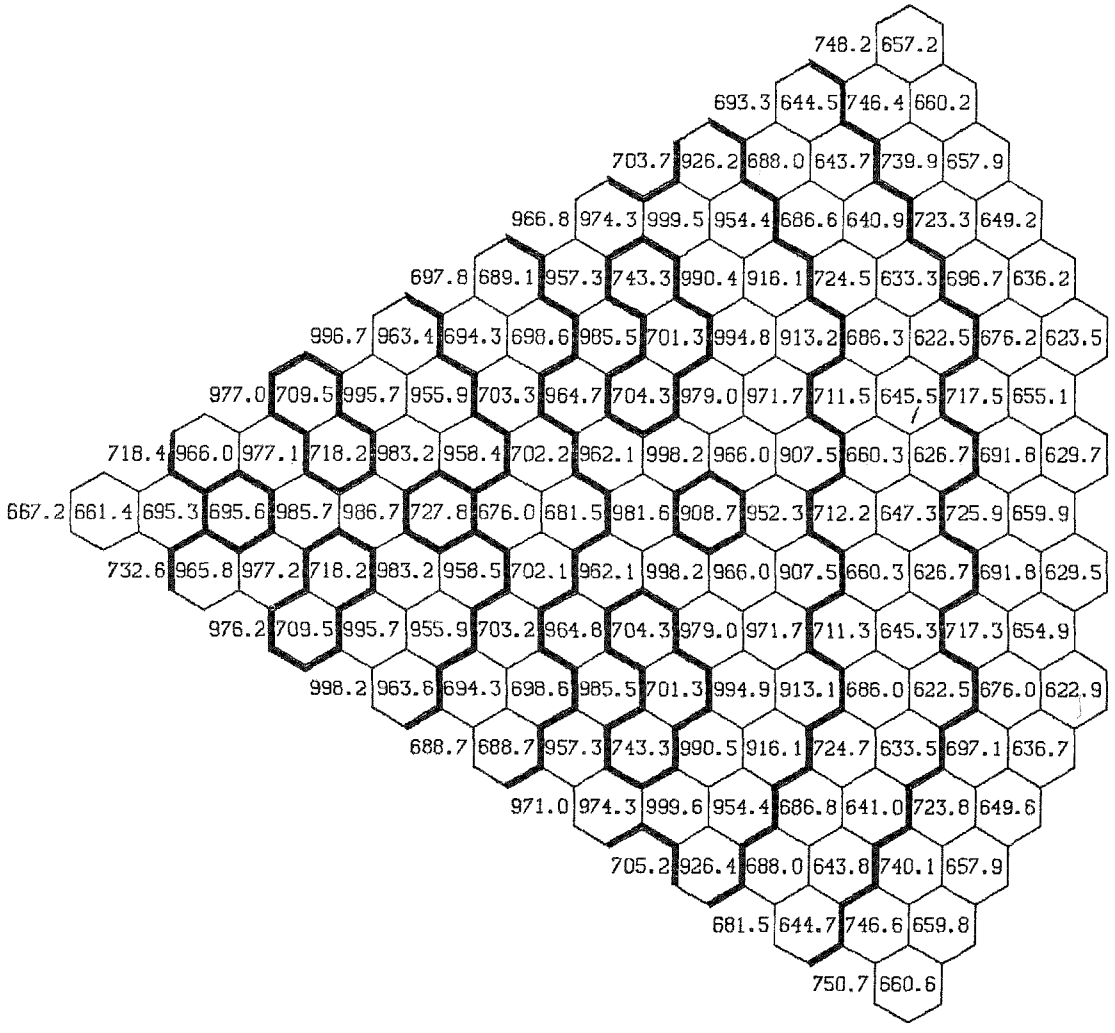

Figure J.6. Average coolant temperatures (^{o}F) at BOC1 at the top of the upper axial blanket. (Orificing based on pin power and equal peak cladding midwall temperatures)

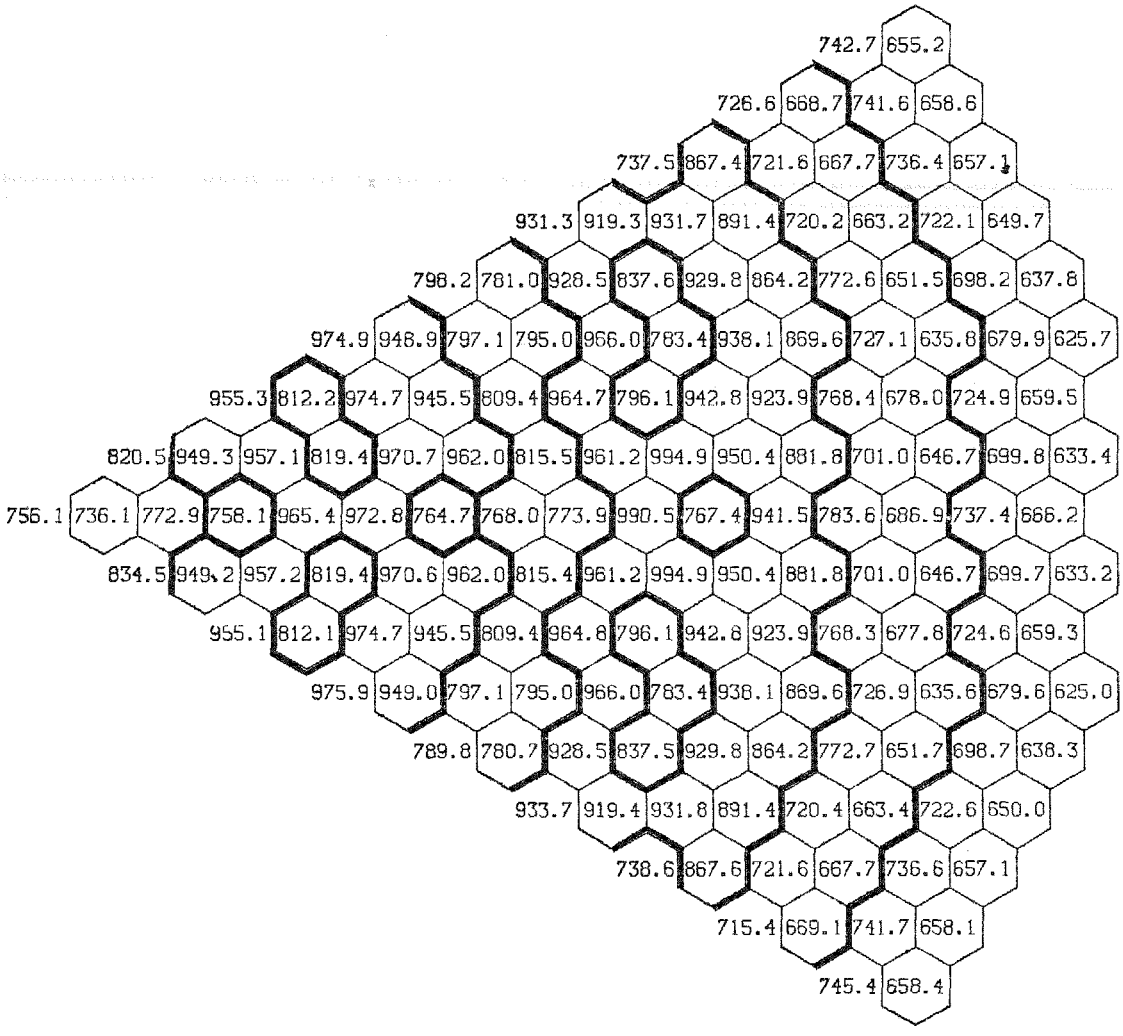

Figure J.7. Average coolant temperature (^{O}F) at EOC1 at the top of the upper axial blanket. (Orificing based on pin power and equal peak cladding midwall temperatures)

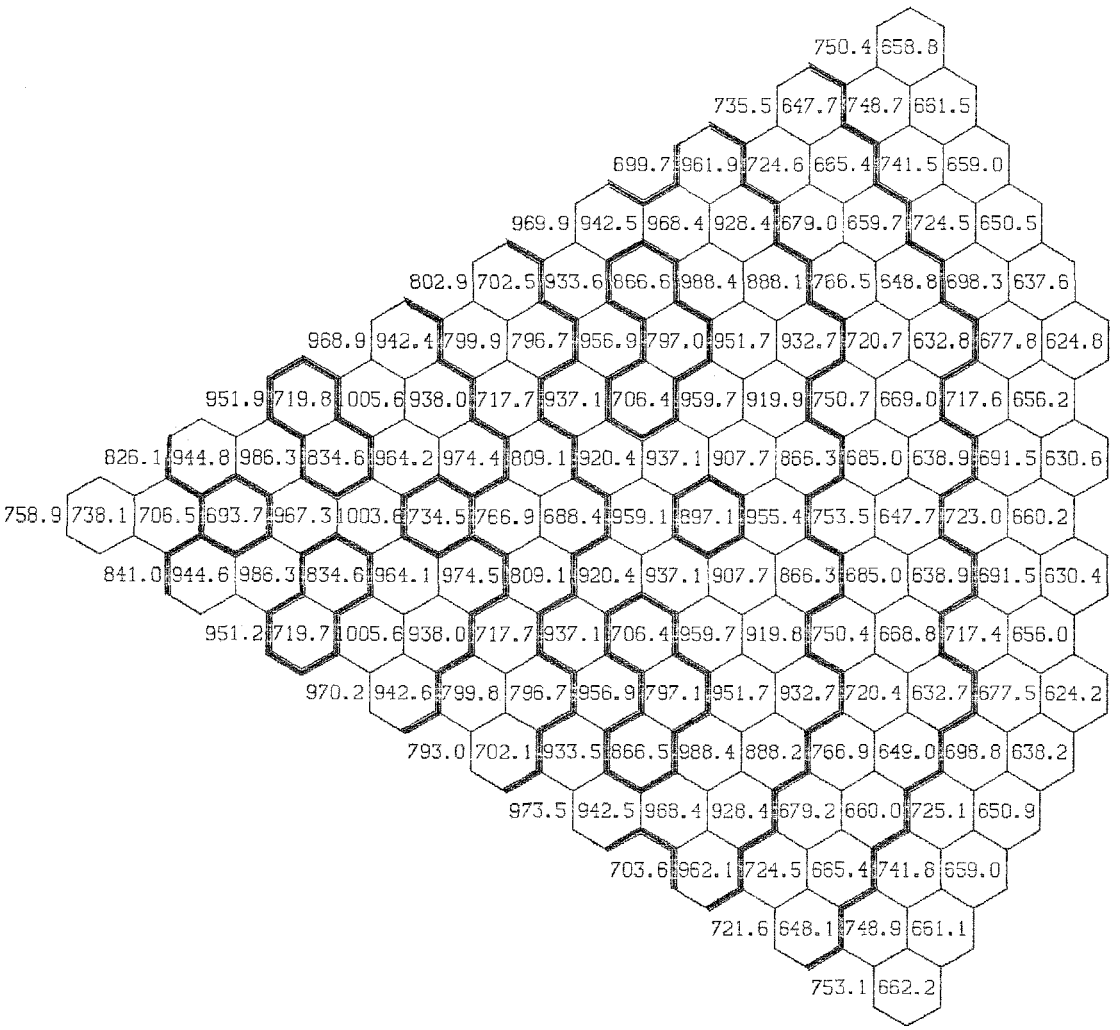

Figure J.8. Average coolant temperatures (^{o}F) at BOC2 at the top of the upper axial blanket. (Orificing based on pin power and equal peak cladding midwall temperatures)

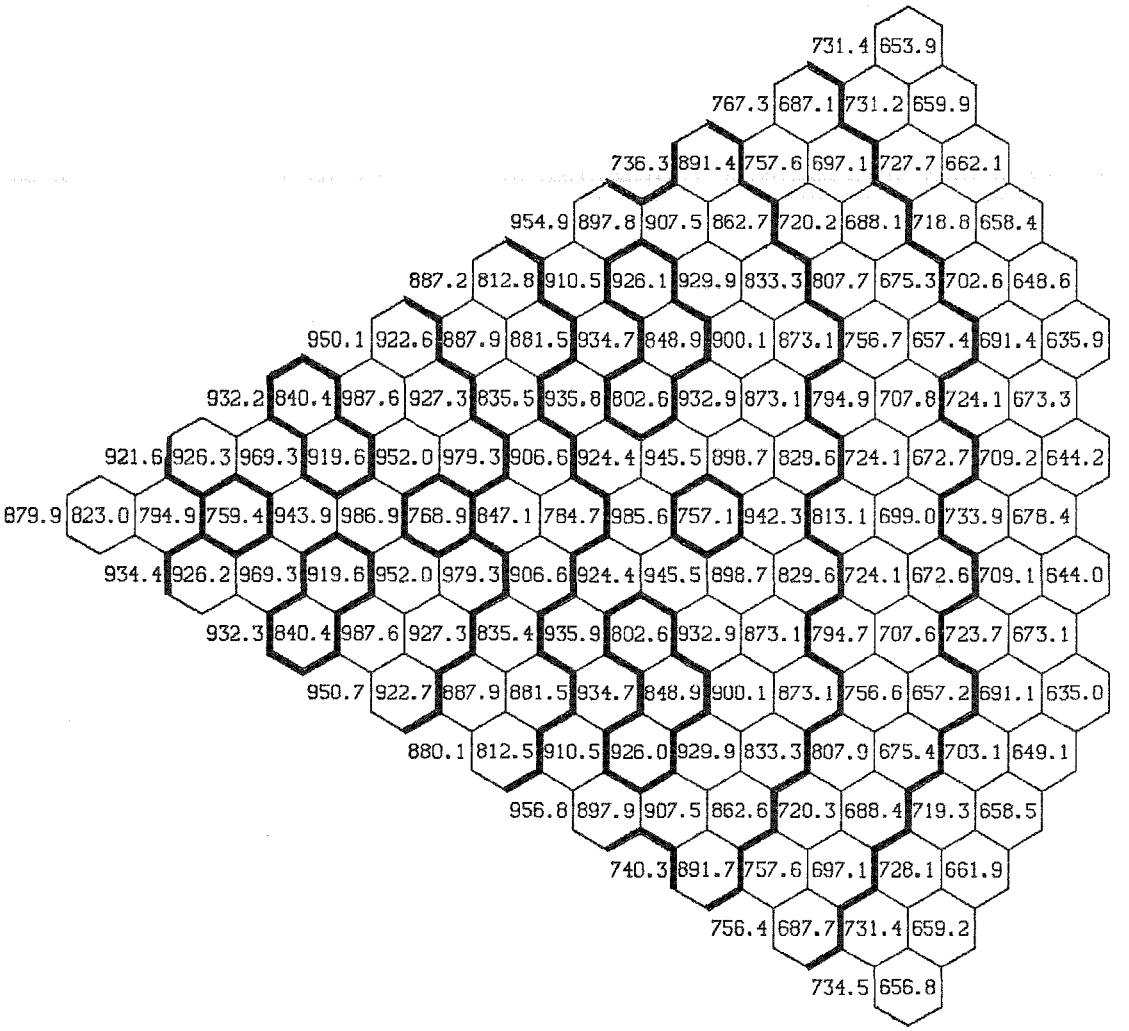

Figure J.9. Average coolant temperatures (^{O}F) at EOC2 at the top of the upper axial blanket. (Orificing based on pin power and equal peak cladding midwall temperatures)

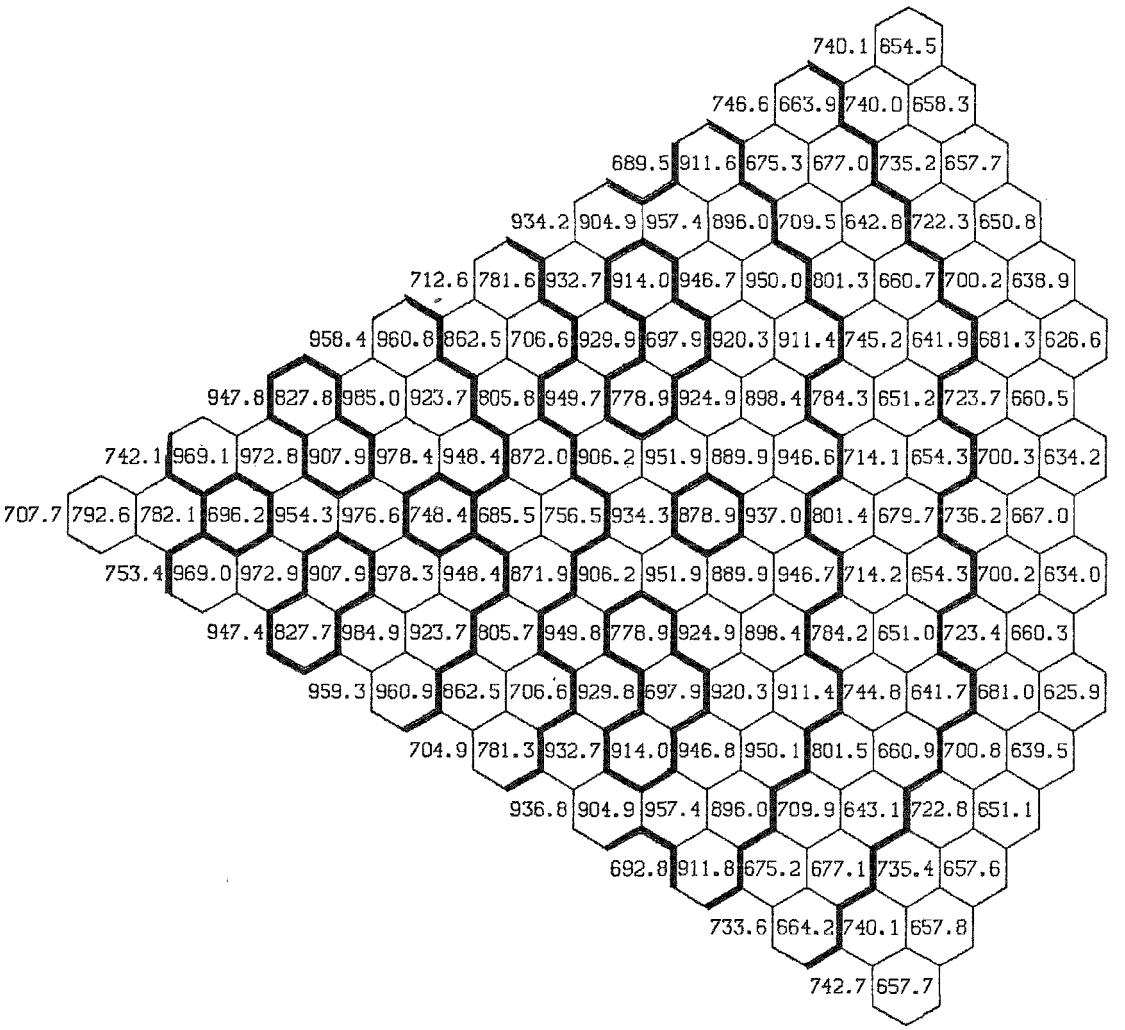

Figure J.10. Average coolant temperatures (^{o}F) at BOC3 at the top of the upper axial blanket. (Orificing based on pin power and equal peak cladding midwall temperatures)

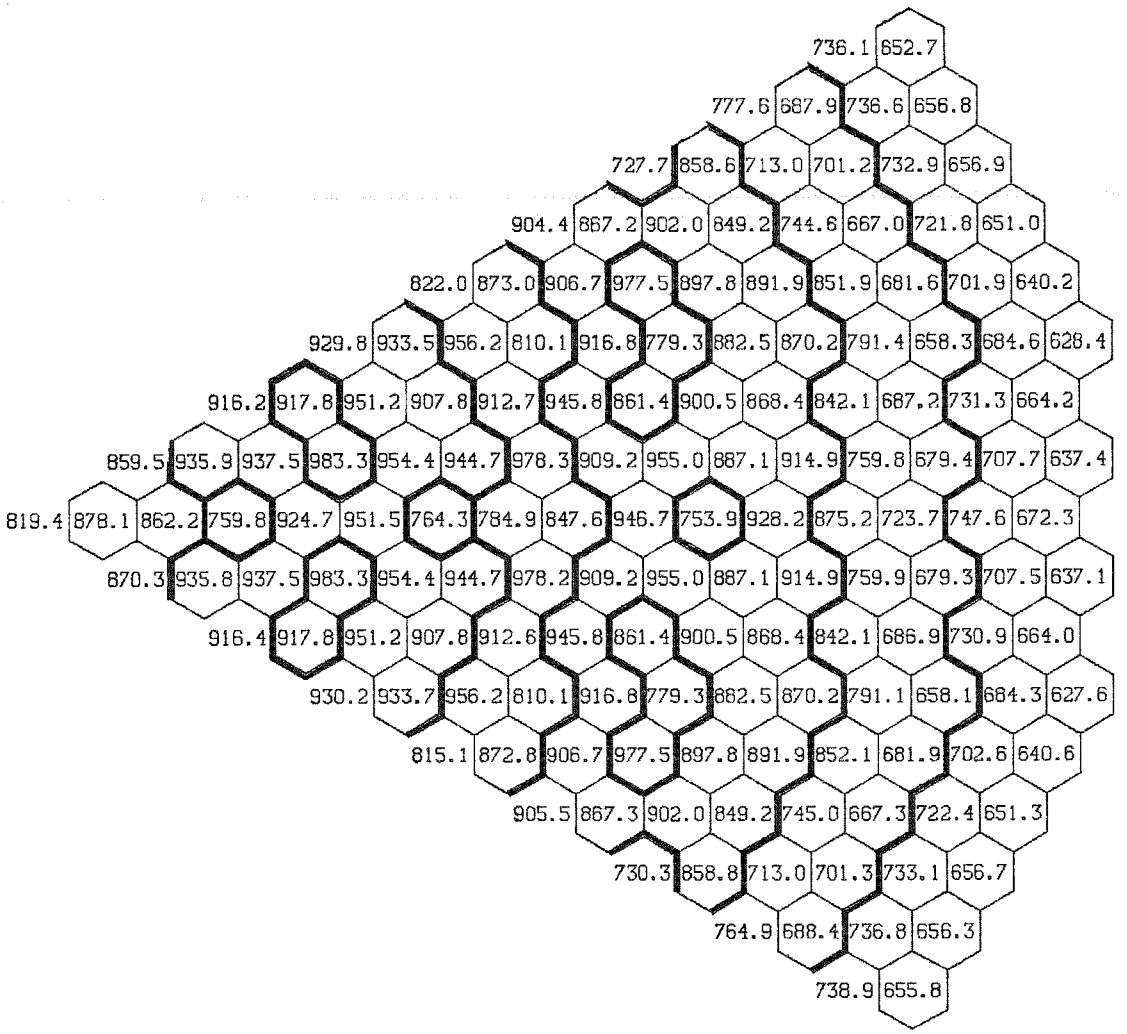

Figure J.11. Average coolant temperatures (^{o}F) at EOC3 at the top of the upper axial blanket. (Orificing based on pin power and equal peak cladding midwall temperatures)

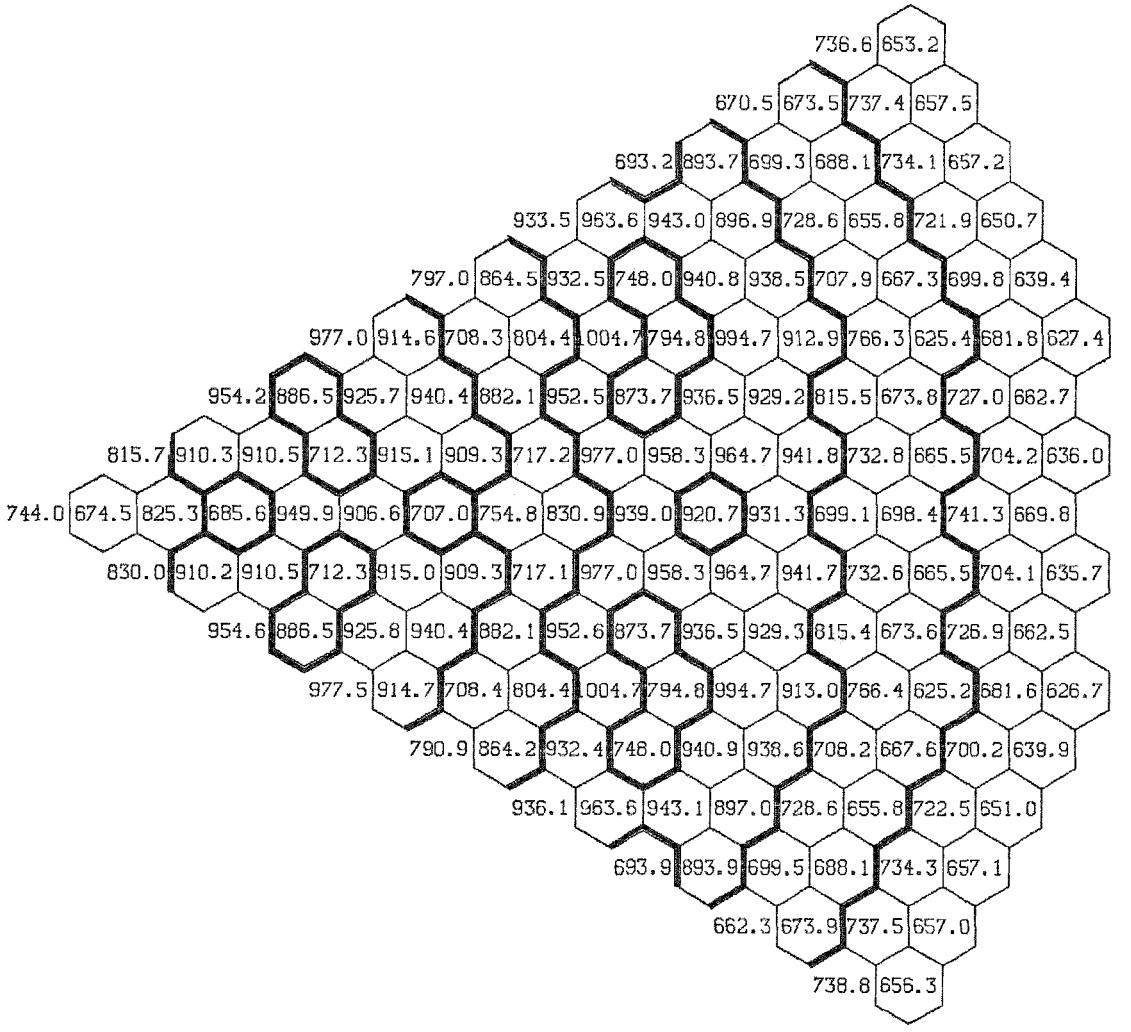

Figure J.12. Average coolant temperatures (^{O}F) at BOC4 at the top of the upper axial blanket. (Orificing based on pin power and equal peak cladding midwall temperatures)

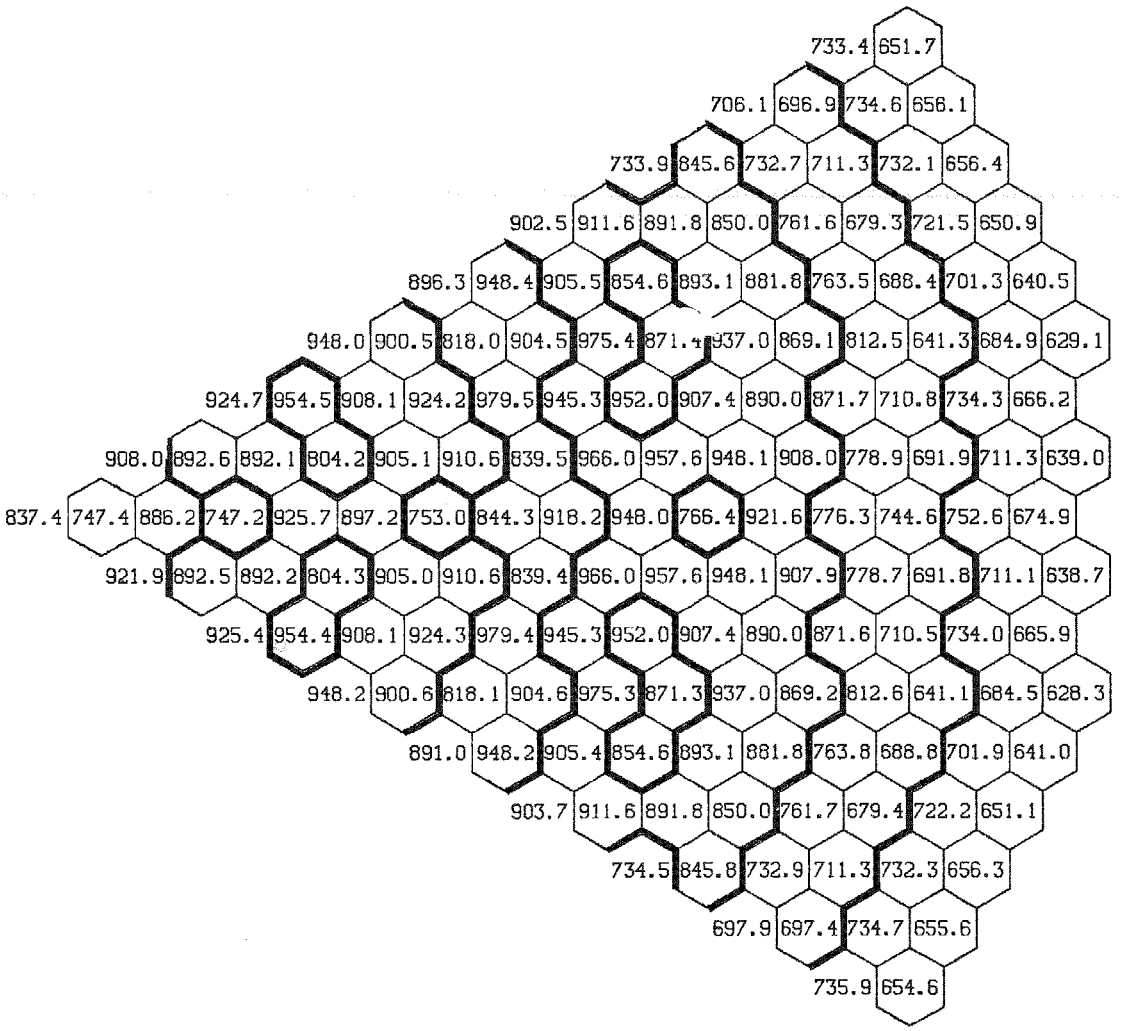

Figure J.13. Average coolant temperatures (^{O}F) at EOC4 at the top of the upper axial blanket. (Orificing based on pin power and equal peak cladding midwall temperatures

Table J.8

PEAK ASSEMBLY COOLANT TEMPERATURES, NOMINAL AND
2σ PEAK CLADDING MIDWALL TEMPERATURES (°F)

	Coolant	Cladding Midwall	
		Nominal	2σ
Discrete Fuel Management	1006	1078	1207
Analysis Based on BOL and EOEC Conditions	1002	1088	1220

WALL TEMPERATURES BOC1 FOR GEOM28 Z=70.0

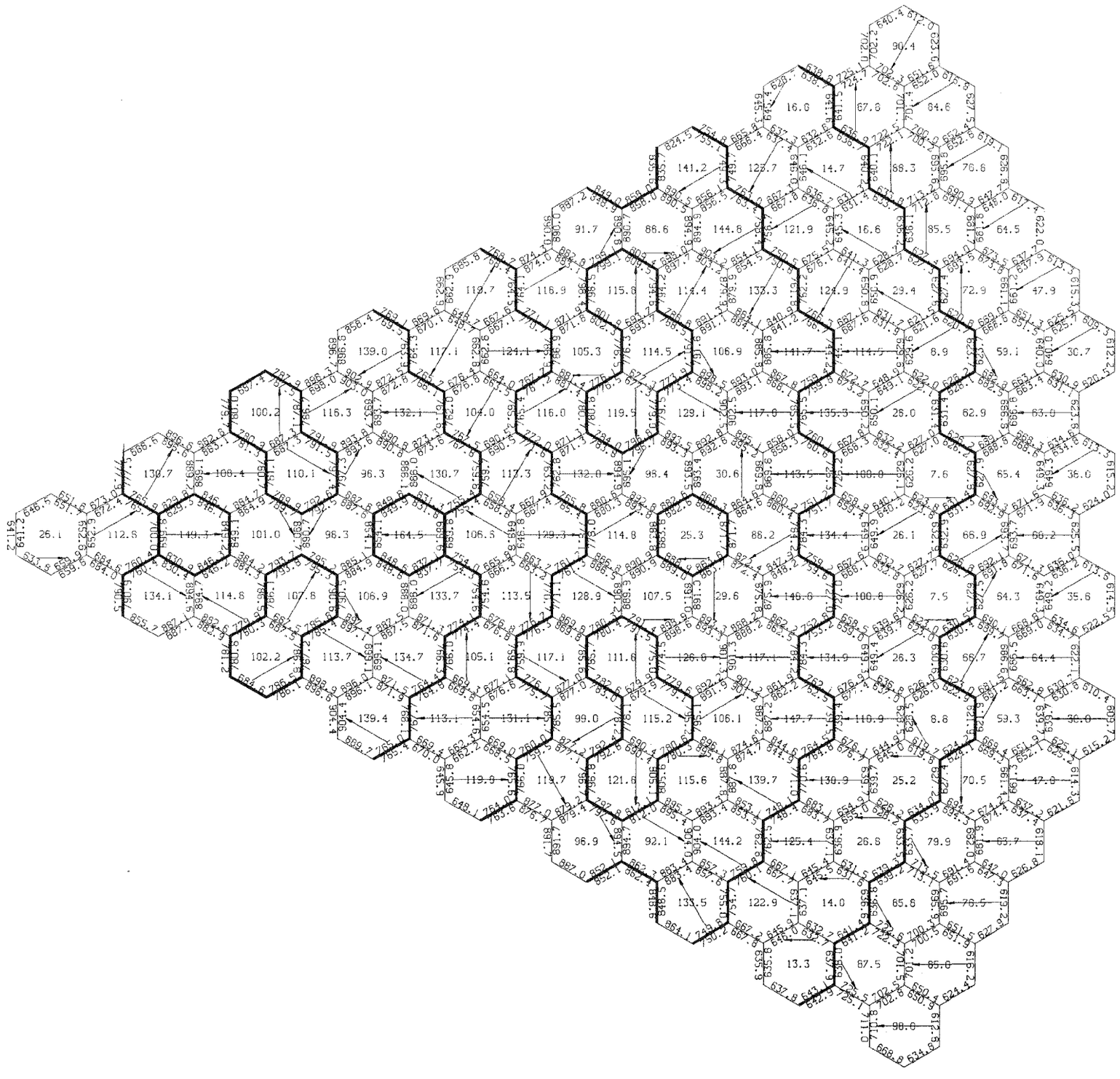

Figure J.14 Average duct wall temperatures (^{o}F) and maximum duct wall temperature differences (^{o}F) at BOC1 at the top of the upper axial blanket

WALL TEMPERATURES EOC1 FOR GEOM28 Z=70.0

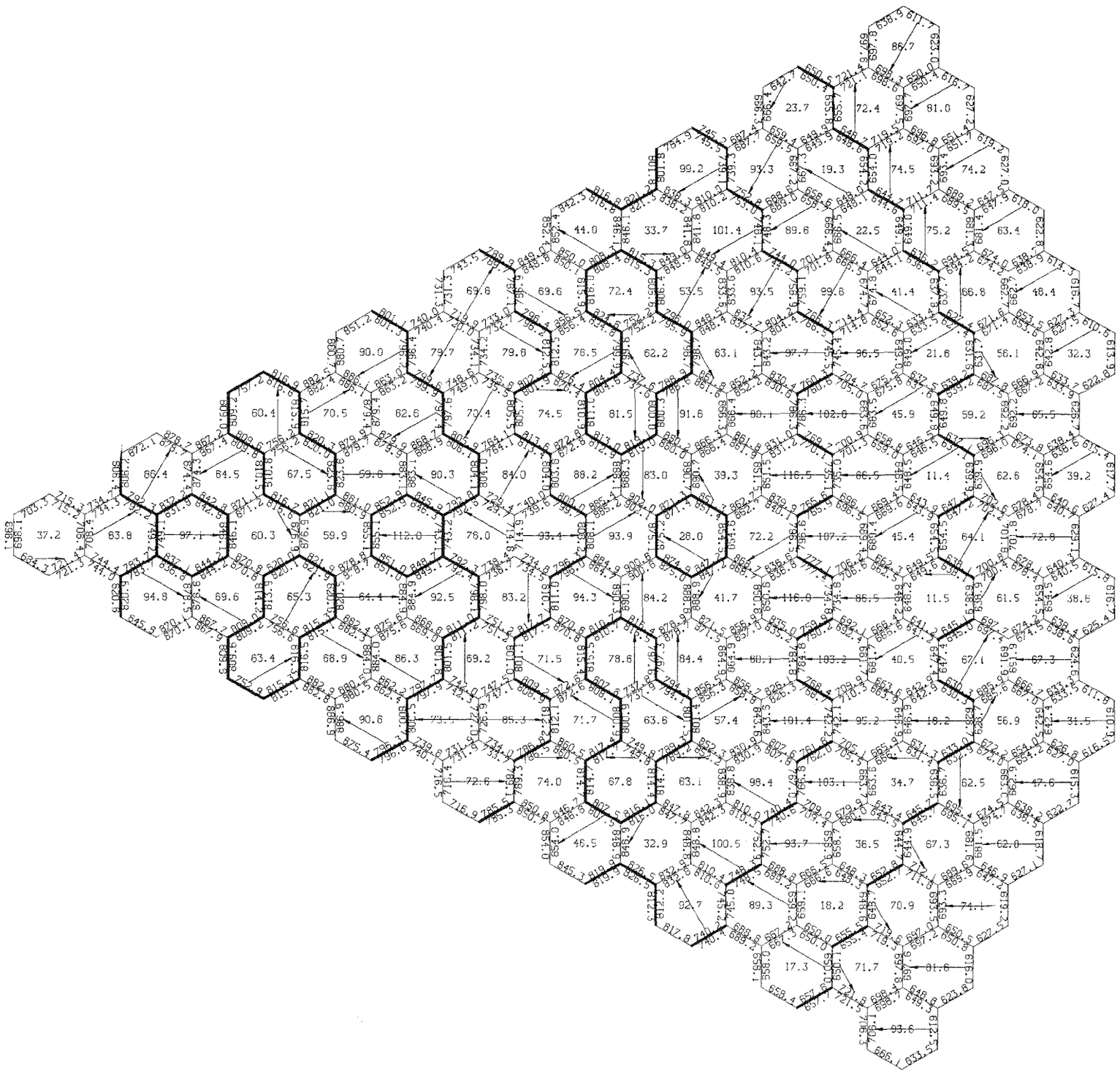

Figure J.15. Average duct wall temperatures (^{o}F) and maximum duct wall temperature differences (^{o}F) at EOC1 at the top of the upper axial blanket

WALL TEMPERATURES BOC2 FOR GEOM28 Z=70.0

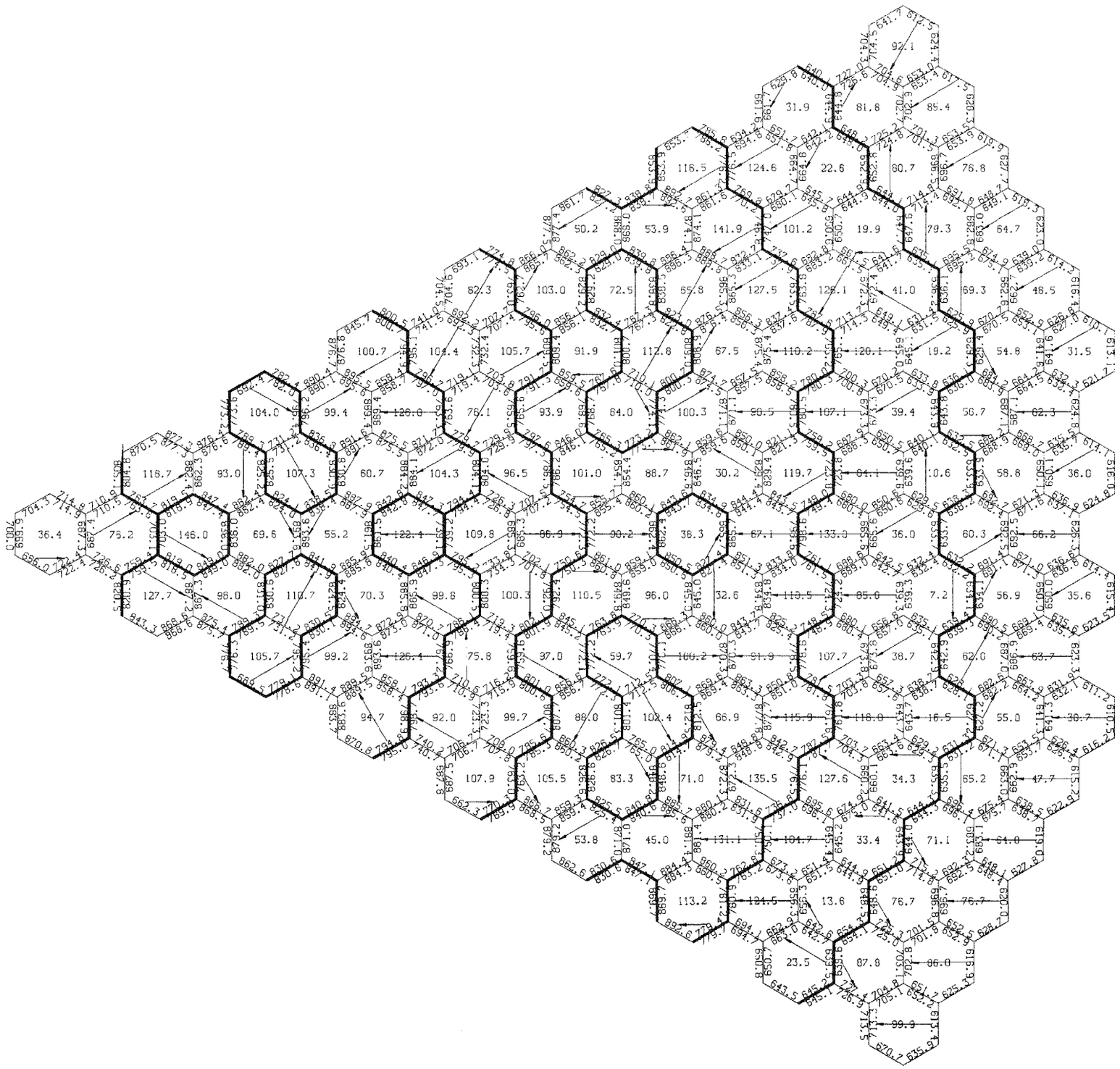

Figure J.16 Average duct wall temperatures (^{O}F) and maximum duct wall temperature differences (^{O}F) at BOC2 at the top of the upper axial blanket

WALL TEMPERATURES EOC2 FOR GEOM28 Z=70.0

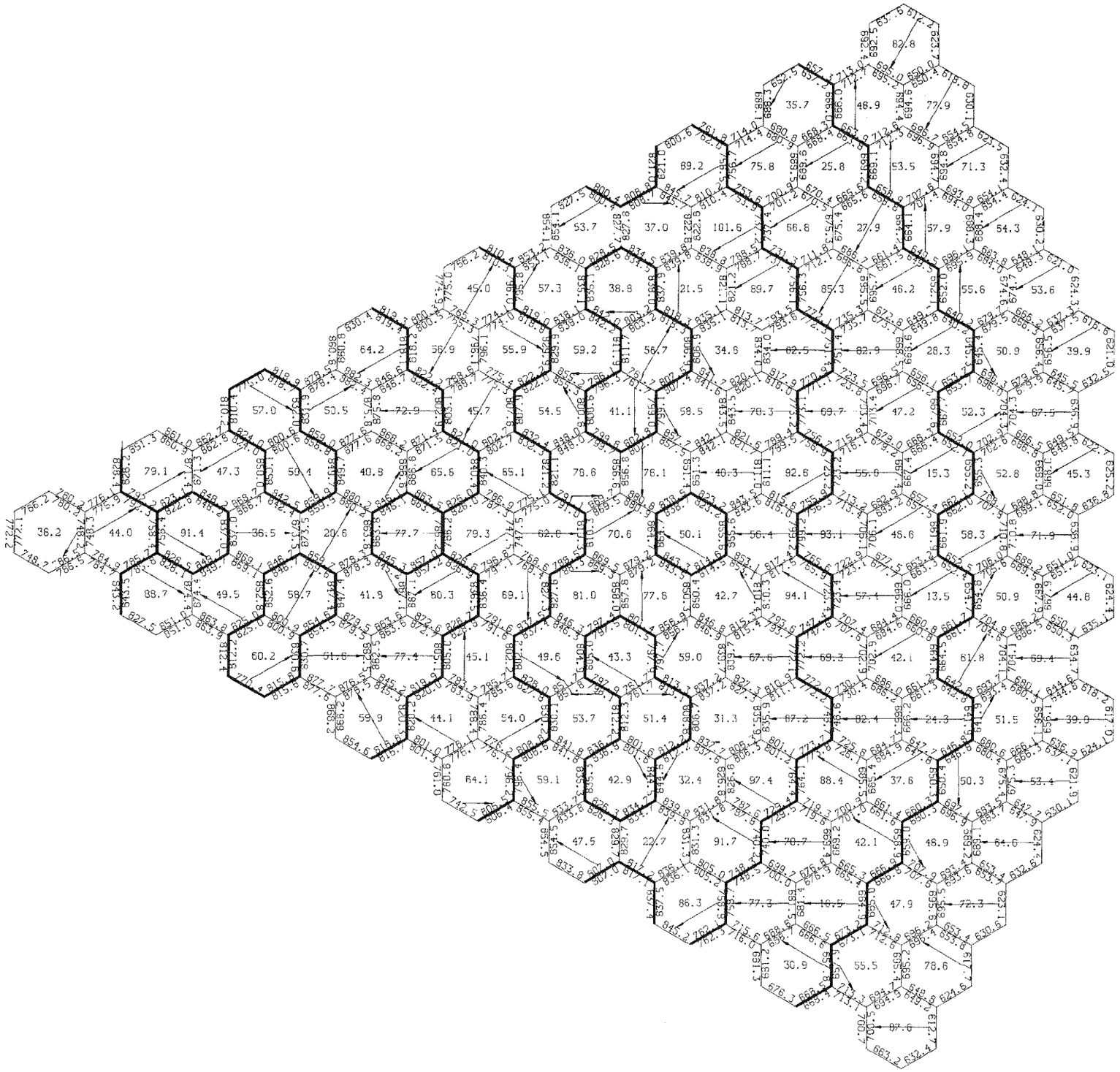

Figure J.17 Average duct wall temperatures (^{o}F) and maximum duct wall temperature differences (^{o}F) at EOC2 at the top of the upper axial blanket

WALL TEMPERATURES BOC3 FOR GEOM28 Z=70.0

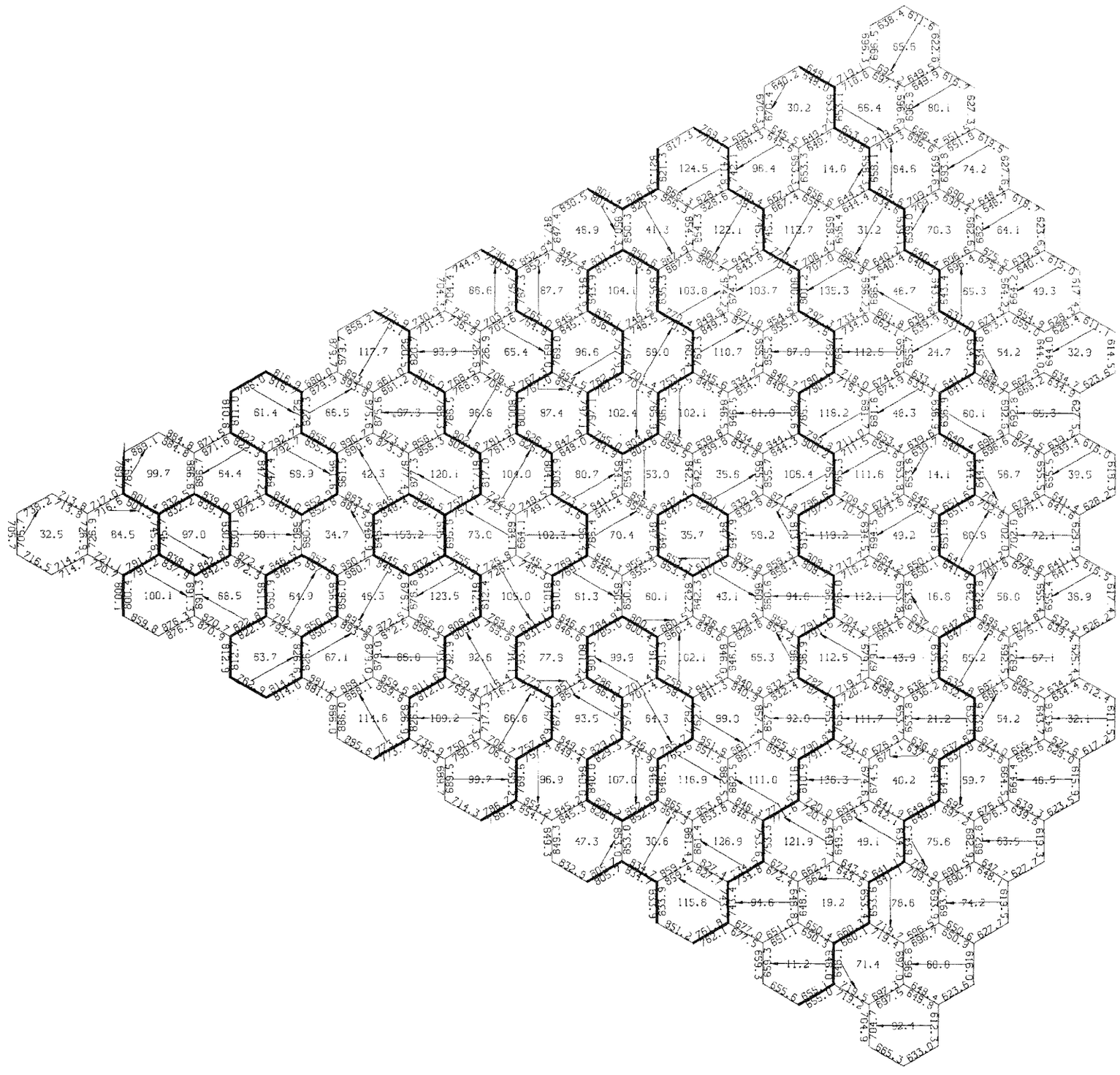

Figure J.18 Average duct wall temperatures (^{o}F) and maximum duct wall temperature differences (^{o}F) at BOC3 at the top of the upper axial blanket

WALL TEMPERATURES EOC3 FOR GEOM28 Z=70.0

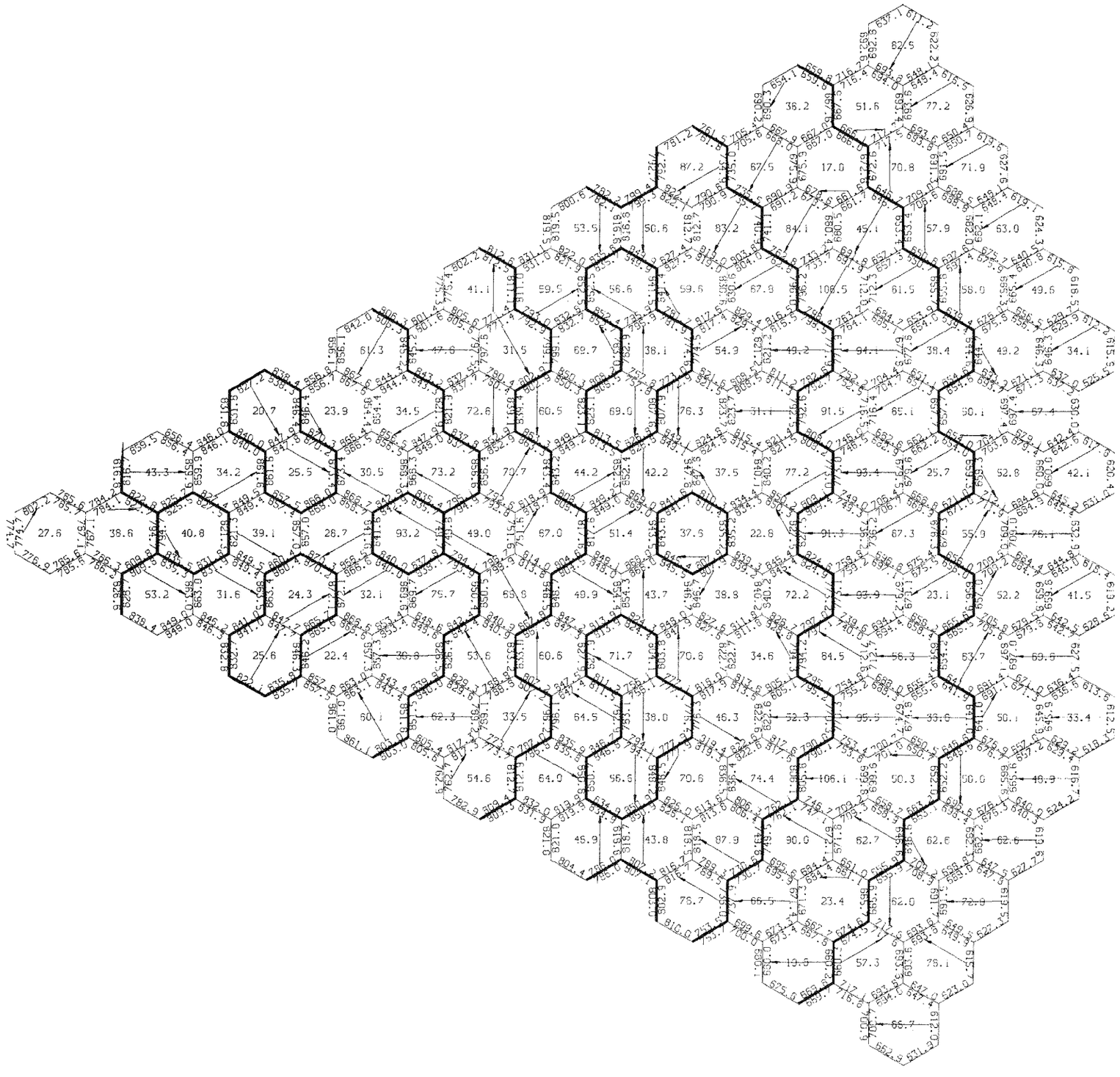

Figure J.19 Average duct wall temperatures (^{o}F) and maximum duct wall temperature differences (^{o}F) at EOC3 at the top of the upper axial blanket

WALL TEMPERATURES BOC4 FOR GEOM28 Z=70.0

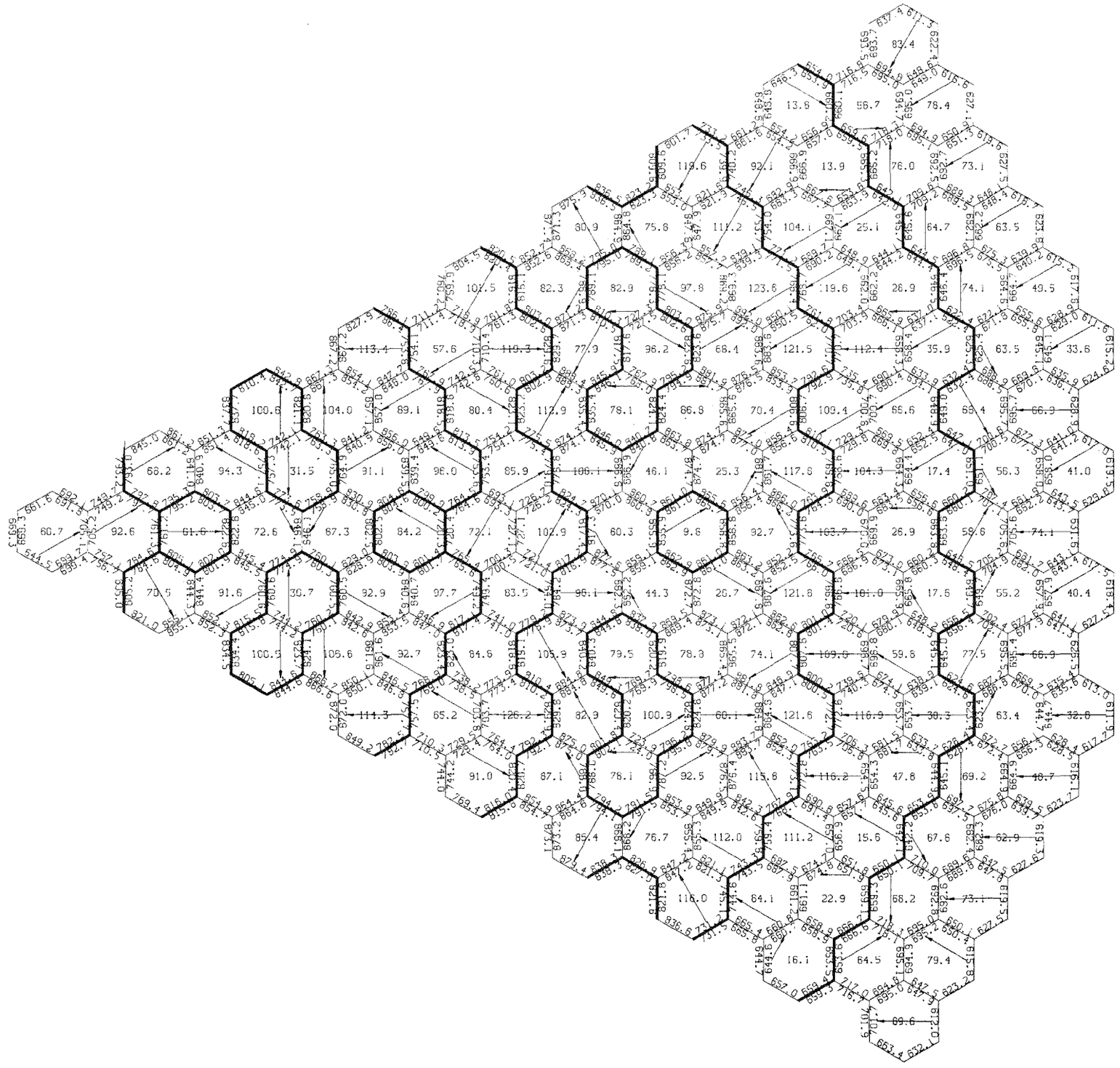

Figure J.20 Average duct wall temperatures (^{O}F) and maximum duct wall temperature differences (^{O}F) at BOC4 at the top of the upper axial blanket

WALL TEMPERATURES EOC4 FOR GEOM28 Z=70.0

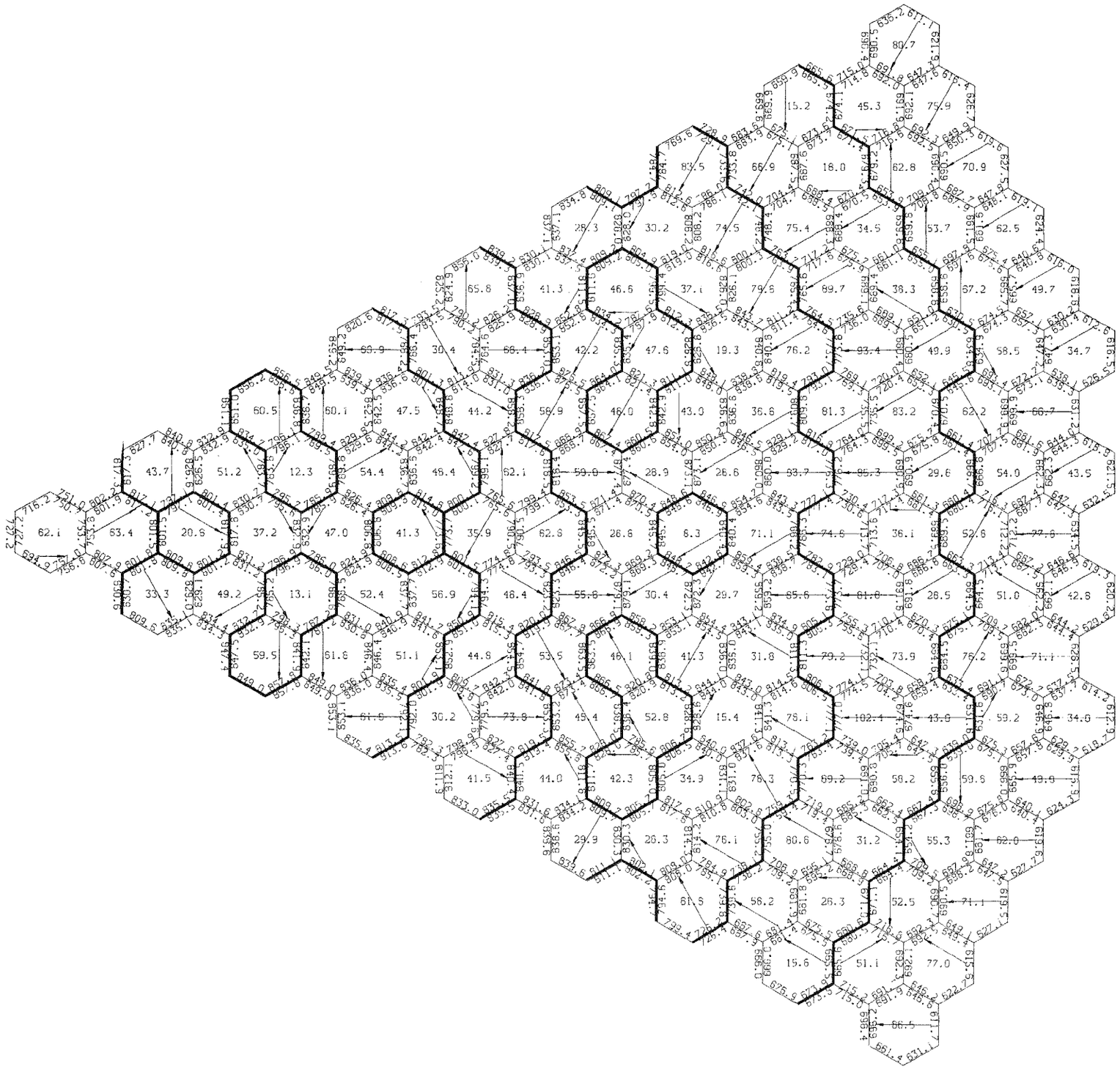

Figure J.21 Average duct wall temperature (^{o}F) and maximum duct wall temperatures differences (^{o}F) at EOC4 at the top of the upper axial blanket

Table J.9

MAXIMUM DUCT WALL TEMPERATURES AND DUCT WALL TEMPERATURE DIFFERENCES

Reactor Region	BOL	EOEC	BOC1	EOC1	BOC2	EOC2	BOC3	EOC3	BOC4	EOC4
					Duct Wall Temperatures (^{o}F)					
Core	915.0	869.6	904.4		895.6	887.1	893.8	870.3	892.0	879.1
Internal Blanket	804.0	844.8	812.1		848.2	859.9	861.6	873.4	849.3	866.9
Radial Blanket	801.2	819.2	785.5		798.6	799.2	810.9	827.5	810.1	816.8
					Duct Wall Temperature Differences (^{o}F)					
Core	161.3	93.4	148.8		141.9	101.6	126.9	87.9	123.6	85.6
Internal Blanket	127.7	55.5	131.1		112.8	79.3	109.2	72.6	126.2	73.8
Radial Blanket	144.8	94.3	135.3		133.0	93.1	136.3	106.5	119.6	102.4

cycle and they are 904^{o} F and 149^{o} F, respectively. In the blanket assemblies, the highest duct wall temperature occurs at EOL conditions and the highest duct wall temperature difference occurs at the beginning of the first cycle. Thus, the highest duct wall temperature for the internal blanket assemblies occurs at the end of the third cycle in an assembly that has reached end of life and is 873^{o} F. The higest duct wall temperature differences in the internal and radial blankets are 131^{o} F and 135^{o} F, respectively. These trends are easily explained by noting that: a) the maximum core power fraction and the minimum blanket power fraction occur at the beginning of the first cycle, and b) in a blanket assembly, the maximum power production occurs at EOL conditions.

For the same orificing strategy, a comparison of the results obtained from the analysis based on discrete fuel management with the results obtained from the analysis that was based on BOL and EOEC conditions (Section 4.2), shows the following:

1. The assignment of assemblies to orificng zones is different for ∿16% of the core and blanket assemblies (Figures 4.2.2.2.2 and J.5).
2. Discrete fuel management gives about 4% higher maximum assembly bundle average pressure drop (Tables 4.2.4.5.1 and J.7).
3. The difference in peak assembly coolant temperatures is negligible (4^{o} F, Table J.8).
4. The difference in peak nominal and 2σ cladding midwall temperatures is small (10^{o} F and 13^{o} F, respectively, Table J.8).
5. The difference in the highest duct wall temperatures and duct wall temperature differences is ∿11^{o} F and ∿13^{o} F, respectively (Table J.9).
6. If individual cycle information is not needed, the analysis based on BOL and EOEC conditions is adequate and requires much less manpower and computation time than the cycle-to-cycle analysis.

APPENDIX K
STRAIGHT BURN VS. MULTI-BATCH FUEL MANAGEMENT

Reactor performance characteristics such as:

a. fissile inventory
b. fissile gain
c. doubling time
d. fuel cycle cost
e. sodium void reactivity and
f. cladding temperatures

are dependent on the fuel management scheme. To investigate the impact of the fuel management scheme on the performance of the 0.28 inch fuel pin diameter design, in addition to the reference scheme discussed in Section 4.1.3.1, the nuclear and thermal-hydraulic performance of the reactor was analyzed for the following schemes:

a. two and three-year straight burn of the core and internal blanket fuel, and
b. refueling every year; core and internal blanket fuel residence time of two years.

In the first case, the radial blanket fuel residence time was six years and at the end of each cycle one third, for two-year straight burn, and one half, for three-year straight burn, of the irradiated radial blanket fuel was replaced with fresh fuel. In the second case, the radial blanket fuel had a residence time of five years and at the end of each cycle one fifth of it was replaced with fresh fuel. In all cases the assembly design is the same as for the reference design which was based on core and internal blanket fuel residence times of three years, radial blanket fuel residence time of five years, and refueling every year. The capacity factor is 70% for the partial core refueling case and 77.5% and 80% for the two-year and three-year straight burn cores, respectively. For comparison purposes, the results of this analysis are presented together with the corresponding results of

the analysis for the reference design.

K.1 Nuclear Analysis

Average fissile fuel enrichments for BOL, BOEC, and EOEC conditions are given in Tables K.1 to K.4. Fissile inventories for the same conditions are given in Tables K.5 to K.8.

The equilibrium cycle fresh fuel feed enrichment increases with core fuel residence time. The two-year fuel residence-time core with refueling every year has the lowest fresh fuel feed enrichment, 17.06%, and the three-year fuel residence-time core with straight burn has the highest fresh fuel feed enrichment, 17.35%. The straight burn reactors have lower BOEC inventories than the corresponding partial refueling reactors. The three-year core fuel residence-time reactor with straight burn has the lowest BOEC fissile inventory, 4,573.7 kg, and its corresponding partial refueling reactor has the highest BOEC fissile inventory, 4,761.6 kg.

The fractions of power produced in the different reactor regions are given in Tables K.9 to K.12. The power swing from the core zones to the internal blanket zones increases with fuel residence time and with switching from partial refueling to straight burn. Thus, the two-year fuel residence-time core with refueling every year has the smallest swing and the three-year straight burn core has the maximum swing. In the first case, the fraction of power produced in the internal blankets increases from 6.35% at BOL to 15.19% at EOEC. In the second case, the fraction of power produced in the internal blankets increases from 5.99% at BOEC to 23.59% at EOEC.

Peak to average power density ratios for each reactor zone, as determined from RZ calcualtions, are given in Tables K.13 to K.16. The fresh fuel enrichement and the BOL control rod distribution that minimize the power peaking factor at BOL and EOEC conditions as well as the core power peaking factor at the same conditions are given in Table K.17. In all cases two enrichment zones have been used. The second enrichment zone consists of the outer ring of core assemblies and the rest of the core assemblies belong to the first enrichment zone. In all cases the peak to average power density ratio is $\sim$1.5%. For the cores that are partially refueled every year, control rings 7 and 11 were used as a primary system.

Table K.1

AVERAGE FISSILE ENRICHMENTS[a] (%)

(Core Fuel Residence Time of Three Years, Refueling Every Year)

Reactor Region	BOL	BOEC[b]	EOEC
Core	17.12	16.46	15.82
Internal Blanket 1	0.00	1.08	2.07
Internal Blanket 2	0.00	1.51	2.84
Internal Blanket 3	0.00	1.35	2.55
Internal Blanket 4	0.00	1.33	2.51
Axial Blanket	0.00	0.61	1.18
Radial Blanket	0.00	0.98	1.43

[a] $\text{Enrichment} = \dfrac{^{239}\text{Pu} + ^{241}\text{Pu}}{^{233}\text{Pu} + ^{240}\text{Pu} + ^{241}\text{Pu} + ^{242}\text{Pu} + ^{235}\text{Pu} + ^{238}\text{U}} \dfrac{\text{kg}}{\text{kg}}$

[b] Fresh fuel feed enrichment = 17.17

Table K.2

AVERAGE FISSILE ENRICHMENT[a] (%)
(Core Fuel Residence Time of Two Years, Refueling Every Year)

Reactor Region	BOL	BOEC[b]	EOEC
Core	17.12	16.69	16.00
Internal Blanket 1	0.00	0.53	1.52
Internal Blanket 2	0.00	0.78	2.20
Internal Blanket 3	0.00	0.70	1.98
Internal Blanket 4	0.00	0.73	2.06
Axial Blanket	0.00	0.31	0.90
Radial Blanket	0.00	1.04	1.52

[a] $\text{Enrichment} = \dfrac{^{239}\text{Pu} + ^{241}\text{Pu}}{^{230}\text{Pu} + ^{240}\text{Pu} + ^{241}\text{Pu} + ^{242}\text{Pu} + ^{235}\text{U} + ^{238}\text{U}} \quad \dfrac{\text{kg}}{\text{kg}}$

[b] Fresh fuel feed enrichment = 17.06

Table K.3

AVERAGE FISSILE ENRICHMENT[a] (%)
(Two-Year Straight Burn)

Reactor Region	BOEC	EOEC
Core	17.12	15.61
Internal Blanket 1	---	2.11
Internal Blanket 2	---	3.00
Internal Blanket 3	---	2.75
Internal Blanket 4	---	2.87
Axial Blanket	---	1.29
Radial Blanket	1.40	2.18

$$^{a}\text{Enrichment} = \frac{^{239}Pu + ^{241}Pu}{^{239}Pu + ^{240}Pu + ^{241}Pu + ^{242}Pu + ^{235}U + ^{238}U} \frac{kg}{kg}$$

Table K.4

AVERAGE FISSILE ENRICHMENTS[a] (%)

(Three-Year Straight Burn)

Reactor Region	BOEC	EOEC
Core	17.35	15.19
Internal Blanket 1	0.00	3.25
Internal Blanket 2	0.00	4.31
Internal Blanket 3	0.00	3.94
Internal Blanket 4	0.00	3.89
Axial Blanket	0.00	1.94
Radial Blanket	0.84	2.33

[a] $\text{Enrichment} = \dfrac{^{239}Pu + ^{241}Pu}{^{239}Pu + ^{240}Pu + ^{241}Pu + ^{242}Pu + ^{235}U + ^{238}U} \dfrac{kg}{kg}$

Table K.5

FISSILE INVENTORIES, kg.

(Core Fuel Residence Time of Three Years, Refueling Every Year)

REACTOR REGION	BOL	BOEC	EOEC
Inner Core	458.6	426.6	396.9
Middle Core	917.3	850.8	789.5
Outer Core	2884.8	2706.3	2536.9
TOTAL CORE	4260.7	3983.7	3723.3
Internal Blanket 1	0.0	35.9	68.6
Internal Blanket 2	0.0	63.3	118.3
Internal Blanket 3	0.0	183.7	346.1
Internal Blanket 4	0.0	83.5	157.2
TOTAL INTERNAL BLANKET	0.0	366.4	690.2
Axial Blanket	0.0	114.6	223.7
Radial Blanket	0.0	296.9	435.1
TOTAL REACTOR	4260.7	4761.6	5072.3

Table K.6

FISSILE INVENTORIES, kg

(Core Fuel Residence Time of Two Years, Refueling Every Year)

REACTOR REGION	BOL	BOEC	EOEC
Inner Core	458.6	440.5	409.8
Middle Core	917.3	879.4	815.4
Outer Core	2884.8	2775.5	2590.2
TOTAL CORE	4260.7	4095.4	3815.4
Internal Blanket 1	0.0	17.6	50.4
Internal Blanket 2	0.0	32.7	91.6
Internal Blanket 3	0.0	95.5	269.6
Internal Blanket 4	0.0	45.9	128.9
TOTAL INTERNAL BLANKET	0.0	191.7	540.5
Axial Blanket	0.0	57.9	169.4
Radial Blanket	0.0	316.3	462.8
TOTAL REACTOR	4260.7	4661.3	4988.1

Table K.7

FISSILE INVENTORIES, kg
(Two-Year Straight Burn)

REACTOR REGION	BOL	BOEC	EOEC
Inner Core		458.5	393.1
Middle Core		917.3	780.0
Outer Core		2884.8	2479.0
TOTAL CORE		4260.7	3652.1
Internal Blanket 1		0.0	69.8
Internal Blanket 2		0.0	124.7
Internal Blanket 3		0.0	373.3
Internal Blanket 4		0.0	179.2
TOTAL INTERNAL BLANKET		0.0	747.0
Axial Blanket		0.0	243.5
Radial Blanket		348.9	660.0
TOTAL REACTOR		4609.6	5303.5

Table K.8

FISSILE INVENTORIES, kg
(Three-Year Straight Burn)

REACTOR REGION	BOEC	EOEC
Inner Core	465.0	366.0
Middle Core	930.0	725.1
Outer Core	2924.8	2351.1
TOTAL CORE	4319.8	3442.2
Internal Blanket 1	0.0	107.2
Internal Blanket 2	0.0	177.6
Internal Blanket 3	0.0	530.7
Internal Blanket 4	0.0	241.0
TOTAL INTERNAL BLANKET	0.0	1056.5
Axial Blanket	0.0	366.1
Radial Blanket	253.9	705.1
TOTAL REACTOR	4573.7	5569.9

Table K.9

POWER DISTRIBUTION[a] (%)

(Core Fuel Residence Time of Three Years, Refueling Every Year)

REACTOR REGION	FIRST CYCLE		EQUILIBRIUM CYCLE	
	BOC	EOC	BOC	EOC
Inner Core	9.83	9.96	9.33	9.21
Middle Core	20.69	20.63	19.60	19.13
Outer Core	59.44	51.04	52.61	46.49
TOTAL CORE	89.96	81.63	81.54	74.83
Internal Blanket 1	0.43	0.96	0.88	1.39
Internal Blanket 2	1.21	2.66	2.37	3.50
Internal Blanket 3	2.77	6.20	5.79	8.72
Internal Blanket 4	1.94	3.35	3.22	4.16
TOTAL INTERNAL BLANKET	6.35	13.17	12.26	17.77
Axial Blanket	1.36	2.09	2.05	2.78
Radial Blanket	2.12	2.90	3.93	4.39
Radial Reflector	0.21	0.21	0.22	0.23

[a] γ-heating included

Table K.10

POWER DISTRIBUTION[a] (%)

(Core Fuel Residence Time of Two Years, Refueling Every Year)

REACTOR REGION	FIRST CYCLE		EQUILIBRIUM CYCLE	
	BOC	EOC	BOC	EOC
Inner Core	9.83	9.96	8.96	9.17
Middle Core	20.69	20.63	19.11	19.20
Outer Core	59.44	51.04	56.35	48.93
TOTAL CORE	89.96	81.63	84.42	77.30
Internal Blanket 1	0.43	0.96	0.60	1.09
Internal Blanket 2	1.21	2.66	1.71	2.94
Internal Blanket 3	2.77	6.20	4.23	7.31
Internal Blanket 4	1.94	3.35	2.70	3.85
TOTAL INTERNAL BLANKET	6.35	13.17	9.24	15.19
Axial Blanket	1.36	2.09	1.69	2.40
Radial Blanket	2.12	2.90	4.42	4.88
Radial Reflector	0.21	0.21	0.23	0.23

[a] γ-heating included

Table K.11

POWER DISTRIBUTION[a] (%)
(Two-Year Straight Burn)

REACTOR REGION	BOL	BOEC	EOEC
Inner Core	9.98	8.16	8.89
Middle Core	20.93	17.87	18.56
Outer Core	59.17	61.40	45.10
TOTAL CORE	90.08	87.43	72.55
Internal Blanket 1	0.43	0.36	1.38
Internal Blanket 2	1.21	1.02	3.55
Internal Blanket 3	2.74	2.57	9.06
Internal Blanket 4	1.92	1.98	4.44
TOTAL INTERNAL BLANKET	6.30	5.93	18.43
Axial Blanket	1.34	1.31	2.87
Radial Blanket	2.08	51.0	5.19
Radial Reflector	0.20	0.23	0.24

[a] γ- heating included

Table K.12

POWER DISTRIBUTION[a] (%)

(Three-Year Straight Burn)

REACTOR REGION	BOEC	EOEC
Inner Core	8.63	8.65
Middle Core	18.68	17.81
Outer Core	60.98	40.45
TOTAL CORE	88.29	66.91
Internal Blanket 1	0.37	2.04
Internal Blanket 2	1.06	4.58
Internal Blanket 3	2.60	11.93
Internal Blanket 4	1.96	5.04
TOTAL INTERNAL BLANKET	5.99	23.59
Axial Blanket	1.31	3.73
Radial Blanket	4.17	5.53
Radial Reflector	0.24	0.24

[a] γ-heating included

Table K.13

PEAK/AVERAGE POWER DENSITY RATIOS

(Core Fuel Residence Time of Three Years, Refueling Every Year)

REACTOR REGION	FIRST CYCLE		EQUILIBRIUM CYCLE	
	BOC	EOC	BOC	EOC
Inner Core	1.328	1.301	1.302	1.279
Middle Core	1.348	1.310	1.308	1.272
Outer Core	1.439	1.450	1.428	1.456
TOTAL CORE	1.420	1.517	1.441	1.492
Internal Blanket 1	3.600	3.110	3.095	2.830
Internal Blanket 2	2.184	2.234	2.211	2.175
Internal Blanket 3	2.599	2.414	2.398	2.326
Internal Blanket 4	2.074	2.218	2.178	2.198
Axial Blanket	3.068	3.203	2.931	3.160
Radial Blanket	4.946	4.794	4.680	4.527

Table K.14

PEAK/AVERAGE POWER DENSITY RATIOS

(Core Fuel Residence Time of Two Years, Refueling Every Year)

REACTOR REGION	FIRST CYCLE		EQUILIBRIUM CYCLE	
	BOC	EOC	BOC	EOC
Inner Core	1.328	1.301	1.318	1.293
Middle Core	1.348	1.310	1.321	1.290
Outer Core	1.439	1.450	1.421	1.427
TOTAL CORE	1.420	1.517	1.410	1.469
Internal Blanket 1	3.600	3.110	3.209	2.919
Internal Blanket 2	2.184	2.234	2.220	2.213
Internal Blanket 3	2.599	2.414	2.516	2.338
Internal Blanket 4	2.074	2.218	2.148	2.206
Axial Blanket	3.068	3.203	3.070	3.432
Radial Blanket	4.946	4.794	4.707	4.541

Table K.15

PEAK/AVERAGE POWER DENSITY RATIOS
(Two-Year Straight Burn)

REACTOR REGION	BOEC	EOEC
Inner Core	1.332	1.274
Middle Core	1.337	1.268
Outer Core	1.405	1.432
TOTAL CORE	1.467	1.484
Internal Blanket 1	3.616	2.757
Internal Blanket 2	2.201	2.207
Internal Blanket 3	2.876	2.332
Internal Blanket 4	2.139	2.218
Axial Blanket	3.483	3.232
Radial Blanket	4.357	4.008

Table K.16

PEAK/AVERAGE POWER DENSITY RATIOS
(Three-Year Straight Burn)

REACTOR REGION	BOEC	EOEC
Inner Core	1.332	1.243
Middle Core	1.338	1.229
Outer Core	1.416	1.480
TOTAL CORE	1.454	1.500
Internal Blanket 1	3.470	2.538
Internal Blanket 2	2.178	2.095
Internal Blanket 3	2.677	2.254
Internal Blanket 4	2.090	2.163
Axial Blanket	3.380	3.445
Radial Blanket	4.760	4.230

Table K.17

FRESH FUEL ENRICHMENTS[a], CONTROL ROD INSERTION PATTERN, AND PEAK/AVERAGE POWER DENSITY RATIOS

Core Fuel Residence Time of Two Years, Refueling Every Year

	BOL	Equilibrium Cycle
Fresh Fuel Enrichments Zone 1/Zone 2	0.1702/0.1847	0.1702/0.1854
Control Rod Insertion Pattern Row 11/Row 7	9.873/1.0	
Peak/Average Power Density Ratio	1.484	1.503[b]

Core Fuel Residence Time of Three Years, Refueling Every Year

Fresh Fuel Enrichments Zone 1/Zone 2	0.1702/0.1847	0.1716/0.1927
Control Rod Insertion Pattern Row 11/Row 7	9.873/1.0	
Peak/Average Power Density Ratio	1.484	1.482[b]

Two-Year - Straight Burn

Fresh Fuel Enrichments Zone 1/Zone 2	0.1715/0.2092	0.1709/0.1953
Control Rod Insertion Pattern Row 11/Row 13	12.0/1.0	
Peak/Average Power Density Ratio	1.547	1.485[b]

[a] $\text{Enrichment} = \dfrac{^{239}Pu + ^{241}Pu}{^{239}Pu + ^{240}Pu + ^{241}Pu + ^{242}Pu + ^{235}U + ^{238}U} \dfrac{kg}{kg}$

[b] EOEC

For the two-year straight burn core, control rings 11 and 13 had to be used as a primary system to optimize the BOL power distribution. As discussed later, the three-year straight burn reactor has a sodium void reactivity well above the design objective of $2.50 and consequently, power shape optimization has not been performed for this design option.

Average and peak discharge burnups per reactor regions are given in Table K.18. The core fuel peak discharge burnup increases with fuel residence time and with switching from partial refueling to straight burn. Thus, the two-year fuel residence-time core with refueling every year, has the lowest peak discharge burnup, 72,724 MWD/T, and the three-year straight burn core has the maximum peak discharge burnup, 121,409 MWD/T. The internal blanket fuel peak discharge burnup follows the same trend and varies from 17,610 MWD/T to 38,414 MWD/T, respectively.

Region-wise breeding ratios are given in Tables K.19 to K.22. Fissile inventories, fissile gain, compound system doubling time, and relative fuel cycle cost are presented in Table K.23. The average breeding ratio of the equilibrium cycle decreases with core fuel residence time and with switching from partial refueling to straight burn. The reactor that has a two-year core and internal blanket fuel residence-time with refueling every year, has the largest equilibrium cycle average breeding ratio, 1.431, and the three-year straight burn reactor has the smallest equilibrium cycle average breeding ratio, 1.386. The BOEC fissile inventory increases with core fuel residence time in the case of the cores that are partially refueled every year. The fissile gain shows the opposite trend. For straight burn, the BOEC fissile inventory decreases and the fissle gain increases with core fuel residence time. Finally, for the same refueling scheme, the compound system doubling time decreases as the core fuel residence time increases. The straight burn reactors have a lower compound system doubling time than the partially refueled reactors and the three-year straight burn reactor has the lowest compound system doubling time, 13.07 years.

Fuel cycle cost decreases as the core fuel residence time increases, and as partial refueling is replaced by straight burn. Thus, the reactor that has a two-year core fuel residence time with refueling every year, has the highest fuel cycle cost, and the three-year straight burn reactor has the lowest fuel cycle cost.

Flowing sodium void reactivities are presented in Tables K.24 to K.26. Both straight burn reactors have higher EOEC sodium void reactivities than the partially

Table K.18

AVERAGE AND PEAK DISCHARGE BURNUPS
(MWD/T)

	Core Fuel Residence Time of Two Years, Refueling Every Year		Core Fuel Residence Time of Three Years, Refueling Every Year		Two-Year Straight Burn		Three-Year Straight Burn	
	Average	Peak	Average	Peak	Average	Peak	Average	Peak
Core	50520	72724	73200	107340	55090	81285	82200	121409
Internal Blanket 1	3410	10448	7130	21120	3800	12109	8540	25654
Internal Blanket 2	7943	17610	15350	33660	8810	19417	17980	38414
Internal Blanket 3	5913	14351	11450	27040	6740	17551	13780	33975
Internal Blanket 4	7535	16410	12870	28620	8650	18844	15340	32621
Axial Blanket	1340	4360	2470	7520	1530	5137	2980	10169
Radial Blanket	5289	24460	4710	21690	8750	35844	7860	35331

Table K. 19
BREEDING RATIOS
(Core Fuel Residence Time of Three Years, Refueling Every Year)

REACTOR REGION	BOL	BOEC	EOEC
Inner Core	0.067	0.065	0.067
Middle Core	0.138	0.136	0.138
Outer Core	0.380	0.347	0.319
TOTAL CORE	0.585	0.548	0.524
Internal Blanket 1	0.046	0.047	0.051
Internal Blanket 2	0.093	0.090	0.091
Internal Blanket 3	0.266	0.260	0.260
Internal Blanket 4	0.138	0.124	0.114
TOTAL INTERNAL BLANKET	0.543	0.521	0.516
Axial Blanket	0.151	0.149	0.151
Radial Blanket	0.230	0.213	0.192
REACTOR TOTAL	1.509	1.431	1.383

Table K.20

BREEDING RATIOS

(Core Fuel Residence Time of Two Years, Refueling Every Year)

REACTOR REGION	BOL	BOEC	EOEC
Inner Core	0.067	0.062	0.066
Middle Core	0.138	0.131	0.137
Outer Core	0.380	0.367	0.333
TOTAL CORE	0.585	0.560	0.536
Internal Blanket 1	0.046	0.044	0.049
Internal Blanket 2	0.093	0.086	0.090
Internal Blanket 3	0.266	0.255	0.258
Internal Blanket 4	0.138	0.132	0.118
TOTAL INTERNAL BLANKET	0.543	0.517	0.515
Axial Blanket	0.151	0.148	0.149
Radial Blanket	0.230	0.231	0.205
REACTOR TOTAL	1.509	1.456	1.405

Table K.21

BREEDING RATIOS
(Two-Year Straight Burn)

REACTOR REGION	BOEC	EOEC
Inner Core	0.055	0.065
Middle Core	0.119	0.135
Outer Core	0.389	0.314
TOTAL CORE	0.563	0.514
Internal Blanket 1	0.038	0.050
Internal Blanket 2	0.078	0.089
Internal Blanket 3	0.246	0.255
Internal Blanket 4	0.140	0.111
TOTAL INTERNAL BLANKET	0.502	0.505
Axial Blanket	0.145	0.149
Radial Blanket	0.254	0.196
REACTOR TOTAL	1.464	1.364

Table K.22

BREEDING RATIOS
(Three-Year Straight Burn)

REACTOR REGION	BOEC	EOEC
Inner Core	0.057	0.066
Middle Core	0.122	0.137
Outer Core	0.380	0.333
TOTAL CORE	0.559	0.536
Internal Blanket 1	0.040	0.054
Internal Blanket 2	0.081	0.088
Internal Blanket 3	0.249	0.255
Internal Blanket 4	0.138	0.102
TOTAL INTERNAL BLANKET	0.508	0.499
Axial Blanket	0.145	0.152
Radial Blanket	0.244	0.177
REACTOR TOTAL	1.456	1.315

Table K.23

FISSILE INVENTORY, FISSILE GAIN, AND COMPOUND SYSTEM DOUBLING TIME

	Refueling Every Year				Straight Burn			
	Core Fuel Residence Time of Two Years		Core Fuel Residence Time of Three Years		Two Years		Three Years	
	BOEC	EOEC	BOEC	EOEC	BOEC	EOEC	BOEC	EOEC
Fissile Inventory (kg)								
Core	4095.4	3815.4	3983.8	3723.3	4260.7	3652.1	4319.8	3442.2
Internal Blanket	191.7	540.5	366.4	690.2	--	747.0	--	1056.5
Axial Blanket	57.9	169.4	114.6	223.7	--	243.5	--	366.1
Radial Blanket	316.3	462.8	296.8	435.1	348.9	660.9	253.9	705.1
TOTAL REACTOR	4661.3	4988.1	4761.6	5072.3	4609. 6	5303.5	4573.7	5569.9
Fissile Gain (kg)/ Cycle	326.8		310.7		693.9		996.2	
CSDT (years)	16.30		15.7		14.46		13.07	
Relative Fuel Cycle Cost	1.00		0.72		0.86		0.57	

Table K.24

FLOWING SODIUM VOID REACTIVITIES ($)

(Core Fuel Residence Time of Three Years, Refueling Every Year)

REACTOR REGION	BOL	EOEC
	Perturbation Results	
Inner Core	0.208	0.396
Middle Core	0.438	0.886
Outer Core	0.806	1.316
TOTAL CORE	1.452	2.598
Internal Blanket 1	0.006	0.041
Internal Blanket 2	0.204	0.268
Internal Blanket 3	0.406	0.553
Internal Blanket 4	0.266	0.247
TOTAL INTERNAL BLANKET	0.882	1.109
Radial Blanket	-0.226	-0.140
Axial Blanket	-0.190	-0.178
Core and Upper Axial Blanket	1.357	2.509
	Corrected*	
Core and Upper Axial Blanket	1.322	2.575

*Section 4.1.3.8

Table K.25

FLOWING SODIUM VOID REACTIVITIES ($)
(Core Fuel Residence Time of Two Years, Refueling Every Year)

REACTOR REGION	BOL	EOEC
	Perturbation Results	
Inner Core	0.208	0.335
Middle Core	0.438	0.768
Outer Core	0.806	1.280
TOTAL CORE	1.452	2.383
Internal Blanket 1	0.006	0.028
Internal Blanket 2	0.204	0.244
Internal Blanket 3	0.406	0.499
Internal Blanket 4	0.266	0.254
TOTAL INTERNAL BLANKET	0.882	1.025
Radial Blanket	-0.226	-0.157
Axial Blanket	-0.190	-0.183
Core and Upper Axial Blanket	1.357	2.291
	Corrected*	
Core and Upper Axial Blanket	1.332	2.372

*Section 4.1.3.8

Table K.26

EOEC FLOWING SODIUM VOID REACTIVITIES ($)
(Straight Burn)

REACTOR REGION	RESIDENCE TIME 2 Years	3 Years
	Perturpation Results	
Inner Core	0.394	0.519
Middle Core	0.917	1.186
Outer Core	1.445	1.541
TOTAL CORE	2.756	3.246
Internal Blanket 1	0.041	0.077
Internal Blanket 2	0.265	0.311
Internal Blanket 3	0.558	0.680
Internal Blanket 4	0.251	0.241
TOTAL INTERNAL BLANKET	1.115	1.309
Radial Blanket	-0.124	-0.093
Axial Blanket	-0.176	-0.158
Core and Upper Axial Blanket	2.668	3.167
	Corrected*	
Core and Upper Axial Blanket	2.738	3.222

*Section 4.1.3.8

refueled reactors. Especially, the three-year straight burn reactor has an EOEC reactivity of $3.22 which is much higher than the design objective of $2.50. The reactor with a two-year core fuel residence time and refueling every year, has the lowest EOEC sodium void reactivity, $2.37.

Since the sodium void reactivity of the three-year straight burn option is much higher than the design objective of $2.50, this option will not be analyzed any further.

K.2 Thermal-Hydraulic Analysis

As discussed in Section 4.2.4.3, the orificing strategy that is based on assigning assemblies to orificing zones according to assembly peak pin power and on equalizing the peak cladding midwall temperatures yields the lowest 2σ peak cladding midwall temperature. This orificing strategy has been used in the thermal-hydraulic analysis of the 0.28 inch fuel pin diameter design for the fuel management schemes investigated in this Appendix; i.e.,

a. Two years straight burn of the core and internal blanket fuel and,
b. Refueling every year, core and internal blanket fuel residence time of two years.

The methodology used in this analysis is the same one discussed in Section 4.2.4. For comparison purposes, the results of this analysis are presented together with the corresponding results of the analysis for the reference design.

The assignment of assemblies to orificing zones is shown in Figures K.1 to K.3. Assembly coolant flow rates, coolant velocities, and assembly bundle pressure drops are given in Tables K.27, K.28, and K.29, respectively. The flow split among the different reactor regions depends on the fuel management scheme. Since the power swing from the core to the blanket assemblies increases as the core and blanket fuel residence time increases, the flow fraction allocated to the blanket assemblies also increases as the core and internal blanket fuel residence time increases from two to three years. Thus, for the reactors that are refueled every year, increasing the core and internal blanket fuel residence time from two years to three years increases the flow fractions allocated to the blanket regions from 24.4% to 28.9%. For the straight burn reactor the flow fraction allocated to the blankets is equal to 26.2%. Since the flow splits among the different reactor regions depend

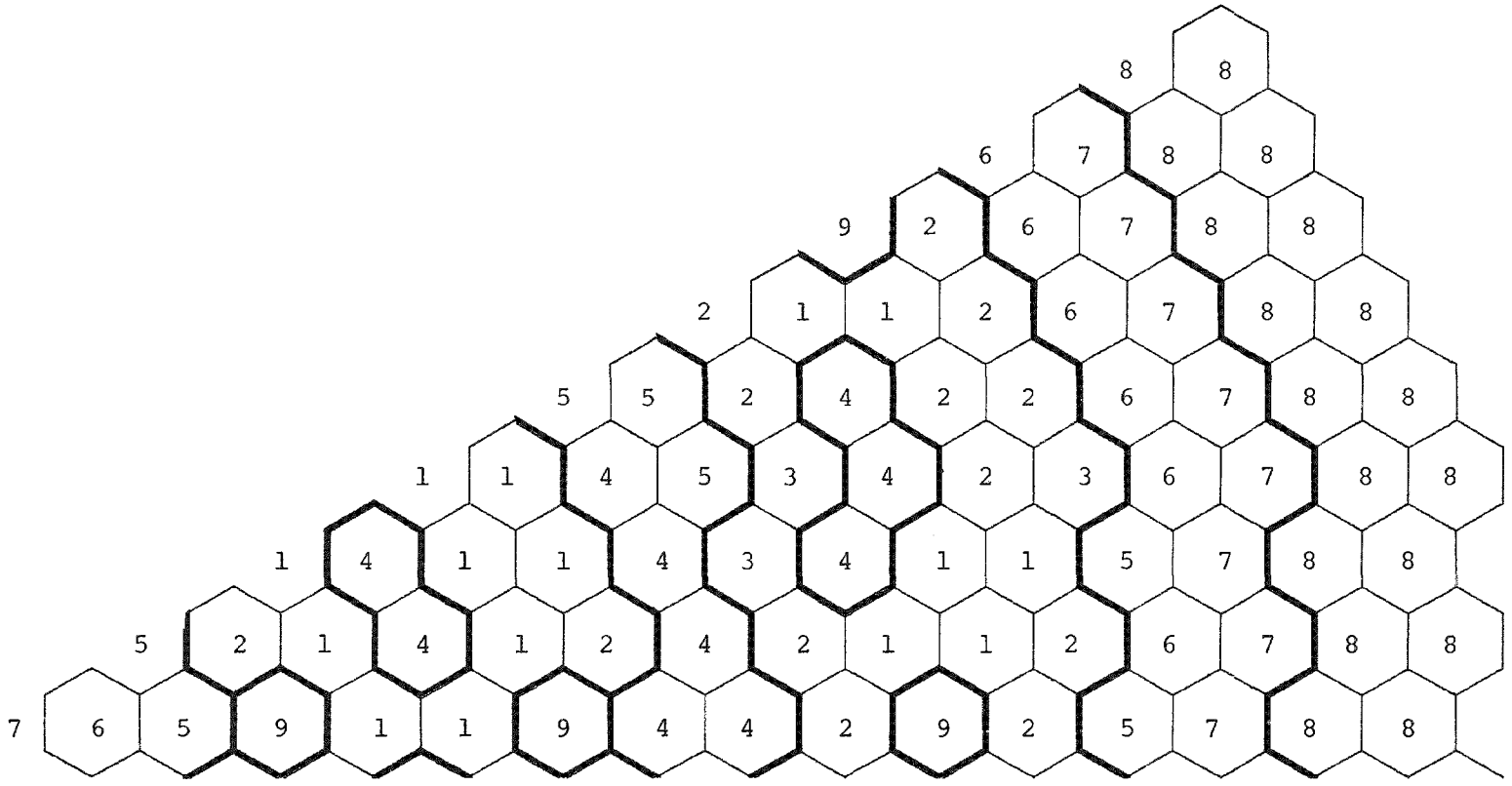

Figure K.1. Assembly assignment to orificing zones (Core fuel residence time of two years,refueling every year).

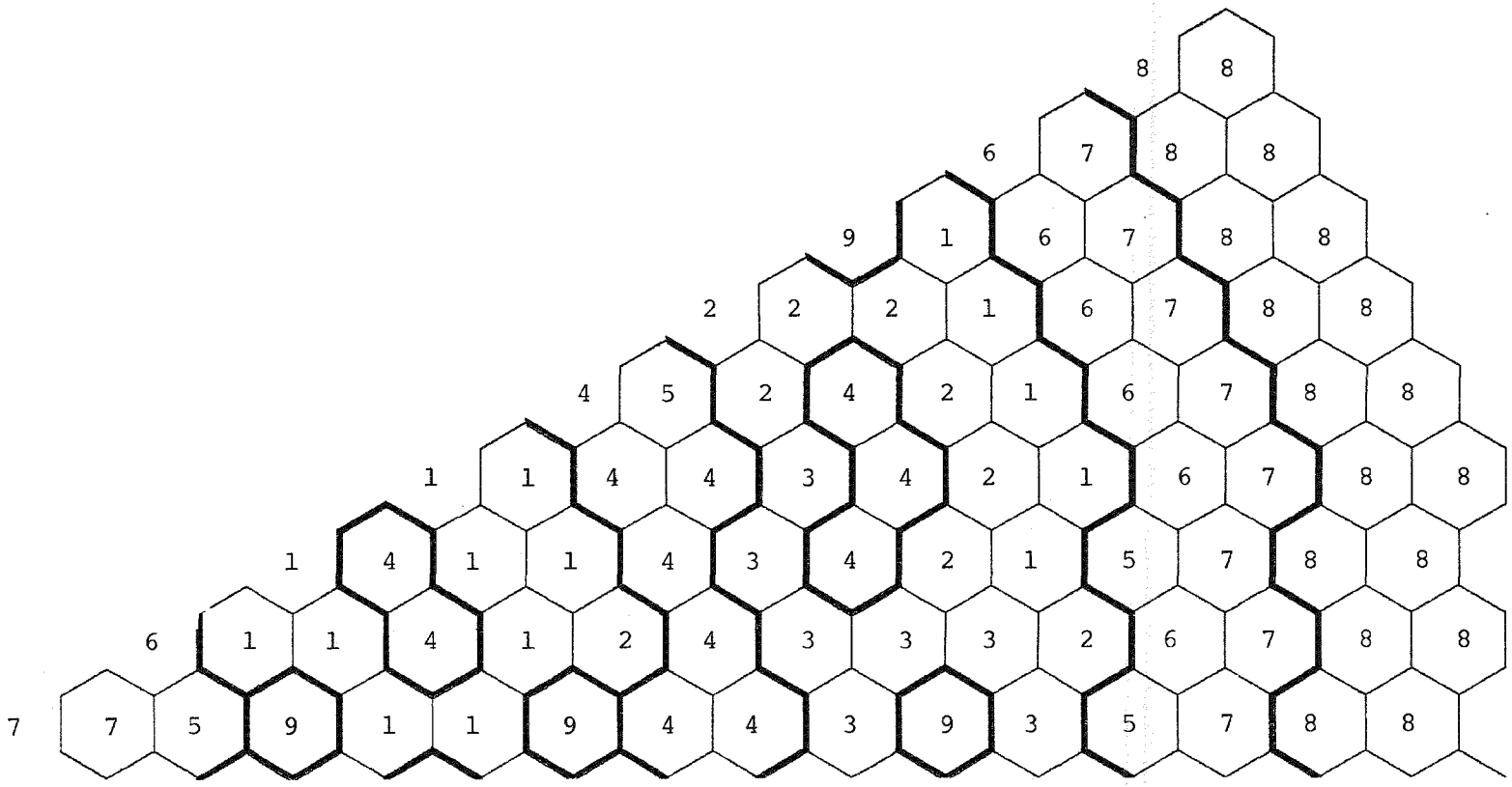

Figure K.2. Assembly assignment to orificing zones (Two-year straight burn).

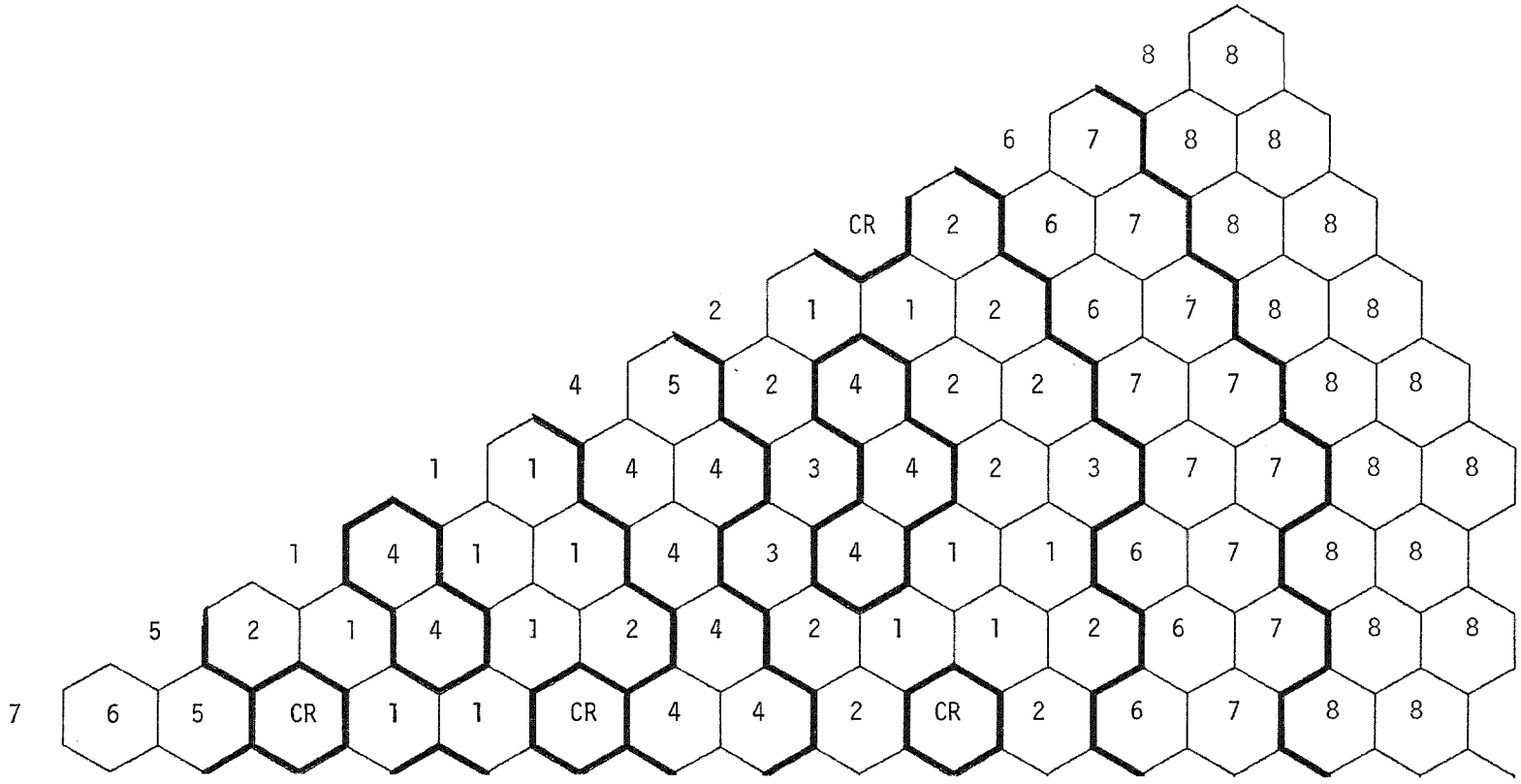

Figure K.3. Assembly assignment to orificing zones according to assembly peak pin power (Reference design).

Table K.27

ASSEMBLY COOLANT FLOW RATES (lbm/hr)

Orificing Zone	Number of Assemblies	Core Fuel Residence Time of Two Years, Yearly Refueling	Number of Assemblies	Two-Year Straight Burn	Number of Assemblies	Core Fuel Residence Time of Three Years, Yearly Refueling
1	156	280,750	156	283,921	156	263,435
2	138	254,457	102	245,665	138	238,972
3	36	236,148	72	221,258	36	222,336
4	108	133,293	126	132,228	126	161,478
5	60	105,326	36	98,363	24	117,395
6	72	63,703	72	78,972	66	76,330
7	91	33,786	97	47,646	115	47,920
8	198	2,109	198	2,109	198	2,107
9	24	10,673	24	10,673	24	10,673
TOTAL	883	116,463,258	883	116,463,258	883	116,463,258

Table K.28

ASSEMBLY BUNDLE AVERAGE COOLANT VELOCITIES (ft/sec)

Orificing Zone	Core Fuel Residence Time of Two Years, Refueling Every Year	Two-Year Straight Burn	Core Fuel Residence Time of Three Years, Refueling Every Year
1	23.8	24.4	22.2
2	21.6	21.1	20.2
3	20.0	17.4	18.7
4	16.9	16.9	20.4
5	13.3	12.5	14.9
6	8.1	10.1	9.6
7	4.3	6.1	6.0

Table K.29

ASSEMBLY BUNDLE AVERAGE PRESSURE DROPS (psi)

Orificing Zone	Core Fuel Residence Time of Two Years, Refueling Every Year	Two-Year Straight Burn	Core Fuel Residence Time of Three Years, Refueling Every Year
1	56.9	59.4	49.7
2	47.5	45.5	47.5
3	41.4	31.8	36.4
4	36.6	36.8	52.0
5	23.8	21.4	29.0
6	9.5	14.4	13.2
7	3.1	5.8	5.7

on the fuel management scheme, the maximum assembly average coolant velocities and the maximum assembly bundle average pressure drops depend on the fuel management scheme too. Thus, the maximum average coolant velocity varies from 22.2 ft/sec to 23.8 ft/sec and the maximum assembly bundle average pressure drop varies from 52 psi to 59.4 psi. The reactor that is refueled every year and has a core and internal blanket fuel residence time of three years (reference design) has the lowest maximum assembly bundle average pressure drop and the straight burn reactor has the highest maximum assembly bundle average pressure drop.

Assembly coolant temperatures for BOL conditions at the top of the upper axial blanket are shown in Figures K.4 to K.6.

Peak assembly coolant temperatures as well as peak nominal and 2σ cladding midwall temperatures are given in Table K.30. The peak assembly coolant temperatures are practically the same for all three fuel management schemes examined. It must be noted that the peak power assembly is not necessarily the assembly that has the peak pin. Consequently, peak assembly coolant temperatures and peak cladding temperatures do not occur always in the same assembly. Since the power swing from the core to the blanket assemblies increases as the core and internal blanket fuel residence time increases, the reference design, that has a core and internal blanket fuel residence time of three years, has a peak 2σ cladding midwall temperature that is 18^{0} F and 35^{0} F, respectively, higher than the corresponding temperature in the two-year straight burn reactor and the reactor that is refueled every year and has a two year core and internal blanket fuel residence time.

K.3 Conclusions

A summary of the values of the main reactor performance parameters, i.e., fissile inventory, fissile gain, doubling time, relative fuel cycle cost, sodium void reactivity, and peak cladding temperature, for the designs analyzed in this Appendix, is given in Table K.31. The reactor with three years core fuel residence time and refueling every year, i.e., the reference design, is the best compromise.

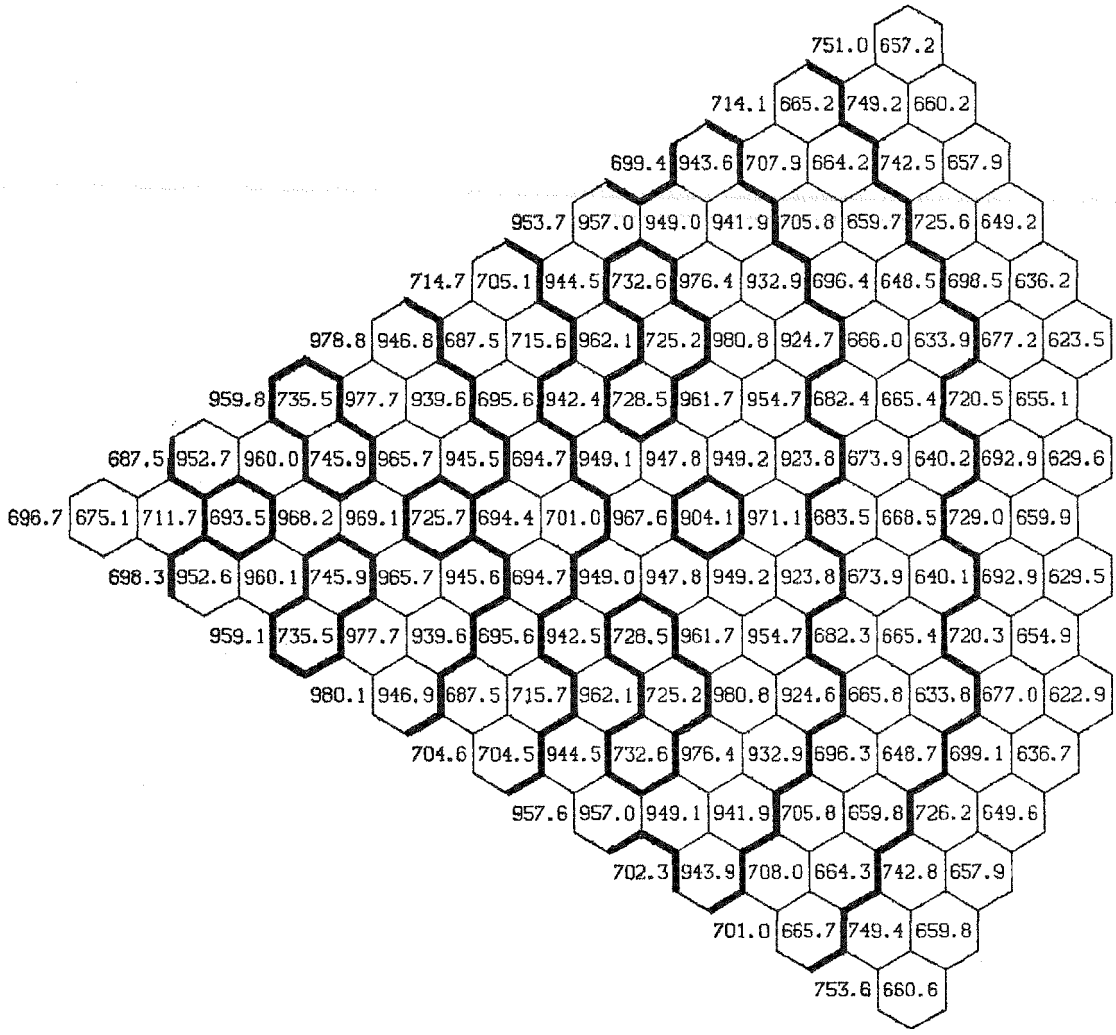

Figure K.4. Average coolant temperatures (^{o}F) at BOL at the top of the upper axial blanket. (Orificing based on pin power and equal peak cladding midwall temperatures, core fuel residence time of two years, refueling every year).

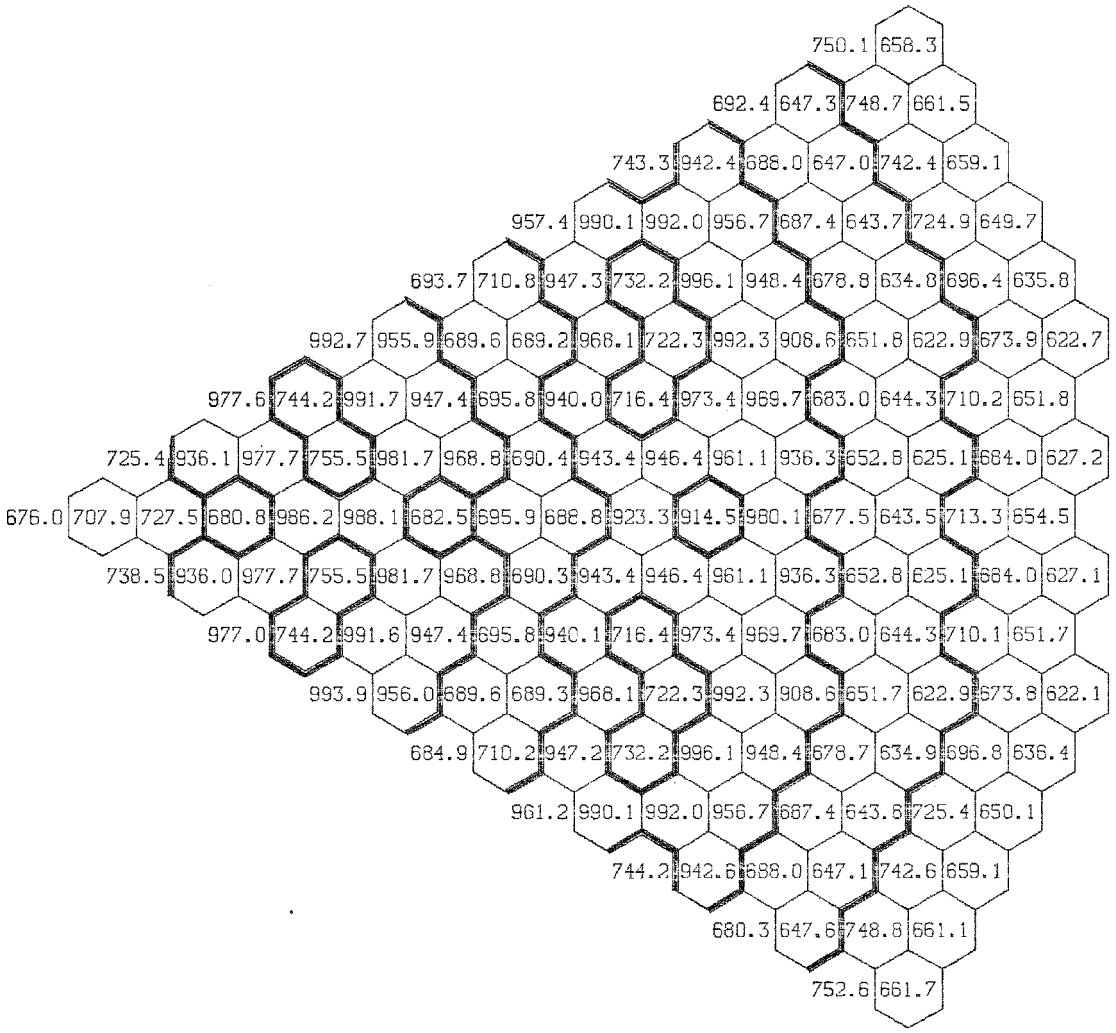

Figure K.5. Average coolant temperatures (^{o}F) at BOL at the top of the upper axial blanket. (Oricicing based on pin power and equal peak cladding midwall temperatures, two year straight burn)

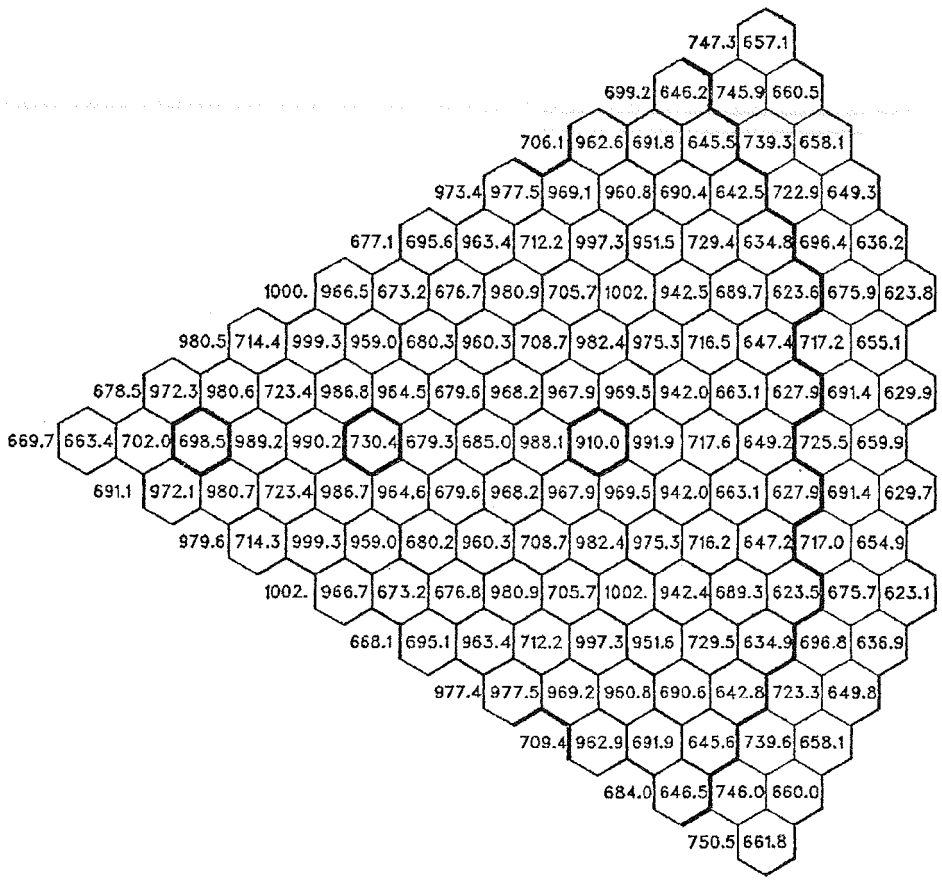

Figure K.6. Average coolant temperatures (^{o}F) at BOL at the top of the upper axial blanket. (Orificing based on pin power and equal peak cladding midwall temperatures, reference design)

Table K.30

PEAK ASSEMBLY COOLANT TEMPERATURES, NOMINAL AND
2σ PEAK CLADDING MIDWALL TEMPERATURES (^{o}F)

	Coolant	Nominal Cladding Midwall	2σ Cladding Midwall
Core Fuel Residence Time of Two Years, Refueling Every Year	981	1060	1185
Two-Year Straight Burn	996	1074	1202
Core Fuel Residence Time of Three Years, Refueling Every Year	1002	1088	1220

Table K.31

FISSILE INVENTORY, FISSILE GAIN, COMPOUND SYSTEM DOUBLING TIME, FUEL CYCLE COST, AND CORE PLUS UPPER AXIAL BLANKET FLOWING SODIUM VOID REACTIVITIES

	Refueling Every Year					
	Core Fuel Residence Time of Two Years		Core Fuel Residence Time of Three Years		Two Year - Straight Burn	
	BOEC	EOEC	BOEC	EOEC	BOEC	EOEC
Fissile Inventory (kg)	4661.3	4988.1	4761.6	5072.3	4609.6	5303.5
Fissile Gain (kg)	326.8		310.7		693.9	
CSDT (Years)	16.3		15.17		14.46	
Relative Fuel Cycle Cost	1.00		0.72		0.86	
Sodium Void Reactivity ($)	2.37		2.58		2.74	
2σ Peak Cladding Midwall Temperature (°F)	1185		1220		1202	

APPENDIX L

NATURAL BORON CARBIDE CONTROL RODS WITH FUEL ASSEMBLY FOLLOWERS

As discussed in Section 4.1.3.6, to satisfy the reactivity control requirements established by the CDS ground rules, 60% and 90% enriched boron is needed for the primary and secondary control systems, respectively. The feasibility of eliminating the need for highly enriched boron was investigated. For this purpose, control rod requirements and worths were determined for a control system that uses natural boron rods with fuel assembly followers. This analysis was performed for the reference 0.28 inch fuel pin diameter design.

The fuel assembly following the control rod was identical to the control assembly with the only difference that the boron pellets were replaced by fuel pellets. The fuel composition was the same as the fuel composition of the adjacent fuel assemblies. Since the reactivity worth of fuel changes with burnup, worths have been determined for fresh and end-of equilibrium cycle fuel composition. The control system worths resulting from using only boron carbide or only fuel as a control material are shown in Table L.1. The primary and secondary control systems requirements established by the Conceptual Design Study(CDS) and the worths of these systems, with fuel and natural born as control materials, are presented in Table L.2. The maximum requirements are 2.65%Δk and 1.88%Δk for the primary and secondary system, respectively. The worth of the primary system is 3.26%Δk and 3.00%Δk for fresh and EOEC fuel composition, respectively, and the corresponding worths of the secondary system are 2.10%Δk and 1.94%Δk. In all cases, the calculated worths exceed the requirements. To satisfy the control requirements using control rods without the fuel assembly followers, enriched boron is needed having 60% and 90% enrichment in the primary and secondary system, respectively. Thus, if fuel assembly followers are used, the need to use highely enriched boron is eliminated.

For a thorough evaluation of a control system that uses control rods with fuel assembly followers, further work is needed to address the following:

1. Detailed design of the fuel assembly follower.

Table L.1

CONTROL SYSTEM WORTHS WITHOUT ANY UNCERTAINTIES

B-10 Enrichment, %	Primary System Worth, % Δk	Secondary System Worth, % Δk
19.8 (Natural)	2.66	1.60
30	3.09	1.84
60	3.70	2.25
90	4.28	2.46
Fresh Fuel	1.57	1.13
Equilibrium Fuel	1.23	0.91

Table L.2

CONTROL REQUIREMENTS DICTATED BY CDS GROUND RULES AND
WORTHS OF NATURAL BORON CARBIDE CONTROL RODS WITH FUEL FOLLOWERS

Primary Control Requirements, %Δk, CDS Ground Rules	Fresh Fuel		Equilibrium Fuel
Hot-to-cold shift		0.94	
Reactivity fault		0.94	
Excess Reactivity at BOEC		0.35	
Criticality uncertainty			± 0.30
Fissile tolerance			± 0.30
TOTAL		2.23	± 0.42
Maximum Requirement		2.65	
Primary Control Worths, %Δk			
Primary control	4.23		3.89
-2σ values*	-0.34		-0.31
Stuck rod**	-0.63		-0.58
TOTAL	3.26		3.00
Secondary Control Requirements %Δk, CDS Ground Rules			
Hot-to-cold shift		0.94	
Reactivity fault		0.94	
TOTAL		1.88	
Maximum Requirements		1.88	
Secondary Control Worths, %Δk			
Secondary control	2.73		2.51
-2σ values *	-0.22		-0.20
Stuck rod**	-0.41		-0.37
TOTAL	2.10		1.94

* Unity bias, 1σ = 4%.

** Interaction factors = 1.785.

2. Impact of the system on:

   a. Core layout
   b. Reactor doubling time
   c. Sodium void reactivity
   d. Reactor power distribution, orificing and peak cladding temperatures
   e. Control rod life
   f. Shielding requirements for the lower support grid plate
   g. Transient reactor performance
   h. Other performance parameters (such as: fuel enrichment, burnup swing, Doppler coefficient, etc...)

During reactor operation, the fuel followers of the secondary system are fully inserted into the core and the fuel followers of the primary system are partially inserted. Since these assemblies produce power as the rest of the fuel assemblies, and at the same time serve as control assemblies, they must be properly designed to avoid violation of design limits.

The presence of the fuel followers in the core during reactor operation, affects the power distribution and the coupling among the core zones. To retain a good power distribution and a low sodium void reactivity, the core layout may have to be modified.

Since the primary system fuel followers are partially inserted in the core during reactor operation, part of these followers extends below the core-lower axial blanket interface. This will increase the flux incident on the lower support grid plate. To avoid violation of fluence design limits, the shielding design of the support grid plate may have to be modified.

Performance parameters, such as fuel enrichments, burnup swing, reactor doubling time, fuel cycle cost, and the Doppler coefficient will be beneficially affected by a control system that consists of natural boron carbide control rods with fuel assembly followers.

APPENDIX M
ADJUSTABLE FLOW SPLIT ANALYSIS

In heterogeneous reactor designs, the buildup of fissile material in the internal blankets during burnup results in a power swing from the core zones to the internal blankets as burnup proceeds. To avoid excessive peak cladding temperatures in the internal blanket assemblies at EOL, these assemblies must be overcooled and core assemblies must be undercooled at BOL. Thus, peak cladding temperatures are higher in heterogeneous than equivalent homogeneous LMFBR designs. This difference in peak cladding temperatures can be reduced, if the flow allocated to the core and blanket assemblies can be adjusted as burnup proceeds, such that the flow matches the power as closely as possible.

The reduction in peak cladding temperature, than can be achieved by adjusting the flow split between the core and blanket assemblies, was investigated using a simple analytical model. Assembly orifices were kept fixed. Calculations were performed for the following fuel management options of the 0.28" fuel pin diameter design:

1. Refueling every year, core and internal blanket fuel residence time of three years and radial blanket fuel residence time of five years.
2. Refueling every year, core and internal blanket fuel residence time of two years and radial blanket fuel residence time of five years.
3. Straight burn of the core and internal blanket fuel for two years, and radial blanket fuel residence time of:

    a. two years,
    b. four years, and
    c. six years.

M.1 Analytical Model

To derive a simple analytical model, the following assumptions have been made:

1. There are as many orificing zones as core and blanket assemblies.
2. The flow distribution between assemblies is selected such that the peak core and blanket assembly coolant temperatures are equal.

The model can easily be extened to:

a. handle orificing zones having more than one assembly,
b. allow for peak blanket assembly coolant temperatures that are different than the peak core assembly coolant temperatures, and
c. deal with cladding temperatures instead of coolant temperatures.

However, the results derived from this simple model will show that there is no need for such extensions.

In a heterogeneous reactor the core power decreases and the blanket power increases with burnup. In the derivation of the analytical model the additional assumption is made that: a) the power of all core assemblies decreases and the power of all internal blanket and radial blanket assemblies increases with burnup,and b) the increase or decrease in assembly power is uniform for all assemblies in a given reactor region (i.e., core, internal blanket, radial blanket). As will be shown later, this assumption is not always true, but the model can be properly revised.

If a straight burn fuel management is employed, the power swing in a given core assembly during a cycle is also the total power swing experienced by this assembly. This is the maximum swing that can be used for this assembly in determining how the flow split between the fuel and blanket assemblies can be adjusted to reduce peak coolant assembly temperatures. If part of the core fuel is replaced at the beginning of each cycle, the beginning-of-cycle (BOC) flow requirements for the core assemblies are determined from the power in these assemblies at BOL. Also, since the assembly orifices are fixed and since the core, after the first cycle, is a mixture of fresh and irradiated assemblies, the maximum swing that can be used for a core assembly in determining the flow split adjustment between the fuel and blanket assemblies, is the swing over one cycle only.

In the blankets, assembly power increases with burnup and in all blanket assembly positions the maximum power production occurs at EOL. If a straight burn fuel management is used, the maximum blanket assembly power swing that can be used in determining the flow split adjustment between the core and blanket assemblies is the swing over one cycle. If part of the blanket fuel is replaced at EOC, the

blanket assembly flow requirements are determined from the power produced in these assemblies at EOL. In addition, since the assembly orifices are fixed and since the blankets, after the first cycle, are a mixture of fresh and irradiated assemblies, the maximum swing that can be used for a blanket assembly in determining the flow split adjustment between core and blanket assemblies, is also the swing over one cycle only.

Since the assembly coolant temperatures peak at BOL in the core assemblies and at EOL in the blanket assemblies, to equalize these peak temperatures the following relations must be satisfied:

$$\frac{f_c^{BOL}}{M_c^{BOL}} = \frac{f_{IB}^{EOL}}{M_{IB}^{EOL}} = \frac{f_{RB}^{EOL}}{M_{RB}^{EOL}} = \frac{f_c^{BOL} + f_{IB}^{EOL} + f_{RB}^{EOL}}{M_c^{BOL} + M_{IB}^{EOL} + M_{RB}^{EOL}} \qquad (1)$$

where

c, IB, RB	=	core, internal blanket and radial blanket, respectively
f	=	fraction of power produced in a given reactor zone
M	=	coolant flow

Taking into account that the zonal flows at time t and at zero time are related by the equation:

$$M_{IB}(t) + M_{RB}(t) + M_c(t) = M_{IB}^o + M_{RB}^o + M_c^o = M$$

and

$$\frac{M_{RB}(t)}{M_{IB}(t)} = r = \frac{f_{RB}^{EOL}}{f_{IB}^{EOL}}$$

then, the time variation of the internal blanket, radial blanket, and core flow is given by the relations:

$$M_{IB}(t) = M_{IB}^o + st$$

$$M_{RB}(t) = M^{o}_{RB} + rst \qquad (2)$$

$$M_{c}(t) = M^{o}_{c} - (r + 1)st$$

where s is the rate of flow change in the internal blanket.

If τ is the length of one cycle, Eqs (1) and (2) give:

$$M^{o}_{c} = \frac{\left[M+s\tau(r+1)\right] \; f^{BOL}_{c}}{f^{BOL}_{c} + f^{EOL}_{IB} + f^{EOL}_{RB}}$$

$$M^{o}_{IB} = \frac{f^{EOL}_{IB}\left[M+s\tau(r+1)\right] - s\tau\left[f^{BOL}_{c} + f^{EOL}_{IB} + f^{EOL}_{RB}\right]}{f^{BOL}_{c} + f^{EOL}_{IB} + f^{EOL}_{RB}} \qquad (3)$$

$$M^{o}_{RB} = M^{o}_{IB} \frac{f^{EOL}_{RB}}{f^{EOL}_{IB}}$$

Since,

$$\frac{\Delta T^{BOL}_{c}}{\overline{\Delta T}} = f^{BOL}_{c} \frac{M}{M^{o}_{c}}$$

$$\frac{\Delta T^{BOC}_{IB}}{\overline{\Delta T}} = f^{BOC}_{IB} \frac{M}{M^{o}_{IB}} \qquad (4)$$

$$\frac{\Delta T^{BOC}_{RB}}{\overline{\Delta T}} = f^{BOC}_{RB} \frac{M}{M^{o}_{RB}}$$

equations (3) give the following relations for the peak assembly coolant temperature rise at BOL for the core $\left(\Delta T^{BOL}_{c}\right)$ and at the beginning of any cycle for the blankets $\left(\Delta T^{BOC}_{IB}$ and $\Delta T^{BOC}_{RB}\right)$:

$$\frac{\Delta T_c^{BOL}}{\overline{\Delta T}} = \frac{f_c^{BOL} + f_{IB}^{EOL} + f_{RB}^{EOL}}{1 + \frac{s\tau}{M}\ (r+1)}$$

$$\frac{\Delta T_{IB}^{BOC}}{\overline{\Delta T}} = \frac{\left(f_c^{BOL} + f_{IB}^{EOL} + f_{RB}^{EOL}\right)\ f_{IB}^{BOC}}{f_{IB}^{EOL} - \frac{s\tau}{M} f_c^{BOL}} \qquad (5)$$

$$\frac{\Delta T_{RB}^{BOC}}{\overline{\Delta T}} = \frac{\Delta T_{IB}^{BOC}}{\overline{\Delta T}}\ \frac{f_{RB}^{BOC}}{f_{IB}^{BOC}}\ \frac{f_{IB}^{EOL}}{f_{RB}^{EOL}}$$

where

$\overline{\Delta T}$ = average temperature rise across the core and blankets.

Since the power produced in the blanket assemblies increases with burnup, the largest ΔT_{IB}^{BOC} and ΔT_{RB}^{BOC} occur at the beginning of the last cycle (BOLC) that a blanket assembly remains in the reactor.

To minimize the peak core and blanket assembly coolant temperatures, the rate of flow change, s, must be such that;

$$\Delta T_c^{BOL} = \Delta T_{IB}^{EOL} = \Delta T_{RB}^{EOL}$$

$$\Delta T_c^{BOL} \geq \overline{\Delta T} \qquad (6)$$

and

$$\frac{\Delta T_c^{BOL}}{\overline{\Delta T}} - 1 = \delta = \text{minimum}$$

To minimize δ, the temperature rises

$$\Delta T_{IB}^{BOLC} \text{ and } \Delta T_{RB}^{BOLC}$$

must be minimized while the
largest of $\left(\Delta T_{IB}^{BOLC} \text{ and } \Delta T_{RB}^{BOLC}\right) \leq \Delta T_c^{BOL}$

Since,

$$\Delta T_{IB}^{EOL} = \Delta T_{RB}^{EOL}$$

the blanket that experiences the smallest power swing during one cycle will have the largest ΔT at BOLC conditions. This blanket is the radial blanket. Thus, the rate of flow change that minimizes δ under constraints (6) (Optimum value of s) also equalizes the temperature rises ΔT_{c}^{BOL} and ΔT_{RB}^{BOLC}. Equations (5) and the relation

$$\Delta T_{c}^{BOL} = \Delta T_{RB}^{BOLC}$$

give the following optimum value for the rate of flow change,

$$s = \frac{M}{\tau}\left[\frac{f_{RB}^{EOL} - f_{RB}^{BOLC}}{(r+1)f_{RB}^{BOLC} + rf_{c}^{BOL}}\right] \qquad (7)$$

M.2 Numerical Results

Peak assembly coolant temperatures predicted by the simple analytical model are presented in Table M.1. Since the total power swing from the core assemblies to the blanket assemblies increases as the fuel residence time increases, the peak assembly coolant temperature also increases as the fuel residence time increases. Thus, as the core and internal blanket fuel residence time increases from two to three years, the peak assembly coolant temperature increases by $\sim 13^{o}$ F. Similarly, as the radial blanket fuel residence time increases from two to six years, the peak assembly coolant temperature increases by $\sim 11^{o}$ F if the flow split is fixed, and by $\sim 24^{o}$ F if the flow split between the core and blanket assemblies is continuously adjusted during the cycle. Continuous adjustment of the flow split between the core and blanket assemblies always reduces the peak assembly coolant temperature. This reduction is $\sim 10^{o}$ F if the core is partially refueled every year. If a straight burn fuel management is used, the reduction in peak assembly coolant temperature depends on the residence time of the radial blanket fuel. The

Table M.1

PEAK IN-LIFE ASSEMBLY COOLANT TEMPERATURES

Rate of Flow Change, s	Refueling Every Year Core Fuel Residence Time	
	2 Years	3 Years
0.0	937.4	950.8
Optimum	927.4	939.6

	Two Years Straight Burn, Radial Blanket Fuel Residence Time		
	2 Years	4 Years	6 Years
0.0	930.5	936.2	941.8
Optimum	898.8	912.9	922.9

maximum reduction, $\sim 32^{0}$ F, is achieved if all the fuel in the reactor has the same residence time. If the blanket fuel residence time is increased to six years, the improvement in peak assembly coolant temperature is reduced to $\sim 19^{0}$ F.

Equation (7), that gives the rate of flow change, s, is based on the assumption that: a) the core assembly power decreases with burnup uniformly in all core assemblies, and b) the blanket assembly power increases with burnup uniformly in all internal blanket assemblies as well as in all radial blanket assemblies. As shown in Figure M.1, this assumption is not always valid. The power increase in the blanket (internal or radial) assemblies is not uniform for all assemblies. In the core, the assembly power not only does not decrease uniformly with burnup but the power of the assemblies in the neighborhood of the control rod located in row 11 increases during the cycle. Thus, for the two-year straight burn reactor, the ratio of the assembly power at the end of the first cycle (P_{EOC}) to its power at the beginning of the first cycle (P_{BOC}) varies from 2.42 to 3.72 in the internal blanket, from 1.71 to 2.47 in the radial blanket, and from 0.70 to 1.15 in the core. If three orificing zones are used in the core, the core assemblies that gain power with irradiation belong to the third orificing zone. As shown in Table M.2, the peak power assembly in this zone is assembly C121 (Figure M.2). For this assembly the ratio P_{EOC}/P_{BOC} is equal to 0.988. If the flow split between core and blanket assemblies is continuously varied with time, such that the optimum rate of flow change, s, as calculated by Eq. (7), is obtained, then, at the end of the first cycle the peak coolant temperature rise for assembly C121 will be 11% higher than its peak coolant temperature rise at the beginning of the cycle. This increase is larger than the 10% reduction achieved by the continuous flow split adjustment scheme. Thus, in this case, if the flow split between core and blanket assemblies is adjusted continously with time: a) the peak coolant temperature reductions shown in Table M.1 can not be achieved, and b) peak assembly coolant temperatures will be worse than for a zero rate of flow change (i.e., fixed flow split).

There are still different ways that can be used to reduce peak coolant temperatures by continously adjusting the flow split between core and blanket assemblies. However, the reduction achieved will be smaller than the one given in Table M.1. One way is to overcool the third orificing zone at BOL such that at the end of the cycle, the peak assembly coolant temperature in this zone is the same as the peak assembly coolant temperature at BOL in the other core orificing zones.

If the third orificing zone is overcooled at BOL, the flow in the rest of the

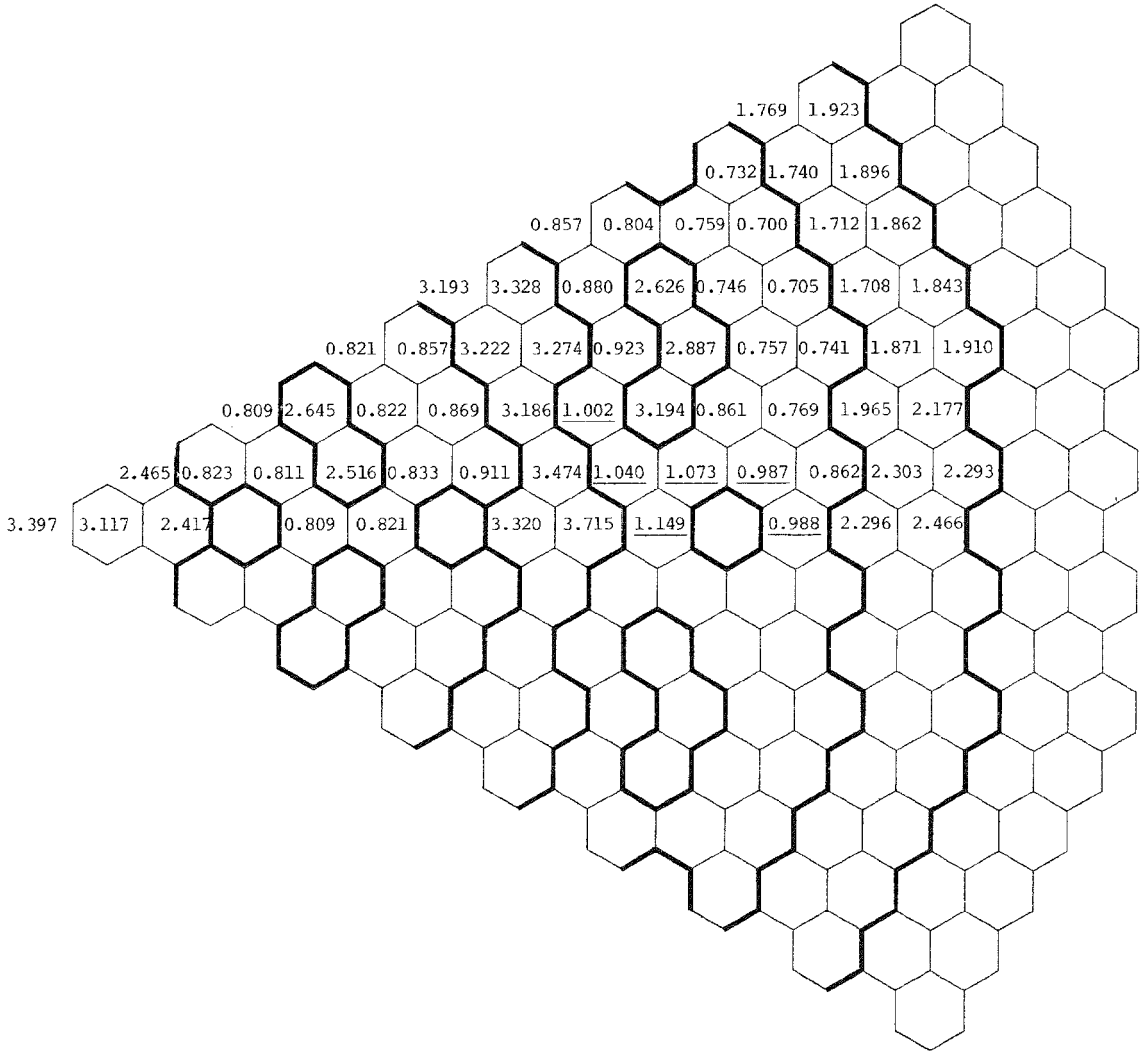

Figure M.1. Assembly P_{EOC}/P_{BOC}

Table M.2

ASSEMBLY POWERS IN THE THIRD CORE ORIFICING ZONE

Assembly	Assembly Power (MW)	
	BOC	EOC
C121	7.66	7.57
C122	7.25	7.16
C114	7.47	6.90
C112	6.98	7.49
C101	6.52	7.49
C102	6.96	7.23
C103	6.91	6.92

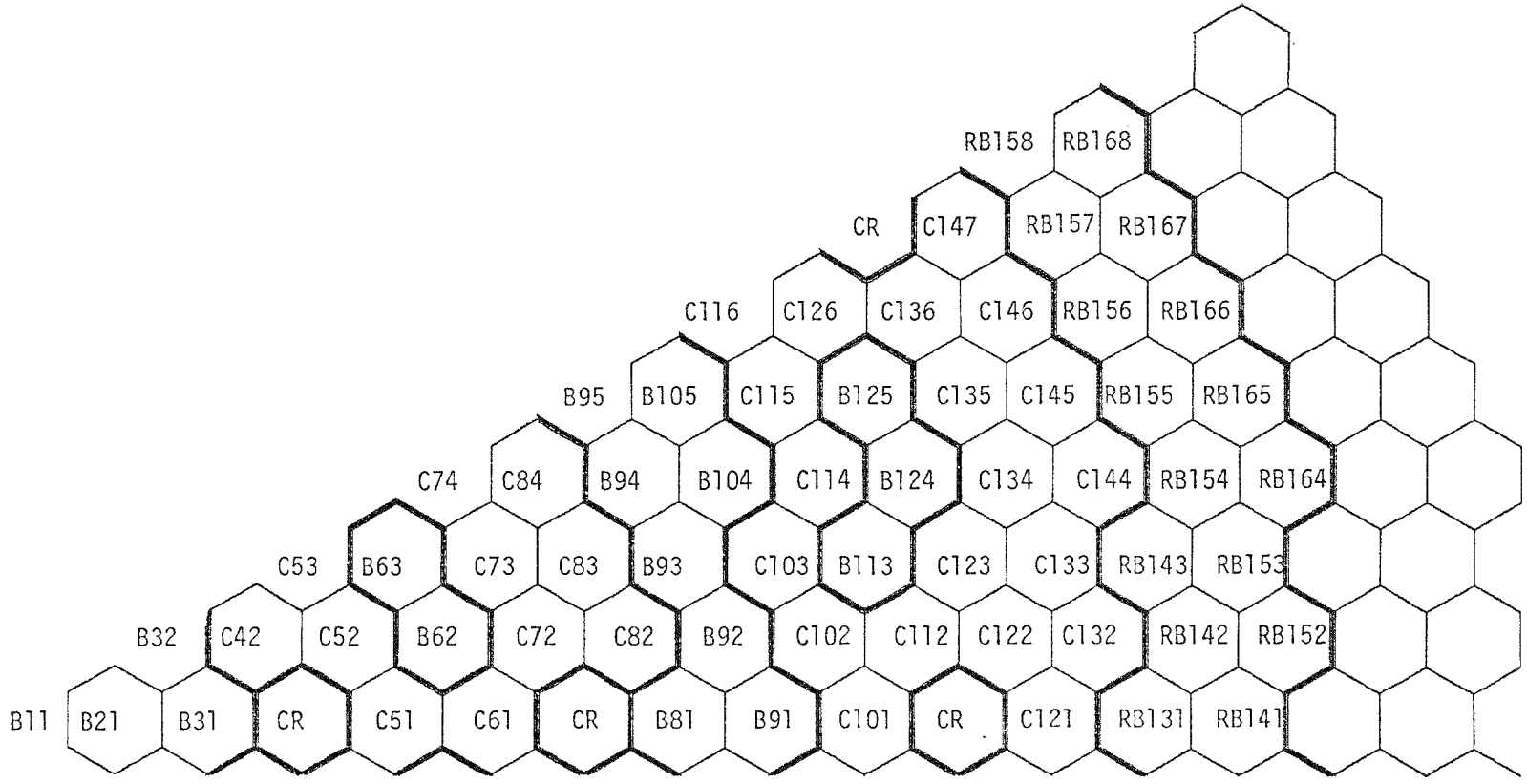

Figure M.2. Core layout (One twelfth of core)

core orificing zones will be reduced at BOL, and consequently, the peak assembly coolant temperature will increase. An estimate of this increase can be obtained as follows. The flow fraction allocated to the third orificing zone is ∿23% of the total core flow. To increase the end-of-cycle flow in the third orificing zone by 11%, its BOC flow has to be increased by ∿9%. This means that the BOC flow allocated to the rest of the core has to be reduced by ∿3%. This reduction will increase the BOL peak assembly coolant temperature rise by ∿9° F and will reduce the improvement in peak assembly coolant temperature, achieved by adjusting the flow split, from 32° F to 23° F.

Another way to reduce peak coolant temperatures, by continuously adjusting the flow split between core and blanket assemblies, is to connect the core assemblies that gain power during the cycle with the coolant feed of the blanket assemblies. In this case, to determine the reduction in peak coolant temperature that can be achieved, the analytical model has to be revised as follows.

M.3 Revised Model

The core assemblies are divided into two groups. In the second group are placed all the assemblies that belong to the third orificing zone (Table M.2). The rest of the core assemblies are placed in the first group. As shown in Table M.2, assembly C121 is the peak power assembly of the third orificing zone at BOC as well as at EOC and its BOC power is slightly higher than its EOC power. Thus, if the coolant feed of the third orificing zone is connected with the coolant feed of the blanket, its flow will increase as burnup proceeds and the coolant temperature of the zone will peak at BOC.

Equations (1) and (2) can be rewritten as

$$\frac{f_{c1}^{BOL}}{M_{c1}^{BOL}} = \frac{f_{c2}^{BOL}}{M_{c2}^{BOL}} = \frac{f_{IB}^{EOL}}{M_{IB}^{EOL}} = \frac{f_{RB}^{EOL}}{M_{RB}^{EOL}} = \frac{f_{c}^{BOL} + f_{IB}^{EOL} + f_{RB}^{EOL}}{M_{c}^{BOL} + M_{IB}^{EOL} + M_{RB}^{EOL}} \qquad (8)$$

$$M_{IB}(t) = M_{IB}^{BOL} + st$$

$$M_{RB}(t) = M_{RB}^{BOL} + rst$$

$$M_c(t) = M_c^{BOL} - (r+1)\, st \tag{9}$$

$$M_{c1}(t) = M_{c1}^{BOL} - \alpha t$$

$$M_{c2}(t) = M_{c2}^{BOL} + \beta t$$

where

c1, c2 = first group of core assemblies, second group of core assemblies.

α, β = rate of flow change in the first and second group of core assemblies, respectively.

Equations (5) that give the peak coolant temperatures, are still valid and for both groups of core assemblies the peak coolant temperature occurs at BOL; therefore,

$$\Delta T_{c1}^{BOL} = \Delta T_{c2}^{BOL} = \Delta T_c^{BOL}$$

To minimize the peak core and blanket assembly coolant temperatures, the rate of flow change, s, must be such that relations (6) are satisfied. However, since the flow of the second group of core assemblies increases with burnup, if the rate of flow change, s, is high enough, the peak assembly coolant temperature in the first group of core assemblies at EOL may become higher than the peak coolant temperature of the same assemblies at BOL. Thus, it must be assured that

$$\Delta T_{c1}^{EOL} \leq \Delta T_{c1}^{BOL} = \Delta T_c^{BOL} = \Delta T_{IB}^{EOL} = \Delta T_{RB}^{EOL}$$

A relation between ΔT_{c1}^{EOL} and the rate of flow change, s, is obtained as follows.

Since the coolant feed of the second group of core assemblies is connected with the coolant feed of the blanket assemblies

$$\frac{M_{c2}(t)}{M_{IB}(t)} = \frac{M_{c2}^{BOL}}{M_{IB}^{BOL}} = \frac{M_{c2}^{BOL} + \beta\tau}{M_{IB}^{BOL} + s\tau} = \frac{\beta}{s} \tag{10}$$

From Eqs. (8)

$$\frac{M_{c2}^{BOL}}{M_{IB}^{EOL}} = \frac{f_{c2}^{BOL}}{f_{IB}^{EOL}} = \lambda \tag{11}$$

and

$$M_{c2}^{BOL} = M_{c1}^{BOL} \frac{f_{C2}^{BOL}}{f_{c1}^{BOL}} = \mu M_{c1}^{BOL} \tag{12}$$

Equations (9), (10), (11) and (12) give

$$\alpha = \frac{\lambda\mu s \; M_{c1}^{BOL}}{\mu M_{c1}^{BOL} - \lambda s\tau} + (r+1)s \tag{13}$$

and

$$M_{c1}^{EOL} = M_{c1}^{BOL} - \left[\frac{s\mu\lambda \; M_{c1}^{BOL}}{\mu M_{c1}^{BOL} - \lambda s\tau} + (r+1)s \right] \tau \tag{14}$$

Since

$$\frac{M_{c1}^{EOL}}{M_{c1}^{BOL}} \frac{\Delta T_{c1}^{EOL}}{\Delta T_{c1}^{BOL}} = \frac{M_{c1}^{EOL}}{M_{c1}^{BOL}} \frac{\Delta T_{c1}^{EOL}}{\Delta T_{c}^{BOL}} = \frac{f_{c1}^{EOL}}{f_{c1}^{BOL}} = p \tag{15}$$

and

$$M_{c1}^{BOL} = M f_{c}^{BOL} \frac{\Delta \bar{T}}{\Delta T_{c}^{BOL}} \tag{16}$$

Eqs. (14), (15), and (16) give the following relation between ΔT_{c1}^{EOL} and s (rate of flow change)

$$\frac{\overline{\Delta T}}{\Delta T_{cl}^{EOL}} = \frac{\overline{\Delta T}}{p\Delta T_c^{BOL}} - \frac{\lambda\mu \frac{s\tau}{M} \frac{\overline{\Delta T}}{\Delta T_c^{BOL}}}{\mu p f_c^{BOL} \frac{\overline{\Delta T}}{\Delta T_c^{BOL}} - \lambda p \frac{s\tau}{M}} - \frac{(r+1)}{p f_c^{BOL}} \frac{s\tau}{M} \qquad (17)$$

As shown in Figure M.3, the rate of flow change, s, that minimizes the peak assembly coolant temperature is such that

$$\Delta T_{cl}^{BOL} = \Delta T_c^{BOL} = \Delta T_{cl}^{EOL}$$

and

$$\Delta T_c^{BOL} = 1.044\ \overline{\Delta T} = 307.7^{o}\ F$$

Since the coolant inlet temperature is equal to 595^{o} F, the resulting peak coolant temperature will be 902^{o} F (595 + 307.7). As shown in Table M.1, if the flow split between core and blanket assemblies is fixed as burnup proceeds, the peak coolant temperature of the two-year straight burn reactor, that has a two year radial blanket fuel residence time, is 930.5^{o} F. If the flow split between core and blanket assemblies is continuously adjusted as burnup proceeds, and the coolant feed of the third core orificing zone is connected to the coolant feed of the blanket assemblies, the peak coolant temperature is reduced by $\sim 28^{o}$ F (from 930.5^{o} F to 902.7^{o} F). This reduction is $\sim 4^{o}$ F smaller than the reduction that would be achieved if the power in all core assemblies was uniformly decreasing with burnup and the flow split between core and blanket assemblies was continuously adjusted (Table M.1). As discussed earlier, if the third core orificing zone is overcooled at BOL the reduction achieved in peak coolant temperature by continuously adjusting the flow split between core and blanket assemblies is $\sim 23^{o}$ F. Thus, connecting the coolant feed of the third core orificing zone with the coolant feed of the blanket assemblies is a more efficient means of reducing the peak coolant temperature. However, this may require a much more complicated design for the inlet coolant plenum.

Finally, if a control system is used that consists of natural boron rods with fuel

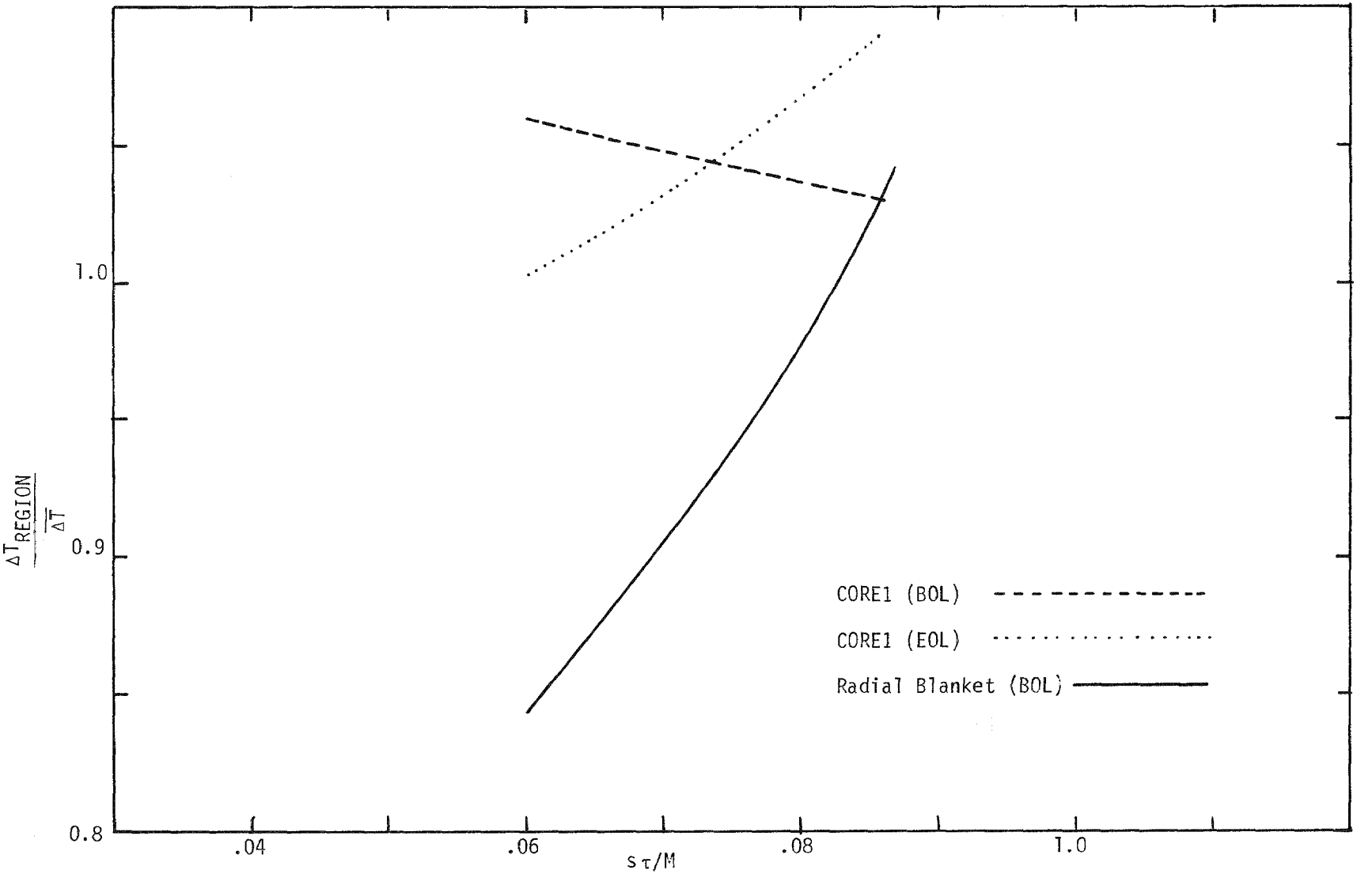

Figure M.3. Peak coolant temperature rise vs. rate of flow change.

assembly followers, the positive power swings, during the cycle, of the assemblies around the primary control rods will be reduced. This reduction is beneficial for the concept of continuously adjusting the flow splits between core and blanket assemblies during the cycle.

A continuous flow split adjustment improves the peak coolant and cladding temperatures by matching, as much as possible, the assembly flow with the assembly power. This, however, reduces voiding incoherence during an accident that leads to sodium boiling. Moreover, the mechanisms that will be used to continuously adjust the flow, may introduce additional accident initiators.

APPENDIX N

VERIFICATION-OF-RESULTS STUDY

N.1 SODIUM VOID REACTIVITY

N.1.1 Introduction

The approach generally used to predict the sodium void reactivity for a liquid metal fast breeder power reactor is to adjust the calculated sodium void reactivity by an appropriate bias factor. There are two general methods which can be used to determine the bias factor[1]. The first method is a basic physics approach in which detailed analytical techniques and cross sections are developed. They are developed so that they yield accurate sodium void reactivities for a variety of critical assemblies. If such techniques and cross sections could be constructed, they could then be used to reliably predict the sodium void reactivity in a power reactor. However, there is no record in the literature of a sodium void reactivity analysis, which can predict both the magnitude and the spatial dependence of the sodium void reactivity for several critical assemblies using a single cross section set and a consistent computational procedure. Hence, the sodium void bias factor is usually determined from measurements and analysis of several critical experiments, which are designed to provide an understanding of a particular power reactor. This bias factor is applied to the power reactor design calculations to obtain the sodium void reactivity for the power reactor.

N.1.2 A Review of Experimental Programs and Their Analysis

Several countries and groups of countries are conducting critical experiments designed to develop an understanding of homogeneous and heterogenous fast breeder reactors. The results of these programs will be briefly discussed. In this survey the notation C/E or (C-E)/C will be frequently encountered. Here, C stands for a calculated sodium void reactivity while E is the measured experimental value. Thus, C/E or (C-E)/C are measures of the agreement between the experimental and the calculated sodium void reactivity.

Japanese Central Blanket Experiments

The Japanese have studied a simple heterogenous core with a central blanket.[2] The blanket is 30 cm thick, 70 cm in diameter, and centered about the midplane of the cylindrical core which is about 120 cm in diameter, 90 cm high and is followed by 35 cm thick axial blankets. In the sodium void measurement, boxes in the upper half of the reactor, equivalent to a cylinder with a 9.3 cm radius centered about the centerline of the reactor, were voided. To analyze the sodium void measurements, exact perturbation theory and two-dimensional (RZ) diffusion theory were used. In the analysis, the 25 group JAERI-Fast Set Version II cross sections were used. Average effective cross sections for a unit cell of the core, internal blanket, axial blanket and the driver region were calculated using a collision probability method. Since the assembly is comprised of smaller plate assemblies, neutron streaming was accounted for by using Benoist anisotropic diffusion coefficients. The calculated sodium void reactivity for the center channel is within 23% of the experimental value. (See Table N.1.2.1). Individual void reactivities for different axial regions vary from a 22% underprediction to a 15% overestimate. Also, the experimental value for the sodium void reactivity for the whole channel is not equal to the sum of the reactivities measured for the various axial segments. Comparison of axial increments with the total axial void reactivity have not been reported for other assemblies.

The CNEN and CEA Experimental Programs Pre-Racine and Racine

The CNEN and CEA have two joint programs called Pre-Racine and Racine, which are being performed on the critical facility MASURCA, at Cadarache.[3-6] The Pre-Racine program examined the neutronic characteristics of a simple heterogeneous core, i.e., a center blanket only, and a homogeneous core. The Racine program, which is currently in progress, will examine more complex heterogenous cores. Only sodium void measurements for the central fertile zone of the heterogeneous core have been reported for the Pre-Racine program. To interpret these measurements, three 25 group cross section sets were generated from CARNAVAL III, CARNAVAL IV, and ENDF/B-Version 4, respectively. The sets obtained from CARNAVAL III and IV assume that the fertile zone is homogeneous, infinite in extent, and a standard flux is used for determining the scattering cross sections. For all three sets, the fertile and fissile regions are treated separately, i.e., it is assumed that there is no interaction between the zones.

Table N.1.2.1[+]

COMPARISON OF EXPERIMENTAL AND CALCULATED SODIUM VOID WORTHS
IN THE CENTRAL 3 X 3 DRAWERS OF ASSEMBLY VII-3-1 (30 cm IB)

Region	Axial Position	Experiment ($10^{-6}\Delta k/k$)	Calculation ($10^{-6}\Delta k/k$)		C/E	
			70 Group	25 Group	70 Group	25 Group
Internal Blanket	1Z	64.4 ± 1.4	58.4	69.0	0.91	1.07
	2Z	54.9 ± 1.1	51.6	62.4	0.94	1.14
	3Z	44.1 ± 1.1	40.6	50.8	0.92	1.15
Core	4Z	39.7 ± 1.1	33.4	35.3	0.84	0.89
	5Z	45.9 ± 1.1	38.6	40.2	0.84	0.88
	6Z	37.9 ± 1.1	32.5	34.4	0.86	0.91
	7Z	18.6 ± 1.2	11.4	14.5	0.61	0.78
	8Z	-14.6 ± 1.0	-20.3	-15.4	1.39	1.05
	9Z	-43.1 ± 1.0	-53.9	-47.3	1.25	1.10
Axial Blanket	10Z	-48.4 ± 1.1	-55.2	-49.4	1.14	1.02
	11Z	-30.7 + 1.0	-34.4	-30.3	1.12	0.99
	12Z	-18.9 ± 1.1	-19.9	-17.5	1.05	0.93
	13 ∿16Z	-21.5 ± 1.1		-25.0		1.16
	1 ∿16Z	115 ± 2		141		1.23

[+]Adapted from Table VI in Reference 2.

Selected results for Pre-Racine experiments and calculations are given in Table N.1.2.2. These results were obtained with two-dimensional (RZ) diffusion theory and a direct eigenvalue calculation. Since the heterogeneous sodium void reactivity is overestimated in all these calculations, the French believe that the error is more likely in the method approximations than in the basic cross section data. They further postulated that the error is caused by the neutron leakage treatment and the spatial spectrum variation. H. Kusters and S. Ganesan give a possible explanation for the large difference between the calculated and the measured sodium void reactivity for Pre-Racine using a simulation calculation of a heterogeneous core with a central fertile region and parameters typical of the SNEAK-9C-POZ core[7]. In this analysis, the central fertile zone was completely voided and two sets of calculations were performed. In the first set, the heterogeneity of the unit cell in the fertile zone was accounted for. In the second set, a completely homogenized fertile zone was used. The difference in the net void effect in these two sets of calculations was about a factor of two[7]. The difference between the measured and calculated Pre-Racine sodium void reactivity for the entire fertile zone is also about a factor of two. (See Table N.1.2.2). Thus, if a heterogeneous unit cell was used in the cross section preparation for the Pre-Racine analysis, the agreement between experiment and calculation would be much better.[7]

At present, there is no data available for the Racine program, but in a survey article on the program, additional data for the Pre-Racine sodium void reactivity is given.[6] A value of 1.21 is given for the ratio of the measured to the calculated sodium void reacitvity, for voiding the core height. The same ratio in Table N.2 ranges from 1.57 to 1.67. No explanation is given for this improvement in the Pre-Racine analysis.

The UK DeBeNe Research Program BIZET

Heterogeneous core geometries have been studied at the zero power facility ZEBRA at Winfrith as a part of the joint UK/DeBeNe research program BIZET.[8,9] Three basic assemblies, BZC, BZD and BZD/1A, have been studied. BZC is a "Salt-and-Pepper Core" with fertile elements arranged in groups of sizes ranging from one to eight power reactor subassemblies. BZD is a "Single Annular Core" with the fertile elements forming a large central island of about 95 cm while BZD/1A is a modified version of BZD. It has a central breeder island of about 67 cm and a thin breeder ring further out in the core. All three assemblies have about the same fissile volume and about the same number of in-core fertile elements. The cores are

Table N.1.2.2[+]

SODIUM VOID REACTIVITIES FOR PRE-RACINE

Voided Zone	Measured*	BASIC CROSS SECTION DATA					
		Carn. III Calculated*	C/E	Carn. IV Calculated*	C/E	ENDFB/4 Calculated*	C/E
R = 15 cm -5<H<+5 cm	27 ± 3	40	1.48	38.6	1.43	38	1.41
R = 15 cm -25 < H<+25 cm	121 ± 3	168	1.39	160.0	1.32	159	1.31
R = 15 cm -45 < H<+45 cm (Core Height)	120 ± 3	200	1.67	188.5	1.57	191	1.59
R = 15 cm -67<H<+67 cm (Reactor Height)	99 ± 3	193	1.95				

* $X10^{-5}$ $\frac{\Delta k}{k}$

\+ Adapted from Refs. 3-5.

roughly 90 cm high and 200 cm in diameter. There is no data available on the measurements or analysis for the assembly BZD/1A

The sodium void reactivities for these cores were calculated using first order perturbation theory with the unperturbed fluxes and the adjoints calculated from XYZ diffusion theory. Thirty-seven group heterogeneous cell-averaged cross sections were used. For the BZC core, a mult-buckling scheme was used in preparation of the cross sections for the fertile regions.

BZC Experimental Assembly

For the most of the sodium void reactivity measurements on BZC, the core was voided only over 40% of its height. This was done to emphasize the spectral and radial leakage components of the void effect. A few measurements were done with 80% of the core height voided to provide a check on the calculated axial distribution of the sodium void reactivity. The comparison of these measurements with the computed results reveals that the sodium void reactivity is predicted much more reliably in the fertile zones (C/E = 0.93 to 1.05) than in the fissle regions (C/E = 0.70 to 0.84). (See Table N.1.2.3.) the results for the fissile regions are not consistent with the results obtained by this group for homogeneous systems. The values of C/E reported for homogeneous assemblies were normally dispersed about unity. Since the measurements were made in regions where axial and radial leakage are secondary effects, the source of error in the calculated sodium void reactivity for the fissile regions is believed to be an incorrect estimate of the spectral component. Further, it has not been established if the more reliable results in the breeder regions are due to the refined cross-section preparation or simply to a fortuitous cancellation of errors.

BZD/1 Experimental Assembly

For the BZC assembly, all of the control rod positions were filled with sodium, but in the BZD configuration, two cases were simulated: BZD/1 had absorbers inserted fifty percent in the control rod positions and BZD/2 had followers fully inserted in the control positions. Only the results for BZD/1 have been reported. The C/E ratios for BZD/1 show a significantly wider dispersion than those fo BZC (Table N.1.2.4). This is attributed to the varying balance between the spectral and leakage components of the sodium void reactivity and the accordingly varying accumulation of errors in the void reactivity. However, a systematic relationship between the

Table N.1.2.3[+]

SODIUM VOID IN ASSEMBLY BZC/1

Region	Position	Void Height	Measured Reactivity (10^{-4} dk/k)	Measured Reactivity Per Kg Sodium (10^{-4} dk/k)	Calculated Reactivity (10^{-4} dk/k)				C-E	$\frac{C}{E}$
					Central	Radial Leakage	Axial Leakage	Total		
Breeder Islands	1		1.41	0.55	1.43	-0.085	-0.032	1.32	-0.092	0.93
	2		0.69	0.41	0.94	-0.27	-0.031	0.65	-0.044	0.94
	6	$\pm$ 18.65 cm	0.87	0.51	1.02	-0.078	-0.038	0.90	+0.030	1.03
	7	$\sim$ 40% of	0.97 $\pm$ 0.03	0.57 $\pm$ 0.015	1.04	-0.017	-0.036	0.98	+0.018	1.02
	8	core height	0.91	0.54	0.97	+0.021	-0.037	0.96	+0.042	1.05
	6....8		1.39	0.54	1.51	-0.037	-0.056	1.42	+0.034	1.02
	15....18		1.73	0.51	1.90	-0.18	-0.061	1.66	-0.066	0.96
	6....8	$\pm$ 37.29 cm $\sim$80% of c/h	2.00	0.39	2.50	-0.064	-0.37	2.07	+0.068	1.03
Fissile Elements	3		0.88	0.41	0.96	-0.25	-0.074	0.63	-0.25	0.72
	4		1.06	0.50	0.93	-0.056	-0.081	0.80	-0.26	0.75
	5		1.10	0.51	0.99	-0.068	-0.079	0.84	-0.26	0.76
	9		1.02	0.48	0.88	+0.049	-0.071	0.86	-0.16	0.84
	10	$\pm$ 18.71 cm	0.87 $\pm$ 0.03	0.41 $\pm$ 0.01	0.77	-0.025	-0.072	0.68	-0.19	0.78
	13	$\sim$ 40% of	0.54	0.51	0.46	-0.033	-0.042	0.39	-0.15	0.72
	14	core height	0.45	0.42	0.49	-0.14	-0.039	0.31	-0.14	0.70
	3....5		1.51	0.47	1.44	-0.19	-0.12	1.13	-0.38	0.75
	11....14		1.90	0.45	1.90	-0.38	-0.16	1.36	-0.54	0.72
	19....21		1.13	0.35	0.98	+0.044	-0.094	0.93	-0.20	0.82
	3....5	$\pm$ 37.43 cm $\sim$80% of c/h	1.99	0.31	2.38	-0.30	-0.77	1.31	-0.68	0.66

+ Table 1 in Reference 8.

Table N.1.2.4+

SODIUM VOID IN ASSEMBLY BZD/1 (ONLY 40% AND 80% VOID HEIGHTS)

Region	Position	Void Height	Measured Reactivity (10^{-4} dk/k)	Measured Reactivity Per Kg Sodium (10^{-4} dk/k)	Calculated Reactivity (10^{-4} dk/k)				C-E	$\frac{C}{E}$
					Central	Radial Leakage	Axial Leakage	Total		
Central Breeder Island	1	± 18.65 cm	-0.04	-0.013	0.48	-0.53	-0.01	-0.06	-0.03	1.71
	2	≈ 40% of core height	-0.59 ± 0.02	-0.21 ± 0.01	-	-	-	-	-	-
	2	± 37.29 cm ≈ 80% c/h	-1.08	-0.19	1.45	-2.35	-0.18	-1.09	-0.01	1.01
Fissile Annulus	3		-0.32	-0.09	1.19	-1.68	-0.14	-0.63	-0.30	1.95
	4		1.21	0.34	1.38	-0.30	-0.20	0.88	-0.33	0.73
	5		1.17	0.33	1.51	-0.45	-0.20	0.86	-0.31	0.73
	6		-0.88	-0.25	0.68	-1.63	-0.09	-1.04	-0.16	1.18
	7		0.69	0.19	1.06	-0.40	-0.16	0.50	-0.19	0.73
	8	± 18.71 cm	0.13 ± 0.02	0.04 ± 0.01	0.76	-0.52	-0.12	0.11	-0.02	0.85
	9		-0.30	-0.08	0.62	-0.90	-0.09	-0.37	-0.07	1.23
	10	≈40% of	-0.75	-0.21	0.49	-1.30	-0.07	-0.88	-0.12	1.16
	11	core height	-1.11	-0.31	0.38	-1.56	-0.04	-1.23	-0.12	1.11
	12		0.30	0.11	0.89	-0.58	-0.13	0.19	-0.11	0.62
	13		0.93	0.33	0.80	-0.13	-0.12	0.55	-0.37	0.60
	4/5		1.42	0.40	-	-	-	-	-	-
	13	± 37.43 cm ≈ 80% c/h	0.91	0.16	1.78	-0.29	-0.94	0.61	-0.31	0.66

Note: Zone 4/5 contains the adjacent rows of 5 lattice positions in zones 4 and 5.

+ Table II in Reference 8.

C/E values and the magnitude of the void reactivities has been noted, i.e.,

C/E < 1 for positive reactivities (predominant spectral term)

C/E > 1 for negative reactivities (predominant leakage term).

Thus, in the calculations, the spectral and leakage terms are consistently under- and over-predicted, respectively. Work is continuing on the explanation of these trends.

U. S. ZPPR Critical Experiments

In the U.S., several sodium void reactivity measurements have been performed with the Zero Power Plutonium Reactor (ZPPR) critical assembly.[1,10-19] ZPPR assemblies 2, 3, and 4 were designed to provide basic data for homogeneous two-zone fast reactors of about 350 MW(e). Each of these had a core height of 916 mm and 458 mm axial blankets. ZPPR assembly 5 is the Engineering Mockup Critical (EMC) for the Clinch River Breeder Reactor (CRBR). The ZPPR 7 and 8 programs were desinged to study annular heterogeneous configurations being considered for CRBR. Each core has three internal blanket rings and central blanket zone. Fourteen variations of the basic design have been studied. ZPPR assemblies 9 and 10 are mock-ups of a homogeneous two-zone fast reactor in the 700 MW(e) class. In all of the ZPPR assemblies, zones of different composition are construced by rearrangement of plates within drawers.

ZPPR/5 Critical Experiments

The heterogeneity effects introduced by the plates had a significant impact on the interpretation of the measurements for ZPPR/5.[12,15] These effects were accounted for in two ways. In the cross section preparation, ENDF/B-IV data was processed with the MC^2-II and SDX computer codes and heterogeneity effects for each cell type were included. Resonance self-shielding was calculated using equivalence theory and flux fine structure was treated by an integral transport perturbation method. A 156 group intermediate library was generated and then collapsed to 28 groups using an infinite medium spectrum for each composition. To account for the heterogeneity effect associated with streaming within the plates, Benoist directionally-dependent diffusion coeffcients were used.

To analyze the measurements in ZPPR/5, two-dimensional (RZ geometry) diffusion theory and exact perturbation calculations were done. These calculations demonstrated that RZ models are not adequate for calculating sodium void reactivities in zones where off-center control rods are present. Table N.1.2.5 gives the results of the measurements and calculations for ZPPR/5. The C/E values range from 1.08 to 1.48 with most being on the order of 1.2 to 1.3. Table N.1.2.5 also shows that if the Benoist diffusion coefficients are not used, the difference between measurement and calculations is greater for most regions in the reactor.

In addition to the sodium void measurements for plate assemblies, void measurements have also been made in a pin calandria zone.[13,14] This made it possible to determine the difficulties in extrapolating sodium void data obtained in a homogeneous plate critical facility to the pin environment of a homogeneous power reactor. The measured sodium void worth is different in the pin and plate zones, 2¢ and -10¢, respectively, but the calculated worths for the two zones are about the same, ∿10¢, since the pin and plate zones were almost identically matched in material composition. This result is said to imply that there exists a substantial difference in sodium void worth in pin and plate environments. This difference is attributed to neutron streaming in the plate environment which does not exist to the same degree in a pin environment.[14]

ZPPR/7 and ZPPR/8 Critical Experiments

Several different configurations were used for the heterogeneous ZPPR/7 and ZPPR/8 cores.[17,19] The ZPPR/8 configurations were similar to those of ZPPR/7, except thorium was used in selected blanket zones. This was reported to make no appreciable difference in the observed results.[19] Thus, only the sodium void measurements for ZPPR/7A will be considered. ZPPR/7 has continuous blanket rings and no control rod positions. The cross sections used in the analysis were generated in a manner analogous to those generated for ZPPR/5 with the core and blanket cells processed individually. The experiemental results were interpreted using RZ geometry with diffusion theory and exact perturbation theory. In general, the calculated results for the heterogeneous ZPPR/7 give less consistent comparisons with experiment, than the results for the homogeneous core, ZPPR/5. A summary of the analysis for ZPPR/5 and ZPPR/7A is given in the following paragraphs:[19]

> ". . . Transport corrections near the midplane were 9-12% for the heterogeneous cores, compared with 1-2% corrections for the homogeneous cores.

Table N.1.2.5+

RESULTS OF ASSEMBLY 5 ANALYSIS USING BENOIST DIFFUSION COEFFICIENTS

Zone Description	Mass of Sodium Voided, kg.	Experimental Worth (¢)	Calculations			C-E	C-E[c]	C/E
			Total	Leakage	Spectral			
Assembly 5A								
1A[a]	46.20	-14.8 ± 0.2	-18.69	-26.94	8.25	-3.89	5.8	1.26
1B	19.71	-22.9 ± 0.2	-24.79	-41.76	16.97	-1.89	9.6	1.08
1C	39.39	29.6 ± 0.3	33.11	-30.33	63.44	3.51	12.7	1.12
1D	59.10	25.5 ± 0.3	30.80	-53.99	84.79	5.30	18.8	1.21
2A[a]	36.53	-10.3 ± 0.2	-12.86	-18.32	5.66	-2.56	4.3	1.25
2B	15.58	-14.4 ± 0.3	-17.36	-28.93	11.57	-2.96	5.1	1.21
2C	31.15	18.1 ± 0.3	24.79	-19.29	44.08	6.69	12.5	1.37
2D	46.74	14.9 ± 0.3	22.04	-36.40	58.44	7.14	16.2	1.48
Assembly 5B								
1A	46.20	-18.3 ± 0.4	-23.41	-35.30	11.89	-5.11	4.9	1.28
1B	19.71	-18.4 ± 0.3	-24.89	-45.17	20.28	-6.49	5.7	1.35
1C[b]	39.39	40.6 ± 0.4	45.37	-35.51	80.88	4.77	14.8	1.12
1D[b]	39.39	52.7 ± 0.2	60.00	-24.07	84.07	7.30	12.7	1.14
1E[b]	19.71	-13.5 ± 0.3	-17.24	-38.97	21.73	-3.74	6.0	1.28
2A	36.53	-13.9 ± 0.3	-16.77	-24.74	7.97	-2.87	4.3	1.21
2B	15.58	-15.7 ± 0.2	-19.19	-32.00	12.81	-3.50	5.2	1.22
2C[b]	31.15	24.0 ± 0.3	27.50	-22.77	50.27	3.50	9.4	1.15
2D[b]	31.15	31.0 ± 0.3	36.29	-15.50	51.79	5.30	8.2	1.17
2E[b]	15.58	-11.6 ± 0.3	-13.68	-27.16	13.48	-2.08	4.7	1.18

[a] A steel change of 24.8 and 20.4 kg was included in the step A worths for zones 1 and 2, respectively. This steel change is also included in the calculations.

[b] Voiding in the lower half of the core was divided into two zones for phase B: (0 to -305 mm) and (-305 to -458 mm) from the midplane.

[c] C-E value calculated with standard diffusion coefficients.

+ Adapted from Table 1 in Reference 1.

Plate-streaming corrections for voiding near the midplane were about 10% for both core types. The corrections became much more significant for some of the axial steps.

Although this study cannot provide a definitive comparison of sodium void reactivity in heterogeneous versus homongeneous LMFBRs of CRBR size, some tentative assessments can be made regarding relative abilities to calculate sodium coefficients. Using consistent methods, C/E ratios for central core voiding were about 1.04 for the heterogeneous core and 1.12 for the homogeneous core with CRPs (control rod positions) (ZPPR-5). No reduction in the specific sodium worth relative to fuel worth was noted for the heterogeneous designs. While plate-streaming corrections were significant for both designs, transport corrections were essential in producing consistent C/E ratios for the heterogeneous cores. Radial leakage to internal blankets did not contribute significantly in reducing the sodium coefficient in the heterogeneous cores, since the radial contribution to the total reactivity is about 6% in both cases. Thus, the dominating factor in reduced sodium void reactivity for the CRBR heterogeneous designs is the smaller number of fuel subassemblies relative to the homogeneous designs. . ."

ZPPR/9 and ZPPR/10 Critical Experiments

Assembly ZPPR/9 is a mock-up of a 700 MW(e) two zone homogeneous LMFBR and serves as a clean physics benchmark. ZPPR/10A and ZPPR/10B have about the same core volumes as ZPPR/9, but they have nineteen control rod positions (CRP). All the CRPs were sodium-filled in assembly 10A, while in 10B seven of the positions were filled with natural B_4C.[18] The cross sections used in the sodium void analysis were obtained as outlined previously. The calculated void reactivities were done using RZ geometry (ZPPR/9) and XYZ geometry (ZPPR/10) with diffusion theory and exact perturbation theory. The results were given in Table N.1.2.6. Included in this table are C/E values obtained with less rigorous modeling. Using XY geometry with a constant buckling and first order perturbation theory (FOP) gives a value within $\pm$ 10% of the experimental results while using RZ geometry with exact perturbation theory (EP) always overpredicts the sodium void reactivity. This is attributed to the homogenization of the control rod positions, which in large cores results in larger errors since the calculated flux shape is more sensitive to the modeling approximation. The general conclusions reached for the large homogeneous core were:[18]

Table N.1.2.6[+]

COMPARISON OF CENTRAL ZONE AND SINGLE-DRAWER
SODIUM VOID REACTIVITIES

	ZPPR-9	ZPPR-10A	ZPPR-10B
Zone radius (m)	0.307	0.419	0.419
Measured reactivity, ¢ (E)[a]	28.43	42.50	36.18
Reference diffusion calculation, ¢ (C)	33.05	49.75	39.45
Correction for streaming	-2.1%	(-2.5%)[b]	(-6.5%)[b]
Correction for mesh	0.0	-0.5%	+3.0%
Correction for transport	-1.1%	+1.0%	+7.2%
Corrected C/E	1.13	1.18	1.20
rz - EP C/E	1.14	1.25	1.43
xy - FOP C/E	1.09	1.14	1.06
C/E, inner core average of single-drawer sodium worth.	1.18 $\pm$ 0.04	1.13 $\pm$ 0.04	1.16 $\pm$ 0.05

[a] Uncertainties are about 2%, and include estimates for errors of reference state ($\sim$1.5%), and random errors in the measurement ($\sim$1.0%).

[b] This correction is already included in the reference method and is shown for completeness in this Table.

[+] Taken from Reference 18.

1. The sodium void reactivities obtained for zones near the center of the assembly are predicted with C/E ratios of 1.17 when refined calculations are done.

2. No substantial change in C/E is observed when comparing the large homogeneous cores with previous smaller ones.

FFTF Results

In addition to the ZPPR assemblies, sodium void reactivities and biases have been determined for the Fast Flux Test Facility (FFTF).[20,21] The analysis for FFTF indicates that the sodium void reactivity can be calculated with a 15 percent uncertainty at the (1σ) confidence level.

N.1.3 General Conclusions

The various analyses of the sodium void measurements in critical assemblies have several characteristics in common. First, twenty or more energy group cross sections are used. These cross sections are generated from ENDF/B-Version IV or equivalent data, and heterogeneous unit cells are used. Also, core and blanket regions are treated individually.

Most of the studies used RZ geometry, diffusion theory, and perturbation theory to calculate the sodium void reactivity. However, some of the most recent analyses use XYZ geometry. The physical construction, i.e., plates in boxes, of the critical assemblies causes enhanced neutron streaming which affects the sodium void reactivity. To compensate for this effect, directional diffusion coefficients were used.

Ignoring the results from the BIZET Program, the C/E ratios for the radially heterogeneous critical assemblies are greater than one, i.e., in the Pre-Racine and the ZPPR analysis the calculated sodium void reactivity is greater than the measured reactivity. In the report on the BIZET Program, the C/E values of less than one are noted as being different from previous results.[8] The C/E ratios for the heterogeneous cores also have more dispersion than those for homogeneous cores. This dispersion is generally attributed to the varying cancellation of errors in the determination of the spectral and leakage components of the sodium void reactivity.

N.1.4 Specific Conclusions

The results reviewed here indicate that the sodium void reactivity calculated for the EPRI heterogeneous LMFBR is conservative. The cross section preparation and the methods used to calculate the sodium void reactivity for the EPRI core are analogous to those used to interpret the ZPPR experiments. These techniques always overpredicted the sodium void reactivity for the critical assemblies. Thus, the calculated sodium void reactivity for the EPRI core is also expected to be greater than the actual void reactivity. Therefore, the calculated flowing sodium void reactivity of $2.58 may be used as an upper bound on the true reactivity and, hence, no further design limitations or improvements are required for this figure of merit.

However, the degree of conservatism in the design is difficult to estimate. None of the critical assemblies have a core as complex or as large as the EPRI core. Thus, correction factors or biases obtained for these experimental cores are not appropriate for the EPRI core.

Further, it is not obvious that the refined techniques used to analyze the experimental cores are necessary for the analysis of the EPRI core. For instance, consider the use of directional diffusion coefficients.

The physical geometry of the critical assemblies introduces neutron streaming which is not characteristic of a fast power reactor. The streaming in the criticals has two components: one which would be present in both a pin and a plate-type assembly, i.e., a true streaming, and a second which is only characteristic of the plate assemblies, i.e., an "artificial" streaming. If the true streaming is the dominant phenomenon in the critical assemblies, then directional diffusion coeffcients should be used in analyzing pin-type reactors, but if the "artificial" streaming is the dominant feature in the plate assemblies, then the use of directional diffusion coefficients depends on how one extrapolates from the plate-type criticals to the pin-type power reactors. For some of the critical assemblies, corrections for the "artificial" plate streaming have been reported. While these corrections are valid for only a given geometry, they indicate that the correction is about 10% for both heterogeneous and homogeneous cores.[19] However, this is inconsistent with the experiment for a homogeneous assembly which specifically examined the extrapolation from a plate-type environment to a pin-type environment.[13,14] In this experiment, the "artificial" streaming clearly dominated, since in the plate-

type assembly, the measured sodium void reactivity was -10¢ while replacing the plates with a pin assembly changed the measured reactivity to +2¢. This is much greater than a 10% change. The literature is not in agreement on which streaming is dominant, i.e., the real or the "artifical" streaming. Thus, directional diffusion coefficients may or may not be necessary to accurately estimate the true streaming in a power reactor.

Hence, it is not possible to precisely estimate the accuracy of the sodium void calculations for the EPRI heterogeneous core. However, the wide range of experiments reviewed here tends to indicate that if reasonable physical models are used in the calculations, the results are conservative and the difference between calculation and experiment is usually less than 20%. There is no reason to suspect that when experimental data for large cores becomes available the C/E ratios will be found to be appreciably different from these observed in the experiments already completed.

N.2 METHODOLOGY ASSESSMENT FOR TEMPERATURE AND PRESSURE DROP CALCULATIONS

N.2.1 Introduction

The accuracy of predictions of coolant pressure drop and temperature distribution in LMFBR core and blanket assemblies depends on the correlations used to predict these parameters. The Novendstern correlations[22] are presently utilized by LMFBR core design codes to determine assembly coolant flow split parameters and pressure drop. Recently, new correlations by Chiu, Todreas and Rohsenow[23,24] for predicting bundle coolant flow split parameters and the bundle average friction factor have been developed.

The purpose of this investigation is to briefly describe both methods, highlighting the assumptions employed in their development, and to determine if Novendstern's methodology is still appropriate or if the new correlations should be utilized for analysis. Assembly subchannel flow distribution, pressure drop and cladding midwall temperatures are the performance parameters.

The major difference between the correlations developed by Novendstern and by Chiu, Todreas and Rohsenow is how they treat the effect of the wire wrap lead on the subchannel flow distribution and on the assembly average friction factor. Both, the assembly average friction factor and subchannel flow distribution are dependent upon each other.

By neglecting the effect of the wire wrap lead on the subchannel flow distribution, Novendstern developed correlations which predict assembly average friction factor and assembly subchannel flow distribution independent of each other.

Chiu developed an iterative scheme that determines both parameters and accounts for the effect of the wire wrap lead on assembly average friction factor and subchannel flow distribution.

N.2.2 Theory

To predict assembly coolant temperatures and pressure drop it is necessary to accurately calculate the flow distribution in the assembly. The flow distribution is quantified by three flow split parameters X_1, X_2 and X_3 which are defined as the ratios of the average axial interior, edge and corner subchannel velocities to the bundle average axial velocity, respectively. (See Figure N.2.2.1). The average axial coolant velocity is averaged over the subchannel cross-section and over one wire lead length for a given subchannel type. Assuming the coolant pressure drop to be equal in all subchannels, the subchannel coolant velocities and hence flow split parameters can be determined using the friction factor relationship

$$\Delta P_b = \Delta P_1 = \Delta P_2 = \Delta P_3$$

or

$$f_b \frac{L}{De_b} \frac{\rho V_b^2}{2g} = f_i \frac{L}{De_i} \frac{\rho V_i^2}{2g} \qquad i = 1,2,3$$

(subscripts 1, 2, 3 and b denote interior, edge, corner subchannels and bundle regions, respectively; all bundle quantities are average values) and the mass continuity equation:

$$\sum_{i=1}^{3} N_i A_i V_i = V_b \sum_{i=1}^{3} N_i A_i$$

or

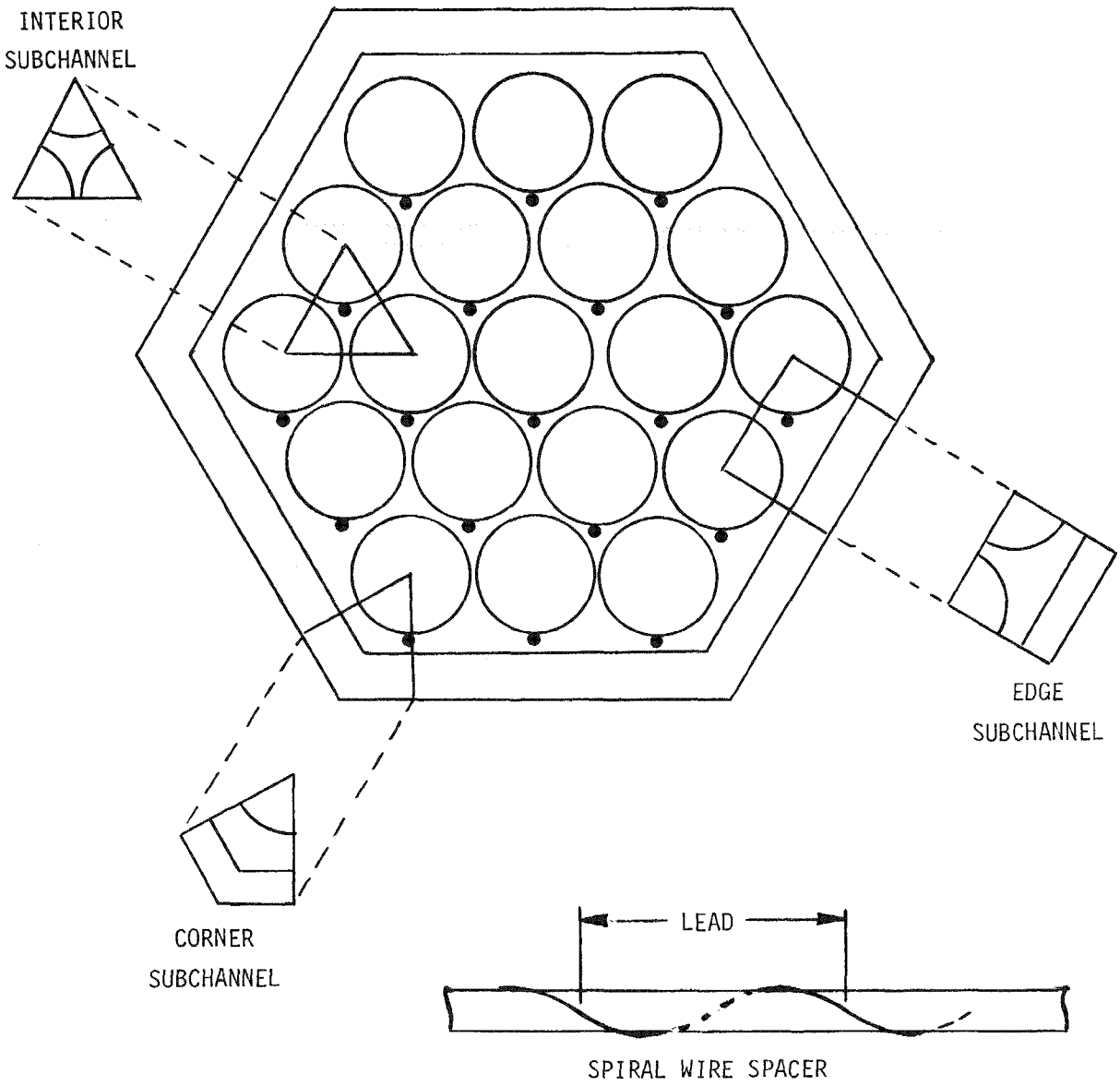

Figure N.2.2.1. Definition of typical subchannels and of wire spacer lead[22].

$$\sum_{i=1}^{3} N_i A_i X_i = \sum_{i=1}^{3} N_i A_i$$

where

V is the velocity in the channel,
L is the length of the channel,
ρ is the density of the coolant,
g is the gravitational constant,
De is the hydraulic diameter,
f is the friction factor,
N is the number of channels in the bundle, and
A is the channel flow area.

N.2.2.1 Novendstern's Approach

Experimental Data Base

In 1972, E. Novendstern outlined a turbulent flow pressure drop model for wire-wrapped fuel rod assemblies. He checked this model against measurements by Rehme[25,26], Reihman[27] and Baumann[28] which are carried out during 1965 to 1969. Of general concern was the accuracy of those pressure drop data. To avoid erroneous pressure drop readings due to the cross flow induced by the wire wrap. Reihmen placed pressure taps above and below the ends of the pins. By using two different lengths of pins for each given geometry, the difference in pressure drops was then attributed only to the length difference. Reihman measured the pressure differential at a given axial position by using six pressure taps located 60° apart around the housing. He found the angular dependence to be small and connected all six taps to a common header.

Baumann et al. investigated various types of spacers and derived correlations for the friction factors depending on the geometry.

Correlations

Novendstern treated only the case of turbulent flow conditions. In this flow regime it was assumed that the friction factor for each subchannel obeys the smooth

channel relationship:

$$f_i = f_i^{smooth} = \frac{0.316}{Re_i^{0.25}}$$

where Re is the Reynolds number. Novendstern acknowledged that this relationship is, in general, somewhat inaccurate in that the corner and edge channels do not have the same friction factor relationship as the interior channel, because of their different geometries. However, due to lack of experimental measurements on individual subchannels this relationship was chosen. Combining the above relationships with the mass continuity equation and assuming equal pressure drop in all subchannels, the expression for the coolant flow distribution factor for the ith subchannel is:

$$X_i = \frac{\sum_{j=1}^{3} N_j A_j}{\sum_{j=1}^{3} N_j A_j (De_j/De_i)^{0.714}}$$

The relationships chosen for the calculation of subchannel friction factors and flow splits neglect the presence of the wire wrap. The effect of the wire wrap on assembly pressure drop was accounted for, however, by introducing a smooth friction factor multiplier, M, into the equation of assembly pressure drop as:

$$\Delta P_b = M f_{smooth} \frac{L}{De_1} \frac{\rho V_1^2}{2g}$$

The following expression for M was derived by assuming that the flow through the interior subchannels follows the wire wrapping.

$$M = \left[\frac{C_1}{(P/D)^{C_2}} + \frac{C_3 \, (P/D)^{C_4} \, Re^{C_6}}{(H/D)^{C_5}} \right]^{0.885}$$

where P/D is the fuel pin pitch to diameter ratio and H/D is the wire lead to fuel pin diameter ratio.

The constants C_1 through C_6 were obtained by correlating the preceeding bundle pressure drop equation with existing pressure drop measurements and found to be:

$$C_1 = 1.034$$
$$C_2 = 0.124$$
$$C_3 = 29.7$$
$$C_4 = 6.94$$
$$C_5 = 2.239$$
$$C_6 = 0.086$$

N.2.2.2 Chiu's Approach

Experimental Data Base

In 1978, Chiu, Todreas and Rohsenow carried out experiments[29,30] to study the flow split behavior in two wire-wrapped 61-pin bundles. Subchannel flow rates for each subchannel were measured using a methodology similar to the isokinetic sampling technique employed in the ANL 91-rod hydraulic test. To insure that the static pressure and hence the flow rate at the end of the subchannel have not been disturbed by the installation of the measuring instruments, the static pressure at the exit of the subchannel has to be equal to the static pressure of the surroundings.

In deriving their correlations, Chiu et al. also used the results of measurements by J. J. Lorenz and Ginsberg[31,32] (1973, 1977), Pedersen et al.[33] (1975), Bartholet et al.[34] (1975), Chen et al.[35] (1974) and Bump[36] (1962).

Correlations

In the turbulent flow regime, the coolant pressure drop in a wire wrapped subchannel was not considered the same as that in a smooth tube channel. Instead, the following two components were taken into account:

1. Form drag pressure drop induced by flow over the wires, ΔP_R,
2. Skin pressure drop characterized by the resultant velocity of both the axial and transverse velocity components of the subchannel flow, ΔP_S.

These two components comprise the subchannel total coolant pressure drop, ΔP,

illustrated in Figure 2.2.2.1 as:

$$\Delta P = \Delta P_S + \Delta P_R$$

where

$$\Delta P_S = \frac{Y}{Re^{0.25}} \frac{L}{De_i} \frac{\rho V_a^2}{2g} ,$$

$$\Delta P_R = \frac{Z}{Re^{0.25}} \frac{L}{De_i} \frac{\rho V_a^2}{2g} ,$$

Y and Z are functions of subchannel geometry and the relationship of the coolant velocity components is shown in Figure 2.2.2.2. V_a is the coolant velocity in the axial direction.

Intersubchannel mixing in an LMFBR assembly is due mainly to the sweeping flow effect.[30] The sweeping flow is a diversion of flow by the wires wrapped about the fuel rods which transport the coolant energy from one subchannel to its adjacent subchannels. Chiu observed during a recent experimental study[37] that: sweeping flow along the duct wall always follows the wires and the sweeping flow in the interior subchannels has the characteristic of changing direction in a very short distance. These facts led to the conclusion that the skin friction is the controlling factor for the total edge subchannel pressure drop and the form drag is the controlling factor for the total interior subchannel pressure drop. In other words,

$$\Delta P_{interior} \simeq f(\Delta P_R)$$

and

$$\Delta P_{edge} \simeq f(\Delta P_S) \quad .$$

These simplifying assumptions were used to derive the following expressions for the flow split parameters at turbulent flow conditions which depend only on geometry:

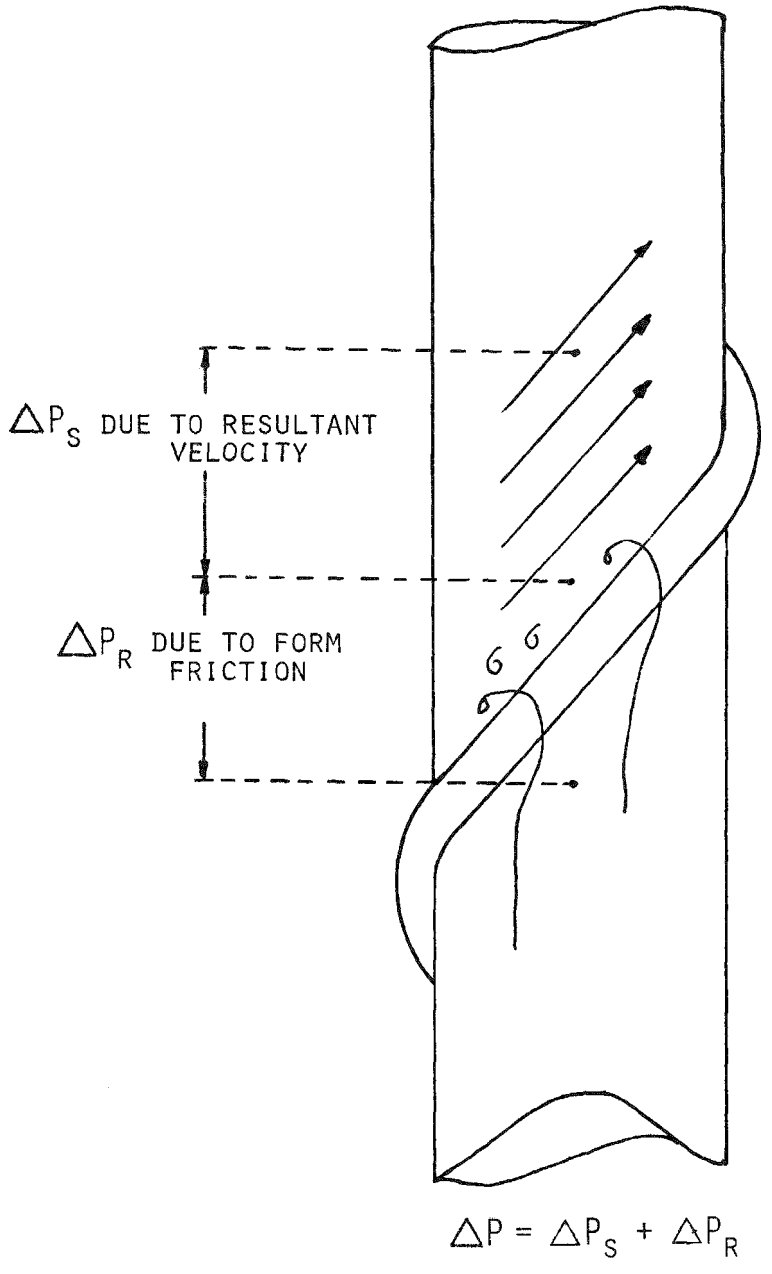

Figure N.2.2.2.1. Proposed subchannel pressure drop model by Chiu et al.

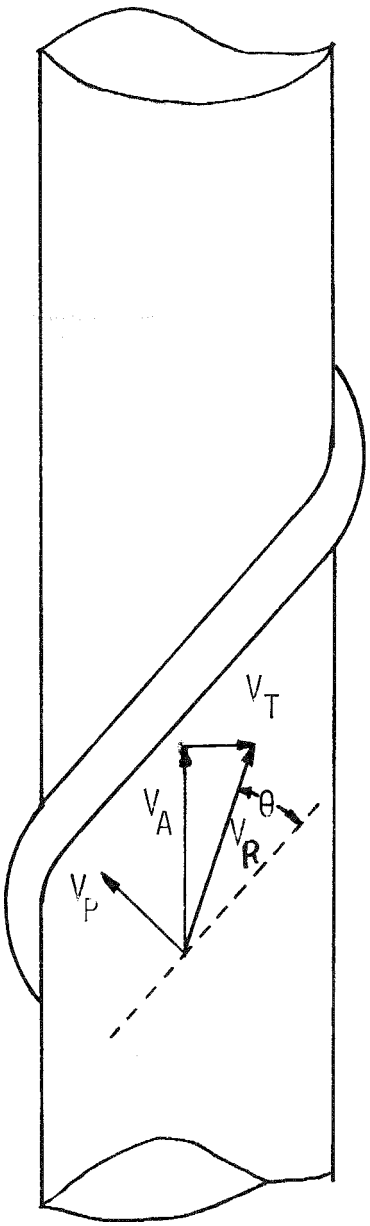

Figure N.2.2.2.2. Velocity components used in the Chiu et al. Model

a. $$X_1 = \frac{A_{s1}N_1 + A_{s2}N_2 + A_{s3}N_3}{A_{s1}N_1 + \left[\frac{C_1\left(\frac{De_1}{H}\right)\left(\frac{A_{r1}}{A'_{s1}}\right)\left(\frac{P^2}{\pi^2P^2+H^2}\right)+1}{\left\{1+\left(C_2 n \frac{V_T}{V_2}\Big|_{gap}\right)^2\right\}^{1.375}}\right]^{0.571} \left(\frac{De_2}{De_1}\right)^{0.714}\left[A_{s2}N_2+A_{s3}N_3\right]},$$

(1)

$$X_2 = \frac{A_{s1}N_1 + A_{s2}N_2 + A_{s3}N_3}{A_{s1}N_1 \left[\frac{\left\{1+\left[C_2 n \frac{V_T}{V_2}\Big|_{gap}\right]^2\right\}^{1.375}}{C_1\left(\frac{De_1}{H}\right)\left(\frac{A_{r1}}{A'_{s1}}\right)\left(\frac{P^2}{\pi^2P^2+H^2}\right)+1}\right]^{0.571} \left(\frac{De_1}{De_2}\right)^{0.714} + A_{s2}N_2 + A_{s3}N_3},$$

(2)

b. $X_3 = X_2$

It was assumed that X_3 is equal to X_2 due to the large amount of sweeping flow along the duct wall. The constants C_1, C_2, and C_3 were determined by analysis of experimental data[23] and found to be:

$C_1 = 2{,}200.0$

$C_2 = 1.9$

$C_3 = 1.2$

The nomenclature utilized by the above formulae is listed below:

A_{ri} : Projected are of wire body in the ith subchannel,

$A_{r1} = (\pi(P - \frac{D}{2})^2 - \pi D^2/4.0)/6.0$, for the interior subchannels,

$A_{r2} = \frac{(\frac{D}{2} + D_W)^2\pi - \frac{\pi D^2}{4}}{4}$, for edge subchannels,

A_{si} : Flow area for ith subchannel including wire wrap (1/2, 1/2, 1/6th wire diameter for subchannels i = 1,2,3, respectively),

A'_{si} : Flow are for ith subchannel without wire wrap,

De_i : Equivalent diameter for ith subchannel including wire wrap,

$\frac{d_{gap}}{n}$: Average width of the transverse flow passage through an edge subchannel,

$$n = \frac{d_{gap}}{((\frac{D}{2} + d_{gap})\frac{P}{2} - \frac{\pi D^2}{16})/\frac{P}{2}} \quad \text{and}$$

d_{gap} : Wire wrap diameter

$\left.\frac{V_T}{V_2}\right|_{gap}$: Ratio of the transverse to axial velocity evaluated in the gap between two edge subchannels

$$\left.\frac{V_T}{V_2}\right|_{gap} = 10.5\left(\frac{D_W}{P}\right)^{0.35} \frac{P}{(\pi^2 P^2 + H^2)^{0.5}} \left(\frac{A_{r2}}{A_{s2}}\right)^{0.5}$$

General Flow Condition Correlations

The methodology used in Reference 24, to derive the correlations for subchannel flow split parameters at turbulent flow conditions was employed to generate an iterative procedure for calculating the assembly subchannel flow distribution and average friction factor. This procedure, summarized below, generates the flow split parameters and average friction factor for a wire wrapped assembly as a function of geometry and Reynolds number.

Step I

Initialize

$$X_1 = 1$$
$$X_2 = 1$$
$$X_3 = 1$$

for a given bundle Reynolds number and calculate the subchannel friction factors using the following five equations:

(subscripts L and T for laminar and turbulent flow, respectively)

$$f_{iL} = C_1 \left(\frac{A_{ri}}{A_{si}}\right)\left(\frac{De_i}{H}\right)\left(1-\frac{P-D}{De_i}\right)\frac{C_3}{Re_i} + \frac{C}{Re_i} \qquad (3.1)$$

($i = 1$ and 2, $C_1 = 3$ and $C_2 = 2$; f_{3L} is assumed equal to f_{2L})

$$f_{2T} = \left[1+\left(1.9n \left.\frac{V_T}{V_2}\right|_{gap}\right)^2\right]^{1.375} \qquad (3.2)$$

$$x\left[1 + C_c\left(\frac{De_2}{H}\right)\left(\frac{P^2}{\pi^2 P^2+H^2}\right)\right]\frac{C_T}{Re_2^{0.15}}$$

$$f_{1T} = f_{2T}\ \frac{De_1}{De_2}\left(\frac{X_{2T}}{X_{1T}}\right)^2 \qquad (3.3)$$

(X_{1T} and X_{2T} are evaluated in equations 1 and 2)

$$f_{3T} = f_{2T}\ \frac{De_3}{De_2} \qquad (3.4)$$

(X_{3T} is assumed equal to X_{2T})

$$f_i = \left(f^{\ell}_{iL} + f^{\ell}_{iT}\right)^{1/\ell} \qquad (i = 1, 2, 3) \qquad (3.5)$$

where C is a function of P/D as suggested in Reference (30); C_3, C_c, C_T and ℓ are the preliminary calibrated[24] constants:

$$C_3 = 950.0$$
$$C_c = 450.0$$
$$C_T = 0.120$$
$$\ell = 1.50$$

Step II

Assume that equal subchannel pressure drops exist for the bundle Reynolds number and combine the values found for f_i with the mass continuity equation to obtain X_1, X_2, and X_3.

Step III

The equal subchannel pressure drop assumption yields the bundle average friction factor via the equation:

$$f_b = f_2\left(\frac{De_b}{De_2}\right) X_2^2 \qquad (4)$$

Finally, the assembly average pressure drop may be predicted by:

$$P_b = f_b \frac{L}{De_b} \frac{\rho V_b^2}{2g}$$

N.2.2.3 Verification

Table N.2.2.3.1 lists the applicable range and error bound for the Novendstern and Chiu correlations. The uncertainty of 14% in the Novendstern bundle friction factor correlation for the turbulent flow regime is consistent with a 95% confidence level. Chiu's correlation for bundle average friction factor for laminar, transition and turbulent flow conditions has an uncertainty of 16% with an 86% confidence level. An uncertainty of 16% is considered to be typical experimental error for pressure drop measurements.[24] Chiu et al. arrived at their uncertainties by evaluating 55 sets of experimental data covering the full range of laminar to

Table N.2.2.3.1

Range of Parameters and Error Bounds for which Correlations are Valid

Novendstern Correlations	Chiu, et al., Correlations
Applicable Range	
2,600 < Re < 200,000	400 < Re < 150,000
9 < H/D < 96	4 < H/D < 96
1.06 < P/D < 1.42	1.06 < P/D < 1.317

Error Bounds

Re	Flow Split Parameters	Bundle Average* Friction Factor	Flow Split Parameters	Bundle Average** Friction Factor
Laminar	-	-	±5%	±16%
Transition	-	-	±10%	±16%
Trubulent	Unknown	±14%	±5%	±16%

Where P/D is the fuel pin pitch to diameter ratio,

H/D is the wire lead to fuel pin diameter ratio and

Re is the bundle average Reynolds number.

* at 95% confidence level

** at 86% confidence level

turbulent flow regimes. Novendstern, on the other hand, arrived at his uncertainty by evaluating only a few existing sets of experimental data covering only the turbulent flow regime. Thus, Chiu and Novendstern used a different data base.

Novendstern did not compare his method for calculating flow split parameters with experimental data. Chiu et al., on the other hand, carried out extensive comparisons[23,24] and found that the uncertainty is $\pm$ 5% in the laminar and turbulent regime and $\pm$ 10% in the transition regime. The 5% interval is less than typical experimental error while the 10% interval reflects the highly unstable nature of experimental data in the transition regime.[23]

To compare the two methods, measurements of edge flow split parameters were used as a basis. A comparison of the interior flow split parameter was not performed because it is not as sensitive as the edge flow split parameter to variations in bundle geometry. This sensitivity can be illustrated by differentiating the mass continuity equation to yield:

$$\Delta X_1 = \frac{A_2 N_2}{A_1 N_1} \Delta X_2$$

The ratio A_2N_2/A_1N_1 is that of the total edge to total interior subchannel flow areas. Since this parameter is less than 1 ($\sim$0.2 and $\sim$0.4 for the 0.28 inch pin diameter core assemblies and 0.447 inch pin diameter blanket assemblies, respectively), a 10% change in the edge flow split parameter X_2 corresponds to about a 2 and 4% change in the interior flow split parameter X_1 for core and blanket assemblies, respectively.

The flow conditions, existing in the core and blanket assemblies of the present 0.28 inch fuel pin diameter design, lie in the turbulent flow regime. Therefore, a comparison with turbulent flow measurements was performed. Listed below are the experimental measurements of assembly subchannel flow that were used as a basis.

LIST OF EXPERIMENTAL EDGE SUBCHANNEL FLOW SPLIT PARAMETERS

Experimenter	# of Pins	D(in)	$\frac{P}{D}$	$\frac{H}{D}$	Re X 10^3	Experimental Results
ANL-91 Lorenz and Ginsberg	91	0.5	1.240	48	9-24	0.99 ± 3%
M.I.T. Chiu et al.	61	0.5	1.067	8	11-16	1.210 ± 5%
M.I.T. Chiu et al.	61	0.5	1.067	4	6-21	1.412 ± 5%

The comparison shown below clearly indicates that Chiu's method is superior to that of Novendstern for predicting subchannel flow splits.

Experimenter	P/D	H/D	Experimental Results: X2	Chiu et al. X2	Novendstern X2
ANL-91 Lorenz and Ginsberg	1.240	48	0.99	1.03 (4.0%)[a]	1.11 (12.1)[a]
M.I.T. Chiu et al.	1.067	8	1.21	1.17 (-3.3%)	1.13 (-6.6%)
M.I.T. Chiu et al.	1.067	4	1.412	1.47 (4.1%)	1.13 (-20.0%)

a $$\frac{X_2 \text{ (predicted)} - X_2 \text{ (experimental)}}{X_2 \text{ (experimental)}} \times 100$$

To better illustrate the impact of Novendstern's and Chiu's methods on the prediction of flow split parameters and bundle friction factors, a blanket and a fuel assembly were analyzed for two different flow conditions each (see Table N.2.2.3.2). The Reynolds numbers corresponded to the minimum and maximum values obtained from

Table N.2.2.3.2

FLOW SPLIT PARAMETERS FOR 0.28" FUEL PIN DIAMETER DESIGN

	Core		Blanket	
Pin Diameter (in.)	0.28		0.447	
P/D	1.171		1.069	
H/D	42.86		8.95	
	Minimum Re	Maximum Re	Minimum Re	Maximum Re
Re	55,354.	68,895.	16,397.	58,344.
Chiu, et al.				
X_1	0.992	0.992	0.942	0.942
X_2	1.035	1.035	1.153	1.158
X_3	1.033	1.034	1.210	1.153
Novendstern				
X_1	0.973		0.951	
X_2	1.127		1.148	
X_3	0.885		0.784	
$\frac{X_i^{Nov.} - X_i^{Chiu.}}{X_i^{Chiu.}} \times 100$				
$\%\Delta X_1$	-1.9	-1.9	1.0	1.0
$\%\Delta X_2$	8.9	8.9	-0.4	-0.9
$\%\Delta X_3$	-14.3	-14.4	-35.2	-32.0

the orificing analysis. As previsously mentioned, the flow conditions existing in the 0.28 inch fuel pin diameter LMFBR core design, lie in the turbulent flow regime for both the core and blanket assemblies. Novendstern's flow split parameter correlations are independent of the H/D ratio. On the other hand, Figure N.2.2.3.1 illustrates that, in the turbulent flow regime, the Chiu Flow split correlations are sensitive to the H/D ratio and that this sensitivity is proportional to the P/D ratio.

The data in Table N.2.2.3.2 show furthermore that Novendstern's flow splits do not depend on the Reynolds number. They are decided strictly from the geometry of the pin bundle.

For the blanket interior and edge subchannels, the flow split predictions made by both methodologies agree with each other to within one percent. For the core interior and edge subchannels, predictions differ by as much as nine percent. Calculated flow splits disagree most for both the core and blanket corner subchannels. In this regions they disagree by 4% and 35% for the core and blanket assemblies, respectively.

Table N.2.2.3.3 compares the results obtained for the bundle friction factor. Both methodologies yield similar results for the cases involving the core assemblies. Novendstern's correlations consistantly predict higher blanket friction factors by as much as 20%.

N.2.3 Applications

The impact of the Chiu and Novendstern correlations on assembly bundle pressure drop and cladding midwall temperature predictions were investigated. Carried along was the often used option of equal subchannel flow splits which assumes that the ratio of subchannel average velocity to the bundle average velocity is the same for all assembly subchannels. To calculate flow splits, temperatures, and pressure drops the thermal-hydraulics analysis codes CORE-3D and ENERGY were used which permit optional use of either Novendstern's methodology (including equal flow splits) or Chiu's methodology.

N.2.3.1 Assembly Performance

A constant coolant flow rate of 265,500 lb/hr through a core assembly (orificing

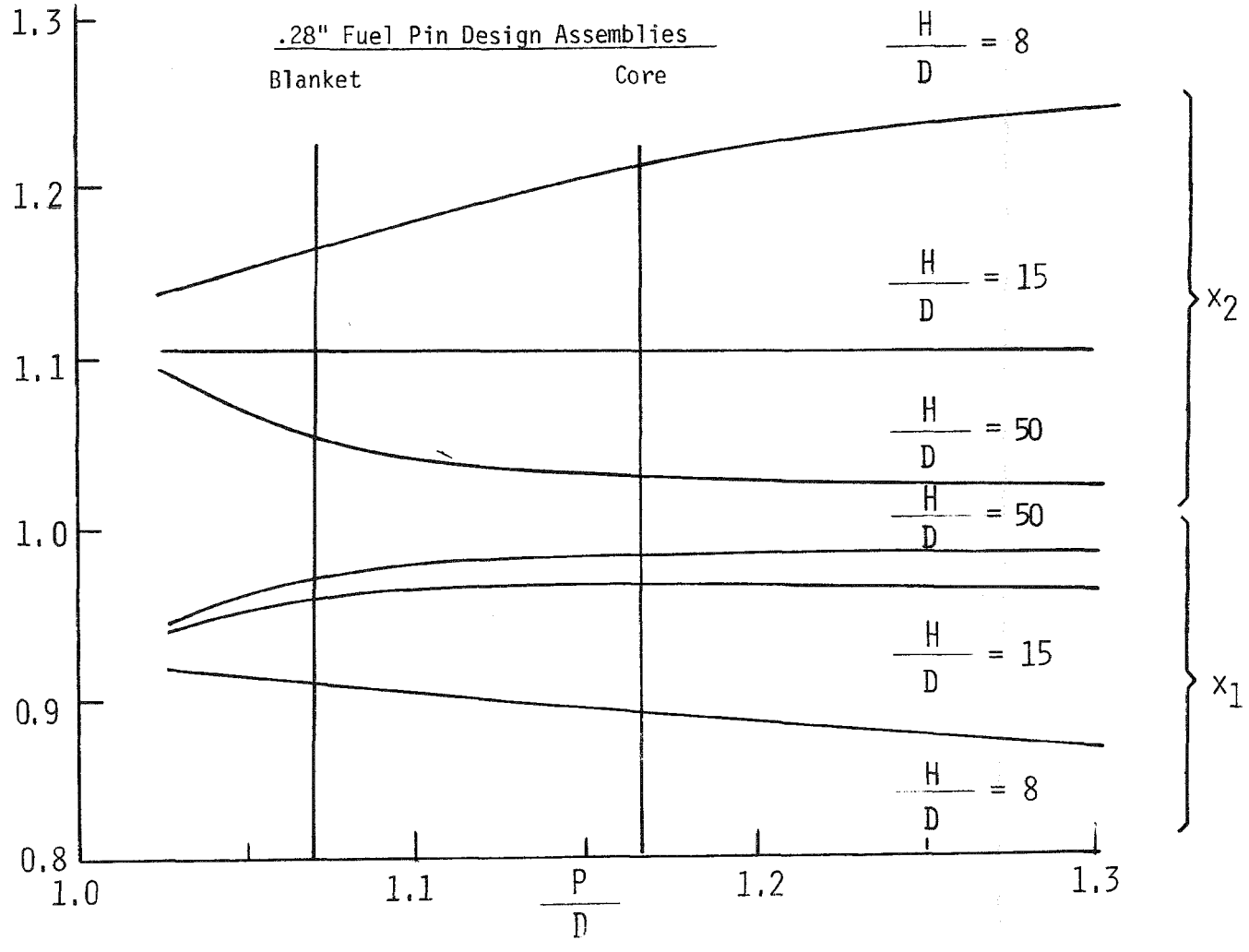

Figure N.2.2.3.1. Prediction of flow split parameters X_1 and X_2 in the turbulent flow regime [23].

Table N.2.2.3.3

BUNDLE AVERAGE FRICTION FACTORS FOR 0.28" FUEL PIN DIAMETER DESIGN

		Core		Blanket
Pin Diameter		0.28		0.447
P/D		1.171		1.069
H/D		42.86		8.95

	Case 1	Case 2	Case 3	Case 4
Re	52,196.	66,245.	15,106.	56,344.
Chiu, et al. f_b	0.0214	0.0206	0.0387	0.0309
Novendstern f_b	0.0216	0.0204	0.0464	0.0349
$\frac{f_b^{Nov.} - f_b^{Chiu.}}{f_b^{Chiu.}} \times 100$	0.9	-1.0	19.9	12.9

zone 1) and 158,301 lb/hr through a blanket assembly (orificing zone 4) is assumed.

If the temperatures predicted by the Chiu correlations are used as a basis as shown in Table N.2.3.1.1, for the core assemblies the Novendstern correlations over-predict by 10^{o} F and the equal flow splits assumption under-predicts by 3^{o} F the nominal peak cladding midwall temperature. For blanket assemblies, the same temperature is under-predicted by 5^{o} F by the Novendstern correlations and by 30^{o} F by the equal flow splits assumption. The Novendstern correlations under-predict the core assembly bundle pressure drop by ∿1% but they over-predict the blanket assembly bundle pressure drop by ∿13%.

N.2.3.2 Core Performance

The Chiu and Novendstern correlations, and the equal flow splits assumption were used to calculate assembly flow rates and cladding midwall temperatures, such that the peak cladding midwall temperature is the same in all orificing zones. Assemblies were assigned to orificing zones according to assembly peak pin power. Assembly bundle pressure drops were also calculated. The results are presented in Table N.2.3.2.1. If the predictions of the Chiu correlations are used as bases, the Novendstern correlations over-predict the nominal peak cladding midwall temperature by 5^{o} F and the equal flow splits assumption under-predicts the same temperature by 11^{o} F. The Novendstern correlations over-predict the maximum pressure drops by 1% and 9% in the core and blanket assemblies, respectively. The combination of the equal flow splits assumption and the Novendstern correlations over-predicts the maximum assembly bundle pressure drop in the core by ∿2% and in the blankets by ∿6%.

N.2.4 Recommendations

Currently used methodologies in LMFBR thermal-hydraulic analysis do not properly take into account the wire lead effect on flow split parameters. Measurements by Chiu et al. have clearly shown that the flow split parameters are very sensitive to the change of the wire lead length. The Chiu methodology takes this effect into account by treating the contributions of form drag and skin friction to the subchannel friction factor. Chiu et al. was therefore, able to derive correlations for the bundle friction factor and subchannel flow splits which are valid over the whole range of interest of Reynolds numbers. Since Novendstern's methodology does not consider the impact of the wire wrap lead on the flow split parameters, Chiu's methodology need be considered superior for the prediction of assembly subchannel flow splits.

Table N.2.3.1.1

ASSEMBLY BUNDLE PRESSURE DROPS AND PEAK CLADDING MIDWALL TEMPERATURES PREDICTED BY THE CHIU AND NOVENDSTERN CORRELATIONS AND THE EQUAL FLOW SPLITS ASSUMPTION

	Flow (lb/hr)	Nominal Peak Cladding Midwall Temperature (^{o}F)	2σ Peak Cladding Midwall Temperature (^{o}F)	Pressure Drop (psi)
		CORE ASSEMBLY		
Chiu	265,500	1084	1216	50.4
Novendstern	265,500	1094	1227	50.0
Equal Flow Splits	265,500	1081	1211	50.0*
		BLANKET ASSEMBLY		
Chiu	158,301	1111	1231	64.3
Novendstern	158,301	1106	1225	72.9
Equal Flow Splits	158,301	1081	1194	50.0*

*Novendstern correlations

Table N.2.3.2.1

ASSEMBLY FLOW RATES, COOLANT VELOCITIES, ASSEMBLY BUNDLE PRESSURE DROPS, AND PEAK CLADDING MIDWALL TEMPERATURES PREDICTED BY CHIU AND NOVENDSTERN CORRELATIONS AND THE EQUAL FLOW SPLITS ASSUMPTION

(Orificing Based on Pin Power and Equal Peak Cladding Midwall Temperatures.)

Zone	Flow Rate ($\frac{lb}{hr}$)	Velocity ($\frac{ft}{sec}$)	Pressure Drop (psi)	Nominal Peak Cladding Midwall Temperature ($^{\circ}F$)
		Chiu et. al.		
1	261,595	22.1	49.1	1092
2	237,303	20.1	41.0	1092
3	220,782	18.6	35.9	1092
4	164,355	20.8	68.9	1092
5	119,883	15.2	38.6	1092
6	77,514	9.8	17.4	1092
7	48,553	6.1	7.4	1092
		Equal Flow Splits		
1	265,500	22.4	50.0*	1081
2	240,897	20.4	42.1	1081
3	224,170	18.9	37.2	1081
4	158,301	20.1	72.9	1081
5	115,468	14.6	41.5	1081
6	74,831	9.4	19.2	1081
7	46,974	5.9	8.4	1081
		Novendstern		
1	263,674	22.3	49.4	1097
2	239,238	20.2	41.6	1097
3	222,628	18.7	36.7	1097
4	161,028	20.4	75.1	1097
5	117,456	14.9	42.8	1097
6	76,122	9.6	19.8	1097
7	47,784	6.0	8.7	1097

* Novendstern Correlation

Novendstern's methodology accounts for the wire wrapping in the pressure drop calculations by applying a multiplier to the smooth tube friction factor. This multiplier, which depends on P/D and H/D, contains six constants used to fit the adjusted friction factor to pressure drop measurements in the turbulent flow regime. Chiu et al. derived a correlation for the friction factor which depends on geometry, flow conditions, and wire lead. This correlation contains four calibrated constants and is valid in the laminar, transition, and turbulent flow regimes.

Novendstern and Chiu et al. used a different data base in the development of their friction factor correlations. Consequently, a direct comparison of the correlations error bounds can not be definitively made. However, Chiu et al. have derived these correlations from a physical standpoint superior to that of Novendstern. Therefore, because the "older" method does not take into account the effect of the wire lead on flow split parameters and since it has only a first-order adjustment of the friction factor to reflect differences in Reynolds number and spacer wire lead, it is recommended to use Chiu's methodology for the thermal-hydraulic analysis.

REFERENCES

1. C. L. Beck, et. al., On the Extrapolation of ZPPR Sodium Void Measurements to the Power Reactor, Fast Reactor Safety and Related Physics, CONF761001, Chicago Illinois (1976).

2. M. Nakano, et. al., An Experimental Study of Heterogeneous LMFBR Core Using FCA Assemblies with Axial Internal Blanket, International Symposium on Fast Reactor Physics, Aix-en-Provence, France (1979).

3. Y. H. Bouget, et. al., Physics Performances of Heterogeneous Fast Reactor Core Concept Studied In Masurca,Trans. Am. Nucl. Soc., 26, 554 (1977).

4. Y. H. Bouget, et. al., Physics Studies of Neutronic Problems Related to the Heterogeneous Fast Reactor Core Concept: Experimental Programme Pre-Racine Performed on MASURCA, Advances in Reactor Physics, CONF780401, Gatlinberg, Tenn. (1978).

5. Y. H. Bouget, et. al., Physics Performances of a Heterogeneous Fast Reactor Core Concept Studied in MASURCA, Nucl. Tech., 44, 61 (1979).

6. Y. H. Bouget, et. al., Main Characteristics of the Racine Programme Developed by DEBNE, CNEN and CEA on MASURCA for the Heterogeneous Core Concept Studies, International Symposium on Fast Reactor Physics, Aix-en-Provence, France (1979).

7. H. Kusters and S. Ganesan, Present Status of Sodium Void Reactivity Predictions in Conventional and Nonconventional Fast Reactor Core Designs, Advances in Reactor Physics, CONF780401, Gatlinberg, Tenn. (1978).

8. H. Geise, et. al., Some Characteristics of Two Heterogeneous Cores and Their Experimental Confirmation, International Symposium on Fast Reactor Physics, Aix-en-Provence, France (1979).

9. F. Helm and J. Sanders, An Outline of the BIZET Experiments and Their Interpretation, International Symposium on Fast Reactor Physics, Aix-en-Provence, France (1979).

10. M. J. Lineberry, et. al., The Maximum Positive Sodium Void Reactivity in a B_4 Poisoned Core - ZPPR Assembly 3, Trans. Am. Nucl. Soc., 17, 456 (1973).

11. M. J. Lineberry and C. L. Beck, Two Dimensional Calculations of Sodium Void Measurements in the ZPPR Demonstration Benchmark Critical Assemblies, Trans. Am. Nucl. Soc., 19, 408 (1974).

12. C. L. Beck, et. al., Streaming Effects in the Analysis of Sodium Void Measurements in ZPPR, Trans. Am. Nucl. Soc., 23, 567 (1976).

13. B. W. Lee, et. al., LMFBR Design Implications of Sodium Void Worths from ZPPR Critical Experiments, Trans. Am. Nucl. Soc., 24, 480 (1976).

14. S. L. Stewart, et. al., Analysis of Simulated HCDA Experiments in ZPPR, Fast Reactor Safety and Related Physics, CONF761001, Chicago, Illinois (1976).

15. R. E. Kaiser, et. al., Simulation of an HCDA Sequence on the ZPPR Critical Facility, Fast Reactor Safety and Related Physics, CONF 761001, Chicago, IL (1976).

16. P. J. Collins, et. al., A Comparison Between Physics Parameters in Conventional and Heterogeneous LMFBRs Using Results from ZPPR, Advances in Reactor Physics, CONF780401, Gatlinberg, Tenn. (1978).

17. M. J. Lineberry, et. al., Physics Studies of a Heterogeneous Luiquid-Metal Fast Breeder Reactor, Nucl. Tech., 44, 21 (1979).

18. M. J. Lineberry, et. al., Experimental Studies of Large Conventional LMFBR Cores at ZPPR, International Symposium on Fast Reactor Physics, Aix-en-Provence, France (1979).

19. P. J. Collins, et. al., Experimental Studies of 350 MW(e) Heterogeneous LMFBR Cores at ZPPR, International Symposium on Fast Reactor Physics, Aix-en-Provence, France (1979).

20. P. A. Ombrellaro, et. al., Biases for Current FFTF Calculational Methods, Advances in Reactor Physics, CONF780401, Gatlinberg, Tenn. (1978).

21. R. A. Bennett, et. al., Status of Safety-Related FFTF Neutronics Parameters, Advances in Reactor Physics, CONF780401, Gatlinberg, Tenn. (1978).

22. E. Novendstern, Turbulent Flow Pressure Drop Model for Fuel Rod Assemblies Utilizing a Helical Wire-Wrap Spacer System, Nucl. Eng. Design, 22, 19 (1972).

23. C. Chiu, N. E. Todreas and W. M. Rohsenow, Turbulent Flow Split Model and Supporting Experiments for Wire Wrapped Core Assemblies, Nucl. Tech, 50, 40 (1980).

24. C. Chiu, N. E. Todreas and W. M. Rohsenow, Subchannel and Bundle Friction Factors and Flow Split Models for Laminar, Transition and Turbulent Flows in Wire Wrapped Nuclear Fuel Assemblies, Thermal-Hydraulic Working Group 4th meeting, Argonne National Laboratory, (Ap. 24, 1979).

25. K. Rehme, Geometry-Dependence of the Pressure Loss in Rod Bundles wth Coiled Wire Spacers and Longitudinal Flow, Transation of Dissertation submitted for a Doctor Degree in Engineering to the Faculty of Mechanical and Process Engineering, University of Karlsrube, Germany, (1976).

26. K. Rehme, The Measurement of Friction Factors for Axial Flow Through Rod Bundles with Different Spacers, Performed on the INR Test-Rig, EURFNR-142P, (1965).

27. T. C. Reihman, An Experimental Study of Pressure Drop in Wire Wrapped FFTF Fuel Assemblies, BNWL-1207, (1969).

28. W. Bauman, V. Casal, H. Hoffman, R. Moeller, and K. Rust, Fuel Elements with Sprial Spacers for Fast Breeder Reactors, EURFNR-571, (1968).

29. C. Chiu, N. Todreas, and W. Rohsnow, Pressure Drop Measurements in LMFBR Wire-Wrapped Blanket Bundles, Trans. Am. Nucl. Soc., 28, 541 (1978).

30. C. Chiu, N. E. Todreas, and W. M. Rohsenow, Flow Split Measurements in LMFBR Blanket Assemblies, COO-2245-41TR, M.I.T., (1978).

31. J. J. Lorenz and T. Ginsberg, Coolant Mixing and Subchannel Velocities in an LMFBR Fuel Assembly, Nucl. Eng. and Design, 40, 315 (1977).

32. T. Ginsberg and J. J. Lorenz, Experimental Mixing Studies in Simulated Wire-Wrap Fuel Assemblies, Proc, Int. Reactor Heat Transfer Conference, Karlshure (1973).

33. D. R. Pedersen, R. D. Pierce, J. J. Lorenz and C. J. Roop, Experimental Investigation of the Hydraulic-Entrance Length and Subchannel-Velocity Profiles in a 91-Element Wire-Wrapped Sub-Assemlby, ANL/RAS 74-5, Argonne National Laboratory (1975).

34. T. G. Bartholet, R. M. Reidt and L. J. Harper, 11:1 Scale Wire-Wrapped Rod Bundle Air Flow Test, Interior Subchannels, WARD-D-0108, Westinghouse Electric Corporation (1975).

35. Y. B. Chen, Ka-Lam Ip, N. E. Todreas, Velocity Measurements in Edge Channesl of Wire-Wrapped LMFBR Fuel Assemblies, Trans. Am. Nucl.. Soc., 19, 323 (1974).

36. T. R. Bump and H. O. Monson, Flow Characterisitics of the EBR-II Core-Type Subassembly, ANL-6549, (1962).

37. C. Chiu, W. M. Rohsenow, and N. E. Todreas, Turbulent Sweeping Flow Mixing Model for Wire Wrapped LMFBR Assemblies, COO-2245-55TR, M.I.T. (1978).

APPENDIX O
IMPACT OF BLANKET POWER-TO-FLOW RATIOS ON SODIUM BOILING INCOHERENCY

One of the inherent safety features of a large heterogeneous LMFBR is the low sodium void reactivity of the active core region. However, the total sodium void reactivity for the active core and the internal blankets is close to that of a homogeneous LMFBR of the same size. Thus, if boiling occurs simultaneously in the core and the internal blankets, the advantage of the low core sodium void reactivity is lost.

An assembly's power-to-flow ratio* determines the steady-state coolant temperature rise through the assembly. Figures O.1 and O.2 show the power-to-flow ratios for the fourth burn cycle discussed in Appendix J. The core and blanket assemblies which reach EOL in this cycle, have nearly equal power-to-flow ratios. Thus, their steady-state outlet temperatures are also nearly equal. If these outlet temperatures were to rise uniformly during a transient, sodium boiling would occur almost simultaneously in both regions and the advantage of the heterogeneous core would not be realized. If this is indeed the case, the incoherence in sodium boiling can be improved by lowering the power-to-flow ratios in the blankets.

To investigate the effect of the blanket power-to-flow ratios on the incoherence of sodium boiling, an unprotected loss-of-flow accident has been analyzed at EOEC conditions with different blanket power-to-flow ratios.

O.1 Modeling of the Unprotected Loss-of-Flow Accident

To analyze the unprotected loss-of-flow accident, the computer code FX2-TH was used. FX2-TH is a two dimensional coupled neutronic thermal-hydraulic code. It uses either two dimensional hexagonal or RZ reactor geometry. The spatial grid used

*The power-to-flow ratio is defined as the ratio of the assembly power to the assembly coolant flow divided by the ratio of the reactor power to the reactor coolant flow.

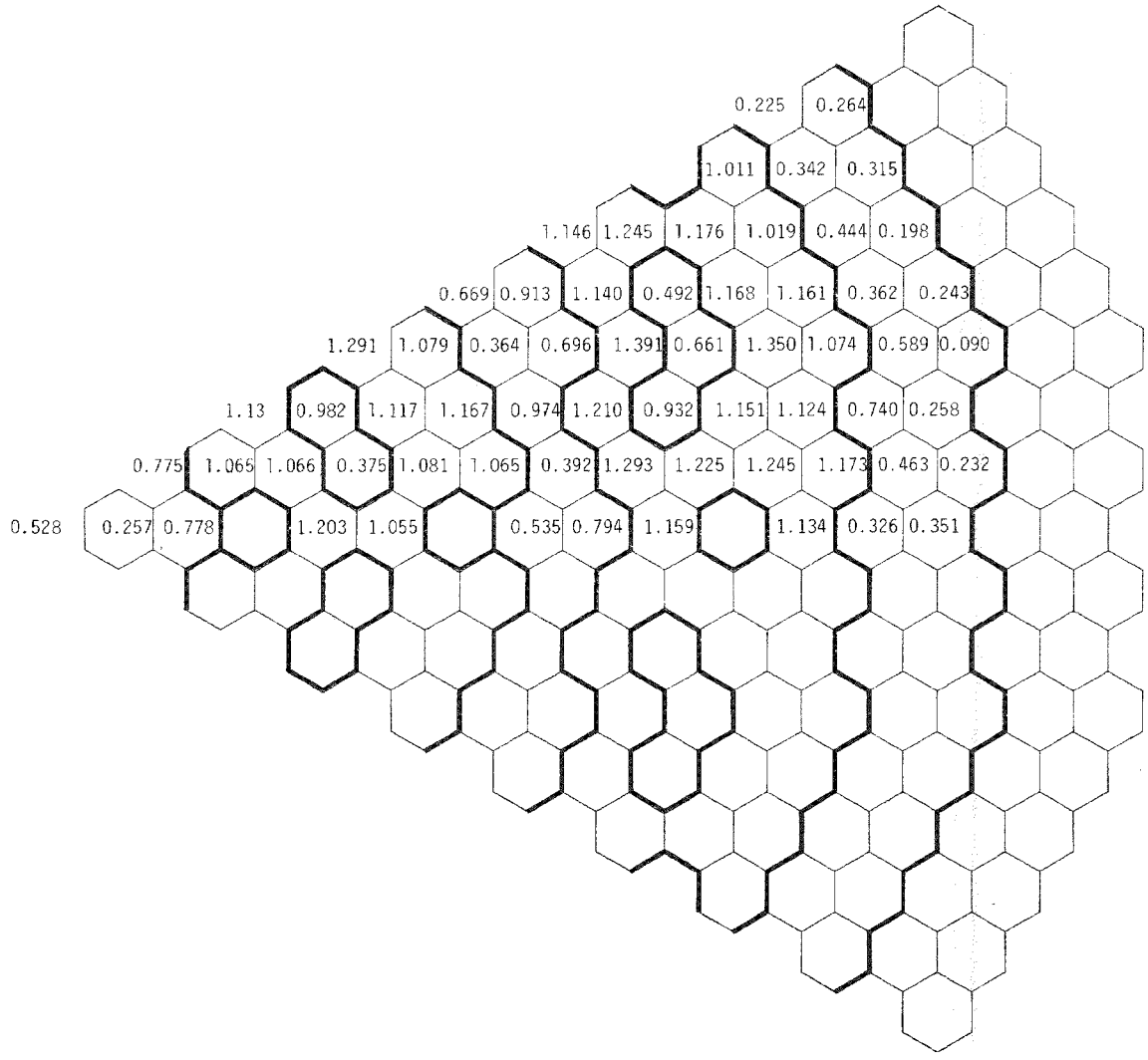

Figure 0.1. Power-to-flow ratios at the beginning of the fourth burn cycle for discrete fuel management.

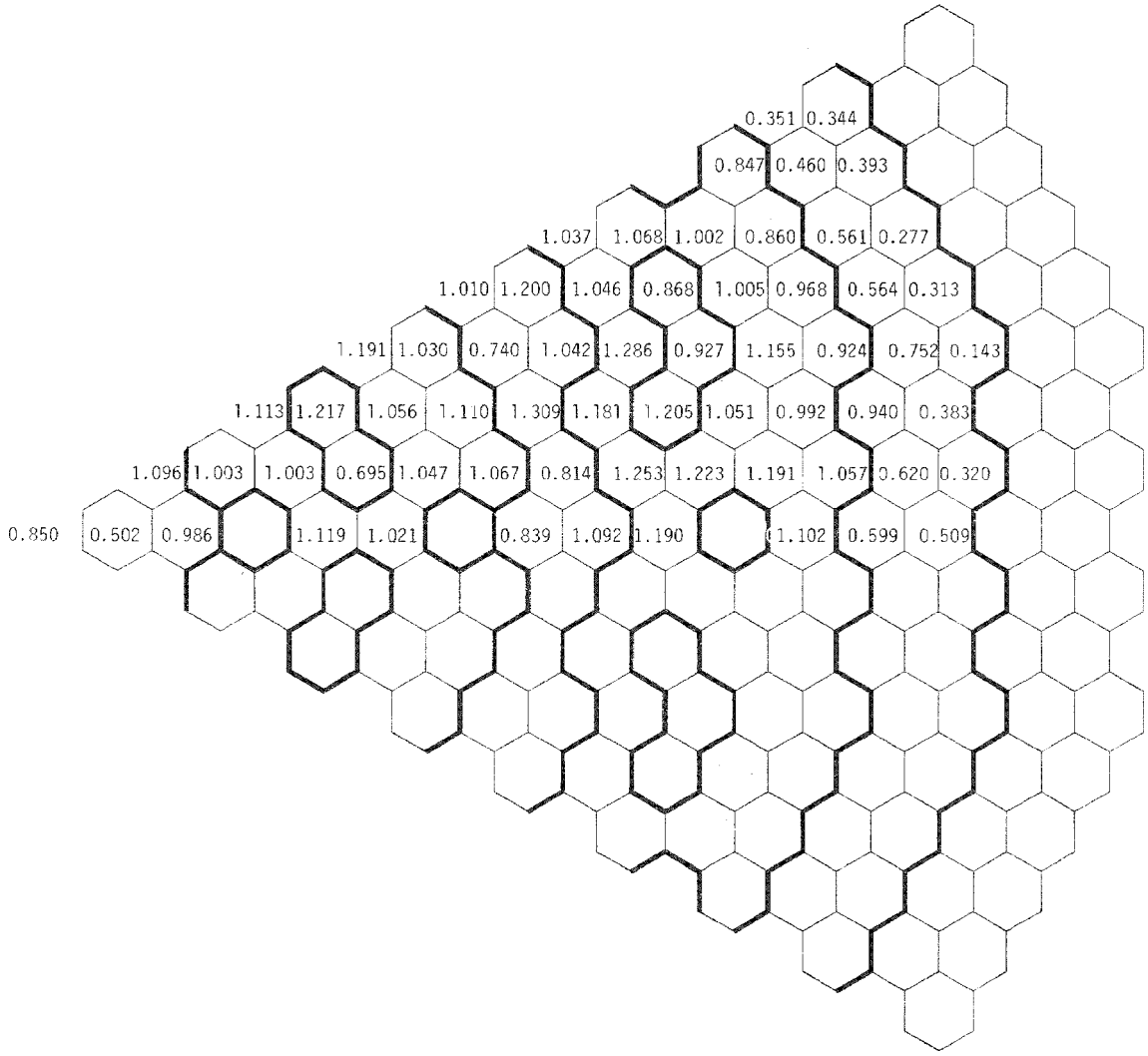

Figure 0.2. Power-to-flow ratios at the end of the fourth burn cycle for discrete fuel management.

to model the reactor, is divided into thermal-hydraulic channels and each channel is represented by its average fuel pin. Since the 2D-hexagonal geometry option in FX2-TH does not allow heat transfer from the fuel to the coolant, the use of the RZ geometry option is the obvious choice for the analysis of the accident under consideration.

The power producing regions of the reactor are divided into 16 thermal-hydraulic channels (Table 0.1 and Figure 0.3). The steady-state coolant flow in each channel was adjusted to give a channel coolant outlet temperature equal to the average coolant outlet temperature of the assemblies in that channel. During the transient, the flow, M, was allowed to decay as

$$M = M_0 \exp\left(-0.179t + 6 \times 10^{-3} t^2 - 7 \times 10^{-5} t^3\right) \qquad (1)$$

where M_0 is the steady-state flow. This flow coastdown is the same as the one used to analyze the unprotected loss-of-flow transient in CRBR[1]. Since the power produced in the blanket assemblies peaks at EOL, EOEC conditions were used in the analysis.

The present version of FX2-TH does not handle sodium boiling. Thus, after the coolant reaches its saturation temperature, the solution given by FX2-TH is no longer valid.

The sodium saturation temperature is a function of the pressure. The total pressure drop across the reactor is taken as 131 psig (the same as that of CRBR). The decay of the pressure during the accident was modeled as[1]

$$\Delta P_{head} = \Delta P_0 f^2$$

where $f = \exp\left(-0.179t + 6 \times 10^{-3} t^2 - 7 \times 10^{-5} t^3\right)$ and t is the time into the flow transient.

The coolant saturation temperature (including 10° C of superheat) as a function of pressure is given in Table 0.2. Table 0.2 also shows the time at which a given coolant pressure is reached at the top of the upper axial blanket for a CRBR type flow coastdown.

Since the FX2-TH model:

a) deals with average pins

Table 0.1

THERMAL-HYDRAULIC CHANNEL ASSIGNMENT, COOLANT FLOW,
POWER-TO-FLOW RATIO, AND OUTLET TEMPERATURE
AT TIME ZERO (BASE CASE)

Thermal Hydraulic Channel	Core Region	Inner Radius	Outer Radius	Coolant Flow (gm/sec)	Power/ Flow Ratio	Outlet Temperature (°F)
1	Blanket (B1)	0.0	7.878	7,057.	0.943	875.52
2	Blanket (B1)	7.878	20.842	68,893.	0.678	796.10
3	Blanket (B1)	20.842	34.337	143,520	0.931	871.97
4	Core (IC)	34.337	43.869	410,040.	1.075	918.79
6	Core (IC)	47.917	61.526	915,100.	1.073	918.09
7*	Blanket (B2)	61.526	72.627	477,700.	1.010	895.82
8+	Core (MC)	72.627	86.653	1,368,600.	1.119	932.23
10	Core (MC)	88.776	100.57	1,267,900.	1.123	933.40
11	Blanket (B3)	100.57	116.04	971,480.	0.849	847.24
12	Blanket (B3)	116.04	122.29	391,060.	0.962	881.31
13	Core (OC)	122.29	142.02	2,914,100.	1.091	923.61
15	Blanket (B4)	143.32	150.91	658,370.	0.885	858.18
17	Core (OC)	152.14	163.92	2,051,300.	0.986	891.66
18	Core (OC)	163.92	178.07	2,074,600	1.008	898.52
19	Radial Blanket	178.07	192.15	555,730.	0.828	841.12
20	Radial Blanket	192.15	206.18	459,650.	0.347	697.50

(Channels 5, 9, 14, 16 are control rods. Channel 21 is the radial reflector. These thermal-hydraulic channels are not active in the present study.)

*Hottest Blanket Channel

+Hottest Core Channel

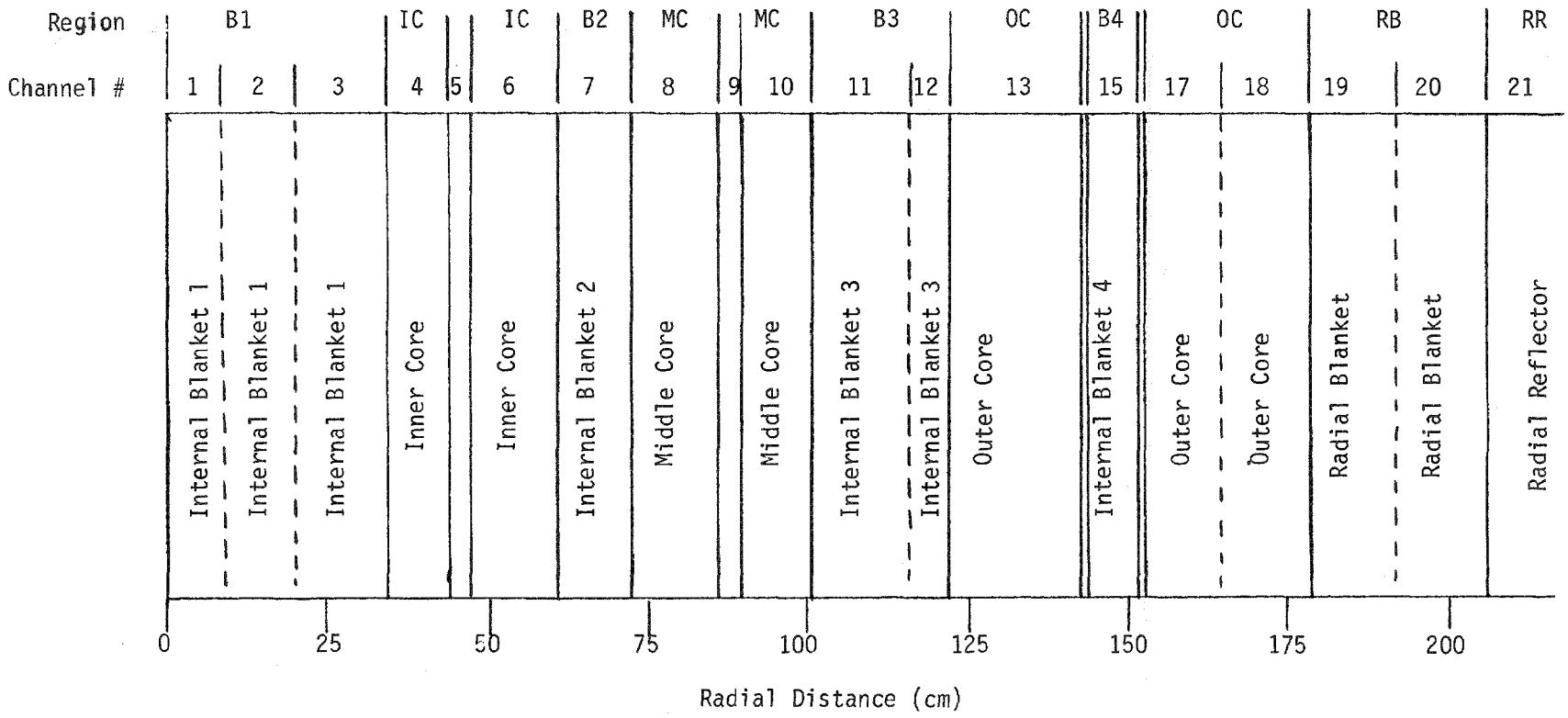

Figure 0.3 Thermal-hydraulic channel model (Channels 5, 9, 14, and 16 are control rods)

Table 0.2

SATURATION PRESSURES AND RELATED
SODIUM BOILING TEMPERATURES FOR A CRBR PUMP COASTDOWN
($10^{o}C$ OF SUPERHEAT ARE INCLUDED)

Time	Saturation Pressure at Top of Upper Axial Blanket (psig)	Boiling Temperature at Top of Upper Axial Blanket (^{o}C)
0.0	55.1	1091.82
1.0	39.0	1053.22
2.0	28.2	1022.02
3.0	20.9	997.00
4.0	15.8	977.13
5.0	12.2	961.40
6.0	9.61	949.03
7.0	7.72	939.27
8.0	6.31	931.57
8.8	5.44	926.63
8.9	5.34	926.07
9.0	5.24	925.52
9.1	5.16	924.99
9.2	5.07	924.47
9.3	4.98	923.96
9.4	4.90	923.46
9.5	4.82	922.93
10.0	4.43	920.72

b) does not include the negative reactivity feedback resulting from axial pin expansion,

the time of boiling initiation, obtained from FX2-TH, is not accurate. However, since the axial pin expansion feedback is small, and since in this analysis only differential and not actual absolute parameter values are of interest, these model limitations do not limit the validity of the conclusions of this anlaysis.

0.2 Analysis of the Unprotected Loss-of-Flow Accident

The unprotected loss-of-flow accident has been investigated for three different blanket power-to-flow ratios and EOEC conditions. In the base case, steady-state flow rates were calculated using the assembly average coolant temperatures shown in Figure 4.2.4.4.6. In the other two cases, the flows in the blanket regions were increases by 10 and 15%, respectively, over the base case flows, but the total reactor flow was held constant.

The steady-state coolant flows, power-to-flow ratios, and the coolant outlet temperatures for the base case are given in Table 0.1. The steady-state coolant outlet temperatures for all three cases are shown in Table 0.3. At steady-state increasing the blanket flow by 10%, lowers the coolant outlet temperature in the internal blanket regions by 10 to 14^{o} C (18 to 25^{o} F) and increases the coolant outlet temperature in the core regions by about 6^{o} C (10^{o} F).

During the unprotected loss-of-flow accident, the reactor power rises continuously for all three cases studied (Figure 0.4). At the initiation of coolant boiling, the reactor power is about 25% greater than its steady-state value. This power rise is a function of the feedback model used. Axial expansion, which was not included here, is a negative feedback and it would keep the reactor power near its steady-state value until coolant boiling.[1]

The power histories for each thermal-hydraulic channel are shown in Tables 0.4-0.6. Coolant outlet temperatures vs. time are given in Tables 0.7-0.9. Power histories for the hottest core, internal blanket and radial blanket channels are given in Figures 0.5-0.7. In all cases, the power increases uniformly in all channels.

For the base case, the steady-state power-to-flow ratios in the hottest core and internal blanket channels differ only by ~11% (Table 0.1). Thus, at steady-state the coolant outlet temperature in the hottest internal blanket channel is ~36^{o} F

Table 0.3

STEADY-STATE COOLANT OUTLET TEMPERATURES (^{o}F)

Thermo-Hydraulic Channel	Core Region	Base Case	Blanket Flow Increased by 10%	Blanket Flow Increased by 15%
1	Internal Blanket	875.52	849.87	838.69
2	Internal Blanket	796.10	777.74	769.77
3	Internal Blanket	871.97	846.57	835.54
4	Core	918.79	930.00	935.89
6	Core	918.09	928.08	933.31
7	Internal Blanket	895.82	868.19	856.20
8	Core	932.23	942.67	948.16
10	Core	933.40	944.78	950.76
11	Internal Blanket	847.24	824.13	814.08
12	Internal Blanket	881.31	855.03	843.62
13	Core	923.61	934.83	940.71
15	Internal Blanket	858.18	834.03	823.53
17	Core	891.66	901.92	907.32
18	Core	898.52	912.16	919.44
19	Radial Blanket	841.12	818.53	808.74
20	Radial Blanket	697.50	688.17	684.12

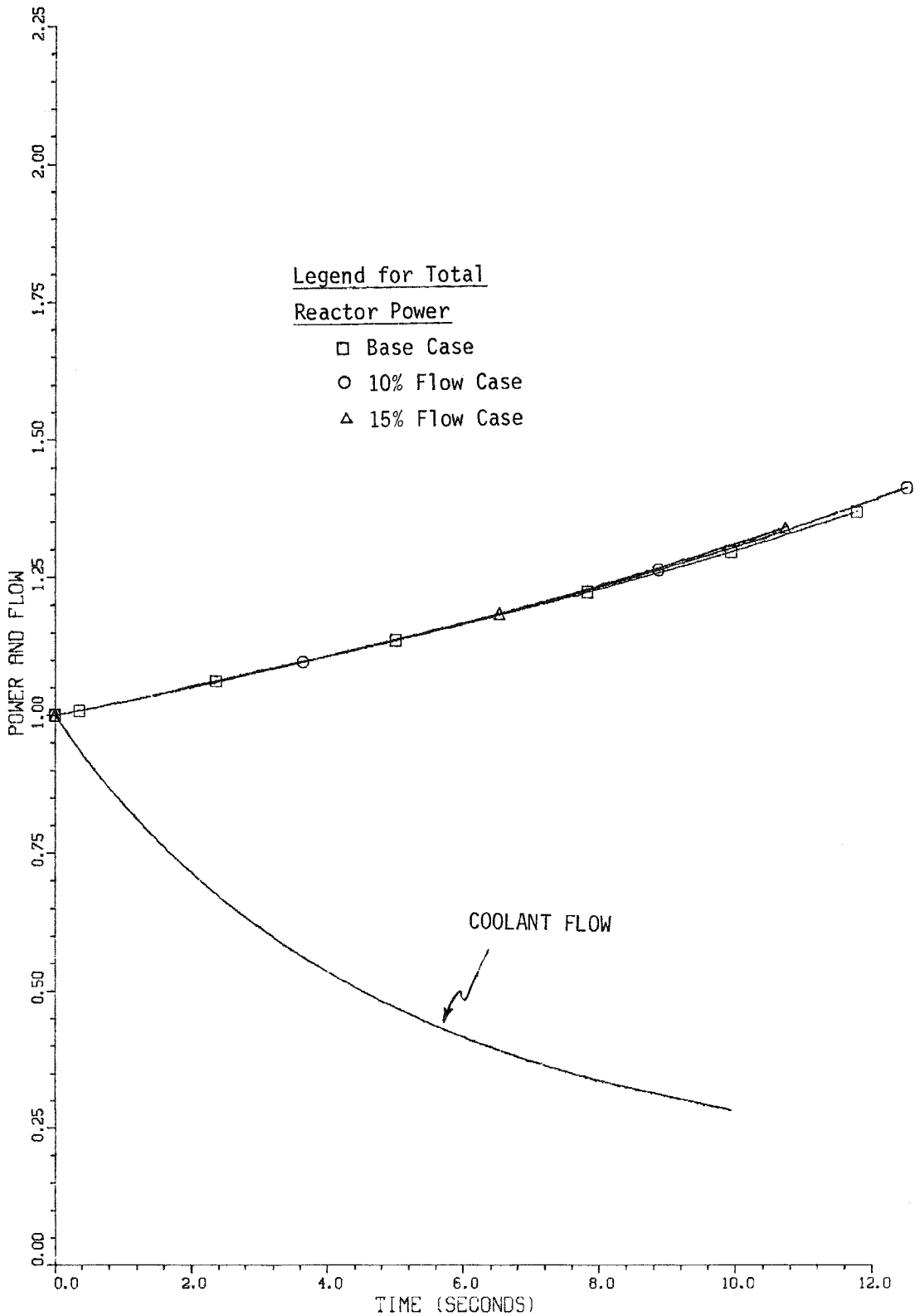

Figure 0.4 Normalized total reactor power and coolant flow vs. time.

Table 0.4

THERMAL-HYDRAULIC CHANNEL POWER VS. TIME. (BASE CASE)

TIME (SEC)	0.0	0.365	2.365	5.000	7.829	9.939	11.780
				Power (MW)			
CHANNEL							
1	1.39	1.42	1.48	1.58	1.70	1.79	1.89
2	9.75	9.99	10.42	11.10	11.92	12.61	13.29
3	27.89	28.58	29.79	31.75	34.14	36.14	38.12
4	91.99	94.23	98.24	104.73	112.67	119.31	125.91
6	204.86	209.58	218.71	233.24	250.97	265.85	280.58
7	100.73	102.84	107.49	114.67	123.40	130.71	137.97
8	319.62	325.58	340.80	363.77	391.57	414.86	437.96
10	297.14	301.85	316.55	338.08	363.93	385.59	407.06
11	172.11	174.05	183.07	195.68	210.61	223.10	235.45
12	78.53	79.07	83.39	89.25	96.09	101.81	107.47
13	663.39	666.08	703.65	753.73	811.86	860.52	908.65
15	121.64	121.86	128.90	138.17	148.83	157.76	166.59
17	422.08	422.33	447.05	479.36	516.47	547.54	578.26
18	436.64	436.51	462.30	495.86	534.27	566.45	598.26
19	96.08	96.02	101.71	109.10	117.51	124.56	131.53
20	33.32	33.29	35.26	37.82	40.73	43.16	45.57

Table 0.5

THERMAL-HYDRAULIC CHANNEL POWER VS. TIME
(BLANKET COOLANT FLOW INCREASED BY 10%)

TIME (SEC)	0.0	0.366	3.646	6.545	8.872	10.790
			Power (MW)			
CHANNEL						
1	1.39	1.42	1.53	1.65	1.75	1.85
2	9.76	10.00	10.78	11.56	12.33	13.02
3	27.90	28.59	30.82	33.07	35.30	37.32
4	91.98	94.23	101.61	109.07	116.46	123.19
6	204.85	209.57	226.19	242.91	259.41	274.40
7	100.73	102.85	111.16	119.43	127.56	134.95
8	319.61	325.58	352.34	378.82	404.64	428.17
10	297.13	301.85	327.18	352.04	376.03	397.88
11	172.13	174.08	189.15	203.77	217.60	230.16
12	78.53	79.08	86.11	92.93	99.25	105.00
13	663.37	666.09	726.21	784.67	838.31	887.14
15	121.64	121.87	133.00	143.85	153.68	162.63
17	422.06	422.33	461.13	499.01	533.18	564.32
18	436.62	436.52	476.81	516.18	551.55	583.78
19	96.10	96.04	104.92	113.59	121.34	128.40
20	33.33	33.30	36.38	39.38	42.06	44.50

Table 0.6

THERMAL-HYDRAULIC CHANNEL POWER VS. TIME
(BLANKET COOLANT FLOW INCREASED BY 15%)

TIME (SEC)	0.0	0.366	3.649	6.526	8.834	10.734
			Power (MW)			
CHANNEL						
1	1.39	1.42	1.54	1.65	1.76	1.86
2	9.76	10.00	10.79	11.57	12.35	13.06
3	27.90	28.59	30.85	33.11	35.36	37.41
4	91.98	94.23	101.67	109.19	116.65	123.46
6	204.85	209.57	226.32	243.16	259.83	275.04
7	100.74	102.85	111.23	119.57	127.77	135.26
8	319.60	325.58	352.54	379.23	405.30	429.10
10	297.13	301.85	327.37	352.42	376.65	398.75
11	172.14	174.10	189.28	204.01	217.99	230.71
12	78.54	79.09	86.17	93.03	99.43	105.25
13	663.36	666.11	726.65	785.52	839.69	889.12
15	121.64	121.88	133.09	144.01	153.94	163.01
17	422.06	422.34	461.41	499.56	534.07	565.58
18	436.62	436.53	477.09	516.75	552.47	585.09
19	96.11	96.05	104.99	113.73	121.56	128.71
20	33.33	33.31	36.40	39.43	42.14	44.61

Table 0.7

THERMAL-HYDRAULIC CHANNEL OUTLET TEMPERATURE VS. TIME
(BASE CASE)

TIME (SEC)	0.0	0.365	2.365	5.000	7.829	9.939	11.780
	Coolant Temperatures (^{O} F)						
CHANNEL							
1	875.52	877.89	940.55	1045.83	1167.93	1266.66	1357.79
2	796.10	799.21	854.89	943.59	1059.87	1153.81	1240.70
3	871.97	876.47	954.54	1077.80	1236.47	1363.19	1479.29
4	918.79	927.97	1040.07	1232.22	1487.03	1699.97	1895.99
6	918.09	927.90	1041.58	1235.41	1494.77	1712.03	1912.73
7	895.82	903.49	1000.76	1156.87	1345.01	1508.63	1652.81
8	932.23	943.02	1061.02	1263.06	1532.93	1759.01	1967.63
10	933.40	943.79	1060.84	1262.23	1529.15	1752.35	1958.09
11	847.24	853.16	933.03	1061.26	1223.44	1356.89	1478.57
12	881.31	887.50	976.23	1117.31	1296.72	1441.85	1573.79
13	923.61	933.84	1047.07	1244.28	1504.13	1721.75	1922.45
15	858.18	864.45	947.97	1081.99	1250.37	1389.29	1515.83
17	891.66	900.81	1002.83	1181.34	1417.73	1615.91	1799.33
18	898.52	906.57	1009.69	1184.97	1416.47	1610.51	1789.79
19	841.12	842.95	897.35	991.09	1096.97	1183.19	1270.42
20	697.50	698.00	716.77	750.65	788.94	823.80	855.84

Table 0.8

THERMAL-HYDRAULIC CHANNEL COOLANT OUTLET TEMPERATURE VS. TIME
(BLANKET COOLANT FLOW INCREASED BY 10%)

TIME (SEC)	0.0	0.366	3.646	6.545	8.872	10.790
	Coolant Temperatures (^{C} F)					
CHANNEL						
1	849.87	852.33	956.73	1075.75	1177.63	1267.99
2	777.74	780.87	872.82	975.65	1070.37	1154.82
3	846.57	851.07	979.41	1120.77	1249.36	1362.83
4	930.00	939.31	1142.76	1390.91	1621.85	1827.41
6	928.08	938.52	1143.64	1393.97	1629.05	1838.75
7	868.19	875.64	1033.54	1205.85	1364.09	1503.95
8	942.67	953.65	1167.33	1427.99	1672.61	1890.59
10	944.78	955.33	1167.76	1427.45	1669.19	1884.47
11	824.13	829.90	959.85	1101.54	1236.33	1354.01
12	855.03	861.12	1005.46	1160.33	1310.27	1438.43
13	934.83	945.21	1155.51	1404.95	1640.57	1850.27
15	834.03	840.13	975.87	1123.81	1263.31	1385.69
17	901.92	911.23	1101.04	1327.41	1541.93	1733.45
18	912.16	920.34	1110.58	1334.53	1545.35	1733.63
19	818.53	820.45	914.72	1016.35	1104.98	1184.04
20	688.17	688.71	722.39	759.40	791.94	824.70

Table 0.9

THERMAL-HYDRAULIC CHANNEL COOLANT OUTLET TEMPERATURE VS. TIME
(BLANKET COOLANT FLOW INCREASED BY 15%)

TIME (SEC)	0.0	0.366	3.649	6.526	8.834	10.734
	Coolant Temperatures (^{O} F)					
CHANNEL						
1	838.69	841.19	943.47	1058.77	1158.42	1246.86
2	769.77	772.88	862.21	961.14	1052.94	1134.86
3	835.54	840.04	964.60	1100.57	1225.24	1335.34
4	935.89	945.27	1151.96	1401.89	1634.27	1840.91
6	933.31	943.83	1151.94	1403.87	1640.03	1850.63
7	856.20	863.53	1015.92	1181.70	1329.80	1468.31
8	948.16	959.22	1176.01	1438.25	1683.95	1903.01
10	950.76	961.39	1180.35	1438.61	1681.61	1897.97
11	814.08	819.79	945.32	1081.78	1211.00	1324.56
12	843.62	849.65	989.20	1138.59	1282.48	1406.39
13	940.71	951.21	1164.94	1415.93	1652.81	1863.77
15	823.53	829.56	960.66	1103.11	1236.85	1354.91
17	907.32	916.72	1109.70	1337.56	1553.45	1746.05
18	919.44	927.68	1121.85	1347.89	1560.65	1750.37
19	808.74	810.70	902.70	1001.57	1088.29	1165.73
20	684.12	684.66	717.75	753.89	785.86	817.66

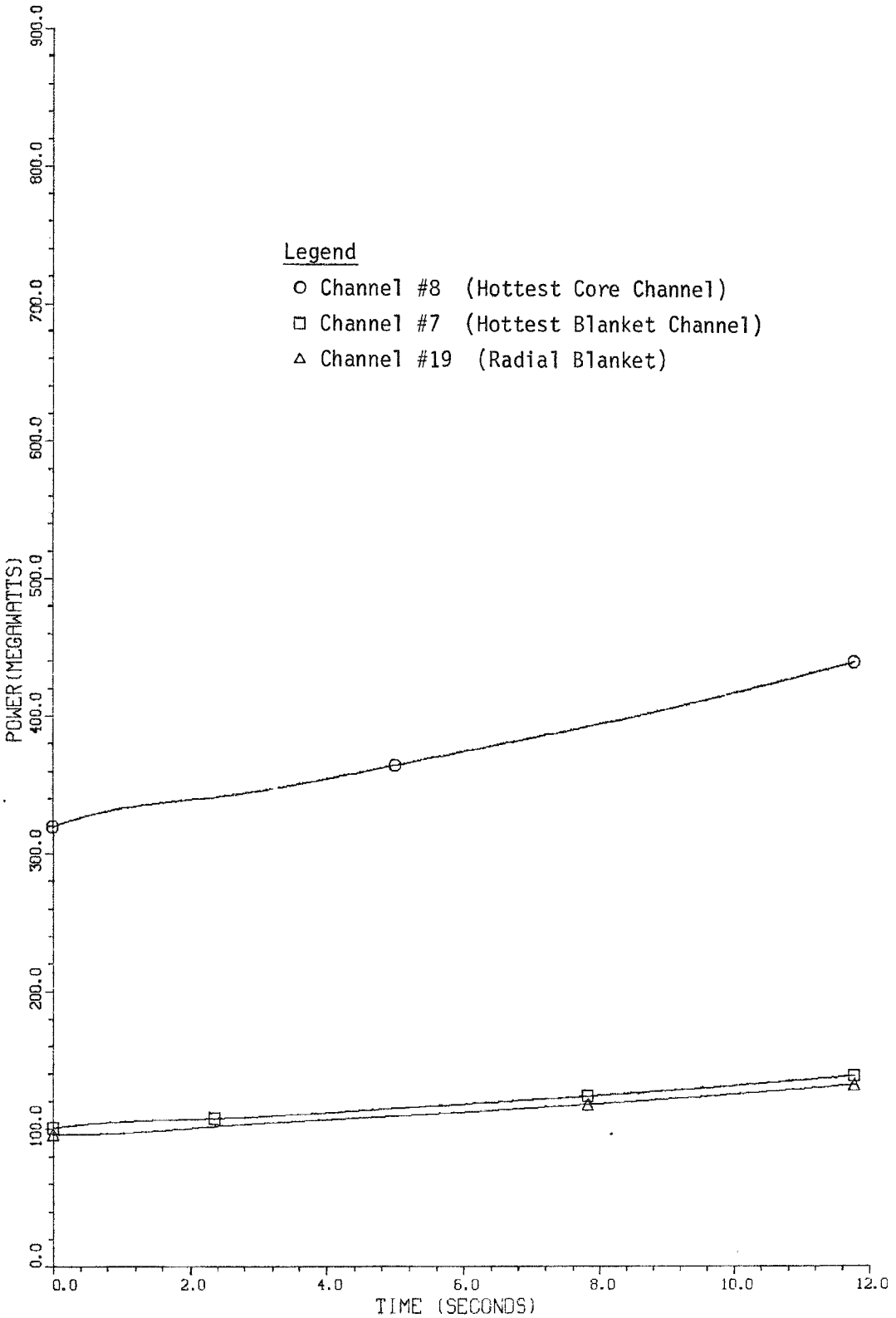

Figure 0.5. Thermal-hydraulic channel power vs. time. (Base Case)

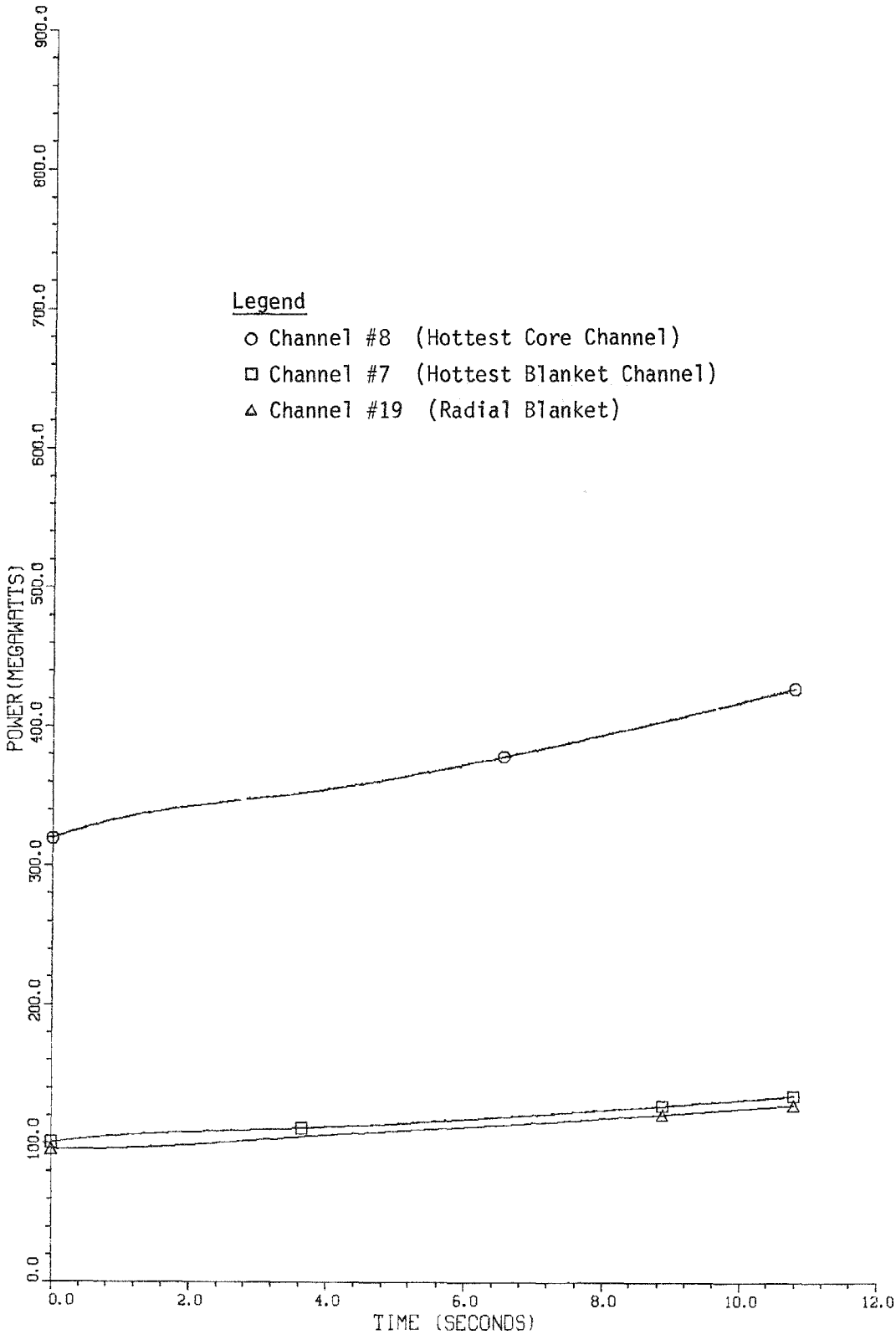

Figure 0.6. Thermal-hydraulic channel power vs. time. (Blanket coolant flow increased by 10%)

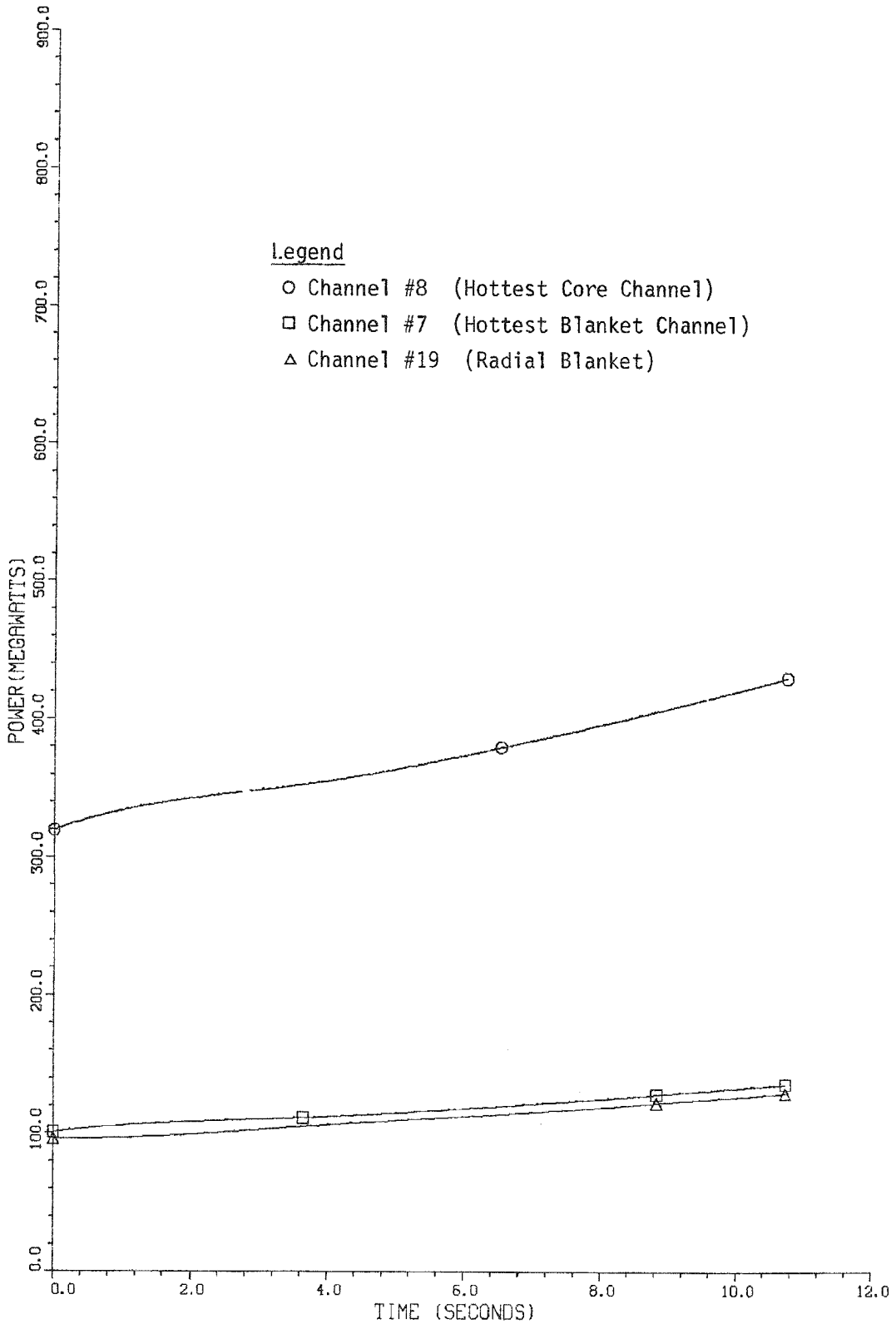

Figure 0.7. Thermal-hydraulic channel power vs. time. (Blanket coolant flow increased by 15%)

lower than the coolant outlet temperature in the hottest core channel. As the accident proceeds, as shown in Figures 0.8 to 0.10, the difference between the coolant outlet temperatures in the hottest core and internal blanket channels increases continuously. Thus, for the base case, when sodium reaches boiling in the hottest core channel, the outlet temperature in the hottest blanket channel is 244^{o} F below the saturation temperature.

The difference between the coolant outlet temperature of the hottest blanket channel and the coolant outlet temperature of the hottest core channel, at the initiation of boiling in the core, is a measure of the delay time between the start of boiling in the core and the start of boiling in the internal blankets. This difference can be used as a measure of the incoherence in sodium boiling between the core and the internal blanket.

The differences between the outlet coolant temperatures of the hottest core and blanket channels, at steady-state and at the initiation of sodium boiling in the core, for the three cases analyzed are shown in Table 0.10. As the flow in the blanket increases by 10% and 15% over its base case value, the differences between the outlet coolant temperatures of the hottest core and blanket channels also increase as follows:

a) at steady-state, from the 36^{o} F base-case value to 75^{o} F and 92^{o} F, respectively.
b) at initiation of core sodium boiling, from the 244^{o} F base-case value to 321^{o} F and 361^{o} F, respectively.

Since, as the blanket flow increases the outlet coolant temperature differences also increase at initiation of core sodium boiling as well as at steady-state, to evaluate the effect of the increased blanket flow on the outlet coolant temperature difference at initiation of core sodium boiling, a "net temperature difference" is calculated. This "net temperature difference" is obtained by subtracting from the outlet coolant temperature difference at initiation of core sodium boiling the outlet coolant temperature difference at steady-state. This "net temperature difference" is a measure of how long sodium boiling will be delayed in the blanket if at steady-state the hottest core and blanket channels have the same coolant outlet temperature.

As shown in Table 0.10, the "net temperature difference" is 208^{o} F, 246^{o} F and 269^{o} F, for the base case, the 10% flow case and 15% flow case, respectively. Thus increasing the blanket flow by 10% and 15% increases the "net temperature difference" by

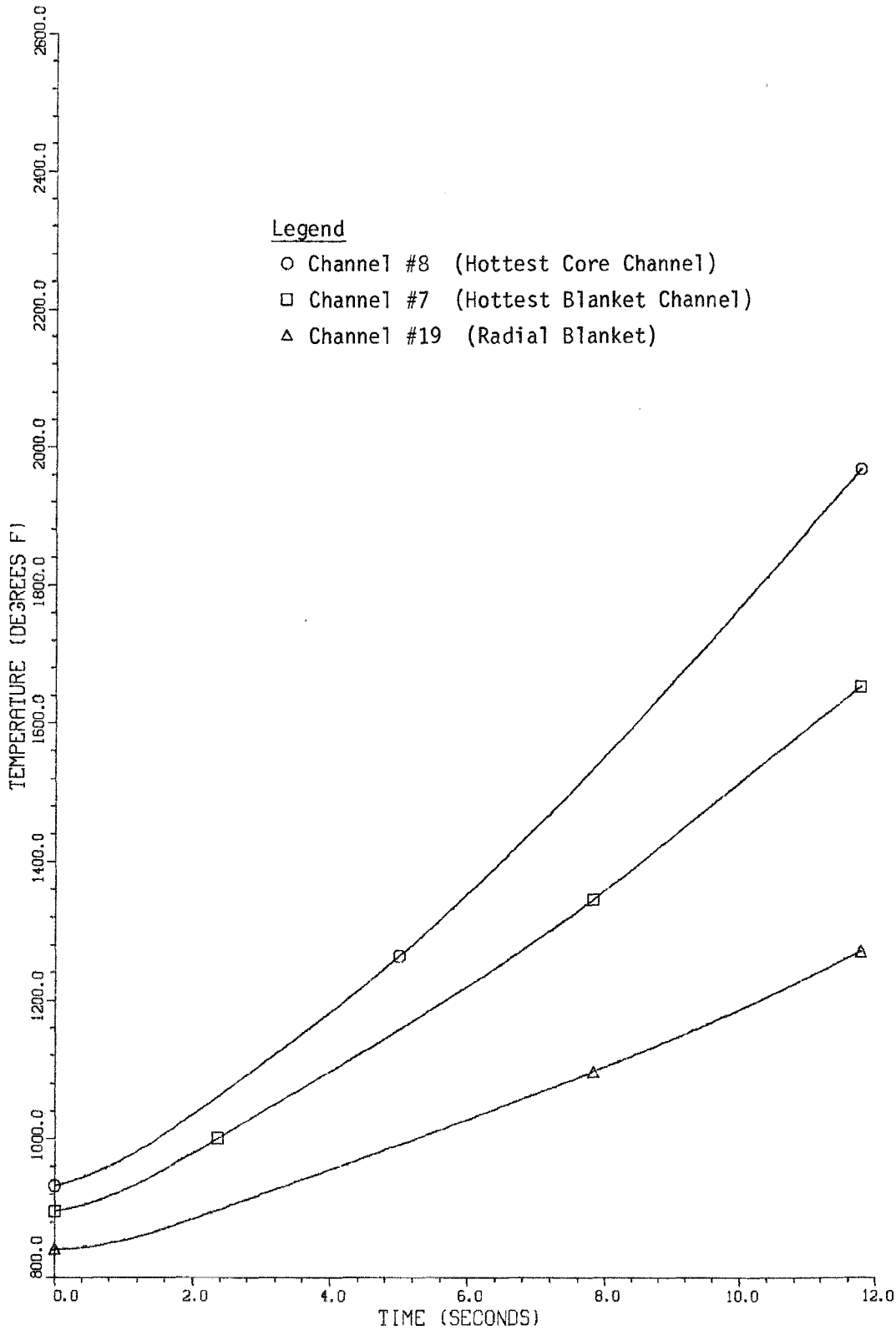

Figure 0.8. Thermal-hydraulic channel coolant outlet temperature vs. time. (Base Case)

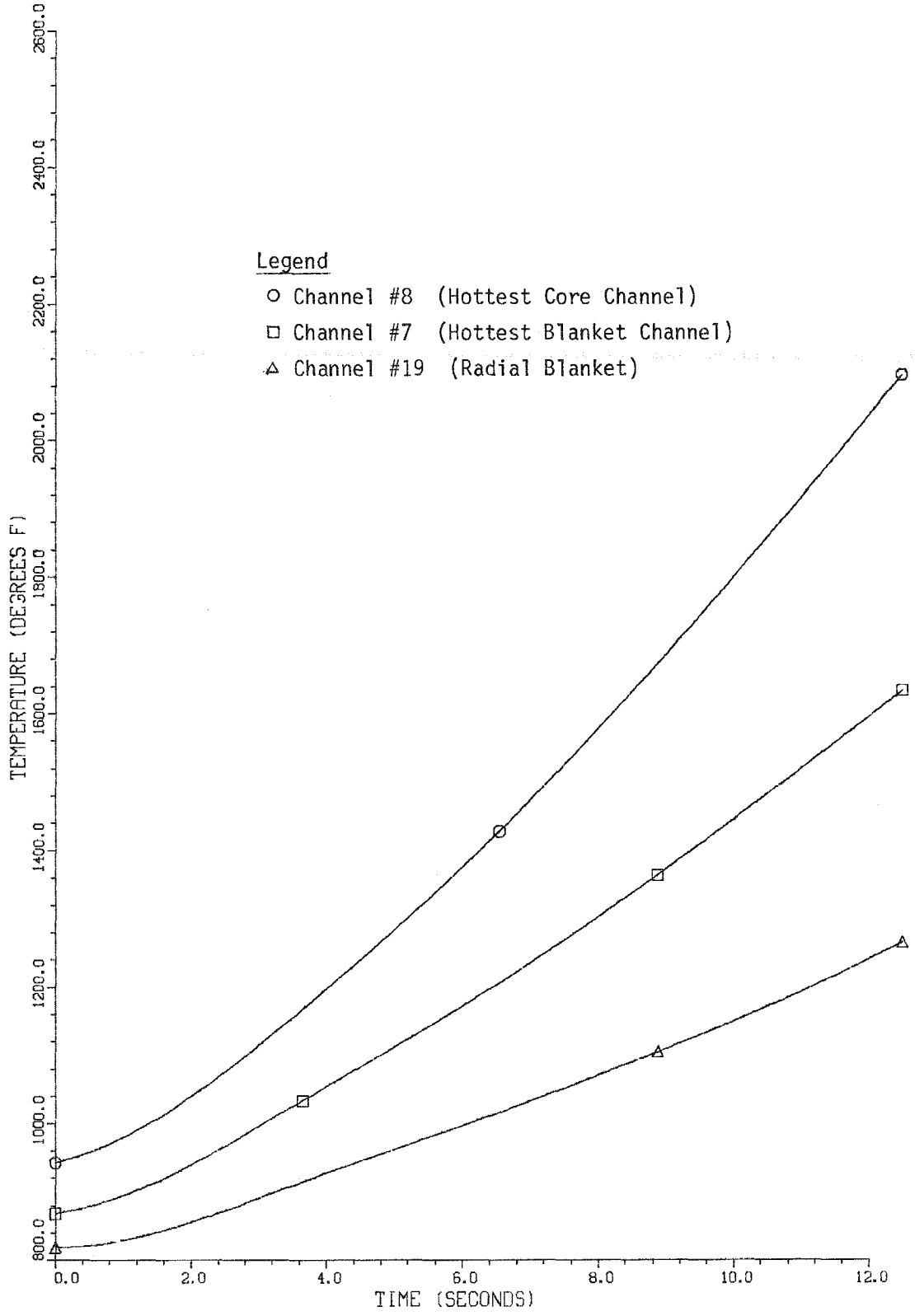

Figure 0.9. Thermal-hydraulic channel coolant outlet temperature vs. time. (Blanket coolant flow increased by 10%)

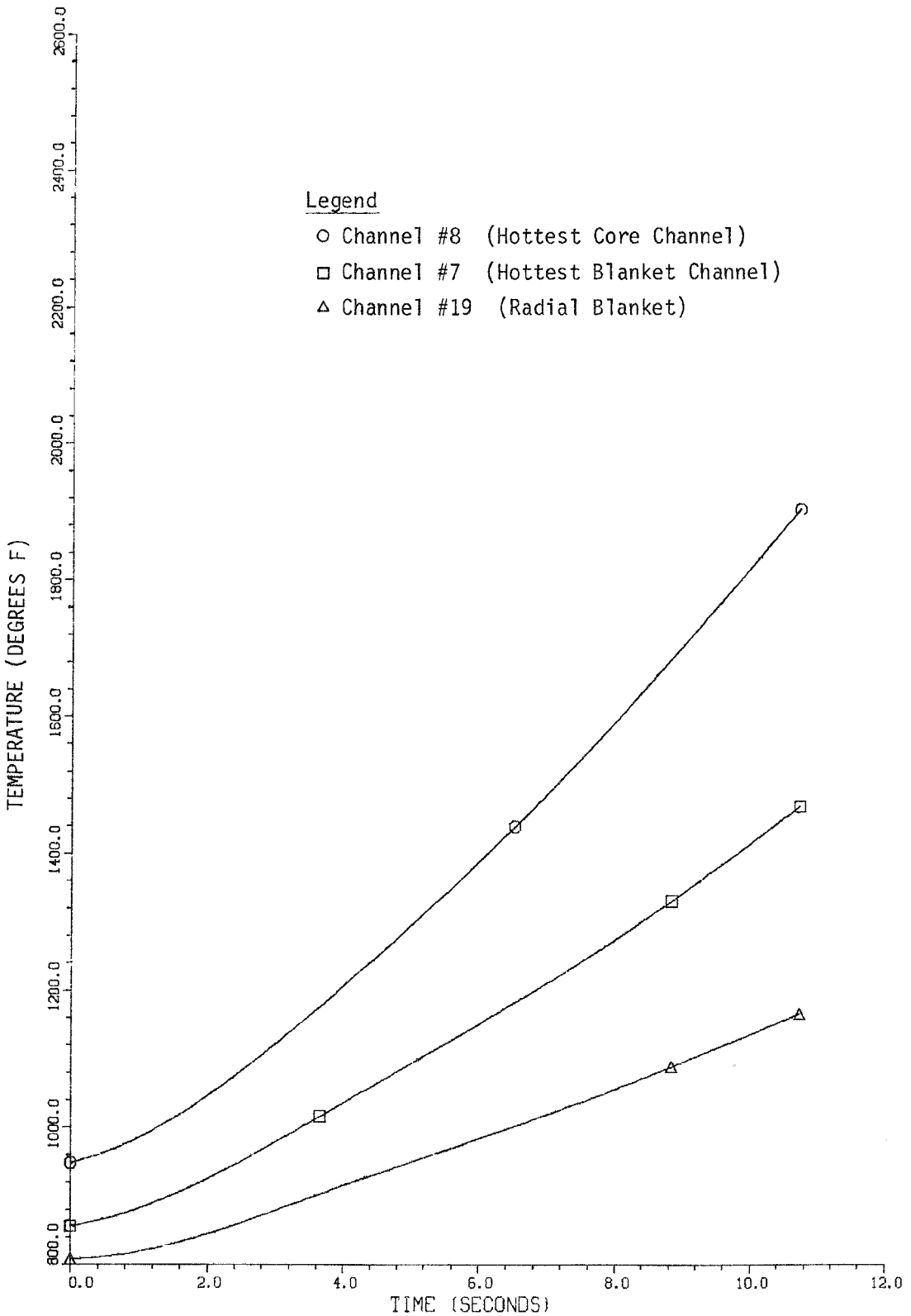

Figure 0.10. Thermal-hydraulic channel coolant outlet temperature vs. time. (Blanket coolant flow increased by 15%)

Table 0.10

DIFFERENCES BETWEEN THE OUTLET COOLANT TEMPERATURES OF THE HOTTEST CORE AND BLANKET CHANNELS AT STEADY-STATE AND AT INITIATION OF COOLANT BOILING IN THE CORE

	Base Case (^{o}F)	Blanket Flow Increased by 10% (^{o}F)	Blanket Flow Increased by 15% (^{o}F)
At steady-state (T_s)	36	75	92
At initiation of coolant boiling in core (T_i)	244	321	361
"Net Difference"*	208	246	269

*($T_i - T_s$)

18% and 29%, respectively.

These results show that even if the hottest core and blanket channels have the same power-to-flow ratio at steady-state (and consequently, the same coolant outlet temperature at steady-state), at initiation of sodium boiling in the core the outlet coolant temperature in the hottest blanket channel is significantly below boiling. Thus, there is an inherent incoherency in sodium boiling between the core and blanket assemblies. Decreasing the blanket power-to-flow ratio increases the incoherency in sodium boiling between the core and blanket assemblies, but this increase is only a fraction of the incoherencey that is inherently present.

To explain why there is an inherent incoherency in sodium boiling between the core and blanket assemblies, even if they have the same power-to-flow ratios at steady-state, the following analysis has been performed.

0.3 Analysis of the Phenomenon of Incoherent Sodium Boiling Between Core and Blanket

From the total energy, $Q_c(\tau)$, produced by the peak core pin from the initiation of the accident up to the time τ, a fraction is removed by the coolant out of the pin channel and the remaining is stored in the channel materials (coolant, fuel and structural materials). Thus,

$$Q_c(\tau) = \int_0^\tau m_c(t)\, C_p \left[T_c(t) - T_{in} \right] dt + P_c(\tau) \qquad (2)$$

where

$m_c(t)$ = peak core channel flow rate at time t
$T_c(t)$ = coolant outlet temperature in the peak core channel at time t
T_{in} = coolant inlet temperature
$P_c(\tau)$ = energy stored in the peak core channel from the initiation of the accident up to time τ
C_p = coolant specific heat

Since the flow decays with time,

$$m_c(t) = m_c(0)\, f\,(t) \qquad (3)$$

where $f(t)$ is given by Eq. (1)

Equations similar to Eqs. (2) and (3) can be written for the peak blanket channel, i.e.,

$$Q_b(\tau) = \int_0^\tau m_b(t)\ C_p\ \left[T_b(t) - T_{in}\right]\ dt + P_b(\tau) \tag{4}$$

$$m_b(t) = m_b(0)\ f\ (t) \tag{5}$$

If $q_c(t)$ is the power produced at time t in the peak core pin, then

$$Q_c(t) = \int_o^\tau q_c(t)\ dt \tag{6}$$

Similarly,

$$Q_b(\tau) = \int_o^\tau q_b(t)\ dt \tag{7}$$

As Figures 0.5, 0.6, and 0.7 show, the power changes uniformly, during the transient, in the core and blankets; i.e.,

$$q_c(t) = q_c(0)\ w(t) \tag{8}$$

$$q_b(t) = q_b(0)\ w(t)$$

Thus,

$$\frac{Q_c(\tau)}{Q_b(\tau)} = \frac{q_c(0)}{q_b(0)} \frac{\int_0^\tau w(t)dt}{\int_0^\tau w(t)dt} = \frac{q_c(0)}{q_b(0)} \tag{9}$$

From Eqs. (2), (3), (4), (5), and (9) it is derived

$$\frac{Q_c(\tau)}{Q_b(\tau)} = \frac{q_c(0)}{q_b(0)} = \frac{m_c(0)}{m_b(0)} \frac{\int_0^\tau f(t)\ C_p\ \left[T_c(t) - T_{in}\right]\ dt + P_c(\tau)}{\int_0^\tau f(t)\ C_p\ \left[T_b(t) - T_{in}\right]\ dt + P_b(\tau)} \tag{10}$$

If $T_c(0)$ is equal to $T_b(0)$, for $T_c(\tau)$ to be equal to $T_b(\tau)$ for any time τ, the following relations must hold

$$\int_0^{\tau} f(t)C_p \left[T_c(t) - T_{in} \right] dt = \int_0^{\tau} f(t)C_p \left[T_b(t) - T_{in} \right] dt = F(t)$$

and from Eq.(10)

$$\frac{q_c(0)}{q_b(0)} = \frac{m_c(0)\ F(\tau) + P_c(\tau)}{m_b(0)\ F(\tau) + P_b(\tau)}$$

or

$$\frac{q_c(0)}{q_b(0)} = \frac{q_c(0)\ F(\tau) + P_c(\tau)\ C_p\ \Delta T}{q_b(0)\ F(\tau) + P_b(\tau)\ C_p\ \Delta T} \tag{11}$$

where

$$\Delta T = T_c(0) - T_{in} = T_b(0) - T_{in}$$

For Eq. (11) to be true, $P_c(\tau)/P_b(\tau)$ must be equal to $q_c(0)/q_b(0)$, and from Eq. (10).

$$\frac{P_c(\tau)}{P_b(\tau)} = \frac{q_c(0)}{q_b(0)} = \frac{Q_c(\tau)}{Q_b(\tau)}$$

or

$$\frac{P_c(\tau)/Q_c(\tau)}{P_b(\tau)/Q_b(\tau)} = 1 \tag{12}$$

In conclusion, for a core and a blanket pin channel, that have the same coolant outlet temperature at steady-state, to have the same coolant outlet temperature during a loss-of-flow transient the following relation must be satisfied

$$\frac{P_c(\tau)/Q_c(\tau)}{P_b(\tau)/Q_b(\tau)} = 1$$

If,

$$\frac{P_c(\tau)/Q_c(\tau)}{P_b(\tau)/Q_b(\tau)} = \mu \quad <1 \tag{13}$$

then,

$$P_c(\tau) = \mu\, P_b(\tau)\, \frac{Q_c(\tau)}{Q_b(\tau)} = \mu P_b(\tau)\, \frac{q_c(0)}{q_b(0)}$$

and from Eq. (10)

$$\frac{q_c(0)}{q_b(0)} = \frac{m_c(0) \int_0^\tau f(t)\, C_p \left[T_c(t) - T_{in}\right] dt + \mu P_b(\tau)\, \frac{q_c(0)}{q_b(0)}}{m_b(0) \int_0^\tau f(t)\, C_p \left[T_b(t) - T_{in}\right] dt + P_b(\tau)} \tag{14}$$

For $T_c(0)$ equal to $T_b(0)$,

$$\frac{m_c(0)}{m_b(0)} = \frac{q_c(0)}{q_b(0)}$$

and Eq.(14)gives

$$\int_0^\tau f(t)\, C_p \left[T_b(t) - T_{in}\right] dt - \int_0^\tau f(t)\, C_p \left[T_c(t) - T_{in}\right] dt$$

$$= \frac{P_b(\tau)}{m_b(0)} (\mu - 1) \tag{15}$$

Since $\mu < 1$, and $f(t) > 0$ for $t > 0$, Eq. (15) gives

$$\int_0^\tau f(t)\, C_p \left[T_c(t) - T_{in}\right] dt > \int_0^\tau f(t)\, C_p \left[T_b(t) - T_{in}\right] dt \tag{16}$$

Equation (16) can be valid for any τ, only if $T_c(t) - T_b(t)$ is greater than zero throughout the transient. This means that if

$$\frac{P_c(\tau)/Q_c(\tau)}{P_b(\tau)/Q_b(\tau)} < 1$$

then during the transient, the blanket coolant outlet temperature will stay below the core coolant outlet temperature, even if these temperatures are equal at steady-state. Thus, if relation (13) holds, then at initiation of sodium boiling in the core, the blanket coolant temperature will be below boiling and there will be a time delay between core and blanket sodium boiling.

As shown in the discussion that follows, relation (13) holds, and consequently, sodium boiling will be incoherent for pin channels which:

a) have the same pin design but different power ratings
b) have different pin designs

The fuel temperature, $T_f(r,z)$, at position (r,z) within the pin is given by the equation

$$T_f(r,z) = T_m(z) - q_l(z) \frac{r^2}{4\pi a^2 k} \qquad (17)$$

where

$T_m(z)$ = fuel center-line temperature at height z
$q_l(z)$ = linear heat rate at height z
k = fuel conductivity
a = radius of the fuel pin

On the other hand,

$$T_m(z) = T_s(z) + q_l(z)\, RH \qquad (18)$$

where

$T_s(z)$ = bulk coolant temperature at height z
R = total thermal resistance (fuel + cladding + coolant film)
H = pin height

The bulk coolant temperature, $T_s(z)$, at point z is given by the equation

$$T_s(z) = T_{in} + \frac{\int_0^z q_l(z)\, dz}{m\, C_p} \tag{19}$$

where

T_{in} = coolant inlet temperature
m = pin channel coolant flow rate

Thus, Eq. (18) can be written as

$$T_f(r,z) = T_{in} + q_l(z) \left[RH - \frac{r^2}{4\pi a^2 k}\right] + \frac{\int_0^z q_l(z)dz}{m\, C_p} \tag{20}$$

The cladding temperature, $T_c(r,z)$, at position (r,z) is given by the relation

$$T_c(r,z) = T_s(z) + q_l(z) \left[\frac{1}{2\pi h(a+b)} - \frac{1}{2\pi k_c} \ln\left(\frac{r}{a+b}\right)\right] \tag{21}$$

where

k_c = thermal conductivity of the cladding
b = cladding thickness
h = coolant heat transfer coefficient

If the reactor state changes from one steady-state to another steady-state, the total enthalpy change, ΔE, of the pin channel (fuel + cladding + coolant) will be

$$\begin{aligned}\Delta E = & \int_0^H \int_0^a \Delta T_f(r,z)\rho_f C_f 2\pi r dr dz \\ & + \int_0^H \int_a^{a+b} \Delta T_c(r,z)\rho_c C_c 2\pi r dr dz \\ & + A_s \int_0^H \Delta T_s(z)\rho_s C_p\, dz\end{aligned} \tag{22}$$

where

$\Delta T_f, \Delta T_c, \Delta T_s$ = fuel, cladding, and bulk coolant temperature changes, respectively.

ρ_f, ρ_c, ρ_s = fuel, cladding, and coolant densities, respectively.

C_f, C_c, C_p = fuel, cladding, and coolant specific heats, respectively.

A_s = coolant flow area for one pin channel

Taking into account Eqs. (19), (20), and (21), Eq. (22) is rewritten as

$$\Delta E = \int_0^H \int_0^a \left\{ \Delta q_1(z) \left[RH - \frac{r^2}{4\pi a^2 k} \right] + \frac{\int_0^z \Delta q_1(z)dz}{mC_p} \right\} \rho_f C_f 2\pi r dr dz$$

$$+ \int_0^H \int_a^{a+b} \left\{ \frac{\int_0^z \Delta q_1(z)dz}{m\, C_p} + \Delta q_1(z) \left[\frac{1}{2\pi h\ (a+b)} - \frac{1}{2\pi k_c} \ln\left(\frac{r}{a+b}\right) \right] \right\} \rho_c C_c 2\pi r dr dz$$

$$+ A_s \int_0^H \frac{\int_0^z \Delta q_1(z)dz}{m\, C_p}\ \rho_s C_p dz \qquad (23)$$

where

Δq_1 = linear heat rate change

If s(z) is the shape of the pin power distribution along the z direction, then

$$\int_0^H \left[\int_0^z q_1(z)dz \right]\ dz = q \int_0^H \left[\int_0^z s(z)dz \right]\ dz = q\ \ S \qquad (24)$$

Since the cladding thickness, b, is much smaller than the fuel pin radius,a, to simplify the presentation, and without any loss of generality the integral

$$I_c = \int_a^{a+b} \left\{ \frac{\int_0^z \Delta q_1(z)dz}{m\, C_p} + \Delta q_1(z) \left[\frac{1}{2\pi h(a+b)} - \frac{1}{2\pi k_c} \ln\left(\frac{r}{a+b}\right) \right] \right\} 2\pi r dr$$

is approximated by

$$I_c = 2\pi ab\left\{\frac{\int_o^z \Delta q_1(z)dz}{mC_p} + \Delta q_1(z)HR_c\right\} \tag{25}$$

where

$$R_c = \frac{1}{2\pi h(a+b)H} + \frac{b}{4\pi(a+b)Hk_c} \tag{26}$$

Also, to simplify the presentation, the variation of the material densities and specific heats with temperature are neglected. After the integrations are performed, Eq. (23) gives

$$\Delta E = \Delta q\left\{\pi a^2 H\left(\frac{S}{HmC_p} + R - \frac{1}{8\pi Hk}\right)\rho_f C_f + 2\pi abH\left(R_c + \frac{S}{HmC_p}\right)\rho_c C_c + A_s H\frac{S}{HmC_p}\rho_s C_p\right\}$$

or

$$\Delta E = \Delta q\phi \tag{27}$$

where

$$\phi = \pi a^2 H\rho_f C_f\left(\frac{S}{HmC_p} + R - \frac{1}{8\pi Hk}\right) + 2\pi abH\rho_c C_c\left(R_c + \frac{S}{HmC_p}\right) + A_s H\rho_s C_p\frac{S}{HmC_p} \tag{28}$$

Consider two pins that at a given steady-state produce q_1 and q_2 watts of power, respectively,and

$$\frac{q_1}{q_2} = \lambda$$

If at another steady-state these pins produce q_1^* and q_2^* watts of power, respectively, and if during the transient, which leads from the first to the second steady-state, the power changes uniformly in both pins, then

$$\frac{q_1}{q_2} = \frac{q_1^*}{q_2^*} = \lambda$$

or

$$\frac{q_1^* - q_1}{q_2^* - q_2} = \lambda$$

The enthalpy changes in these pins (fuel + cladding + coolant) will be

$$\Delta E_1 = \Delta q_1 \, \phi_1$$

$$\Delta E_2 = \Delta q_2 \, \phi_2$$

or

$$\frac{\Delta E_1}{\Delta E_2} = \frac{q_1}{q_2} \frac{\phi_1}{\phi_2} = \lambda \frac{\phi_1}{\phi_2} \qquad (29)$$

The total energy, $Q_1(\tau_1)$, produced by the first pin during the transient is

$$Q_1(\tau_1) = q_1 \int_0^{\tau_1} w(t)dt$$

where τ_1 is the time required for the first pin to reach the new steady-state condition.

Similarly, for the second pin

$$Q_2(\tau_2) = q_2 \int_0^{\tau_2} w(t)dt$$

and

$$\frac{Q_1(\tau_1)}{Q_2(\tau_2)} = \frac{q_1}{q_2} \frac{\int_0^{\tau_1} w(t)dt}{\int_0^{\tau_2} w(t)dt}$$

or

$$\frac{q_1}{q_2} = \frac{Q_1(\tau_1)\int_0^{\tau_2} w(t)dt}{Q_2(\tau_2)\int_0^{\tau_1} w(t)dt} = \frac{Q_1(\tau_1)}{Q_2(\tau_2)} \quad \nu = \lambda \tag{30}$$

where

$$\nu = \frac{\int_0^{\tau_2} w(t)dt}{\int_0^{\tau_1} w(t)dt} \tag{31}$$

The amounts of energy stored in the channel materials of the two pins during the transient, are

$$P_1(\tau_1) = \Delta E_1$$

$$P_2(\tau_2) = \Delta E_2$$

and

$$\frac{P_1(\tau_1)}{P_2(\tau_2)} = \frac{\Delta E_1}{\Delta E_2} = \lambda \frac{\phi_1}{\phi_2} \tag{32}$$

Since,

$$\lambda = \nu \frac{Q_1(\tau_1)}{Q_2(\tau_2)}$$

Eq. (32) gives

$$\frac{P_1(\tau_1)/Q_1(\tau_1)}{P_2(\tau_2)/Q_2(\tau_2)} = \nu \frac{\phi_1}{\phi_2} \tag{33}$$

Since both pins have the same coolant outlet temperature at the first steady-state, they will also have the same coolant outlet temperature at the second steady-state. If both pins reach the second steady-state at the same time, then,

$$\tau_1 = \tau_2 = \tau \ , \ \nu = 1$$

and, as was shown earlier,

$$\frac{P_1(\tau)/Q_1(\tau)}{P_2(\tau)/Q_2(\tau)} = 1$$

If both pins are either core or blanket pins and if small differences in ρ_f, ρ_c, C_f, C_c, k, R and R_c, due to cladding and fuel temperature differences, are neglected, then Eq. (28) gives

$$\phi_1 - \phi_2 = S(\pi a^2 \rho_f C_f + 2\pi ab\rho_c C_c + A_s \rho_s C_p) \left(\frac{1}{m_1 C_p} - \frac{1}{m_2 C_p}\right)$$

or

$$\phi_1 - \phi_2 = S\Delta T(\pi a^2 \rho_f C_f + 2\pi ab\rho_c C_c + A_s \rho_s C_p)\left(\frac{1}{q_1} - \frac{1}{q_2}\right)$$

where ΔT is the coolant temperature rise at steady-state. For $q_1 > q_2$

$$\phi_1 - \phi_2 < 0$$

Since ϕ is always positive,

$$\frac{\phi_1}{\phi_2} < 1$$

and for

$$\frac{P_1(\tau)/Q_1(\tau)}{P_2(\tau)/Q_2(\tau)}$$

to be equal to one, ν must be greater than one [Eq. (33)].

If ν is greater than one, then,

$$\int_0^{\tau_2} w(t)dt > \int_0^{\tau_1} w(t)dt$$

or τ_2 must be greater than τ_1. This is contrary to the assumption that $\tau_1 = \tau_2$.

In conclusion, if both pins are either core or blanket pins and they do not have the same power rating, they will not reach the second steady-state at the same time. It will take longer, for the pin that has lower rating, to reach the second steady-state coolant outlet temperature. In other words, during the transient, the coolant of the pin that has lower power rating will reach a given outlet temperature some time later than the coolant of the other pin.

If the first pin is a core pin and the second pin is a blanket pin, then,

$$\frac{\phi_1}{\phi_2} = \left\{ \pi a_1^2 H \rho_{f1} C_{f1} \left(\frac{S_1 \Delta T}{H q_1} + R_1 - \frac{1}{8\pi H k_1}\right) + 2\pi a_1 b_1 H \rho_{c1} C_{c1} \left(R_{c1} + \frac{S_1 \Delta T}{H q_1}\right) + A_{s1} H \rho_{s1} C_{p1} \frac{S_1 \Delta T}{H q_1} \right\} \Bigg/ \left\{ \pi a_2^2 H \rho_{f2} C_{f2} \left(\frac{S_2 \Delta T}{H q_2} + R_2 - \frac{1}{8\pi H k_2}\right) + 2\pi a_2 b_2 H \rho_{c2} C_{c2} \left(R_{c2} + \frac{S_2 \Delta T}{H q_2}\right) + A_{s2} H \rho_{s2} C_{p2} \frac{S_2 \Delta T}{H q_2} \right\} \quad (34)$$

The power distribution in the core and the blankets has about the same cosine shape in the axial direction and

$$S_1 \approx S_2 \approx S = \int_0^H \left[\int_0^z s(z) dz \right] dz \approx H/2$$

The values of the quantities $\rho_f, C_f, R, k, b, \rho_c, C_c, R_c, \rho_s$ and C_p in the core are not significantly different than their values in the blanket. Thus, if q_2 is not much larger than q_1, and if a_2 is significantly larger than a_1, as the case is in practical reactor designs, then

$$\frac{\phi_1}{\phi_2} < 1$$

For example, for the reactor analyzed in this report, Eq. (34) gives

$$\frac{\phi_1}{\phi_2} = \frac{1795.4\left(\frac{93.3}{q_1} + 0.0242\right) a_1^2 + 160.1\left(\frac{93.3}{q_1} + 3.58\times10^{-4}\right) a_1 + 35.25 \frac{93.3}{q_1}}{1795.4\left(\frac{93.3}{q_2} + 0.0116\right) a_2^2 + 148.5\left(\frac{93.3}{q_2} + 2.11\times10^{-4}\right) a_2 + 48.74 \frac{93.3}{q_2}}$$

or

$$\frac{\phi_1}{\phi_2} \approx \frac{(\frac{93.3}{q_1} + 0.0242)\ a_1^2}{(\frac{93.3}{q_2} + 0.0116)\ a_2^2} \approx \frac{a_1^2}{a_2^2}\ \frac{q_2}{q_1}$$

For $a_1 = 0.32$ cm and $a_2 = 0.535$ cm.,

$$\frac{\phi_1}{\phi_2} \approx \left(\frac{0.32}{0.535}\right)^2\ \frac{q_2}{q_1}$$

Thus, if

$$q_2 < 2.8q_1$$

then

$$\frac{\phi_1}{\phi_2} < 1$$

In practical designs, there is no significant difference between the peak power ratings of the core and blanket pins and

$$q_2 << 2.8q_1$$

Consequently,

$$\frac{\phi_1}{\phi_2} << 1$$

and for the same reasons discussed earlier, during the transient the coolant in the peak blanket pin will reach a given outlet temperature some time later than the coolant in the peak core pin.

In summary, the analysis presented shows that:

1) For two pin channels that have the same coolant outlet temperature at steady-state, to have the same coolant outlet temperature during a loss-of-flow transient the ratio

$$\frac{P_1(\tau)/Q_1(\tau)}{P_2(\tau)/Q_2(\tau)}$$

must be equal to one.

2) For two pin channels where the ratio

$$\frac{P_1(\tau)/Q_1(\tau)}{P_2(\tau)\ Q_2(\tau)}$$

is smaller than one, sodium boiling during a transient will be incoherent even if these channels have the same coolant outlet temperature at steady-state.

3) Two core or two blanket pin channels that have the same coolant outlet temperature at steady-state, will not start boiling at the same time if they have different power ratings.

4) If the blanket pins have a larger diameter, and consequently, a larger heat capacity than the core pins, then sodium boiling during a transient will be incoherent between core and blankets, even if at steady-state the blankets have the same coolant outlet temperature as the core. Boiling in the blanket will start some time later than in the core.

Reference

1. Project Management Corporation. CRBR Preliminary Safety Analysis Report. (1975).

APPENDIX P

INCENTIVES FOR VENTED DUCT DESIGNS

One way to improve breeding performance is to reduce the pressure drop across the duct wall of an assembly by "venting" the duct because the reduced pressure differential will permit a reduction in the duct wall thickness. The intent of this analysis was to determine the incentives for venting ducts. For this purpose, a series of breeding performance calculations were carried out where duct wall thickness and interassembly gap were varied. The latter change was necessary to take into consideration duct rounding due to irradiation creep which increases rapidly with decreasing duct wall thickness. The parametric approach was prefered over an analysis of specific designs because:

- it is difficult to accurately predict the bypass flow because of slots in the assembly duct above the core region and the resulting reduction in pressure drop.
- even for 20% CW316SS the creep and swelling correlations are still changing significantly whenever new high-fluence data becomes available.

The reference reactor for this investigation is described in Table P.1. The core layout is shown in Figure P.1.

Equilibrium cycle analyses were carried out with the REBUS code system using 8-group cross sections processed by the MC^2-2 code system and derived from the ENDF/-B-IV data. The calculations were carried out in RZ geometry. The control rods were represented as concentric rings containing B_4C in a concentration which gave the same worth as in hexagonal geometry calculations where the control rods were discretely mocked up.

The results of this analysis are shown in Figure P.2. A 10 mil reduction in duct wall thickness reduces doubling time by slightly less than 6 months. The same reduction in sodium gap reduces the doubling time by less than one month. A reduction

Table P.1

DESIGN PARAMETERS

Fuel Pin/Blanket Pin	
Cladding O.D., in.	0.26/0.425
Cladding Thickness, in.	0.013/0.013
Fuel Smear Density, % T.D.	88/90
Fuel Assembly/Blanket Assembly	
Pins Per Assembly	271/127
p/d	1.197/1.070
Lattice Pitch, in.	5.653/5.653
Duct Thickness, in.	0.113/0.113
Interassembly Gap, in.	0.215/0.215
Nominal Peak Linear Heat Rating, kw/ft	
Core	13.4
Internal Blanket	12.8
Radial Blanket	8.7
Number of Assemblies	
Inner Core	36
Middle Core	72
Outer Core	222
Internal Blanket 1	19
Internal Blanket 2	24
Internal Blanket 3	78
Internal Blanket 4	36
Control	24
Radial Blanket	174
Shield	198

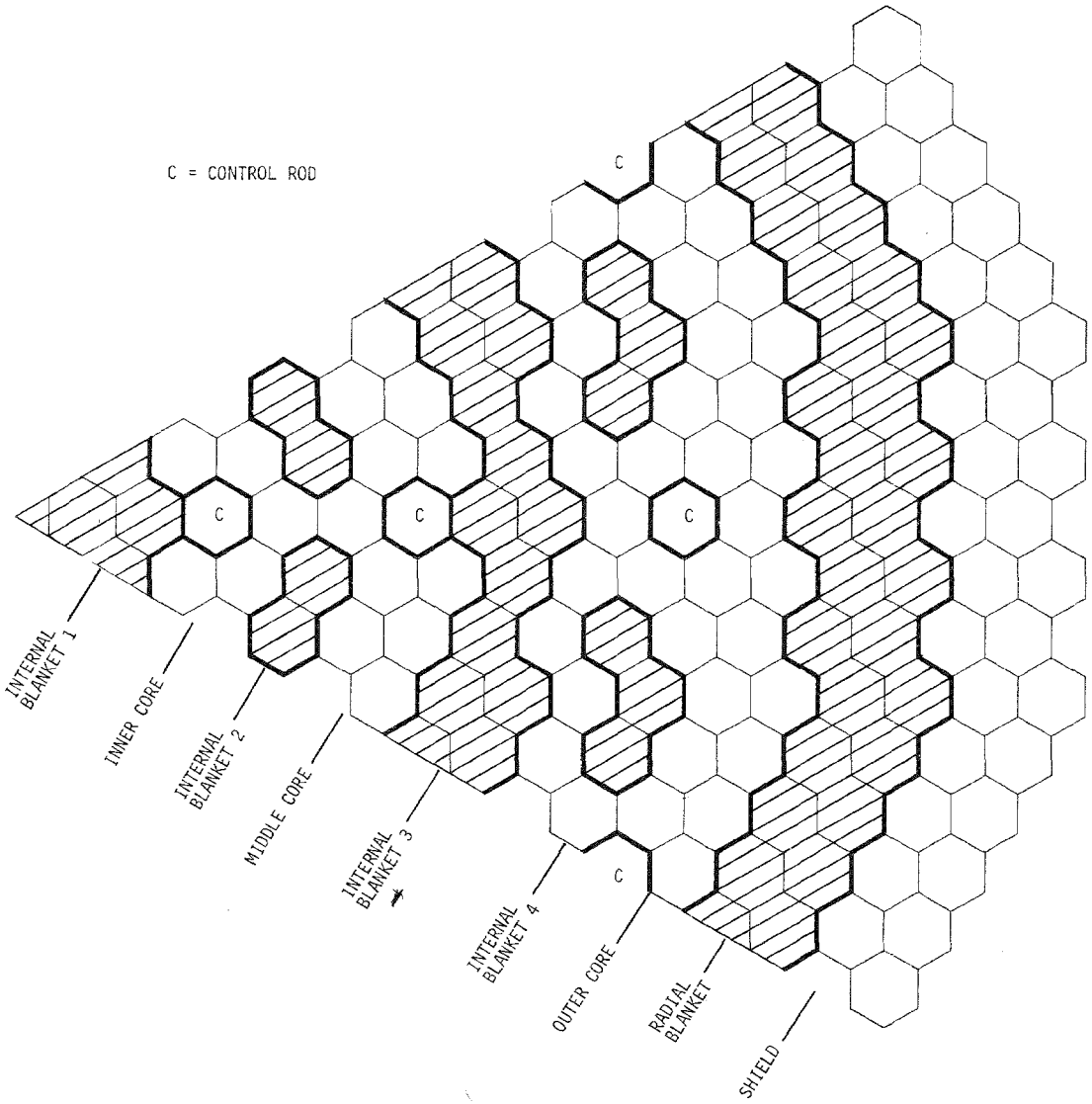

Figure P.1. Core Configuration for Reference Reactor

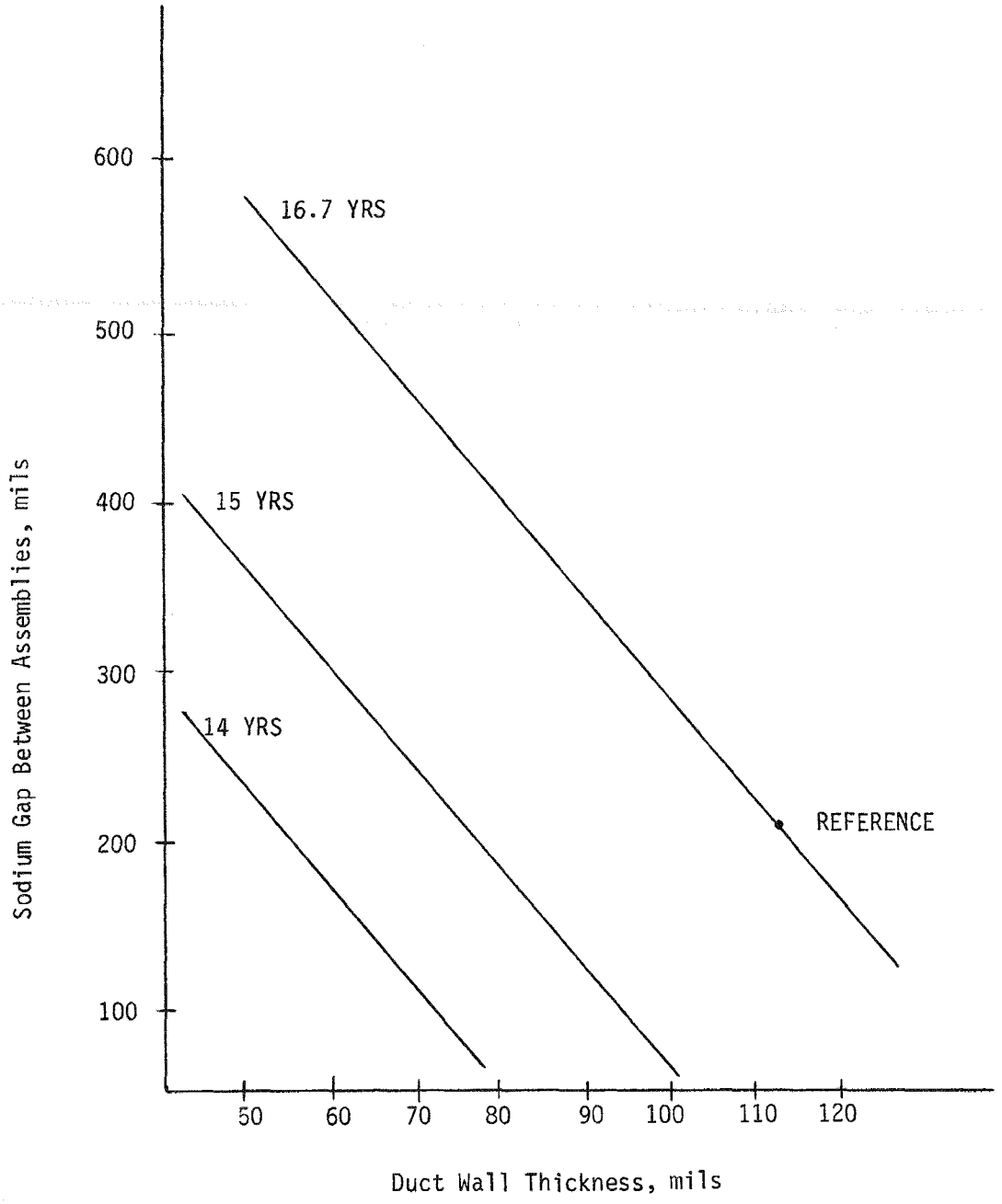

Figure P.2. Doubling Time as a Function of Sodium Gap and Duct Wall Thickness

in sodium gap size of 60 mil is equivalent to a 10 mil reduction in duct wall thickness in regard to doubling time.

A 10 mil reduction in duct wall thickness requires a pressure drop reduction of approximately 20%. This pressure drop reduction is the equivalent of a 20 inch reduction in effective length of the fuel bundle. A one year reduction in doubling time requies a 20 mil reduction in duct wall thickness. This in turn requires a 40% reduction in pressure drop which is the equivalent of a 40 inch effective length reduction for the bundle. For the design under consideration this must be considered the upper limit in improving breeding performance.